Towards Understanding of the Local Structure and Li-Ion Dynamics in Solid Electrolyte Candidates Using Solid-State NMR

Thesis submitted in accordance with the requirements of the University of Liverpool for the degree of Doctor in Philosophy

by

Benjamin B. Duff

Department of Chemistry

March 2023

Towards Understanding of the Local Structure and Li-Ion Dynamics in Solid Electrolyte Candidates Using Solid-State NMR

Benjamin B. Duff

Abstract

It is of great interest to develop solid state ionic conductors to replace liquid electrolytes in next-generation Li-ion battery technologies due to the significant effect upon everyday life that comes from the enhancement of power output, safety and lifetime of current generation Li-ion batteries. Research teams from all over the world are continuously examining potential candidates to produce such materials, but challenges like lithium electrochemistry stability and poor ionic conductivity make it difficult to reach the goal. Li-containing materials providing fast ion transport pathways are fundamental in Li solid electrolytes and the future of all-solid-state batteries. Understanding the structures as well as the Li-ion pathways, is paramount for further developments in next-generation Li solid electrolytes. Solid-state nuclear magnetic resonance (NMR) spectroscopy is an invaluable analytical technique in the research of solid-state Li-ion conductors due to the capability of probing both the structures and ion dynamics on the atomic level and across a wide range of timescales that are often inaccessible by other experimental techniques. In this thesis, advanced solid-state NMR techniques have been utilised in order to probe the structures of a series of newly synthesised materials as well as access the Li-ion dynamics from the ultra-slow (sub-HZ) to the ultra-fast (MHz) scales.

Firstly, static ^{7}Li line narrowing NMR, ^{6}Li magic-angle spinning, ^{6}Li-^{6}Li exchange spectroscopy and ^{7}Li relaxometry were used in order to fully characterise the ion mobility pathways in two newly synthesised lithium aluminium sulfides, Li_3AlS_3 and $Li_{4.3}AlS_{3.3}Cl_{0.7}$, where in the former, ^{7}Li variable temperature revealed the presence of both mobile and immobile Li ions while in the latter a single type of fast-moving ion is present and responsible for the higher conductivity of this phase. ^{6}Li-^{6}Li exchange spectroscopy spectra of Li_3AlS_3 revealed that the slower moving ions hop between non-equivalent Li positions in different structural layers. The absence of the immobile ions in $Li_{4.3}AlS_{3.3}Cl_{0.7}$, as revealed from ^{7}Li line narrowing experiments, suggested an increased rate of ion exchange between the layers in this phase compared with Li_3AlS_3. Secondly, ^{7}Li line narrowing and relaxation measurements allowed for the quantification of the Li-ion jump rates in the anion substituted phase $Li_{3.3}SnS_{3.3}Cl_{0.7}$. Detailed analysis of the frequency dependence of the NMR relaxation rates indicated low-dimensional Li-ion diffusion, which when combined with the results from the nuclear density obtained from the maximum entropy method, revealed the Li-ion pathway to be one-dimensional. Finally, a series of ^{6}Li and ^{31}P NMR techniques in conjunction with density functional theory allowed for the characterisation of the structure of the ultraphosphate phase $Li_3P_5O_{14}$. A number of complimentary ^{7}Li NMR techniques also allowed for the quantification of the ion dynamics and confirm the ion pathway to be three-dimensional. These results signify the importance of solid-state NMR for the research of new Li-ion conductors as not only a complimentary analytical technique to other methods, but also a primary standard for the experimentally

obtained ion mobility pathways and quantification on timescales inaccessible to other methods.

Thesis overview

Chapter 1 covers basic principles of NMR along with an introduction to the solid-state NMR methods and theory used within this thesis.

Chapter 2 provides a general introduction to battery technology as well as a literature review of selected NMR techniques used to probe ion dynamics in this field.

Chapter 3 is comprised of three published papers concerning two newly synthesised aluminium sulfides, Li_3AlS_3 and $Li_{4.3}AlS_{3.3}Cl_{0.7}$ entitled "Computationally Guided Discovery of the Sulfide Li_3AlS_3 in the Li–Al–S Phase Field: Structure and Lithium Conductivity" and "$Li_{4.3}AlS_{3.3}Cl_{0.7}$: A Sulfide–Chloride Lithium Ion Conductor with Highly Disordered Structure and Increased Conductivity". These two papers are focussed on the first reporting of these materials along with various analytical techniques used to probe these new phases, this chapter combines the NMR contribution to these two collaborative works, where NMR was used in order to contribute to the structural elucidation of these phases. The NMR from these two papers is combined with a third paper entitled "Towards Understanding of the Li-Ion Migration Pathways in the Lithium Aluminium Sulphides Li_3AlS_3 and $Li_{4.3}AlS_{3.3}Cl_{0.7}$ via ^{6,7}Li Solid-State Nuclear Magnetic Resonance Spectroscopy" focussed on probing the ion dynamics in both materials via a range of ^{6,7}Li solid-state NMR techniques.

Chapter 4 is comprised of the NMR contribution to the collaborative paper entitled "Element selection for crystalline inorganic solid discovery guided by unsupervised machine learning of experimentally explored chemistry"

encompassing the detailed analysis of the Li-ion mobility in the newly discovered material $Li_{3.3}SnS_{3.3}Cl_{0.7}$ through ^{7}Li variable temperature NMR experiments.

Chapter 5 contains the NMR contribution to the recent reporting of the ultraphosphate phase $Li_3P_5O_{14}$ entitled “Extended Condensed Ultraphosphate Frameworks with Monovalent Ions Combine Lithium Mobility with High Computed Electrochemical Stability” as well as an ongoing project focussing on probing the Li-Ion dynamics via a range of solid-state NMR techniques.

Chapter 6 gives an overall conclusion and future outlook for the project.

Note: All chapters which contain work based on publication have been amended to include the supporting information into the main text. All chapters should be considered standalone, in that abbreviations and equations will be repeated if not previously mentioned in that chapter.

Acknowledgements

Finally after four and a half years, this thesis has come together. First and foremost I would like to say a big thank you to both of my supervisors Professor Matthew Rosseinsky and Professor Frédéric Blanc for giving me this opportunity to study for my PhD at the University of Liverpool, I will be forever grateful to both of you. Matt and his group have provided me with the samples required in order to complete my studies as well as the opportunity to work on so many collaborative projects that have carved the path to where I am today. The many meetings we have had to discuss research and for feedback on writing papers have been invaluable. Fred, I cannot thank you enough for all the help and support you have given me over the years. The constant corrections, persistence and patience you have given me have allowed me to develop into the researcher I am today. Hopefully enough of your immense knowledge in NMR has been passed on to me these past few years to help me in the future, I look forward to continuing working together for as long as possible.

I would also like to express my gratitude to the many other PhD students, post docs and research coordinator in the Rosseinsky group, particularly Dr Luke Daniels for his help in all matters to do with research and scientific writing, Dr Jacinthe Gamon the first collaborator I had for my very first paper back in 2019 and we have worked together on many papers since.

Formally, I would like to acknowledge the University of Liverpool and the Faraday Institution (SOLBAT) for the funding required for my doctoral training, without which there would not have been a position available for me. The UK

high field solid-state NMR Facility used in this research for high field data was funded by EPSRC and BBSRC, as well as the University of Warwick including via part funding through Birmingham Science City Advanced Materials Projects 1 and 2 supported by Advantage West Midlands (AWM) and the European Regional Development Fund (ERDF). Assistance from the facility Managers, Dr Dinu Iuga and Dr Trent Franks is also appreciated. I would also like to thank EPSRC for the funding of the 800 MHz spectrometer here at Liverpool, where a large number of experiments in this thesis were recorded.

Ashlea and Andrea were the first two guides in my journey towards gaining a PhD. The three of us all went through tough times in the early years but we always had each other to fall back on and rant to if needed. You both were always my first port of call when things ~~often~~ sometimes went wrong. Without you both I do not know if I would have made it through the first year of my PhD and although we have been separated now, I hope you know I will always be there for both of you if needed.

In the last few years of my PhD after Ashlea and then Andrea graduated, the group welcomed some new faces. Lucia, Aine and Stuart in particular have been great friends to me over the last few years, spending many a night in the pub (and lab) helping each other in whatever way we can and providing support whenever any of us needed it. Not to forget the newest members of the group who have already fit in perfectly and I am looking forward to working with you all more in the future.

I also want to thank my family. My mum and dad who I am sure understand absolutely everything I say about my research during our late evening calls

when I work late. Mum, you have always supported and loved me unconditionally, whether I am right or wrong I know you will always have my back and support me. You have cared for me my entire life, from dressing me as a child to doing my washing while I was at university and making the best roast dinners in the world. I know whatever I do in my life, whether it a success or a failure you will always be there to be my biggest fan or to console me. Dad, you have not only been my dad but also my friend. Whether it is communicating through TV and movie quotes, stupid inside jokes, playing games or pretending to understand when I talk about work, you always know what to do to make me laugh. Without the support from both of you and guidance all my life, I would never have made it where I am today. Thank you both so much. I guess Josh was also there. Josh, my brother and biggest rival growing up and still to this day. Probably the reason why I am so competitive and want to be the best at everything, which is likely one of the factors behind me choosing to do a PhD in the first place, so yeah thanks I guess… and I look forward to having more free time now to spend with my new niece and nephew Harper and Kyle and sister Leanne.

Finally, Gem. I quite simply would not have been able to do this without you. My first port of call, my rock. Whether it is making me feel better after a bad day or having a nice hot meal ready for me after working late, you have been there for me every day from the first. I know the last few years have been tough for you, taking care of both of us while working full-time and I will be forever grateful to you for everything you have done for me these past eight years. I love you.

Awards, Presentations and Publications

Awards

2021 Runner-up prize for best poster presentation at RSC Annual NMR Discussion Group Postgraduate virtual meeting

2022 Runner-up prize for best oral presentation at RSC Annual NMR Discussion Group Postgraduate meeting in Manchester

Presentations

2019 Poster presentation at the RSC Solid State Chemistry group meeting in Liverpool.

2021 Poster/short talk at the Experimental Nuclear Magnetic Resonance Virtual Conference.

Poster/short talk at RSC Annual NMR Discussion Group Postgraduate virtual meeting (runner-up prize).

Poster presentation at the Faraday Institution Virtual Conference.

2022 Oral presentation at the UK solid-state NMR facility annual symposium in Warwick

Oral presentation at RSC Annual NMR Discussion Group Postgraduate meeting in Manchester (runner-up prize).

Poster presentation at the Rocky Mountain Conference on Magnetic Resonance in Colorado, USA.

Publications

"Computationally Guided Discovery of the Sulfide Li_3AlS_3 in the Li–Al–S Phase Field: Structure and Lithium Conductivity" Jacinthe Gamon, Benjamin B. Duff, Matthew S. Dyer, Christopher Collins, Luke M. Daniels, T. Wesley Surta, Paul M. Sharp, Michael W. Gaultois, Frédéric Blanc, John Bleddyn Claridge, and Matthew J. Rosseinsky, *Chem. Mater.*, **2019**, 31, 9699-9714. Chapter 3 contains the NMR contribution from this publication.

"$Li_6SiO_4Cl_2$: A Hexagonal Argyrodite Based on Antiperovskite Layer Stacking" Alexandra Morscher, Matthew S. Dyer, Benjamin B. Duff, Guopeng Han, Jacinthe Gamon, Luke M. Daniels, Yun Dang, T. Wesley Surta, Craig M. Robertson, Frédéric Blanc, John B. Claridge, and Matthew J. Rosseinsky, *Chem. Mater.*, **2021**, 33, 2206-2217.

"Polymorph of $LiAlP_2O_7$: Combined Computational, Synthetic, Crystallographic, and Ionic Conductivity Study" Elvis Shoko, Yun Dang, Guopeng Han, Benjamin B. Duff, Matthew S. Dyer, Luke M. Daniels, Ruiyong Chen, Frédéric Blanc, John B. Claridge, and Matthew J. Rosseinsky, *Inorg. Chem.*, **2021**, 60, 14083-14095.

"Element selection for crystalline inorganic solid discovery guided by unsupervised machine learning of experimentally explored chemistry" Andrij Vasylenko, Jacinthe Gamon, Benjamin B. Duff, Vladimir V. Gusev, Luke M. Daniels, Marco Zanella, J. Felix Shin, Paul M. Sharp, Alexandra Morscher, Ruiyong Chen, Alex R. Neale, Laurence J. Hardwick, John B. Claridge, Frédéric Blanc, Michael W. Gaultois, Matthew S. Dyer, and Matthew J.

Rosseinsky,. *Nat Commun*, **2021**, 12, 5561. Chapter 4 contains the NMR contribution from this publication.

“Extended Condensed Ultraphosphate Frameworks with Monovalent Ions Combine Lithium Mobility with High Computed Electrochemical Stability” Guopeng Han, Andrij Vasylenko, Alex R. Neale, Benjamin B. Duff, Ruiyong Chen, Matthew S. Dyer, Yun Dang, Luke M. Daniels, Marco Zanella, Craig M. Robertson, Laurence J. Kershaw Cook, Anna-Lena Hansen, Michael Knapp, Laurence J. Hardwick, Frédéric Blanc, John B. Claridge, and Matthew J. Rosseinsky, *J. Am. Chem. Soc.*, **2021**, 143, 18216-18232. Chapter 5 contains the NMR contribution from this publication.

“Li+ Dynamics of Liquid Electrolytes Nanoconfined in Metal–Organic Frameworks” Marco Farina,[†] Benjamin B. Duff,[†] Cristina Tealdi, Andrea Pugliese, Frédéric Blanc, and Eliana Quartarone, *ACS Appl. Mater. Interfaces*, **2021** 13, 53986-53995.

“$Li_{4.3}AlS_{3.3}Cl_{0.7}$: A Sulfide–Chloride Lithium Ion Conductor with Highly Disordered Structure and Increased Conductivity” Jacinthe Gamon, Matthew S. Dyer, Benjamin B. Duff, Andrij Vasylenko, Luke M. Daniels, Marco Zanella, Michael W. Gaultois, Frédéric Blanc, John B. Claridge, and Matthew J. Rosseinsky, *Chem. Mater.*, **2021**, 33, 8733-8744. Chapter 3 contains the NMR contribution from this publication.

“Cation Disorder and Large Tetragonal Supercell Ordering in the Li-Rich Argyrodite $Li_7Zn_{0.5}SiS_6$” Bernhard T. Leube, Christopher M. Collins, Luke M.

Daniels, Benjamin B. Duff, Yun Dang, Ruiyong Chen, Michael W. Gaultois, Troy D. Manning, Frédéric Blanc, Matthew S. Dyer, John B. Claridge, and Matthew J. Rosseinsky, *Chem. Mater.*, **2022**, 34, 4073-4087.

"Off-the-Shelf $Gd(NO_3)_3$ as an Efficient High-Spin Metal Ion Polarizing Agent for Magic Angle Spinning Dynamic Nuclear Polarization" Stuart J. Elliott, Benjamin B. Duff, Ashlea R. Taylor-Hughes, Daniel J. Cheney, John P. Corley, Subhradip Paul, Adam Brookfield, Shane Pawsey, David Gajan, Helen C. Aspinall, Anne Lesage, and Frédéric Blanc, *J. Phys. Chem. B*, **2022**, 126, 6281-6289.

"Control of Ionic Conductivity by Lithium Distribution in Cubic Oxide Argyrodites $Li_{6+x}P_{1-x}Si_xO_5Cl$" Alexandra Morscher, Benjamin B. Duff, Guopeng Han, Luke M. Daniels, Yun Dang, Marco Zanella, Manel Sonni, Ahmad Malik, Matthew S. Dyer, Ruiyong Chen, Frédéric Blanc, John B. Claridge, and Matthew J. Rosseinsky, *J. Am. Chem. Soc.*, **2022**, 144, 22178-22192.

"Towards Understanding of the Li-Ion Migration Pathways in the Lithium Aluminium Sulphides Li_3AlS_3 and $Li_{4.3}AlS_{3.3}Cl_{0.7}$ via $^{6,7}Li$ Solid-State Nuclear Magnetic Resonance Spectroscopy" Benjamin B. Duff, Stuart J. Elliott, Jacinthe Gamon, Luke M. Daniels, Matthew J. Rosseinsky, and Frédéric Blanc, *Chem. Mater.*, **2023**, 35, 27-40. Chapter 3 contains the NMR contribution from this publication.

"A Database of Experimentally Measured Lithium Solid Electrolyte Conductivities Evaluated with Machine Learning" Cameron J. Hargreaves, Michael W. Gaultois, Luke M. Daniels, Emma J. Watts, Vitaliy A. Kurlin,

Michael Mora, Yun Dang, Rhun Morris, Alexandra Morscher, Kate Thompson, Matthew A. Wright, Beluvalli-Eshwarappa Prasad, Frédéric Blanc, Chris M. Collins, Catriona A. Crawford, Benjamin B. Duff, Jae Evans, Jacinthe Gamon, Guopeng Han, Bernhard T. Leube, Hongjun Niu, Arnaud J. Perez, Aris Robinson, Oliver Rogan, Paul M. Sharp, Elvis Shoko, Manel Sonni, William J. Thomas, Andrij Vasylenko, Lu Wang, Matthew J. Rosseinsky, Matthew S. Dyer, *npj Comput Mater*, **2023**, 9:9.

List of Abbreviations

0D	Zero-dimensional
1D	One-dimensional
2D	Two-dimensional
3D	Three-dimensional
ASSB	All solid-state battery
BPP	Bloembergen-Purcell-Pound
BVS	Bond valence sum
CSA	Chemical shift anisotropy
DAS	Dynamic angle spinning
DOR	Double rotation
DFT	Density functional theory
DQF	Double quantum filtered
EFG	Electric field gradient
EIS	Electrochemical impedance spectroscopy
EXSY	Exchange spectroscopy
FID	Free induction decay
FWHM	Full-width at half maximum
hcp	Hexagonal close-packed
HETCOR	Heteronuclear correlation
HT	High temperature
INADEQUATE	Incredible natural abundance double quantum experiment
LISICON	Lithium superionic conductor
MAS	Magic angle spinning
MEM	Maximum entropy method
ML	Machine learning
MQF	Multiple quantum filtered
MQMAS	Multiple quantum magic angle spinning
NASICON	Sodium superionic conductor
NMR	Nuclear magnetic resonance spectroscopy
NOE	Nuclear overhauser effect
NOESY	Nuclear overhauser effect spectroscopy
OPP	One particle potential
PAS	Principal axis system
PFG	Pulsed field gradient
REDOR	Rotational-echo double-resonance
rf	Radiofrequency
SAE	Spin-alignment echo
SLR	Spin-lattice relaxation
Sof	Site occupancy factor
SS-NMR	Solid-state nuclear magnetic resonance spectroscopy
TQF	Triple quantum filtered
VAE	Variational autoencoder
VT	Variable temperature
XRD	X-ray diffraction

Table of Contents

1. Introduction

1.1 Nuclear Magnetic Resonance Spectroscopy[1,2]

1.1.1 Spin angular momentum

It is well known that atoms, molecules and nuclei possess two distinct forms of momentum. The first, classical angular momentum arises in rotating objects or executes a trajectory along a curved path, much like the earth orbiting around the sun. Spin is the second variety of angular momentum and is an intrinsic property to the majority of nuclei in nature. However, spin angular momentum, **I** is not related in any way to rotation but rather an intrinsic property of particles. In quantum mechanics, spin angular momentum I is quantized in units of the reduced Planck's constant, ħ and the allowed quantized values of **I** are:

$$\mathbf{I} = \hbar\sqrt{\mathrm{I}(\mathrm{I}+1)} \qquad \text{(Eq. 1.1)}$$

where I is the principal spin quantum number and is any positive value of n/2 e.g 1/2, 1, 3/2, etc. Atomic nuclei consist of protons and neutrons, which are examples of nucleons and consist of three quarks. These quarks also possess spin angular momentum equal to 1/2 and under typical laboratory conditions, where one of the quarks has a spin antiparallel to the other two, leading to a resulting net spin in the nucleon of 1/2.

The interaction between a nuclear spin and an external magnetic field is expressed by the nuclear magnetic moment, μ. The scalar product of μ and the magnetic field, B leads to the magnetic energy E_{mag}:

$$E_{mag} = -\boldsymbol{\mu} \cdot \mathbf{B} \qquad \text{(Eq. 1.2)}$$

The vast majority of nuclei in the periodic table have one or more isotopes that are NMR active that is in the presence of an external magnetic field possess a nuclear magnetic moment proportional to the nuclear spin angular momentum **I**:

$$\hat{\mu} = \gamma \hat{I} \qquad \text{(Eq. 1.3)}$$

where γ is a proportionality constant known as the gyromagnetic ratio.

The available energy levels of a nuclear spin can be described in terms of **I**. The nuclear spins have 2(I+1) energy levels available, in the absence of a magnetic field, these energy levels are degenerate. This degeneracy is removed by the nuclear Zeeman interaction once under the influence of an external magnetic field, B_0 giving rise to small difference in the population of spins aligned parallel to the magnetic field versus spins aligned anti-parallel, thus resulting in polarization and a net magnetic moment in the bulk sample aligned with the magnetic field (**Figure 1.1**). The resulting energy difference is expressed as:

$$\Delta E = \gamma \hbar B_0 \qquad \text{(Eq. 1.4)}$$

this energy difference is inherently small and the transitions between these non-degenerate nuclear spin states that is observable in nuclear magnetic resonance (NMR) spectroscopy. Signal intensity in NMR is dependent on the population difference between these energy levels and be expressed using a Boltzmann distribution:

$$\frac{n_{upper}}{n_{lower}} = e^{-\frac{\Delta E}{k_B T}} \qquad \text{(Eq. 1.5)}$$

where k_B is the Boltzmann constant and T is temperature. The population difference is inherently very small and hence endeavours are often made to increase this population difference through increasing the magnetic field strength and hence ΔE, as well as decreasing the temperature.

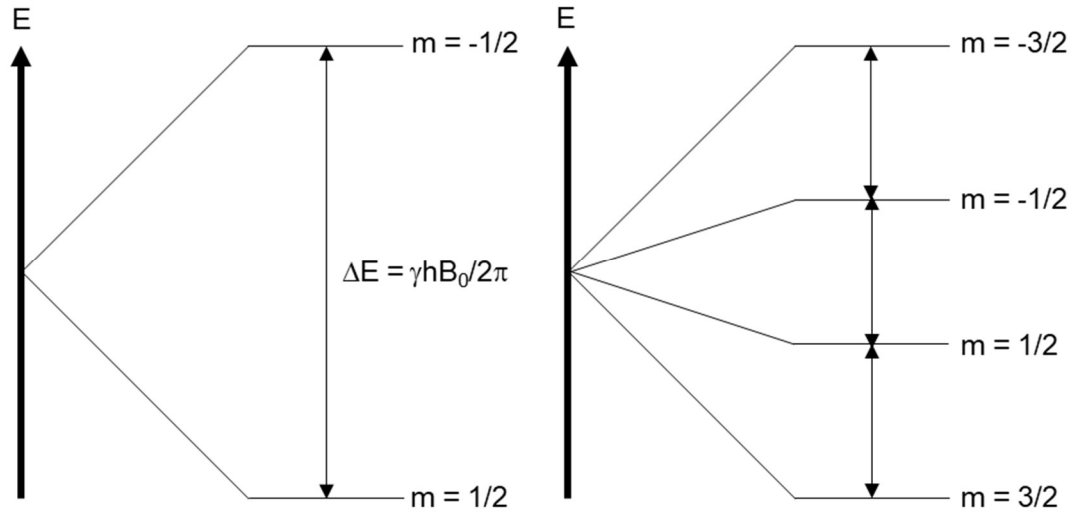

Figure 1.1 Energy level diagram for the transition of electrons between nuclear spin states in an external magnetic field B_0 aligned with the page, for (left) I = 1/2 and (right) I = 3/2. ΔE is the energy difference between spin states, h is Planck's constant and γ is the gyromagnetic ratio of the relevant nucleus.

Whilst under the influence of an external magnetic field the nuclear spins in the sample of interest are known to undergo a process known as precession. The frequency at which these nuclear spins precess is known as the Larmor frequency, ω_0 is proportional to the strength of the magnetic field and is expressed as:

$$\omega_0 = -\gamma B_0 \qquad \text{(Eq. 1.6)}$$

NMR spectroscopy offers insights into the local environments of nuclei of interest due to the inherent sensitivity to the local electronic environment of the

nucleus. Electron density around a nucleus induces local magnetic fields that perturb the frequency of precession of the nuclear magnetic moment i.e ω_0. These induced magnetic fields, $B_{induced}$ are also dependent on B_0 as well as the chemical shielding σ, the surrounding electrons cause this shielding effect on the nucleus, with different shielding effects resulting from different chemical environments e.g valences, bonding etc. The current induced by an external magnetic field generates an induced local magnetic field, B_{loc} which relates to B_0 through a second-rank chemical shielding tensor σ:

$$B_{loc} = B_0(1-\sigma) = \begin{pmatrix} \sigma_{xx} & \sigma_{xy} & \sigma_{xz} \\ \sigma_{yx} & \sigma_{yy} & \sigma_{yz} \\ \sigma_{zx} & \sigma_{zy} & \sigma_{zz} \end{pmatrix} B_0 \qquad \text{(Eq. 1.7)}$$

where x, y and z are the axis frame. As a result, the resonance condition of a nucleus in a magnetic field becomes:

$$\nu = \frac{\gamma B_0}{2\pi}(1-\sigma) \qquad \text{(Eq. 1.8)}$$

Equation 1.7 can then be transformed with three vectors that represent a suitable frame of reference known as the principal axis system, PAS ensuring the resulting matrix is diagonal and the tensor can as such be defined by three principal values. For chemical shielding these terms are defined as σ_{XX}^{PAS}, σ_{YY}^{PAS} and σ_{ZZ}^{PAS} and are associated with the PAS x, y and z axes respectively. The shielding tensor in the PAS can hence be written as:

$$\begin{pmatrix} \sigma_{XX}^{PAS} & 0 & 0 \\ 0 & \sigma_{YY}^{PAS} & 0 \\ 0 & 0 & \sigma_{ZZ}^{PAS} \end{pmatrix} \qquad \text{(Eq. 1.9)}$$

The values of these terms may then be used to define an isotropic component of the shielding tensor, σ_{iso}:

$$\sigma_{iso} = \frac{1}{3}\left(\sigma_{xx}^{PAS} + \sigma_{yy}^{PAS} + \sigma_{zz}^{PAS}\right) \quad \text{(Eq. 1.10)}$$

In order for the measurable frequencies in NMR to be magnetic field independent, they are expressed as chemical shifts δ, in parts per million, ppm. The chemical shift is measured with respect to a reference sample and divided by the resonance frequency in order to generate the frequency difference:

$$\delta = 10^6 \frac{\nu_{sample} - \nu_{reference}}{\nu_{reference}} \quad \text{(Eq. 1.11)}$$

where ν_{sample} and $\nu_{reference}$ are the nuclear Larmor frequencies of the same isotope in the sample being measured and a reference compound respectively. Thus the isotropic chemical shift δ_{iso} is expressed as:

$$\delta_{iso} = \frac{\sigma_{iso,ref} - \sigma_{iso}}{1 - \sigma_{iso,ref}} \quad \text{(Eq. 1.12)}$$

where $\sigma_{iso,ref}$ and $\sigma_{ıso}$ are the isotropic shielding tensors of the reference compound and the sample respectively.

1.1.2 The vector model

A simple representation of a how nuclei behave once perturbed from thermal equilibrium is shown in **Figure 1.2** This representation is known as the vector model, where the individual magnetic moments arising from the nuclear spins in the sample, begin to arrange themselves parallel with the applied magnetic field, this alignment is referred to as the bulk magnetization vector. The individual magnetic moments are not all able to adopt the lowest energy arrangement in which they align with the magnetic field, due to thermal motion, however there is a small preference for alignment with the field and when averaged across the sample, gives rise to the bulk vector.

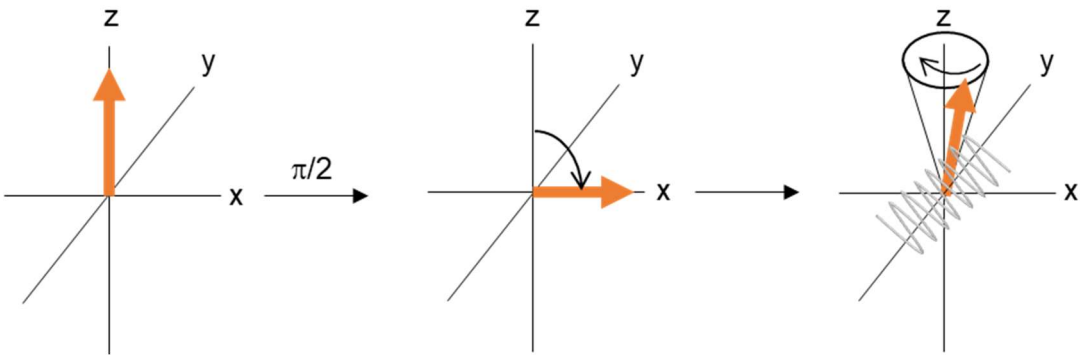

Figure 1.2 Schematic representation of the vector model associated with a simple NMR experiment, where the bulk magnetization vector (orange) is tilted away from thermal equilibrium by a 90° rf pulse along the y-axis and the vector precessing within a conducting NMR coil.

Once the magnetic moments have reached equilibrium the vector is fixed in size and direction. However, in order to detect a signal in NMR spectroscopy this nuclear magnetization vector needs to be tilted away from equilibrium. This is achieved through an oscillating electromagnetic pulse, which generates an oscillating magnetic field B_1, this generates a weak magnetic field

oscillating for a short time interval in, for instance along the y-axis, known as a radiofrequency (rf) pulse. The magnetization vector is now tilted towards the x-axis and is no longer aligned with B_0. Once the rf field is switched off, the magnetization will begin to precess about the z-axis and return to equilibrium. Crucially the coil used to detect the precession of the magnetization vector (**Figure 1.2**) can be used to generate the oscillating magnetic field.

The magnetic part of the rf field can be expressed as two vectors rotating in opposite directions in the xy-plane (**Figure 1.3**). The two counter-rotating fields have the same magnitude B_1 and both rotate at the transmitter frequency ω_{tx}, therefore at time zero both vectors are aligned and give a total field of $2B_1$. As time proceeds, the vectors rotate in opposite directions and the x-component decreases to zero as the vectors rotate to 90° and then increase again along –x as the angle exceeds 90°. However since one of these vectors will inherently be rotating in the opposite direction to the direction of Larmor precession, it will have no significant interaction with the magnetization and can hence be ignored. This allows for the transformation into a co-ordinate system which rather than being static (laboratory frame) like previously, is rotating about the z-axis in the same direction and at the same frequency (**Figure 1.3**). This means that any spins precessing at exactly the Larmor frequency will appear still and any spins at a slight variation of this frequency will only move very slowly. In other words, moving to the rotating frame removes the time-dependency of the field.

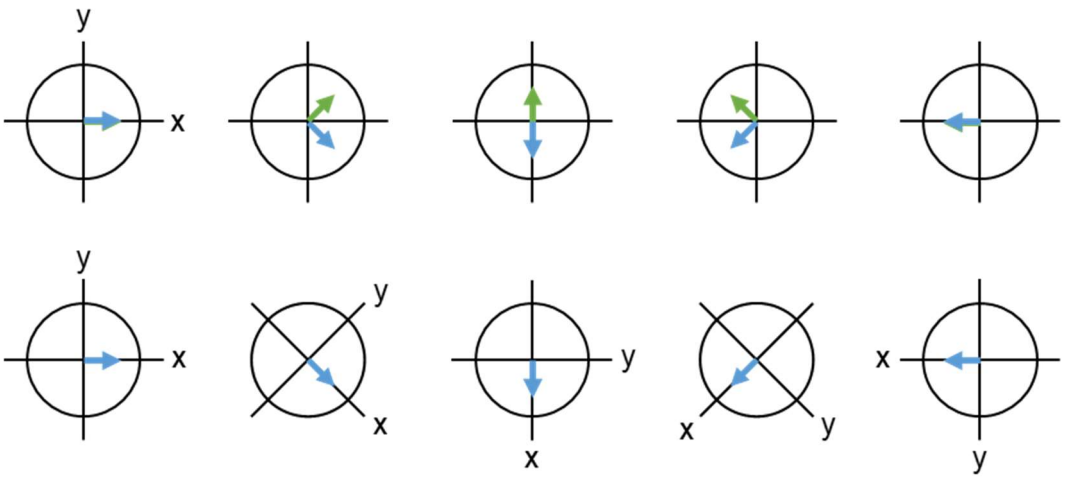

Figure 1.3 (Top) Illustration of how two counter-rotating fields with the same magnitude rotate at the transmitter frequency when viewed in a fixed axis system also known as the laboratory frame of reference. (Bottom) How the same field viewed in an axis system rotating at the transmitter frequency about the z-axis; where in this rotating frame of reference, the rotating field appears static.

1.2 Solid-state NMR

1.2.1 Interactions in Solid-state NMR

The interactions of nuclei in a magnetic field are described by Hamiltonian operators which define the energy of the various interactions (**Table 1.1**) (**Equation 1.13**).[3] These interactions are responsible for the lineshape and positioning of the NMR signals:

$$\hat{H} = \hat{H}_z + \hat{H}_J + \hat{H}_{CSiso} + \hat{H}_{CSaniso} + \hat{H}_D + (\hat{H}_Q) + (\hat{H}_P) + (\hat{H}_K) \qquad \text{(Eq. 1.13)}$$

that correspond to the Hamiltonians associated with the different interactions involved in NMR, namely the Zeeman, J coupling, isotropic and anisotropic chemical shift, dipolar coupling, quadrupolar coupling, paramagnetic coupling and Knight shift. These interactions and the corresponding Hamiltonians are summarised in **Table 1.1**.

Table 1.1 Summary of the interactions in NMR and the corresponding expressions

Hamiltonian	Interaction	Equation
$\hat{H}_z$	Zeeman Splitting	$-\gamma B_0 \hat{I}_z$
$\hat{H}_J$	J Coupling	$J_{12}\hat{I}_{1z}\hat{I}_{2z}$
$\hat{H}_{CS}$	Isotropic Chemical Shift	$-\gamma \hat{I}_z B_0 \sigma_{iso}$
	Anisotropic Chemical Shift	$-\gamma \hat{I}_z B_0 \sigma_{aniso} \eta (3\cos^2\theta - 1)$
$\hat{H}_D$	Heteronuclear Dipolar Coupling	$d_{ij}(3\cos^2\theta - 1)\hat{I}_{1z}\hat{I}_{2z}$
	Homonuclear Dipolar Coupling	$d_{ij}(3\cos^2\theta - 1)\left[3\hat{I}_{1z}\hat{I}_{2z} - \hat{I}_1\hat{I}_2\right]$
$\hat{H}_Q$	Quadrupolar Coupling	$\frac{eQ}{2I(2I-1)}\mathbf{I}\cdot\mathbf{V}\cdot\mathbf{I}$
$\hat{H}_P$	Paramagnetic Coupling	$\hat{H}_0 + \hat{H}_Z + \left(\hat{H}_{contact} + \hat{H}_D\right)$
$\hat{H}_K$	Knight Shift	$-\sum_i^N \gamma_i \cdot \hat{I}_i \cdot \hat{K}_i \cdot B$

The nature of the Zeeman interaction has been described in **section 1.1.1**, the remaining interactions perturb this Zeeman interaction. The chemical shift Hamiltonian, $\hat{H}_{CS}$ relates to the nuclear spin interaction with the surrounding electrons. The isotropic chemical shift has been defined in **section 1.1.1**, however in the absence of Brownian motion, the anisotropic chemical shift differs depending on the orientation of the sample, see **section 1.2.1.1**. The dipolar coupling interaction, $\hat{H}_D$ relates to the direct interaction of two dipoles with each other, either of the same nuclei (homonuclear) or differing nuclei (heteronuclear). This interaction depends on both the interatomic distance between the two nuclei, as well as the orientation of the resulting dipolar vector

with B_0. J Coupling, $\hat{H}_J$ is an indirect through-bond interaction of the nuclear magnetic moments mediated by the bonding electrons. The quadrupolar coupling interaction, $\hat{H}_Q$, is only relevant to nuclei with I > 1/2 due to the electronic charge distribution not being spherically symmetrical, which allows the electric field gradient to interact with the nucleus perturbing the energy levels as shown in **Figure 1.6**. Paramagnetic coupling is only present in species which have an unpaired electron. This electron interacts with the surrounding nuclei in a manner expressed in $\hat{H}_P$ (**Table 1.1**), where $\hat{H}_0$ is the field and nuclear spin-free electronic part containing information on the interactions arising from kinetic energy and electrostatic interactions involving the electrons and nuclei and $\hat{H}_{contact} + \hat{H}_D$ are the Fermi contact and dipolar effects, which together describe the strong interaction known as the electron-nucleus hyperfine coupling. Knight shift is present in metallic species where $\hat{H}_K$ describes the interaction between conduction electrons and the nuclear spins, which is summarised in **Table 1.1** for an ensemble of N number of spins i and $\hat{\mathbb{K}}$ is a second-rank tensor similar to the chemical shielding tensor. None of the materials discussed in this thesis are metallic or possess unpaired electrons and hence $\hat{H}_P$ and $\hat{H}_K$ are not relevant going forward.

Many of these interactions contain an orientation dependent term ($3\cos^2\theta$-1). This term is averaged to zero in the liquid state, due to Brownian motion, resulting in the overall NMR signal in the solution state to be:

$$\hat{\mathbb{H}}_{solution} = \hat{\mathbb{H}}_z + \hat{\mathbb{H}}_J + \hat{\mathbb{H}}_{CSiso} + (\hat{\mathbb{H}}_Q) \qquad \text{(Eq. 1.14)}$$

without this rapid tumbling, the Hamiltonians for anisotropic chemical shift, dipolar coupling and quadrupolar interactions are not averaged out, resulting

in broad lines within the solid state spectrum, the result of which gives the following for the overall NMR signal, in the solid state:

$$\hat{H}_{solid} = \hat{H}_z + \hat{H}_J + \hat{H}_{CSiso} + \hat{H}_{CSaniso} + \hat{H}_D + (\hat{H}_Q) \qquad \text{(Eq. 1.15)}$$

1.2.1.1 Chemical Shift Anisotropy

Chemical shift is a measure of the extent to which the nuclear spin is shielded from the external field by surrounding electrons. The shielding occurs as B0 induces an electronic current in bonding electrons surrounding the nucleus, these circulating electrons in turn generate an additional magnetic field which opposes or reinforces B_0. This induced magnetic field will inherently not be spherical. In a powdered solid sample, the crystallites will be oriented in every possible direction with respect to B_0 (**Figure 1.4**), this gives rise to a distribution of observed chemical shifts as the different orientations give rise to different chemical shifts. This effect is known as chemical shift anisotropy (CSA) where the chemical shielding anisotropy, σ_{aniso} relates to σ_{iso} through the relationship:

$$\sigma_{aniso} = \sigma_{zz}^{PAS} - \sigma_{iso} \quad \text{(Eq. 1.16)}$$

and an asymmetry parameter η:

$$\eta = \frac{\sigma_{yy}^{PAS} - \sigma_{xx}^{PAS}}{\sigma_{aniso}} \quad \text{(Eq. 1.17)}$$

and the isotropic chemical shift:

$$\delta_{iso} = \frac{\delta_{11} + \delta_{22} + \delta_{33}}{3} \quad \text{(Eq. 1.18)}$$

where δ_{11}, δ_{22} and δ_{33} are the principle components of the chemical shift and are illustrated in **Figure 1.4**. The CSA is a first order interaction which is often in the range of kHz and can be on the scale of tens of kHz.

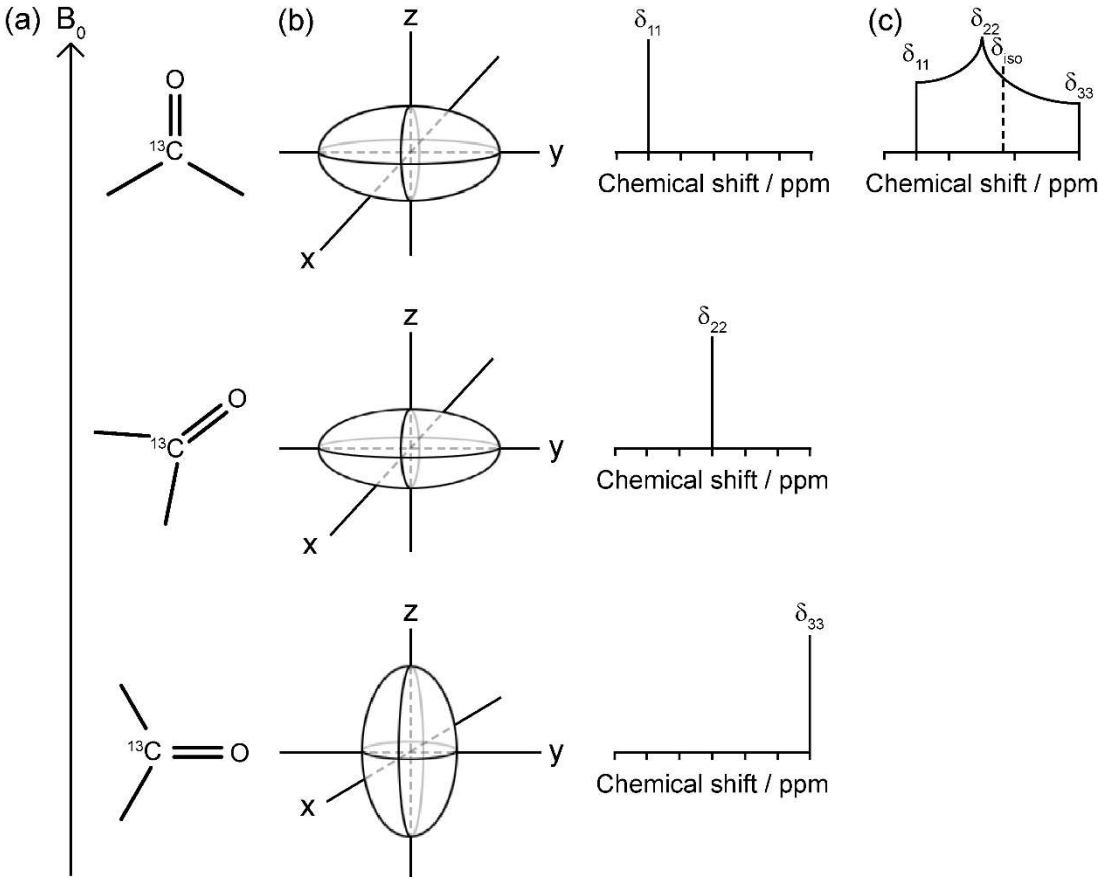

Figure 1.4 (a) Three possible arrangements of a frozen molecule of ^{13}C enriched acetone with respect to B_0 and a depiction of their corresponding chemical shift tensor. (b) The resonances associated with the respective orientations produced at varying chemical shift. (c) Typical powder pattern created from an infinite number of lines due to every orientation of the sample with respect to B_0 being possible.

1.2.1.2 Dipolar coupling

As previously mentioned in **section 1.2.1**, nuclear spins possess a magnetic dipole moment, which interact with one another through space. This dipolar coupling is orientation dependent and is hence only observed in the case of restricted motion in solids. **Table 1.1** describes the Hamiltonian associated with dipolar coupling with the dipolar coupling constant d_{ij} governing the magnitude of this interaction which is often of the scale of tens of kHz:

$$d_{ij} = -\frac{\mu_0}{4\pi}\frac{\hbar\gamma_i\gamma_j}{r_{ij}^3} \qquad \text{(Eq. 1.19)}$$

with μ_0 being the vacuum permittivity, ħ is the reduced Planck's constant, γ_i and γ_j are the gyromagnetic ratios for i and j respectively and r_{ij} is the interatomic distance between spins i and j. The dipolar coupling interaction is a first order interaction and as mentioned previously, the strength of which is often tens of kHz, which dominates the spectrum leading to extremely broad solid-state NMR spectra, particularly in the case of high γ nuclei such as ^{1}H. However this interaction contains a large amount of structural information, due to the strong dependence on the interatomic distance, as well as the molecular orientation with respect to B_0 (**Figure 1.5**), allowing for several NMR experiments to exploit this in order to obtain the distance between nuclei of interest.[4-8]

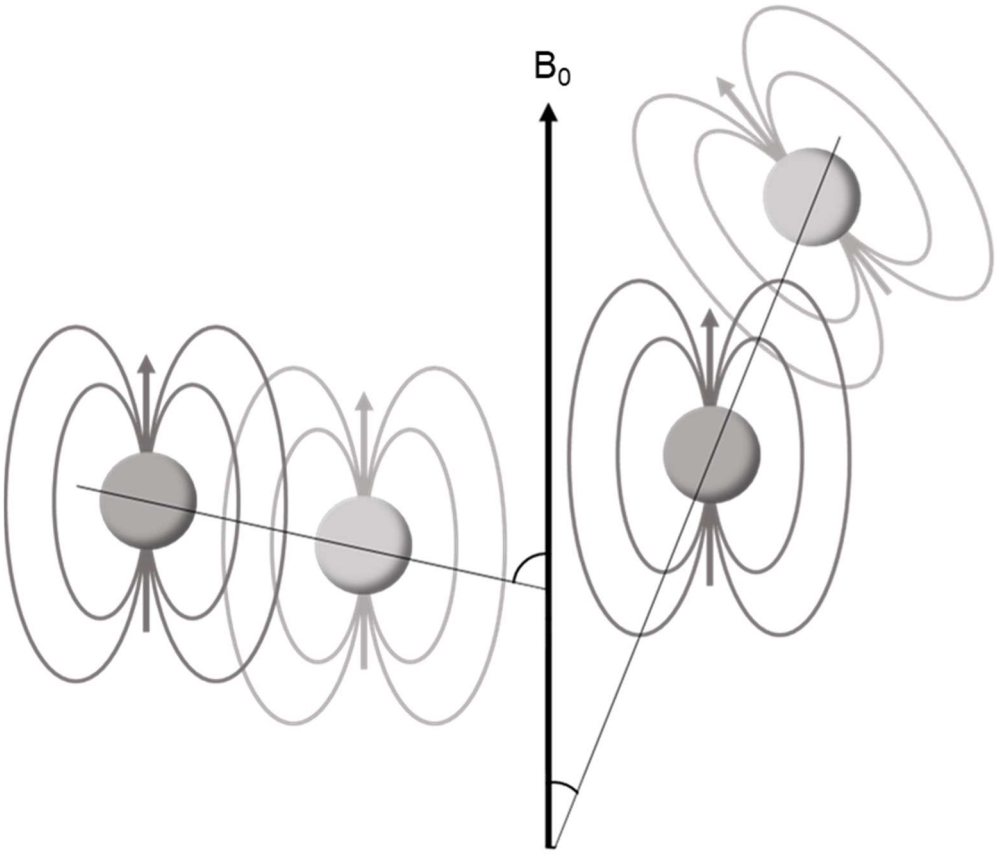

Figure 1.5 Illustration of the dipole-dipole interaction and the angular dependence of the dipolar coupling between two spins (grey arrows) with respect to B_0. The loops represent the magnetic field lines generated by the nuclear dipole.

1.2.1.3 Quadrupolar interaction[9]

The majority (~74%) of active NMR nuclei have I > 1/2, in this case the electric charge of the nucleus is not distributed uniformly and the nucleus can no longer be adequately modelled using a sphere; rather, it is better described using an ellipsoid (**Figure 1.6(a)**). This physical characteristic gives rise to another nuclear property, known as the nuclear electric quadrupole moment (Q), which interacts with local electric field gradients (EFGs) of the molecule that arise due to the asymmetric distribution of the surrounding electron density (**Figure 1.6(b)**). The magnitude of this interaction is typically found to be on the order of hundreds of kHz or MHz and depends on the immediate environment of the nucleus such as the nuclei and electrons in close proximity, as well as geometry of bonds attached to the nucleus, as well as the magnitude of Q and the orientation of the molecule with respect to B_0.

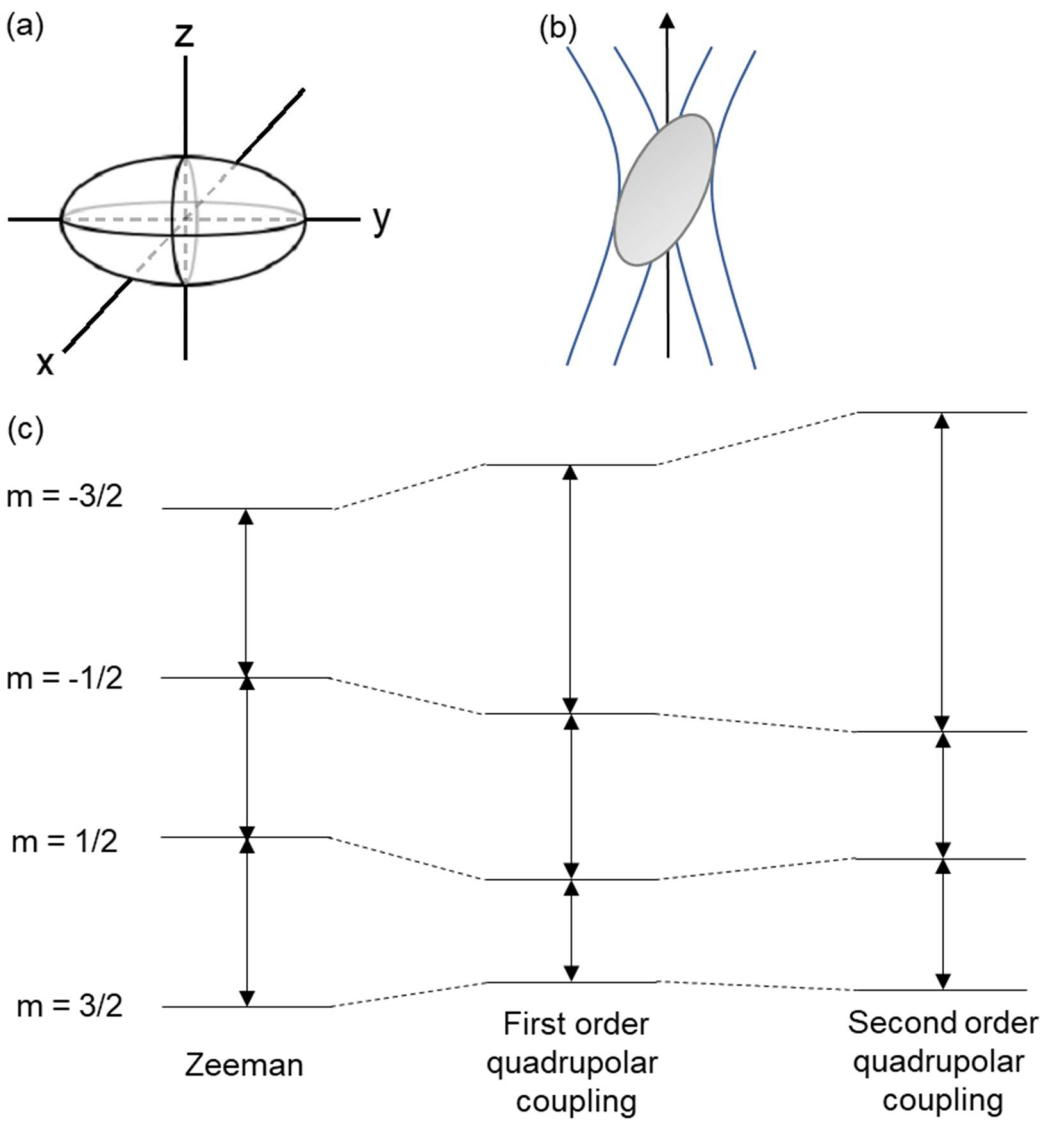

Figure 1.6 (a) Ellipsoid representation of the asymmetric distribution of the electric charge in quadrupolar nuclei. (b) Schematic of a I>1/2 nucleus with an electric quadrupole moment Q, in an electric field gradient (blue lines). Precession of Q in the EFG gives rise to discrete quadrupolar coupling energies (c) where the energy levels are further perturbed in environments with large values of C_Q in which a first order linear expansion is insufficient to express $\hat{H}_Q$ and hence a second order perturbation is required.

As was the case with chemical shift, the EFG in solids can be expressed using a second-rank tensor V:

$$V = \begin{pmatrix} V_{xx} & V_{xy} & V_{xz} \\ V_{yx} & V_{yy} & V_{yz} \\ V_{zx} & V_{zy} & V_{zz} \end{pmatrix} \quad \text{(Eq. 1.20)}$$

where x, y and z are the axis frame and this expression can then be transformed with three vectors that represent the PAS:

$$V = \begin{pmatrix} V_{xx}^{PAS} & 0 & 0 \\ 0 & V_{yy}^{PAS} & 0 \\ 0 & 0 & V_{zz}^{PAS} \end{pmatrix} \quad \text{(Eq. 1.21)}$$

where the diagonalized components here correspond to the principle axes of the EFG tensor and are defined by: V_{zz}^{PAS}>V_{yy}^{PAS}>V_{xx}^{PAS}. However unlike in the case of the chemical shift tensor, the principle axes of the EFG tensor are traceless. The EFG at a quadrupolar nucleus is characterised with respect to the largest principle value of the EFG tensor V_{zz}^{PAS} as well as the asymmetry of the EFG tensor η_Q:

$$\eta_Q = \frac{\left(V_{xx}^{PAS} - V_{yy}^{PAS}\right)}{V_{zz}^{PAS}} \quad \text{(Eq. 1.22)}$$

The magnitude of the quadrupolar interaction is often characterized by the quadrupolar coupling constant, C_Q:

$$C_Q = \frac{e^2 V_{zz}^{PAS} Q}{h} \quad \text{(Eq. 1.23)}$$

where e, V_{zz}^{PAS} and h are the charge of the electron, the largest principal component of the EFG and Planck's constant respectively. However the quadrupolar splitting parameter, ω_Q^{PAS} is also used:

$$\omega_Q^{PAS} = \frac{3\pi C_Q}{2I(2I-1)} \qquad \text{(Eq. 1.24)}$$

Since there are 2I+1 energy levels available energy levels for a quadrupolar nuclei in an external magnetic field, for a spin 3/2 nucleus there are 4 available energy levels (**Figure 1.6(c)**). There are now two distinct types of transitions: a central transition (with $m_I = +1/2 \leftrightarrow m_I = -1/2$), which are unaffected by the quadrupolar interaction to first order; and two satellite transitions (with $m_I = -3/2 \leftrightarrow m_I = -1/2$ and $m_I = +1/2 \leftrightarrow m_I = +3/2$), with frequencies of $\omega_0 - 2\omega_Q$ and $\omega_0 + 2\omega_Q$, respectively. The quadrupolar splitting parameter, ω_Q, is given by:

$$\omega_Q = \omega_Q^{PAS} P_2(\cos\theta) = \frac{\omega_Q^{PAS}}{2}(3\cos^2\theta - 1) \qquad \text{(Eq. 1.25)}$$

where $P_2(\cos\theta)$ is the second-order Legendre polynomial, for simplicity axial symmetry has been assumed and the angle θ describes the orientation of the PAS of the EFG.

The magnitude of the quadrupolar coupling can be extremely large, on the order of MHz, hence in this case the associated Hamiltonian cannot be expressed with a first order approximation. Instead $\hat{H}_Q$ is written as a series

$$\hat{H}_Q = \hat{H}_Q^1 + \hat{H}_Q^2 + \ldots \qquad \text{(Eq. 1.26)}$$

where the number in superscript corresponds to the order of the term in the quadrupolar Hamiltonian. $\hat{H}_Q$ can easily be comparable with the Zeeman splitting and hence the energy levels become perturbed (**Figure 1.6(c)**). All transitions are affected by the second-order quadrupolar interaction, with the correction to the frequency given, for a transition q and assuming $\eta_Q = 0$, by:

$$\omega = \frac{(\omega_Q^{PAS})^2}{\omega_0}\left(A^0(I,q) + A^2(I,q)P_2(\cos\theta) + A^4(I,q)P_4(\cos\theta)\right) \qquad \text{(Eq. 1.27)}$$

where $P_4(\cos\theta)$ is the fourth-order Legendre polynomial and $A^n(I,q)$ are spin and transition-dependent coefficients.[10]

1.3 Magic Angle Spinning

Magic-angle spinning (MAS) is a technique that is routinely used in the majority of SS-NMR experiments, primarily to remove the effects of anisotropic interactions. This generates NMR resonances that are significantly narrower than for static experiments. In solution state NMR, the effects of anisotropic interactions are rarely observed due to rapid molecular tumbling, averaging out the orientation dependence in these interactions. MAS simulates this motion in order to achieve a similar result, this process occurs through the orientation dependence of the nuclear spin interactions for these interactions (**Table 1.1**), where the dependence is of the form $3\cos^2\theta-1$, where θ is the angle between the applied field and the spinning axis. The root of which occurs when θ is equal to 54.74° (**Figure 1.7**) therefore provided that the spinning rate is of a higher frequency than the strength of the anisotropic interactions, the anisotropic interactions are averaged to zero. Without sufficient spinning speed the modulation of the interaction frequencies at the rotor frequency results in the residual anisotropic interactions being manifested within spinning side bands, at a distance relating to the spinning speed of either side of the isotropic peak.

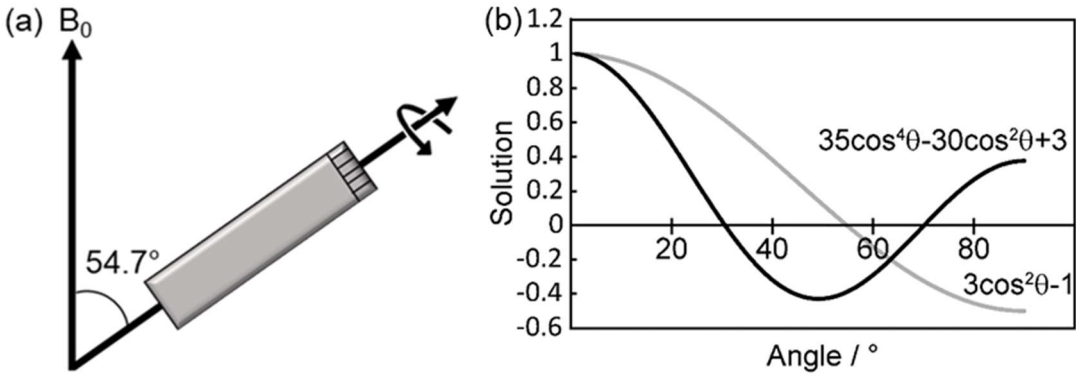

Figure 1.7 (a) Schematic of a rotor spinning at the magic angle of 54.7° with respect to the external magnetic field, B. (b) Angular dependence of the magnitude of anisotropic NMR interactions. The grey line labelled $3\cos^2\theta-1$ corresponds to the first order geometric component of $\hat{H}_{CS,ainso}$, $\hat{H}_D$ and $\hat{H}_Q$ and the black line labelled $35\cos^4\theta-30\cos^2\theta+3$ corresponds to the second order geometric component of $\hat{H}_Q$.

In the case of quadrupolar nuclei where the magnitude of the quadrupolar interaction is comparable with the Zeeman splitting, the Hamiltonian is expressed as a series. The second order quadrupolar interaction does not have the same angular dependence as the other anisotropic interactions. The dependence for this interaction takes the form of $35\cos^4\theta-30\cos^2\theta+3$, where the roots of which are 30.6 and 70.1° therefore in the case of quadrupolar nuclei, there is no one angle at which the rotor can be spinning in order to average out all anisotropic interactions. Instead more complex experimental procedures must be implemented in order to obtain isotropic spectra, such as double rotation (DOR),[11] dynamic-angle rotation (DAS)[12] or more commonly multiple quantum magic angle spinning (MQMAS)[10,13] see below.

1.4 Relaxation theory

1.4.1 Relaxation in the laboratory frame

Relaxation in NMR occurs immediately after the rf field is switched off, longitudinal relaxation, T_1 is the rate at which the longitudinal magnetisation of a nuclear spin system returns to thermal equilibrium.

When the rf field is switched off relaxation processes are introduced according to the Bloch-equations:

$$\frac{dM_x}{dt} = -\frac{dM_x}{T_2} \qquad \text{(Eq. 1.28)}$$

$$\frac{dM_y}{dt} = -\frac{dM_y}{T_2} \qquad \text{(Eq. 1.29)}$$

$$\frac{dM_z}{dt} = -\frac{M_{z,eq} - M_z}{T_1} \qquad \text{(Eq. 1.30)}$$

where M_x, My and M_z are the x, y and z components of the bulk magnetization, $M_{z,eq}$ is the magnetization at thermal equilibrium, T_2 is the transverse relaxation time and T_1 is the longitudinal or spin-lattice relaxation (SLR) time. The linear form of the combination of **equations 1.28** and **1.29** yields the rate equation for T_2:

$$M_{x,y}(t) = M_{x,y}(0)\exp\left(-\frac{t}{T_2}\right) \qquad \text{(Eq. 1.31)}$$

which is defined as the expression by which $M_{x,y}$, the transverse component of the magnetization vector, exponentially decays to return to equilibrium. While the linearization of **equation 1.30** gives:

$$M_z(t) = M_{z,eq} - \left(M_{z,eq} - M_z(0)\right)\exp\left(-\frac{t}{T_1}\right) \quad \text{(Eq. 1.32)}$$

where $M_z(0)$ is the longitudinal relaxation at time = 0.

T_1^{-1} is affected by the fluctuation of local magnetic fields caused by the motion of an atom or functional group. These fluctuating fields are described by the time-dependent correlation function G(t), containing information on the atomic diffusion process and the correlation time τ_c, which is in the same order of magnitude to the mean residual time τ of the spin between jumps.[14-16] In the Bloembergen-Purcell-Pound (BPP) theory, the correlation function G(t) decays exponentially and follows the equation below:

$$G(t) = G(0)\exp\left(-\frac{|t|}{\tau_c}\right) \quad \text{(Eq. 1.33)}$$

where G(0) is the value of the correlation function at time t = 0. Fourier transform of **equation 1.33** gives the spectral density function J at the Larmor frequency ω_0:

$$J(\omega_0) = G(0)\left(-\frac{2\tau_c}{1 + \omega_0{}^2\tau_c{}^2}\right) \quad \text{(Eq. 1.34)}$$

The rate at which the bulk magnetization returns to equilibrium depends on the local environment of the observed nuclei and the random fluctuating magnetic field variations as well as the relative mobility of the nuclei, i.e the correlation time, τ_c. There are four main mechanisms for promoting relaxation: dipolar, quadrupolar, paramagnetic and CSA. Since the dominant relaxation mechanisms associated with the materials of interest in this thesis are dipolar and quadrupolar coupling, these two mechanisms will be discussed in detail, while the remaining two mechanisms will only be discussed briefly.

Dipolar coupling mediated relaxation between two nuclei depends on d_{ij} as well as τ_c:

$$\frac{1}{T_1} = K\left(\frac{\tau_c}{1+\omega_0^2\tau_c^2} + \frac{\tau_c}{1+4\omega_0^2\tau_c^2}\right) \quad \text{(Eq. 1.35)}$$

where ω_0 is the Larmor frequency and K is the local fluctuating magnetic field term, which for dipolar coupling corresponds to:

$$K = \frac{2}{5}\left(\frac{\mu_0}{4\pi}\right)^2 \frac{\gamma^4\hbar^2}{r^6} I(I+1) \quad \text{(Eq. 1.36)}$$

The quadrupolar relaxation mechanism arises from the tumbling of molecules initiating interactions between the nucleus and the surrounding non-spherically symmetric electron charge distribution. This interaction depends heavily on the magnitude of the quadrupolar moment, Q as well as the resulting C_Q resulting in the local fluctuating magnetic field term, K for quadrupolar coupling induced relaxation to be:

$$K = \frac{3}{200} C_Q^2 \left(1 + \left(\frac{\eta_Q^2}{3}\right)\right) \frac{2I+3}{I^2(2I-1)} \quad \text{(Eq. 1.37)}$$

therefore nuclei with low Q such as some I = 1 nuclei such as ^{6}Li, often have long T_1 times.

The CSA relaxation mechanism arises from the orientation dependence of the magnetic field experienced by the nucleus and hence the fluctuating magnetic field generated by adjacent species is also orientation dependent, promoting relaxation. For paramagnetic relaxation, paramagnetic ions contribute largely to relaxation through a dipolar mechanism between unpaired electrons and

nuclear spins. Since the γ for electrons are extremely large, the resulting d_{ij} is also extremely large and hence the large magnetic moment of electrons means that paramagnetic species are particularly effective at promoting relaxation.

1.4.2 Relaxation in the rotating frame

The previous discussion on relaxation of nuclear magnetization in the presence of a constant magnetic field B_0 refers to relaxation in the laboratory frame. However if another time-dependent magnetic field, B_1 that rotates in the plane perpendicular to B_0 at the Larmor frequency of the nuclei is continuously applied the nuclei are said to be spin-locked. The resulting relaxation time, deemed the spin-lattice relaxation in the rotating frame, $T_{1\rho}$ is greatly extended beyond transverse relaxation and can be likened to T_1 at the low magnetic field B_1 rather than B_0. The expression relating $T_{1\rho}$ to the spectral density retains the same K constants as for T_1, however different spectral densities are utilised:

$$\frac{1}{T_{1\rho}} = K\left(\frac{3}{2}\frac{\tau_c}{1+4\omega_1^2\tau_c^2} + \frac{5}{2}\frac{\tau_c}{1+\omega_0^2\tau_c^2} + \frac{\tau_c}{1+4\omega_0^2\tau_c^2}\right) \qquad \text{(Eq. 1.38)}$$

where ω_1 is spin-lock probe frequency.

For systems where dipolar relaxation is the dominant mechanism, the Bloembergen-Purcell-Pound (BPP) model[14] is applied to extract Li^+ jump rates τ_c^{-1}. The BPP theory denotes that τ_c is proportional to the spectral density function $J(\omega)$ of the NMR spectra (**equation 1.38**). When the thermally activated SLR rates are plotted against reciprocal temperature using the Arrhenius function, a volcano plot is made (**Figure 1.8**). The maximum point of this volcano plot denotes where the spectral density $J(\omega)$ is at its maximum, therefore the jump rate τ^{-1} are on the order of the probe frequency and could be extracted: $\omega_0\tau_c \approx 0.62$ for T_1^{-1} values and $2\omega_1\tau_c \approx 0.5$ for $T_{1\rho}^{-1}$ values.[16,17]

The τ_c^{-1} values obtained then expected to follow the Arrhenius behaviour according to the equation:

$$\tau_c^{-1} = \tau_{c,0}^{-1} \exp\left(-\frac{E_a}{k_B T}\right) \quad \text{(Eq. 1.39)}$$

where $\tau_{c,0}^{-1}$ is the pre-exponential factor (i.e. the number of hops per unit time of a particle), E_a is the activation barrier of the diffusion process and k_B is the Boltzmann constant. The inverse correlation time τ_c^{-1} is on the same order of magnitude as jump rate τ^{-1} and are used conjunctly, where τ_c is linked with the microscopic property of the fluctuating magnetic fields, while τ^{-1} defines the macroscopic ion diffusion.

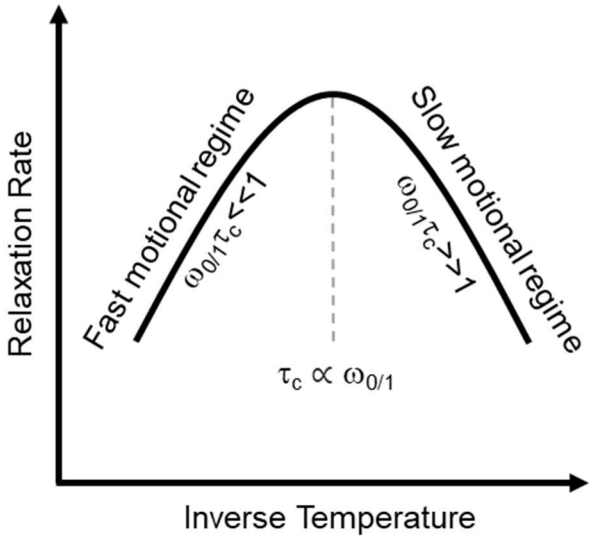

Figure 1.8 Schematic representation of the temperature dependence of NMR SLR rates.

The high temperature side of the volcano plot is the fast motion regime where $\omega_{0(1)}\tau_c << 1$. The relationship between the $T_{1(\rho)}^{-1}$ values on the high temperature flank measured at different frequencies give information on the

dimensionality of the Li^+ diffusion process (**Table 2.**), as the spins undergo several jumps before a single precession of the probe frequency.[16,18] The activation barrier is free from correlative effects and corresponds to full translational diffusion of the mobile ion, i.e.; Li^+ motion from one site to its neighbouring site.

1.4.3 Frequency dependence of spin-lattice relaxation in the rotating frame

One of the factors in the correlation function G(t) (**equation 1.33**) is described as a pair distribution function:

$$P(r_0, r, t) = (8\pi Dt)^{-n/2} \exp\left(-\frac{|r - r_0|^2}{8Dt}\right) \quad \text{(Eq. 1.40)}$$

where r_0 is the original position of the nuclei, r is the position of the nuclei after time t, n is the dimension of diffusion (n = 1 for 1D, 2 for 2D, and 3 for 3D)[18] and D is the diffusion coefficient derived from the Einstein-Smolchowski equation:

$$D = \frac{fa^2}{2n}\tau^{-1} \quad \text{(Eq. 1.41)}$$

where f is the correlation factor and a is the average hopping distance of the mobile ion (in cases for Li^+ ion conductors, Li^+). Upon Fourier transform of **equation 1.40**, the relationship of three-dimensional spin diffusion in liquids at high temperature can be derived as $J(\omega) \propto 1/D$.[17,18] The value of the constant coefficient in the $J(\omega) \propto 1/D$ relationship for solids and liquids are analogous and therefore this relationship is used for 3D spin diffusion in solids. The derived relationship between frequency and spin lattice relaxation in the rotating frame at high temperature for three dimensional diffusion is:

$$J_{3D}(\omega) = \left(\frac{nd_p^2}{aD}\right)\left[\delta - \beta_{poly}\left(\frac{\omega a^2}{D}\right)^{\frac{1}{2}} + \cdots\right] \quad \text{(Eq. 1.42)}$$

where n is the number density of the spins, d_p is a constant , δ is a dimensionless coefficient calculated from mean-field theory, β_{poly} is a

coefficient arising from polycrystalline averaging, dependent on the symmetry of the unit cell.

From **equation 1.42** it can be seen that the $\omega^{1/2}$ term is still present in the expression but is a third order expansion and therefore is small enough to be considered negligible, therefore one can derive that $J(\omega) \propto \tau$ and that the $T_{1(\rho)}^{-1}$ values for 3D Li^+ ion diffusion are independent of the probe frequency in the fast motion regime.

For 2D diffusion processes, one must consider the effect of ions diffusing in a plane rather than in all directions like 3D diffusion. The resulting relationship was determined to be:

$$J(\omega) = f_1(\theta)\left(\frac{\pi n}{a^2 D}\right)\ln\left(\frac{2D}{\omega L^2}\right) \qquad \text{(Eq. 1.43)}$$

where $f_1(\theta)$ is the first order term in the angular dependence of the spectral density on a 2D lattice with four or six fold rotation, n is the number density of spins, and L is a length parameter introduced to keep the argument of the logarithm dimensionless. The relationship between the spectral density and frequency was determined to be $J(\omega) \propto \ln\omega^{-1}$ and was later confirmed by probing HNO_3 diffusion between graphite sheets.[19] This relationship combined with **equation 1.41** can be used to derive the relationship $J(\omega) \propto 1/D \ln(-D/\omega)$. One can then derive $J(\omega) \propto \tau\ln(1/\omega\tau)$, i.e. $T_{1(\rho)}^{-1}$ values are shown proportional to $\tau\ln(1/\omega\tau)$. This is also known as Richards' semi empirical model, with this relationship being identified using electron spin resonance.[20,21]

For systems with 1D Li^+ diffusion processes, the spectral density at the high

temperature limit is given by the expression:

$$J(\omega) = f_1(\theta)\frac{2n}{a^4(\omega D)^{1/2}} \qquad \text{(Eq. 1.44)}$$

therefore it can be shown that $J(\omega) \propto \omega^{-1/2}$ this relationship combined with **equation 1.4**1, derives the expression $J(\omega) \propto (\tau/\omega)^{1/2}$, and that $T_{1(\rho)}^{-1}$ values follow the square root of residual time in a single site over the probed frequency.

The low temperature side of the BPP curve on the other hand, corresponds to the slow motion regime where the motion of spins between sites is restricted and do not exchange between sites before a single precession of the probe frequency and is therefore not affected by the diffusion dimensionality. In this regime, $\omega_{0(1)}\tau_c >> 1$, which makes:

$$1 + \omega_{0(1)}\tau_c = \omega_{0(1)}\tau_c \qquad \text{(Eq. 1.45)}$$

and therefore

$$J(\omega_{0(1)}) \propto \frac{2\tau_c}{{\omega_{0(1)}}^2\tau_c^2} \sim \omega_{0(1)}^{-2}\tau^{-1} \qquad \text{(Eq. 1.46)}$$

and so one can derive that the $T_{1(\rho)}^{-1}$ values in this regime are frequency dependant. The activation energy E_a extracted in this regime is related to the energy required for local hop motion between local energy minima within the energy well including of the ion unsuccessful jumps between sites, rather than long range translational Li^+ ion diffusion.[22] The full equations expressing the spectral densities at the low temperature limits for 3D, 2D and 1D diffusion are:

$$J^{3D}(\omega) = \frac{4c}{b^6\omega^2\tau}\left(S_0(H) - \frac{1}{z}[S(H) + S_1(H)\right) \quad \text{(Eq. 1.47)}$$

$$J^{2D}(\omega) = \frac{4c}{b^6\omega^2\tau}\left\{[f_1(\theta) + 2f_2(\theta)]\left[s_0 - \left(\frac{1}{Z}\right)(s + s_1)\right] + \frac{2}{Z}f_2(\theta)(s_1 - s_1')\right\} \quad \text{(Eq. 1.48)}$$

$$J^{1D}(\omega) = f_1(\theta)\frac{12.37c}{b^6\omega^2\tau} \quad \text{(Eq. 1.49)}$$

where b is the lattice parameter and $S_0(H)$, $S(H)$ and $S_1(H)$ are dimensionless lattice sums given for cubic crystals in reference[23], values of lattice sums s_0, s, s_1 and s_1' are given in reference,[18] $f_1(\theta)$ and $f(\theta)$ are the first and second order terms in the angular dependence of the spectral density, respectively. Therefore at the high frequency (low temperature) limits of the BPP curve all three dimensionalities of diffusion are proportional to $\tau^{-1}\omega^{-\beta}$ where β is the model parameter ranging between 1 and 2. BPP theory predicts that the volcano plot is symmetric and the quadratic frequency dependence of $J(\omega)$, and by extension $T_{1(\rho)}^{-1}$ values, is proportional to ω^{-2}. Many cases, however, are asymmetric and deviate from this model due to dimensionality of the diffusion and disorder in the studied system. The activation barrier for diffusion of Li^+ ions in solid conductors in the slow motion regime are affected by structural disorder in the material, Coulombic interactions and correlation effects of the mobile ions.[16,24,25] This asymmetry has a frequency dependence of $T_{1(\rho)}^{-1} \propto \omega^{-\beta}$ which therefore would give the low temperature limit relationship as $J(\omega) \propto \tau^{-1}\omega^{-\beta}$.

Table 2. Summary of frequency dependence of spin-lattice relaxation in the rotating frame

Dimensionality	Low frequency limit (High T)	High frequency limit (Low T)
1D	$(\tau/\omega)^{0.5}$	$\tau^{-1}\omega^{-\beta}$
2D	$\tau \ln(1/\omega\tau)$	$\tau^{-1}\omega^{-\beta}$
3D	τ	$\tau^{-1}\omega^{-\beta}$

1.5 NMR Experiments used in this thesis

The following NMR experiments are utilised throughout this thesis and the understanding of the pulse sequences and how the nuclear spins react is crucial to ensuring the correct interpretation of results and generating meaningful data.

1.5.1 One pulse

As was previously explained (**section 1.1.2**) in order to observe an NMR signal, the bulk magnetization vector must be tilted away from equilibrium through a rf pulse in this case a $\pi/2$ pulse. Once the vector has been tilted away from the z-axis into the transverse plane (**Figure 1.9**) the nuclei will precess within the magnetic field. This precession induces a current at the resonating frequency of the nucleus in the coil surrounding the sample, and as the magnetization begins to relax this induced current will decay over time and the resulting signal is known as the free induction decay (FID). This FID is then Fourier transformed converting it from the time domain to the frequency domain, generating a typical NMR spectrum.

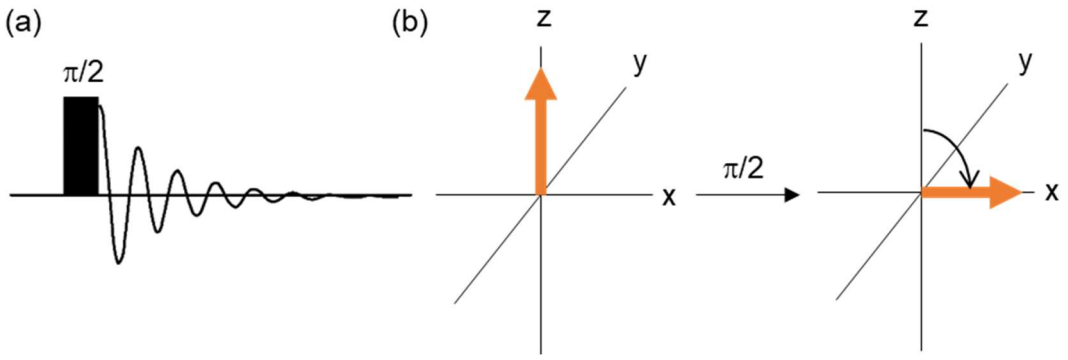

Figure 1.9 (a) Schematic representation of a one pulse experiment. (b) The vector model representation for the effect of a 90° rf pulse on the bulk magnetization vector (orange) during the pulse sequence.

1.5.2 Spin-echo

As previously mentioned in **section 1.4.1**, the decay of the NMR signal in the xy-plane over time due to transverse relaxation is known as T_2. Typically T_2 in solid samples is short, particularly when anisotropic interactions are strong. These samples also tend to have rapidly decaying FIDs, therefore the short dead time before opening the receiver of the spectrometer (this is required in order to not record the 'ringing' of the coil') can lead to significant losses in signal through T_2 relaxation, as a large portion of the beginning of the FID is not recorded. This can be overcome by applying an inversion (π) pulse after a dephasing time τ, any dephasing experienced is "refocused" back to the opposite axis resulting in all signals being refocused at the end of the second τ period and the FID recorded typically after τ as shown in **Figure 1.10** below.

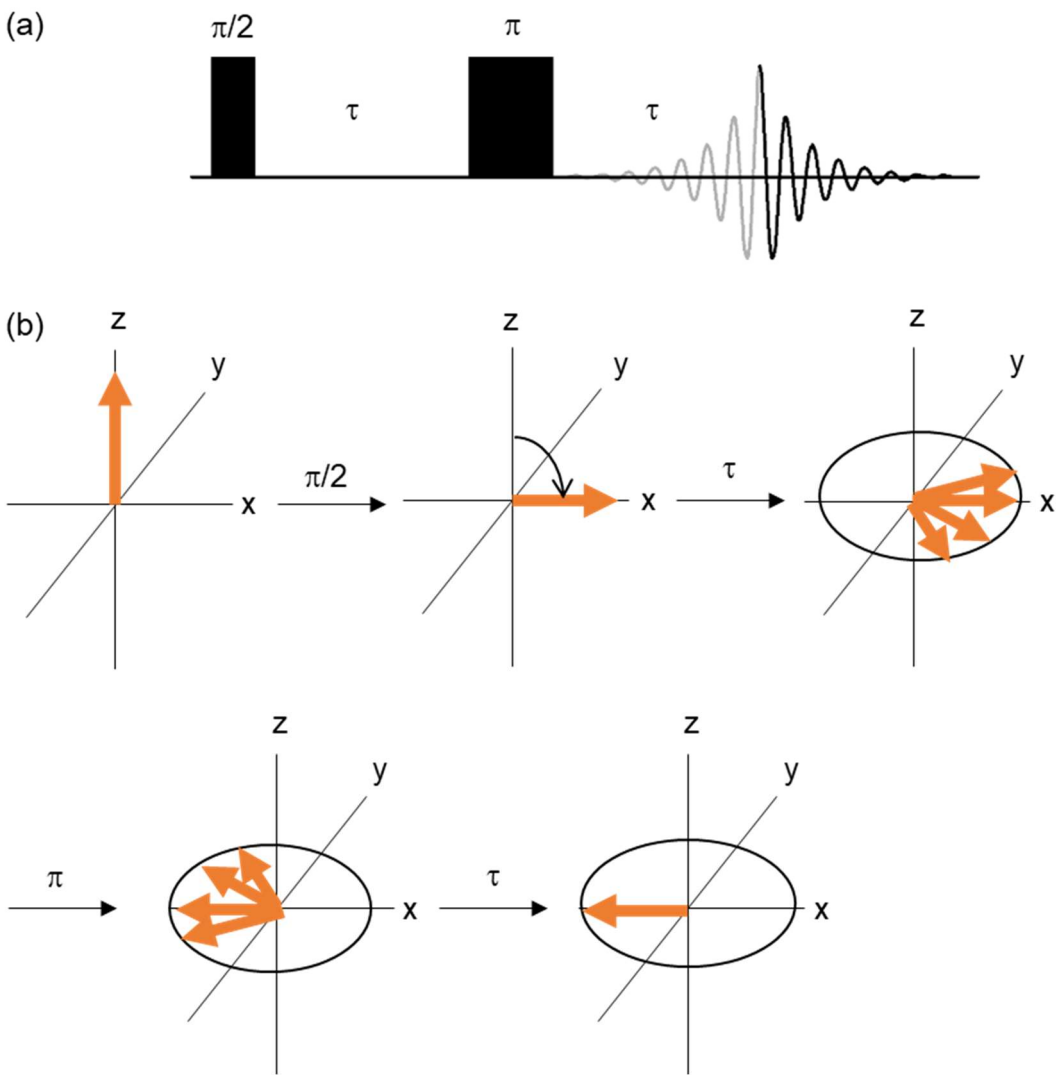

Figure 1.10 (a) Schematic representation of the spin echo pulse sequence and (b) the corresponding vector model associated with the spin echo experiment.

1.5.3 Spin-alignment echo

The underlying principle idea of spin-alignment echo (SAE) NMR spectroscopy arises from taking advantage of the interactions between Q and a non-vanishing EFG tensor at its site. In other words, ions that move between electrically non-equivalent sites experience different NMR quadrupolar frequencies. Therefore fluctuations of the quadrupole frequencies ω_Q due to ions moving between electrically non-equivalent sites lead to a decay of the SAE amplitude, S (see below), which is the primary observable in SAE NMR spectroscopy. The well-known Jeener-Broekaert pulse sequence is utilised in order to take advantage of this (**Figure 1.11(a)**).

In order to extract correlation times, the stimulated echo, which appears after the final pulse, is recorded as a function of mixing time τ_m keeping the evolution (or preparation) time τ_p constant. The first two pulses, a $\pi/2$ pulse followed by $\pi/4$ pulse whose phase is shifted by 90°, generate the so-called spin-alignment state.[26] The resulting echo amplitudes are then processed and plotted as a function of τ_m and the data fit to the expression:

$$S_{(\tau_p,\tau_m)} = (1 - S_\infty)\exp\left[-\left(\frac{\tau_m}{\tau_c}\right)^\alpha\right] + S_\infty \exp\left[-\left(\frac{\tau_m}{T_1}\right)\right] + S_{0,\infty} \qquad \text{(Eq. 1.50)}$$

where S_∞ and $S_{0,\infty}$ are the normalised echo amplitude after the first and second plateaus respectively and α is a stretch exponential (**Figure 1.11(b)**).

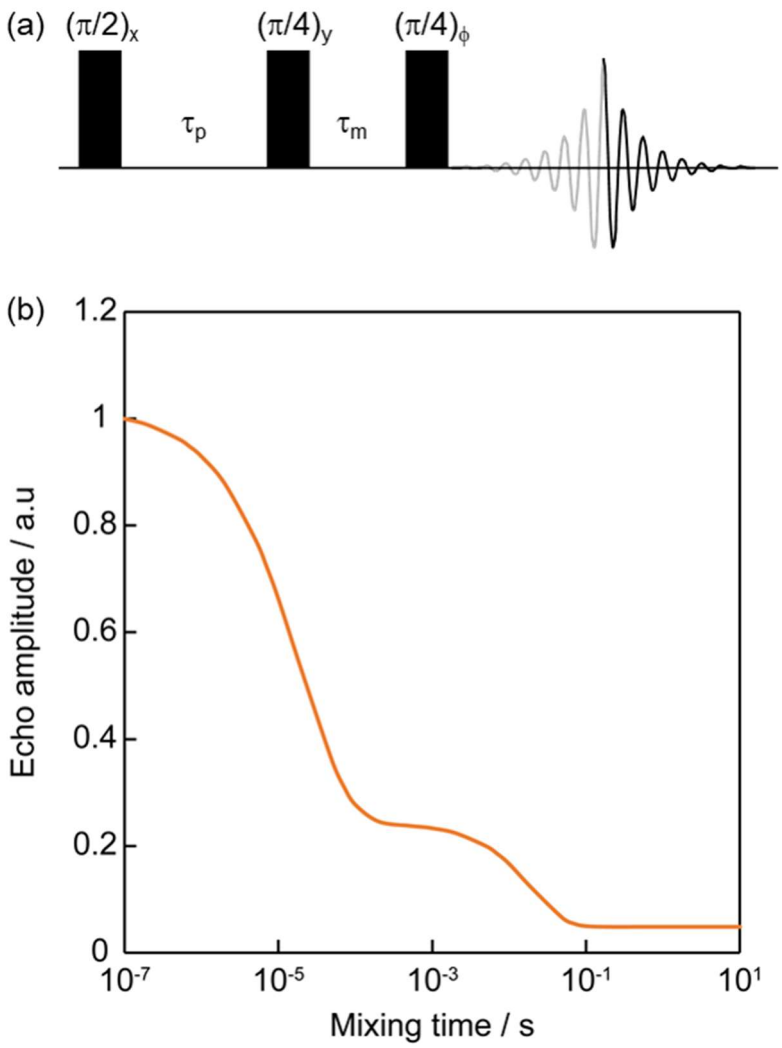

Figure 1.11 (a) Schematic of the Jeener-Broekaert pulse sequence which is adapted for spin-alignment echo experiments. (b) A simulation of how the amplitude of the echo decays as a function of the mixing time. The initial decay process contains information on the Li jump rate, while the secondary decay which is shifted to larger mixing times arises from quadrupolar SLR effects.

1.5.4 Multiple-quantum filtered NMR

The Muliple-Quantum Filtered (MQF) NMR pulse sequence (**Figure 1.12(a)**) is a method utilised in order to distinguish between central and satellite transitions. MQF NMR can also be used in order to measure the longitudinal relaxation time of I>1/2 nuclei by incrementing τ_1.[27-29]

In Double-Quantum Filtered (DQF) NMR, the central transition is suppressed while the quadrupolar satellites associated with transitions between the ±3/2 <-> ±1/2 energy levels have opposite phase to one another. In Triple-Quantum Filtered (TQF) NMR, the central transition remains while the quadrupolar satellites have inverted phase (**Figure 1.12(b)**). With suitable phase cycling, double (θ = 54.7°) or triple (θ = 90°) quantum coherence can be targeted for filtration.

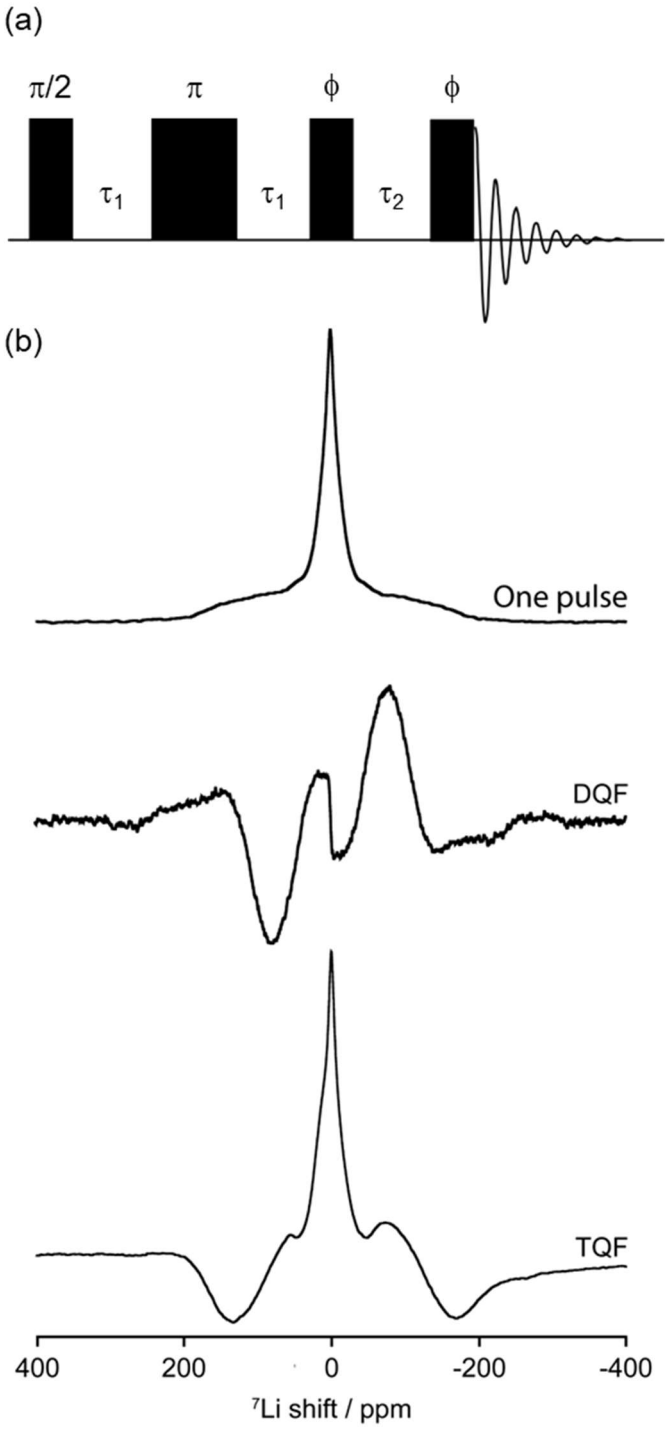

Figure 1.12 (a) Schematic of the multiple-quantum filtered NMR experiment, where with suitable phase cycling double ($\theta = 54.7°$) or triple ($\theta = 90°$) quantum coherence can be targeted for filtration. (b) Example spectra of a ^{7}Li one pulse, DQF and TQF spectrum of the same materials. (Example spectra are taken from **Chapter 3**)

1.5.5 Two-dimensional NMR

Two-dimensional (2D) NMR techniques can be used to probe selective NMR interactions and are often very useful in unequivocal determination of the structure of a molecule. In 2D NMR signals are recorded as a function of two time variables, which can be Fourier transformed to provide two frequency axes, resulting in a correlation describing an interaction/correlation dependent on the particular experiment. A general 2D NMR scheme is laid out in **Figure 1.13** below and consists of preparation, evolution, mixing and detection periods. The value of Δ_1 during the evolution period is increased incrementally over each acquisition to build up a time domain dataset which when Fourier transformed will yield a 2D frequency domain spectrum.

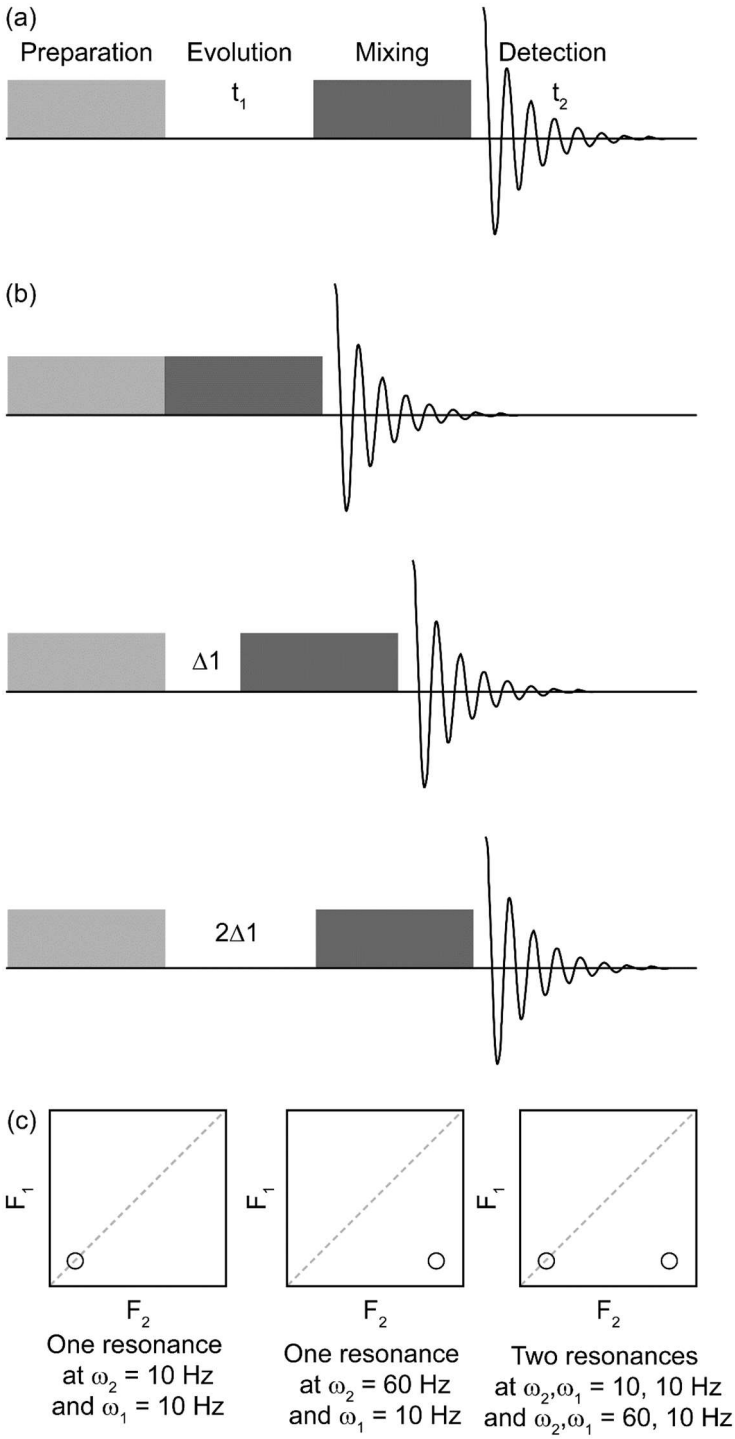

Figure 1.13 (a) A basic summary of a 2D pulse sequence, showing the preparation, evolution, mixing time and detection elements. (b) An illustration of how the evolution period $\Delta 1$ between the preparation and mixing time elements is incremented. (c) A schematic representation of the resulting spectrum and some basic possible outcomes in 2D NMR with 1 or 2 resonances.

1.5.6 Saturation recovery

Saturation recovery is utilised in order to measure the SLR rate in the laboratory frame, T_1 (**Figure 1.14(a)**). The experiment works through saturating the bulk magnetization in the xy-plane so that the net magnetization is zero through a saturation pulse train of a series of $\pi/2$ pulses. The magnetization is then allowed to relax back along the z-axis through a delay τ_d, followed by a final read out $\pi/2$ pulse transferring the magnetization back into the transverse plane and the resulting FID is acquired (**Figure 1.14(b)**). Through incrementing τ_d and collecting the resulting FIDs an exponential build-up curve of longitudinal magnetization is generated which plateaus at $5*T_1$.

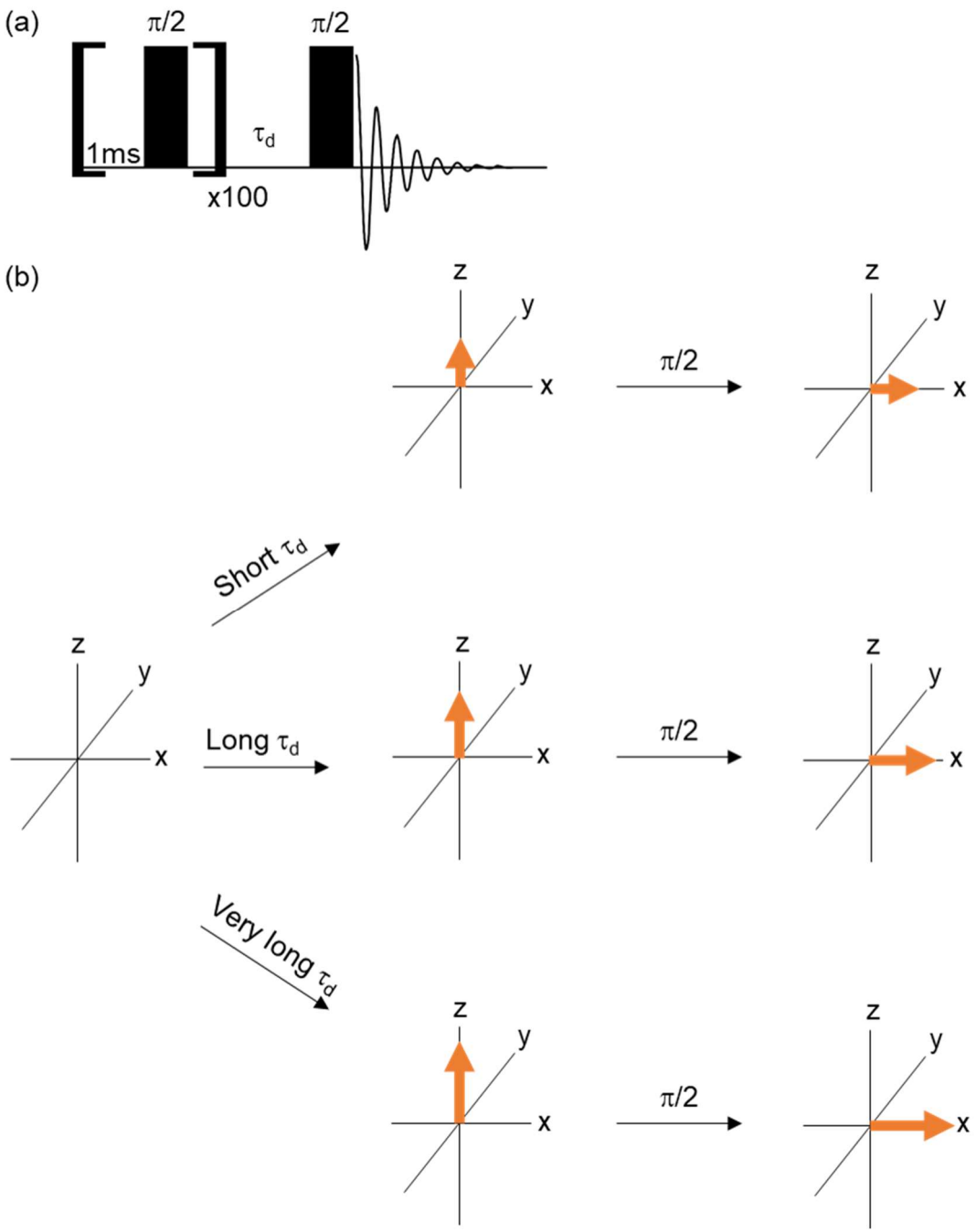

Figure 1.14 (a) A schematic of the saturation recovery NMR pulse sequence in which τ_d is incremented at values specified by the operator. (b) The vector model representation of how the bulk magnetization behaves during the experiment depending on whether the delay τ is short ($<T_1$) long ($\sim T_1$) or very long ($\sim 5 \times T_1$), leading to an exponential build up of NMR signal.

1.5.7 Spin-locking NMR

Spin-lock pulses are used in order to measure the SLR rate in the rotating frame, $T_{1\rho}$. The advantage of this is that the resulting dynamics processes are on a much shorter timescale compared to T_1 as the timescale of motion is defined by the spin-lock frequency (on the order of ms) compared to the Larmor frequency (on the order of ns). As explained in **section 1.4.2**, the resulting relaxation time is greatly extended beyond transverse relaxation and can be likened to T_1 at the low magnetic field B_1 rather than B_0. The method to measure $T_{1\rho}$ is shown in **Figure 1.15**, where the bulk magnetization is transferred into the xy-plane through a $\pi/2$ pulse and then locked into the plane through a continuous rf pulse of frequency w1 for a time τ_p. During this rf pulse, the nuclear spins relax and the resulting FID is collected after τ_p. Through incrementing τ_p an exponential decay of the magnetization under rf pulsing is collected.

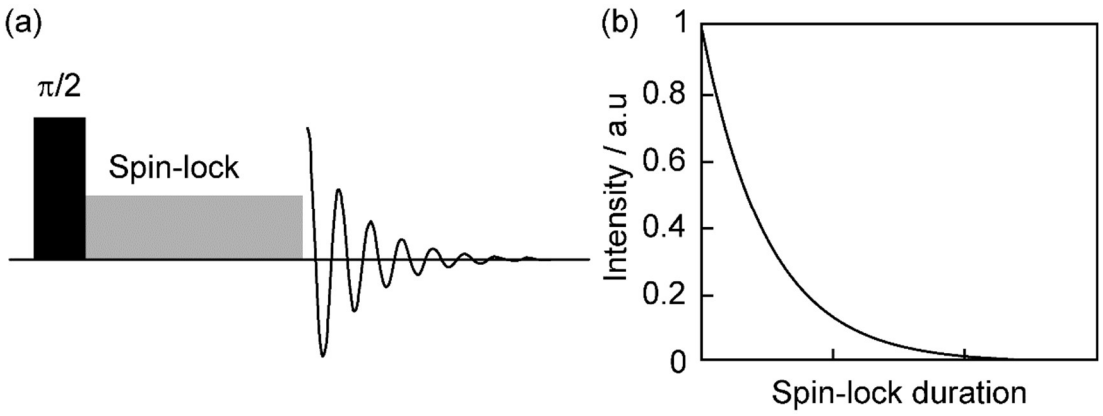

Figure 1.15 (a) A schematic of the spin-lock NMR experiment in order to obtain a value for $T_{1\rho}$, where the power of the spin-locking pulse affects the time constant obtained. (b) A simulated exponential decay curve for how the signal intensity decays with the duration of the spin-locking pulse.

1.5.8 Exchange Spectroscopy

The Nuclear Overhauser Effect (NOE) Spectroscopy (NOESY) experiment (**Figure 1.16(a)**), which is commonly used in solution state NMR, can also be utilised in solids in order to probe the interaction between neighbouring nuclei through dipolar coupling mediated spin-diffusion or chemical exchange, rather than the NOE. Exchange spectroscopy (EXSY) experiment is a homonuclear 2D NMR experiment which correlates two nearby sites of the same nuclei by the presence of cross peaks in the 2D NMR spectra. The experiment works in the same way as NOESY however the mechanism by which cross peaks is observed is different. After the initial 90° rf pulse, the magnetisation is left to precess around on the xy-plane for time t_1. A second rf pulse is applied along the opposite axis of the initial pulse, which brings the magnetisation back along the z-axis for mixing time τ_m, where sites may interact. Finally, a third rf pulse is applied and NMR signal is acquired. If there is interaction between the sites, during τ_m a cross peak is observed (**Figure 1.16(b)**), as these nuclei resonate at different frequencies during t_1 and t_2.[30]

Two possible interactions give cross peaks – spin diffusion and chemical exchange. Spin diffusion arises from the magnetisation transfer of the nuclei through dipole-dipole interactions, while chemical exchange originates from physical motion of the nuclei. The two processes can be differentiated by performing EXSY experiments at different MAS rates, as higher MAS averages dipole-dipole interactions reducing intensities of the cross peaks, while cross peaks originating from chemical exchange are unaffected (depending on the change in ω_r as a large change may lead to increased MAS frictional heating and lead to an increase in cross peak intensity).

Spin diffusion NMR experiments observe the transfer of nuclear magnetization via through space dipole-dipole interactions and has been used to calculate the d_{ij} and hence determine the internuclear distances among a range of systems.[4-8] d_{ij} is proportional to the cube root of the nuclei concentration and the square of the nuclei gyromagnetic ratio, nuclei with sufficiently high values (e.g. ^{1}H, ^{7}Li, ^{31}P etc.) are often used in these experiments and provide qualitative and quantitative information on spatial proximities.

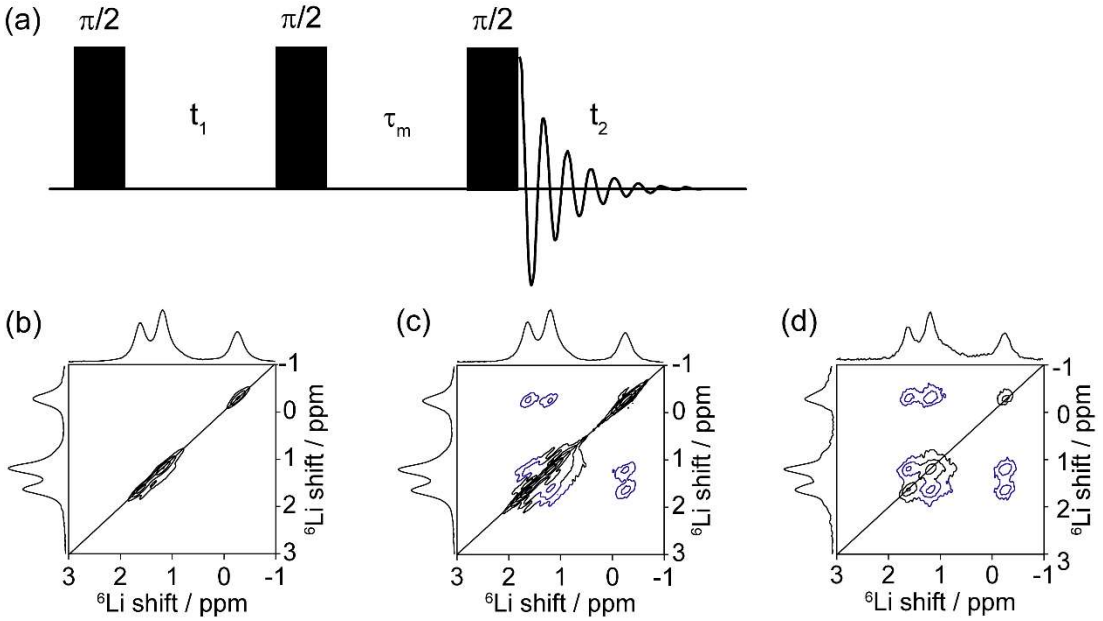

Figure 1.16 (a) A schematic representation of the Exchange spectroscopy NMR pulse sequence. This pulse sequence is identical to the commonly utilised liquid state Nuclear Overhauser Effect Spectroscopy NMR experiment. (b-d) Example ^{6}Li-^{6}Li EXSY experiments with increasing mixing time, τ_m, with values of (a) 0 (b) 0.03 and (c) 4 s, diagonal and cross peaks are shown in black and blue respectively.

1.5.9 Multiple quantum magic-angle spinning

The MQMAS experiment is an important experiment in achieving high-resolution spectra for half-integer spin nuclei while spinning the sample at a single angle. This is experimentally significantly easier to implement than DOR or DAS where multiple spinning angles are required.

As mentioned above (**section 1.2.1.3**), the second and fourth-rank anisotropic terms prevents the removal of the second-order interaction by MAS about any one angle alone. MQMAS NMR involves the correlation of multiple-quantum coherences acquired indirectly in t_1, before conversion to observable central-transition coherences, which evolve in t_2. The multiple-quantum transition is chosen as, like the central transition, it is not affected by the first-order quadrupolar interaction. The result is a two-dimensional spectrum containing a series of ridge lineshapes (one for each distinct species), with an isotropic, high-resolution spectrum obtained from a projection onto an axis orthogonal to the ridges (**Figure 1.17**).

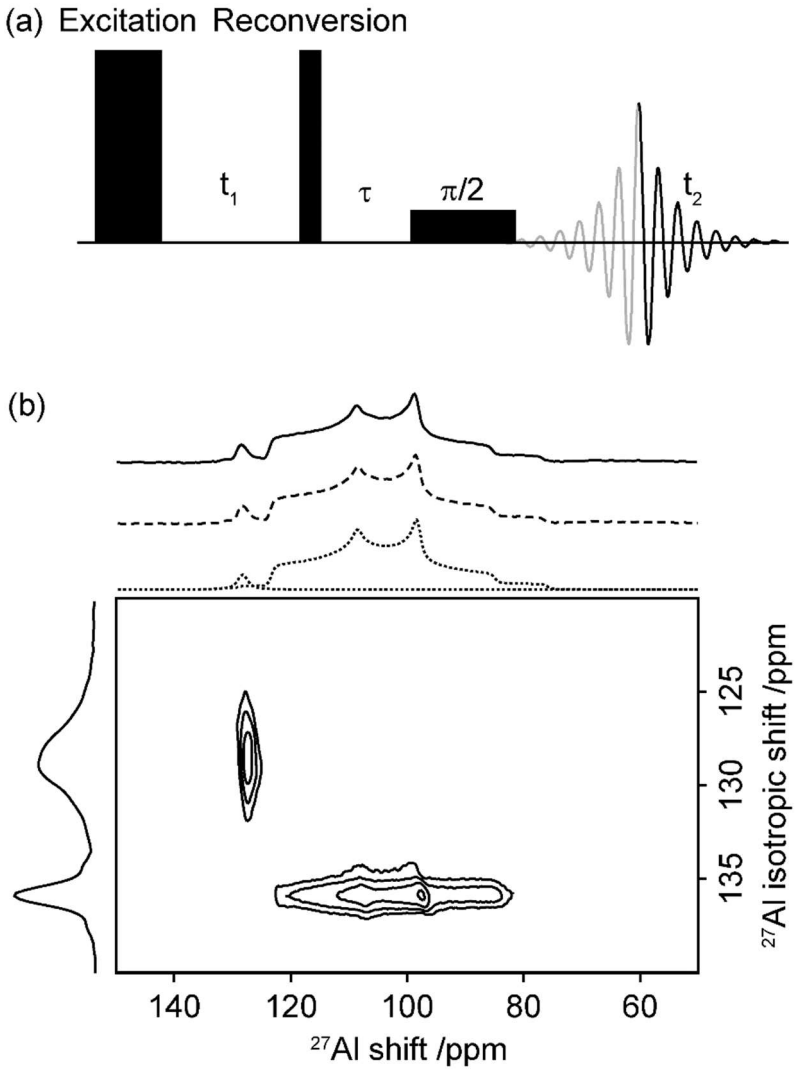

Figure 1.17 (a) Schematic representation of a z-filtered multiple-quantum magic-angle spinning NMR experiment, where t_1 and t_2 are the evolution time and τ is the z-filter delay. (b) A ^{27}Al 3QMAS NMR spectrum of Li_3AlS_3 recorded at 9.4 T and a MAS rate of 10 kHz showing two Al sites. The vertical F_1 dimension represents the isotropic ^{27}Al shift while the horizontal F_2 dimension shows the standard MAS spectrum. The resonance centred at ~130 ppm in the F_2 dimension corresponds to a cubic ^{27}Al environment while the resonance centred at ~100 ppm in the F_2 dimension represents a highly asymmetric ^{27}Al environment. The example spectrum is taken from chapter 3.

1.6 Timescales in NMR

NMR is an extremely powerful technique in order to probe dynamic processes where the motion of atoms, functional groups or entire molecules change with time and often temperature. The key to the study of dynamics by NMR lies in the wide range of timescales that can be accessed (**Figure 1.18**) ranging from very fast motional processes in the order of 10^{-12} s^{-1} probed by measuring spin-lattice relaxation times to much slower motion on the timescale of 10^{-3} s^{-1} or s^{-1} accessed by EXSY NMR and SAE experiments. This is in sharp contrast to the averaged structural picture with length and time produced by other spectroscopic methods such as impedance spectroscopy.

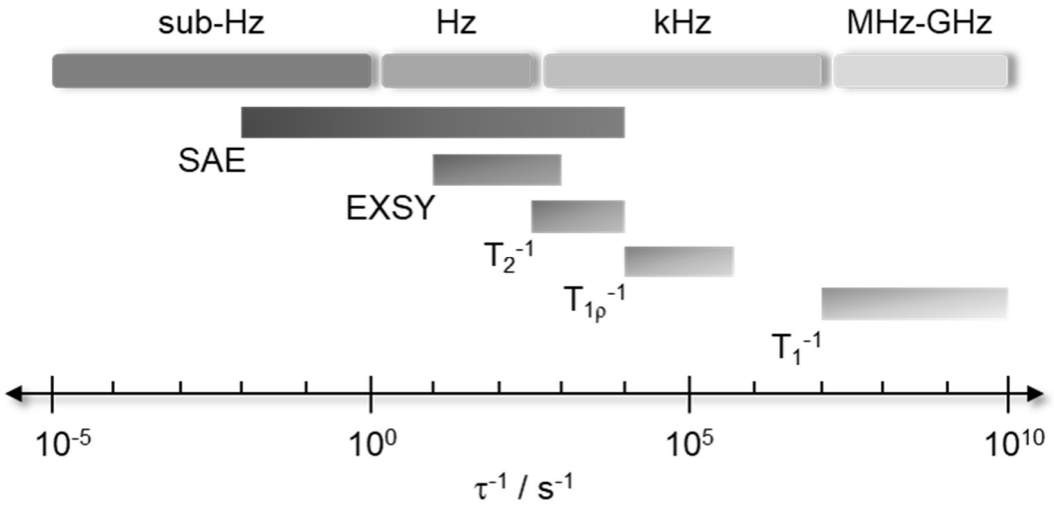

Figure 1.18 Timescales of different NMR measurements including SAE, EXSY, transverse relaxation rate T_2^{-1}, spin lattice relaxation in the laboratory frame T_1^{-1} and the rotating frame $T_{1\rho}^{-1}$. Typically, macroscopic diffusion takes place on the Hz and kHz scale while chemical exchange can range from Hz-MHz, more rapid motion such as molecular rotations often occur on the MHz-GHz scales.

1.7 Conclusion

The techniques presented in this chapter are only a small portion of those that are used within the field of NMR and there are many more techniques which can provide analogous information on dynamics and structure of materials. However, these solid state NMR techniques are those selected and used routinely throughout this thesis to probe solid ion conductors on a variety of timescales, ranging from sub-Hz to MHz.

1.8 References

1. Levitt, M. E., *Spin Dynamics: Basics of Nuclear Magnetic Resonance*. 2nd ed.; Wiley: 2008; p 740.
2. Keeler, J., *Understanding NMR Spectroscopy*. Wiley-Blackwell: 2010; p 526.
3. Apperley, D. C.; Harris, R. K.; Hodgkinson, P., *Solid-State NMR: Basic Principles and Practice*. 1st ed ed.; Momentum Press: New York, 2012.
4. Tjandra, N.; Bax, A., Direct Measurement of Distances and Angles in Biomolecules by NMR in a Dilute Liquid Crystalline Medium. *Science* **1997,** *278* (5340), 1111.
5. Thieme, K.; Schnell, I., Determination of Long-Range Distances and Dynamic Order Parameters by Dipolar Recoupling in High-Resolution Magic-Angle Spinning NMR Spectroscopy. *Journal of the American Chemical Society* **2003,** *125* (40), 12100.
6. Chevelkov, V.; Fink, U.; Reif, B., Accurate Determination of Order Parameters from $^{1}H,^{15}N$ Dipolar Couplings in MAS Solid-State NMR Experiments. *Journal of the American Chemical Society* **2009,** *131* (39), 14018.
7. Canales, A.; Jiménez-Barbero, J.; Martín-Pastor, M., Review: use of residual dipolar couplings to determine the structure of carbohydrates. *Magnetic Resonance in Chemistry* **2012,** *50* (S1), S80.
8. Makrinich, M.; Nimerovsky, E.; Goldbourt, A., Pushing the limit of NMR-based distance measurements – retrieving dipolar couplings to spins with extensively large quadrupolar frequencies. *Solid State Nuclear Magnetic Resonance* **2018,** *92*, 19.
9. Ashbrook, S. E., Recent advances in solid-state NMR spectroscopy of quadrupolar nuclei. *Physical Chemistry Chemical Physics* **2009,** *11* (32), 6892.
10. Medek, A.; Harwood, J. S.; Frydman, L., Multiple-Quantum Magic-Angle Spinning NMR: A New Method for the Study of Quadrupolar Nuclei in Solids. *Journal of the American Chemical Society* **1995,** *117* (51), 12779.
11. Samoson, A.; Lippmaa, E.; Pines, A., High resolution solid-state N.M.R. *Molecular Physics* **1988,** *65* (4), 1013.

12. Llor, A.; Virlet, J., Towards high-resolution NMR of more nuclei in solids: Sample spinning with time-dependent spinner axis angle. *Chemical Physics Letters* **1988,** *152* (2), 248.

13. Amoureux, J. P.; Fernandez, C.; Steuernagel, S., Z Filtering in MQMAS NMR. *Journal of Magnetic Resonance - Series A* **1996,** *123* (1), 116.

14. Bloembergen, N.; Purcell, E. M.; Pound, R. V., Relaxation Effects in Nuclear Magnetic Resonance Absorption. *Phys. Rev.* **1948,** *73* (7), 679.

15. Mehrer, H., *Diffusion in solids: fundamentals, methods, materials, diffusion-controlled processes*. Springer Berlin Heidelberg: Berlin, 2007; Vol. 155.

16. Heitjans, P.; Kärger, J. r., *Diffusion in condensed matter : methods, materials, models*. Springer: 2005; p 965.

17. Abragam, A., *The Principles of Nuclear Magnetism*. Oxford University Press: Oxford, 1961.

18. Sholl, C. A., Nuclear spin relaxation by translational diffusion in liquids and solids: high- and low-frequency limits. *Journal of Physics C: Solid State Physics* **1981,** *14* (4), 447.

19. Avogadro, A.; Villa, M., Nuclear magnetic resonance in a two-dimensional system. *The Journal of Chemical Physics* **2003,** *66* (6), 2359.

20. Richards, P. M.; Salamon, M. B., Exchange narrowing of electron spin resonance in a two-dimensional system. *Physical Review B* **1974,** *9* (1), 32.

21. Richards, P. M., *Magnetic Resonance in Superionic Conductors*. Springer Berlin Heidelberg: Berlin, 1979; p 141.

22. Böhmer, R.; Jeffrey, K. R. R.; Vogel, M., Solid-state Li NMR with applications to the translational dynamics in ion conductors. *Progress in Nuclear Magnetic Resonance Spectroscopy* **2007,** *50* (2-3), 87.

23. Barton, W. A.; Sholl, C. A., Nuclear spin relaxation by transitional diffusion in solids. V. Reciprocal-space formalism and mean-field theory Related content Nuclear spin relaxation by translational diffusion in solids: V. Reciprocal-space formalism and mean-field theory. **1980,** *13*, 2579.

24. Kuhn, A.; Narayanan, S.; Spencer, L.; Goward, G.; Thangadurai, V.; Wilkening, M., Li self-diffusion in garnet-type $Li_7La_3Zr_2O_{12}$ as probed directly by diffusion-induced ^7Li spin-lattice relaxation NMR spectroscopy. *Physical Review B - Condensed Matter and Materials Physics* **2011,** *83* (9), 1.

25. Heitjans, P.; Schirmer, A.; Indris, S., *NMR and β-NMR Studies of Diffusion in Interface-Dominated and Disordered Solids*. Springer-Verlag Berlin Heidelberg: The Netherlands, 2005.

26. Wilkening, M.; Heitjans, P., From Micro to Macro: Access to Long-Range Li^+ Diffusion Parameters in Solids via Microscopic $^{6,7}Li$ Spin-Alignment Echo NMR Spectroscopy. *ChemPhysChem* **2012,** *13* (1), 53.

27. Jaccard, G.; Wimperis, S.; Bodenhausen, G., Multiple-quantum NMR spectroscopy of S=3/2 spins in isotropic phase: A new probe for multiexponential relaxation. *Interactions The Journal of Chemical Physics* **1986,** *85*, 4546.

28. Eliav, U.; Navon, G., Measurement of dipolar interaction of quadrupolar nuclei in solution using multiple-quantum NMR spectroscopy. *Journal of Magnetic Resonance - Series A* **1996,** *123* (1), 32.

29. Huynh, T. V.; Messinger, R. J.; Sarou-Kanian, V.; Fayon, F.; Bouchet, R.; Deschamps, M., Restricted lithium ion dynamics in PEO-based block copolymer electrolytes measured by high-field nuclear magnetic resonance relaxation. *The Journal of Chemical Physics* **2017,** *147* (13), 134902.

30. Claridge, T. D. W., *High-Resolution NMR Techniques in Organic Chemistry*. Elsevier: Netherlands, 2016.

2. Lithium Ion Batteries and Associated Literature

There is an ever growing need for modern society to move away from the limited supply of fossil fuels and the subsequent rising levels of carbon dioxide in the atmosphere and hence reducing society's dependence on the internal combustion engine is paramount in the move towards a sustainable future. As a result, governments worldwide have recently put legislation in place to support the widespread use of electric vehicles. For example, the UK government hopes to end the sale of conventional petrol and diesel cars and vans by 2040 in a move to decrease CO_2 emissions. However, electric vehicles require a suitable energy storage device in order to function. Current generation electric vehicles make use of portable, rechargeable lithium ion batteries in order to achieve this. Lithium ion batteries are a widely used and pivotal in many other areas of modern day society such as personal electronics, solar energy storage and pacemakers. However petrol and diesel cars still heavily outweigh electric vehicles on the roads, and there are still concerns regarding infrastructure, battery capacity and safety. Hence there is a need to further innovate in battery technology in order to overcome these concerns.

This chapter gives an introduction to battery technology and aims to review the literature for energy storage materials with a focus on the main families of solid state Li electrolytes, as well as the NMR techniques used in order to probe the structure and ion mobility mechanisms. The structural differences of

the different classes of materials are highlighted, along with the NMR techniques in order to characterize the ion diffusion mechanisms. This chapter focusses on crystalline inorganic solid-electrolytes, however other materials classes such as polymer and glass composites are also promising candidates for next generation electrolyte materials, on this subject other exhaustive reviews are available.[1-4]

2.1 Li-Ion Cells

With the ever increasing demand for improved energy storage technology, lithium-ion cells continue to draw a large degree of attention due to their high energy density, long lifespan and high open circuit voltage.[5] With an impressive energy to weight ratio, technologies using lithium are increasing in abundance, including many types of batteries. Modern day commercial batteries consist of three main components, a positive electrode (cathode) and a negative electrode (anode) which are connected externally through a circuit and are separated by a liquid electrolyte, where a lithium containing salt is dispersed in organic solvents. Lithium-ion batteries discharge by way of Li-ions flowing from the anode through an electrically conducting liquid electrolyte solution to intercalate with the cathode material (**Figure 2.1**). Electrons then flow through the external circuit for charge balance reasons, generating an electrical current.

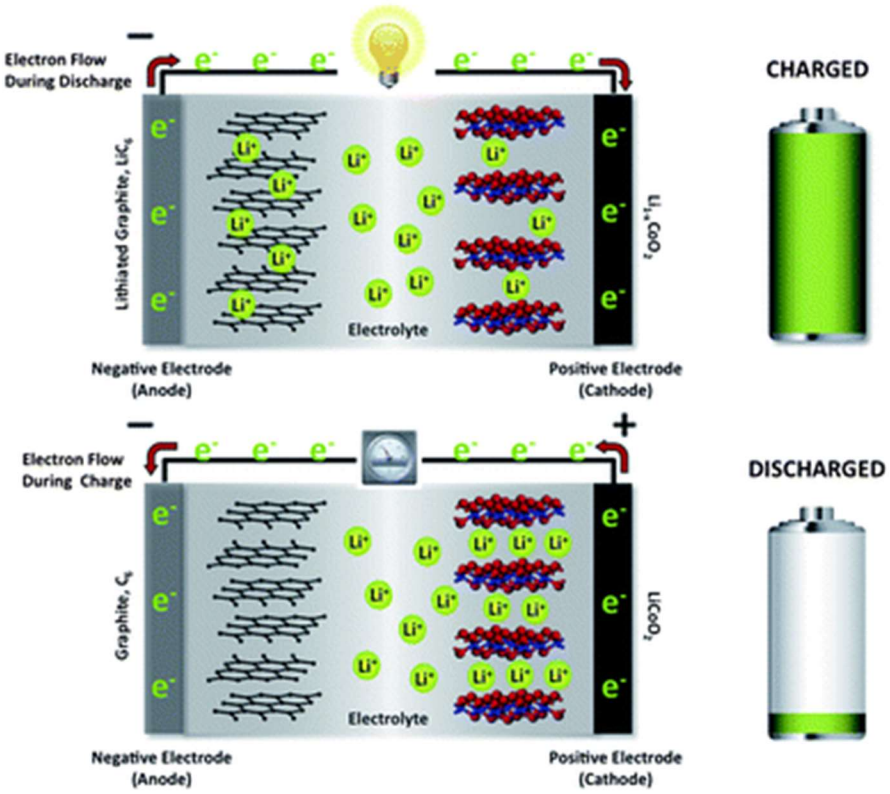

Figure 2.1. A schematic illustration of the working principles of $Li_xC_6/Li_{1-x}CoO_2$ electrodes separated by a liquid electrolyte to form a lithium-ion cell. During discharge, Li^+ ions flow from the negative electrode to the positive electrode through the electrolyte, while concurrently electrons flow from the negative electrode to the positive electrode via the external circuit in order to charge balance. Lithium ions diffuse from a lithiated graphite (Li_xC_6) structure (the anode) into delithiated $Li_{1-x}CoO_2$ (the cathode) with concomitant oxidation and reduction of the two electrodes, respectively. The reverse process occurs during charge. Figure reprinted from reference[2].

2.1.1 Positive Electrode

The first intercalation oxide positive electrode (cathode) to be discovered, $LiCoO_2$,[6] is still in use today in batteries for consumer devices and was first commercialised in a rechargeable Li-ion battery in 1991 by SONY.[5,7] $LiCoO_2$ has a trigonal (space group R3-m) layered structure, consisting of a cubic closepacked oxygen array with transition metal and lithium ions occupying octahedral sites in alternating layers (**Figure 2.2(a)**). During charging, $LiCoO_2$ is oxidised to $Li_{1-x}CoO_2$ (**Scheme 2.1**) and the generated lithium ions migrate through the electrolyte and are intercalated at the negative electrode, which undergoes electrochemical reduction. When the battery is discharged to produce a current, the anode is oxidised and the lithium ions return to their position within the cathode which in turn undergoes electrochemical reduction.

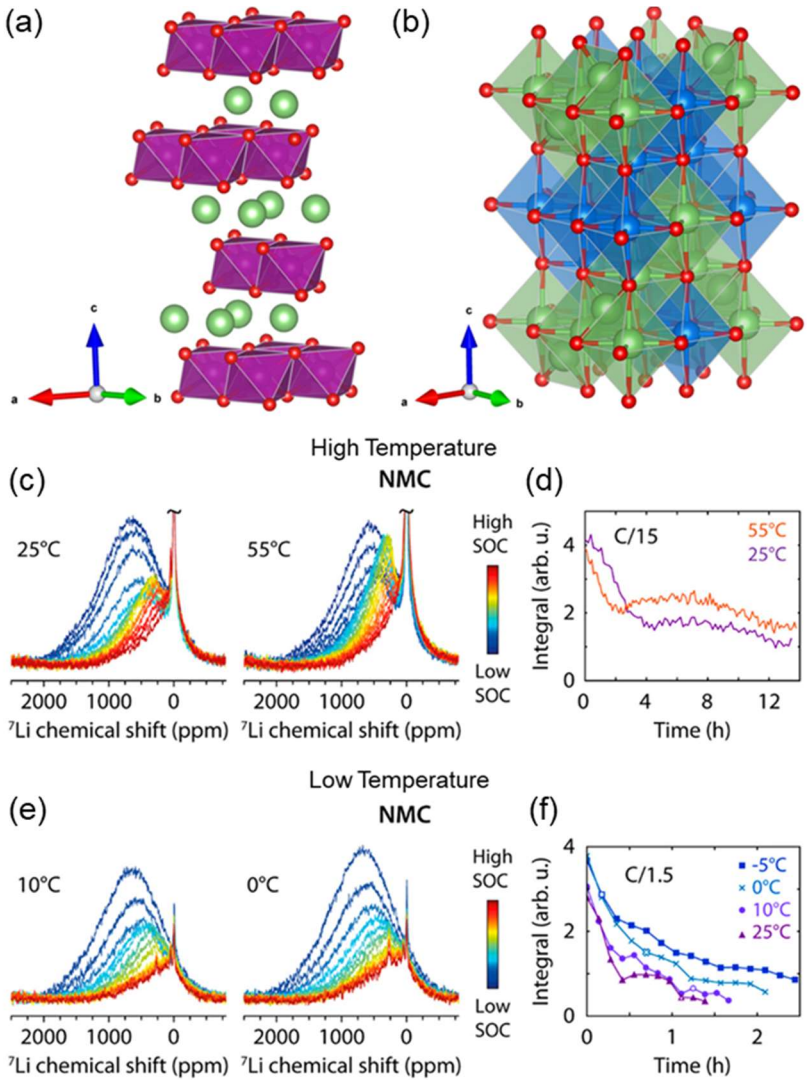

Figure 2.2. Crystal structure of (a) $LiCoO_2$ and (b) $LiMn_2O_4$. Li atoms and polyhedra are represented in green, Co in purple, Mn in blue and O in red. Structural parameters were obtained from references [8] and [9] respectively and replotted in VESTA. (c-f) Li-ion mobility in $LiNi_{0.8}Mn_{0.1}Co_{0.1}O_2$ (NMC811) as a function of temperature as probed by operando NMR experiments on a NMC811/graphite full-cell, cycled between 4.3 and 2.5 V. 7Li NMR spectra of NMC811 (c,e) and the integrated signal intensities (d,f) during charge at variable temperatures. Adapted with permission from reference[10]. Copyright 2020 American Chemical Society.

Other examples include manganese oxides, such as the spinel $LiMn_2O_4$ (**Figure 2.2(b)**), are less expensive and toxic than cobalt oxides and can offer improved lithium ion diffusion and, thus, high rate capabilities. $LiMn_2O_4$ possesses the spinel structure composed of a ccp array of X anions with A- and B-site cations occupying some or all of the tetrahedral and octahedral sites and undergoes a similar intercalation process as $LiCoO_2$ upon charging and discharging, as outlined below.

$$Li_{1-x}CoO_2 + xLi^+ + xe^- \rightleftharpoons LiCoO_2 \quad (2.1)$$

$$Li_{1-x}Mn_2O_4 + xLi^+ + xe^- \rightleftharpoons LiMn_2O_4 \quad (2.2)$$

Further cathode material research has produced several other phases for commercial use have emerged for example: $LiNi_xCo_yAl_zO_2$[11-15] and $LiNi_xMn_yCo_zO_2$[16-19] which are isostructural to $LiCoO_2$ but with greater specific capacities. The decreased amounts of Co in these compounds reduces cost and improves performance.

NMR investigations of cathode materials can provide both structural as well as ion dynamics information. While long-range structural information is typically available from diffraction methods, solid-state NMR is an extremely useful tool for characterizing local structure in these materials, even in highly disordered systems. However since cathode materials often contain paramagnetic constituents, the resulting spectra are often complicated by the paramagnetic interaction and Knight shift[20-22] (**Chapter 1 section 1.2.1**) One example of NMR usage in cathode research is shown in **Figure 2.2** Grey *et.al*

demonstrated the capability of operando ^{7}Li NMR to monitor the ion mobility processes occurring in both electrodes of a full lithium ion battery individually. Using specialised equipment that allows for the measurement of ^{7}Li NMR spectra during battery cycling, the authors report *in operando* NMR measurements of the charging process at temperatures between -5 and 55 °C. As the state of charge increases, there is a decrease in ^{7}Li signal intensity, followed by a recovery at lower shift. The spectra measured at 55 °C show the fast decrease and subsequent recovery of signal intensity occurs earlier during charge and leads to a more intense and sharper signal compared to the data at 25 °C. Accordingly, the local minimum in the integration curve (**Figure 2.2(c)**) occurs after shorter charging time. This result confirms previous measurements[23] that the local minima are caused by changes in Li-ion mobility, and more precisely by a transition from the slow motion to the fast motion regime. Li-ion mobility is reduced with decreasing temperature, as seen via the shift of the local minimum to higher SOC and its eventual disappearance.

2.1.2 Negative Electrode

At present, there are only two types of commercialized negative electrode (anode) materials: those based on carbon (primarily graphite)[24,25] (**Figure 2.3(a)**) and the oxide spinel $Li_4Ti_5O_{12}$ (**Figure 2.3(b)**)[26-30] as well as silicon[31,32] and silicon oxide[33-35] based anodes.

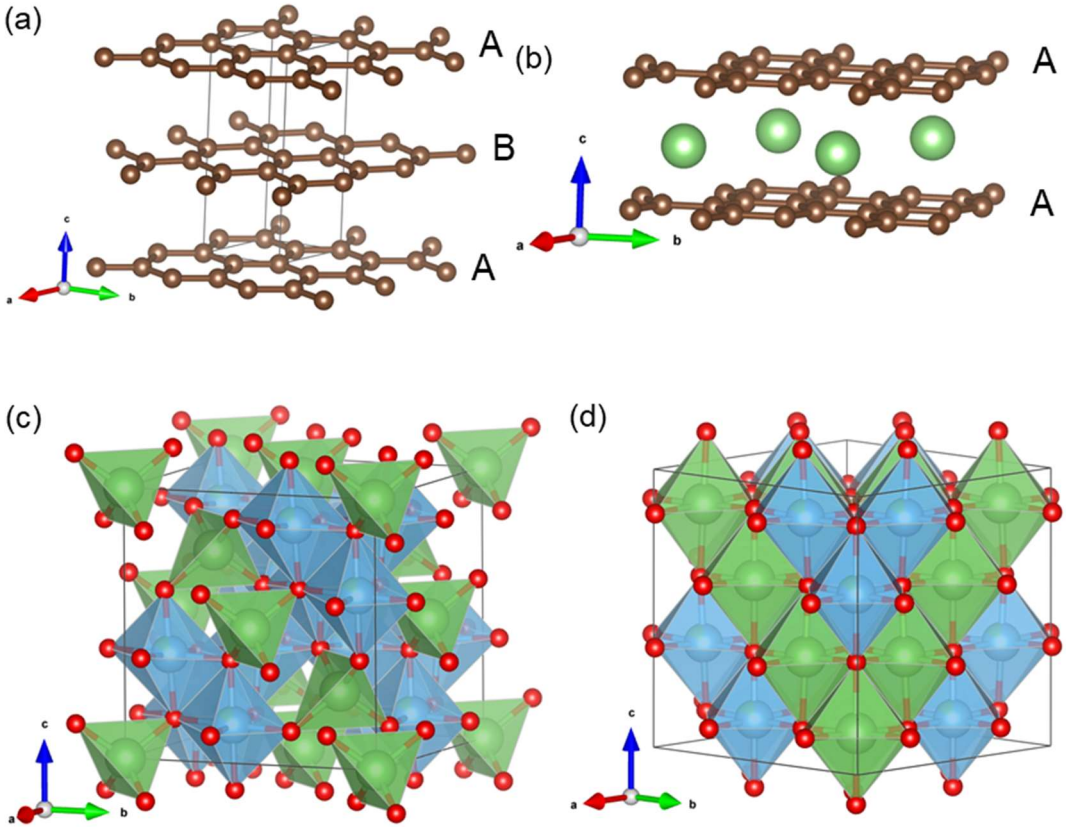

Figure 2.3. Crystal structures of (a) graphite, (b) lithiated graphite (where C and Li atoms are depicted in brown and green respectively), (c) Li_4TiO_{12} where the Li atoms occupy the tetrahedral 8a sites and (d) $Li_7Ti_5O_{12}$ where the Li atoms occupy the octahedral 16c sites (where Li, O and Ti atoms and polyhedra are shown in green red and blue respectively. Structural parameters are taken from references [36] and [37] respectively and replotted in VESTA.

Graphite consists of graphene sheets staggered in either an AB (hexagonal, the most common form) or ABC (rhombohedral) stacking arrangement (**Figure 2.3(a)**). Upon insertion of lithium ions, the graphene sheets stack directly on top of one another in an AA arrangement, and staging occurs; i.e. compounds form in which there are periodic arrays of unoccupied galleries, with the number dependent on the value of x in Li_xC_6. The spinel lithium titanium oxide, $Li_4Ti_5O_{12}$, is an alternative to graphite, but its use is restricted to applications that do not require high energy density because of its high operating voltage (1.5 V vs. Li/Li^+). It reversibly accommodates lithium to form the rock salt phase, $Li_7Ti_5O_{12}$ upon full lithiation. During this process, the atoms rearrange and the Li atoms move from the tetrahedral 8a sites to the octahedral 16c sites.

$$C_6 + Li^+ + e^- \rightleftharpoons LiC_6 \quad (2.3)$$

$$Li_4Ti_5O_{12} + xLi^+ + xe^- \rightleftharpoons Li_{4+x}Ti_5O_{12} \quad (2.4)$$

Detailed NMR and diffraction investigations of $Li_{4+x}Ti_5O_{12}$ reveal that for values of x = 0 (full 8a occupation) and x = 3 (full 16c occupation) Li-ion mobility is extremely limited.[38] However when 0 < x < 3 a solid solution is formed, containing domains where either 8a or 16c Li sites are dominantly occupied.[39,40] Due to the small length scale of these domains, Li-ion mobility occurs from one domain to the next through the solid solution as observed through EXSY NMR (**Figure 2.4**). As mentioned in **Chapter 1 section 1.5.8** cross-peaks can be observed via chemical exchange, in this case between the two distinct resonances associated with Li residing in the 8a and 16c sites,

which increase in intensity with increasing mixing time, τ_m. The fitting of the cross-peak build-up (**Figure 2.4(c)**) resulted in a Li-ion jump rate, τ^{-1} between the 8a and 16c sites of ~400 s^{-1} and further NMR calculations lead to a diffusion coefficient of approximately 4 x 10^{-12} cm^2 S^{-1}.

Meanwhile, the ultraslow Li-ion mobility in $Li_4Ti_5O_{12}$ has been captured by spin-alignment echo and SLR measurements (**Figure 2.4(d)**), where between 295 and 400 K extremely slow τ^{-1} values ranging from 1 to 2200 s^{-1} with large activation energies of 0.94(1) eV were measured.

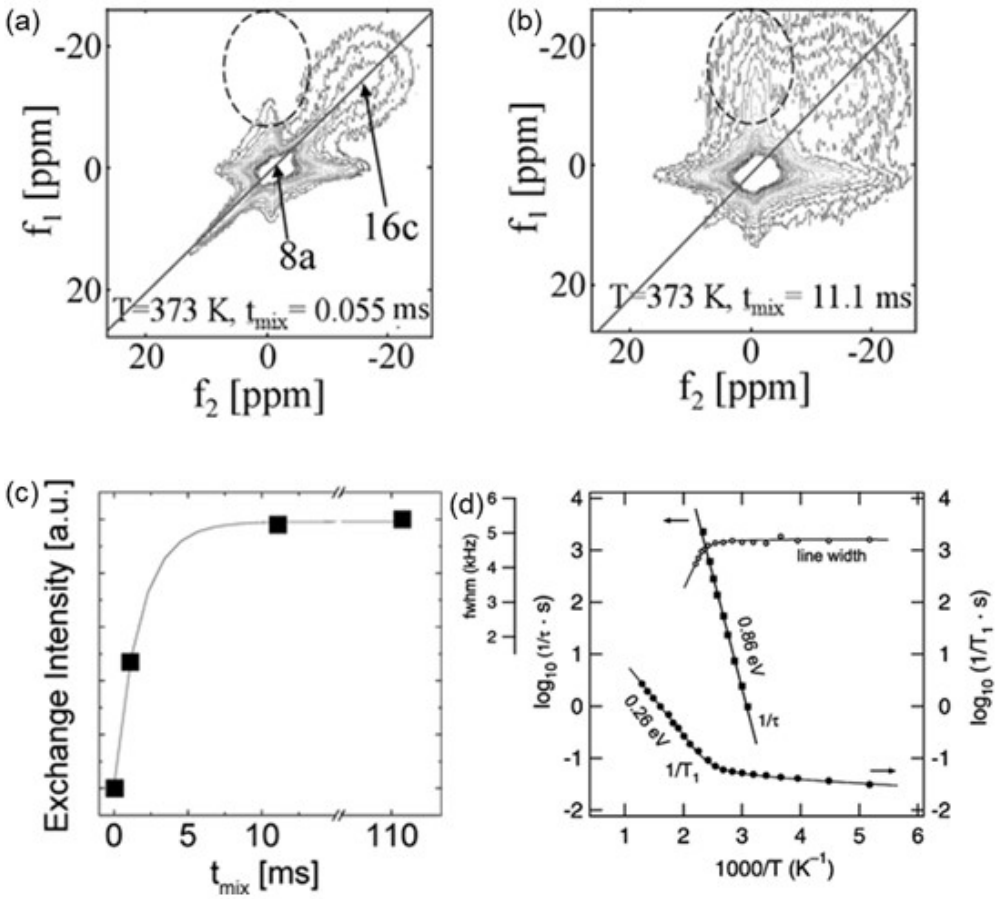

Figure 2.4. ^{7}Li MAS EXSY NMR centred on the central region in $Li_6Ti_5O_{12}$ collected at 373 K with τ_m values of (a) 0.055 and (b) 11.1 ms respectively. For increasing τ_m, cross signal intensity becomes visible in the marked region indicating Li-ion diffusion between the 8a and 16c sites. (c) Cross-peak intensity between 8a and 16c sites *vs* τ_m, including a fit assuming hopping between 8a and 16c resulting in a τ_c of 2.3 ms. (d) τ^{-1} vs. 1/T obtained from ^{7}Li spin-alignment echo NMR measurements of $Li_4Ti_5O_{12}$. For comparison, spin–lattice relaxation rates $1/T_1$ and full width at half maximum (FWHM) of the ^{7}Li NMR central transition are also shown. (a-c) Adapted with permission from reference[40]. Copyright 2009 American Chemical Society. (d) Reproduced from reference[38] with permission from the Royal Society of Chemistry.

2.1.2.1 Lithium Silicides

The concept of using silicon as a negative electrode material stems from its exceptionally high specific capacity, far surpassing that of the more conventional carbon anodes.[41-44] However this technology is still limited by both a reduction in capacity during cycling and the high volumetric change of Si-based anodes.[43,44] One material of note is $Li_{12}Si_7$, which has been reported to display high conductivity of Li-ions, with a jump rate of ~10^5 s^{-1} at 150 K and reached 10^9 s^{-1} at 425 K.[45] These values were obtained using ^{7}Li NMR spectroscopic techniques such as ^{7}Li line narrowing and SLR rate measurements (**Figure 2.5**). The results in this paper were pivotal in furthering the application of SS-NMR in the characterisation of ion mobility pathways in solids, as this was the experimental verification of the mathematical proof determined by Sholl *et. al.*[46] relating the frequency dependence of the high temperature flank of the BPP curves in the rotating frame (**Figure 2.5(c)**). Three Li-ion diffusion processes were observed, a quasi-1D process occurring in two well-separated 1D partial structure elements along the [100] direction and two 3D processes that occur at a much slower rate. The activation energies associated with the two 3D processes and the quasi-1D process were reported to be 0.55, 0.32 and 0.18 eV respectively.

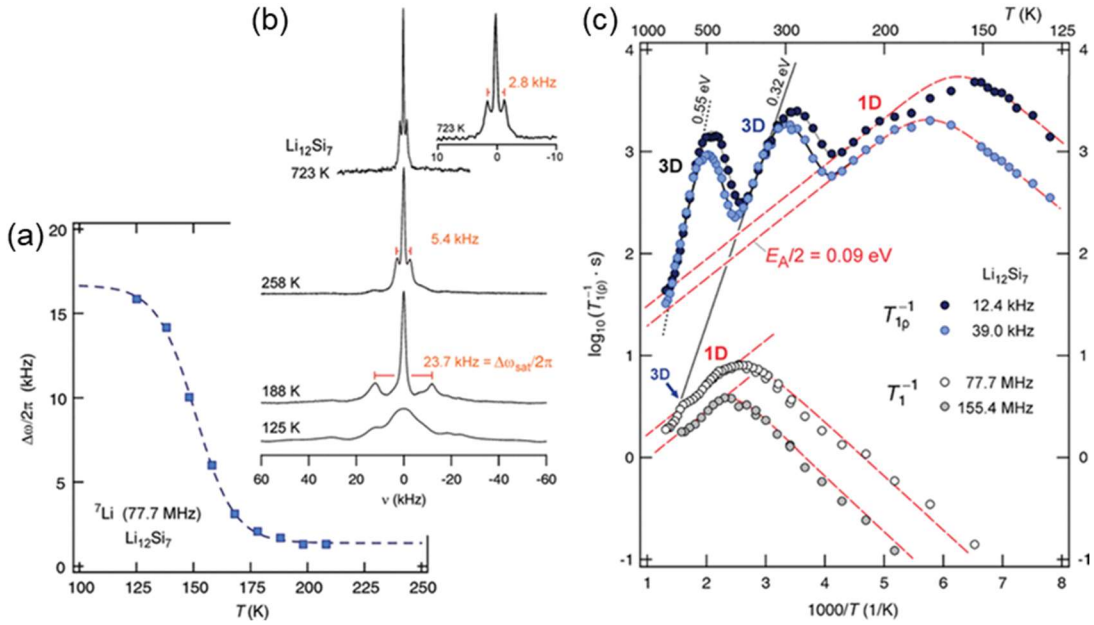

Figure 2.5. (a) ^{7}Li NMR spectra recorded at various temperatures (125, 188, and 258 K at $\omega_0/2\pi$ = 155.4 MHz and 723 K at 77.7 MHz). The spectral distances of the quadrupolar satellites ($\Delta\omega_{sat}/2\pi$) are indicated. (b) Motional narrowing of the line width (full width at half-maximum) of the central ^{7}Li NMR transition. (c) Arrhenius plots of the ^{7}Li NMR SLR rates in the laboratory frame, T_1^{-1}, at $\omega_0/2\pi$ = 155.4 and 77.7 MHz and those in the rotating frame, $T_{1\rho}^{-1}$, at $\omega_1/2\pi$ = 39.0 and 12.4 kHz. Dashed lines are guides to the eye. Figures adapted with permission from reference [45]. Copyright 2013 American Chemical Society.

2.1.3 Liquid state electrolytes

Typical commercial electrolytes are composed of organic lithium salts such as $LiPF_6$ in a non-aqueous solvent,[5,47,48] commonly comprised of dimethyl carbonate, diethyl carbonate, ethyl methyl carbonate, ethylene carbonate, propylene carbonate (**Figure 2.6**) or a combination of multiple, due to their inertness toward strong reducing agents such as lithium. Commonly a porous polymeric layer consisting of polyethylene and/or polypropylene are also added in liquid electrolytes as a separator layer to avoid contact between the anode and cathode. The pore sizes of these separators are smaller than the particle sizes of the electrodes, while allowing Li^+ ions to travel through. These organic liquid electrolytes have led to safety hazards covered in detail by global news in recent years.

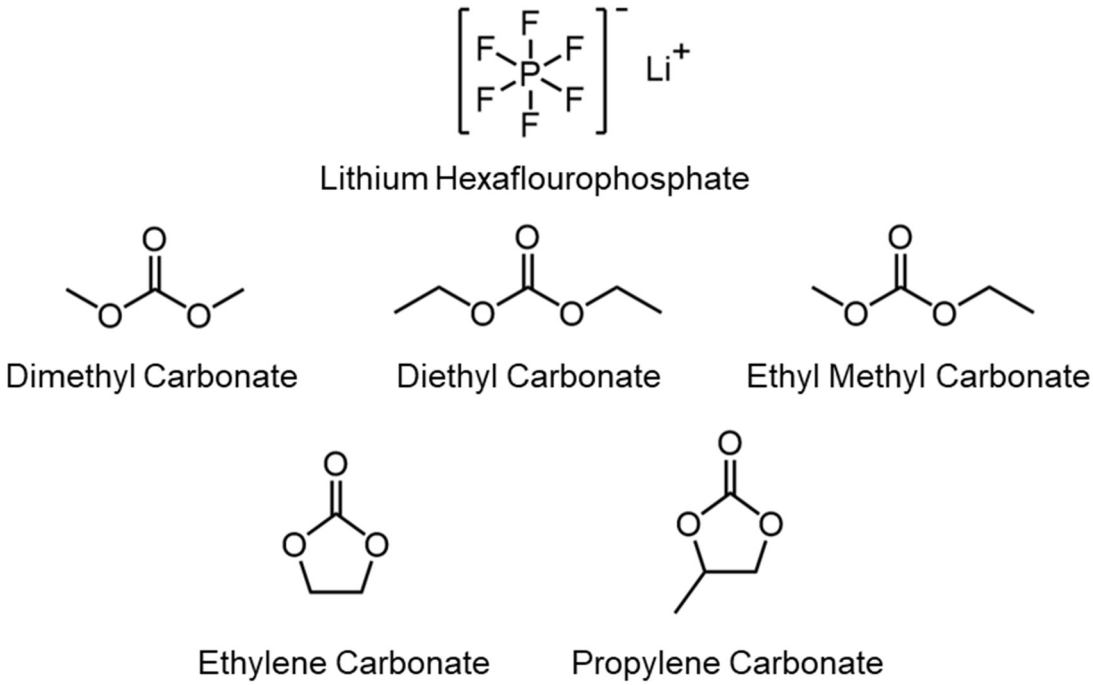

Figure 2.6. Chemical representations of common liquid electrolyte components, where the structures of the commonly used Li salt LiF_6 and non-aqueous organic solvents dimethyl carbonate, diethyl carbonate, ethyl methyl carbonate, ethylene carbonate and propylene carbonate are shown.

2.1.4 Solid-state Electrolytes

Current generation lithium ion batteries with liquid electrolytes composed of a Li salt in a solvent, offer high performance arising from high ionic conductivity and excellent wetting of the electrode surfaces.[49] However even with the inclusion of a flame retardant material such as phosphate solvents like trimethyl phosphate[50,51] or (ethoxy)-pentafluorocyclotriphosphazene,[52] the organic mixture used to dissolve the Li salt is toxic and not completely non-flammable. One approach to approach this issue is to replace the liquid electrolyte with highly conductive solid ion conductors which do not contain flammable content.

By comparison, the application of a SSE mitigates this safety concern and is further coupled with an increased energy density.[53] However, overcoming the intrinsically lower ionic conductivity of solids compared with liquids as well as meeting the requirement for electrochemical stability *vs.* electrodes remains a substantial challenge in the deployment of ASSBs.[54,55]

A room temperature lithium conductivity target of 10^{-3} S cm^{-1} has been set for SSEs[54,56] based on the conductivities of current generation liquid electrolytes and has now been met in several different families of materials, including garnets ($Li_{6.65}Ga_{0.15}La_3Zr_{1.9}Sc_{0.1}O_{12}$),[57] glass–ceramics ($Li_2S$-$P_2S_5$),[58] thio-LISICONs ($Li_{9.54}Si_{1.74}P_{1.44}S_{11.7}Cl_{0.3}$),[59] halide-based SSEs (Li_3YBr_6)[60] and argyrodites ($Li_{6.6}Si_{0.6}Sb_{0.4}S_5I$).[61] Nevertheless, these materials still suffer from limitations such as one or more of the following: air and moisture sensitivity,

high production costs and poor compatibility with electrode materials. New high-performance materials can be discovered by deploying design rules developed by understanding the mechanisms of lithium ionic conduction and the limiting factors to diffusion processes in solid state electrolytes.[62]

2.2 Literature Review of Selected Lithium Electrolytes

2.2.1 Garnets

These garnet crystal structure possesses the general formula of $A_3B_2(XO_4)_3$, where A-sites, B sites and X-sites are 6, 8 and 4 coordinate, respectively. Li containing garnets $Li_5La_3M_2O_{12}$ (M = Nb, Ta)[63] and cubic $Li_7La_3Zr_2O_{12}$ (LLZO)[64] (**Figure 2.7(a)**) were initially studied as potential Li^+ ion conductors. Of the materials investigated studied, cubic LLZO looked the most promising, owing to its low activation barrier to Li^+ ion diffusion (~0.34 eV) with a room temperature conductivity of ~5 x 10^{-4} S cm^{-1}, however it was found difficult to reproduce due to the presence of a tetragonally distorted modification of LLZO[65] which has a significantly lower conductivity of 10^{-7} S cm^{-1} compared to the cubic phase. Doping LLZO with aluminium increases the room temperature stability of the cubic phase,[66-69] which lead to an increase in conductivity, matching the original LLZO values.[68]

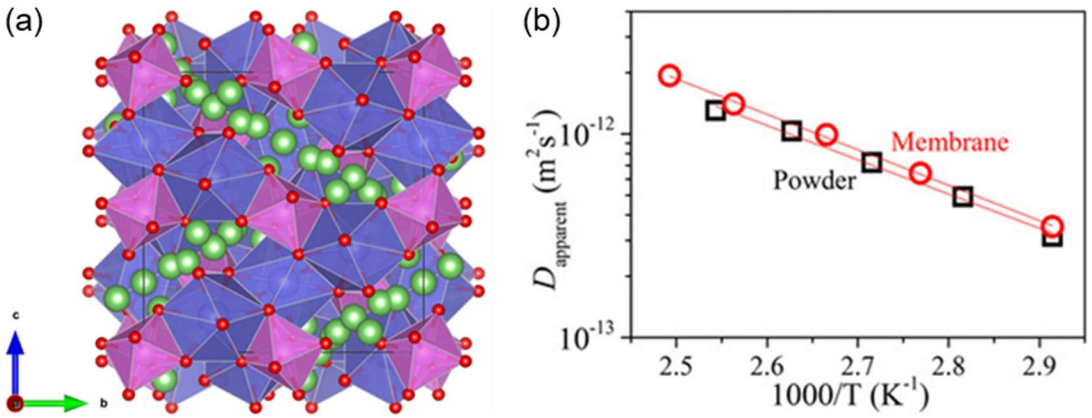

Figure 2.7. (a) Crystal structure of cubic $Li_7La_3Zr_2O_{12}$ where Li, La, Zr and O atoms and polyhedra are represented in green, purple, pink and red respectively. Structural model taken from reference[70] and is replotted in VESTA. (b) Arrhenius plots of the diffusion coefficient versus inverse temperature, pulsed field gradient parameters of gradient strength = 9.8 T m^{-1} and observation time = 70 ms for the membrane (red circle) and powder (black square) samples. Reproduced from reference[71] with permission from the AIP publishing.

These phases have been investigated by solid-state NMR, with a pure cubic LLZO being studied both as a membrane and in the powdered form, via pulsed field gradient (PFG) NMR in order to observe lithium ion migration on the μm length scale (**Figure 2.7(b)**). This investigation lead to apparent diffusion coefficients, D as a function of temperature (at a gradient strength, g of 9.8 T m^{-1} and observation time, Δ of 70 ms) in order to create an Arrhenius plot that lead to values of the activation energy for Li-ion mobility of 0.34 eV, matching the previously difficult to replicate impedance measurements.

In the aluminium containing LLZO samples, the activation barrier to Li^+ diffusion was also approximately 0.34 eV and matched the value found in the original LLZO paper.[64] The current best garnet Li^+ ion conductor is the Ga-doped sample $La_3Zr_2Li_{6.55}Ga_{0.15}O_{12}$[72] (LZLGO). The authors utilised ^{71}Ga solid-state NMR to evaluate the crystallographic position and symmetry of the Ga site in the LZLGO structure, which was found to sit in an axial symmetric tetrahedral hole expected in a cubic garnet. ^7Li and ^1H solid-state NMR was used to monitor the effect of moisture uptake. LiOH formation was observed and the increase in ^7Li T_1 was attributed to topotactic exchange of Li^+ and H^+ ions. Al/Ga doped garnets have high ionic conductivities and are stable with lithium electrodes. However, are not stable in contact with moisture or CO_2 in the ambient atmosphere. It is important to improve LLZO stability through material modifications.

2.2.2 NASICON

Sodium superionic conductor (NASICON) type solid electrolyte materials possess the general formula of $NaM_2(PO_4)_3$ with a rhombohedral structure. Two [MO_6] octahedra and three [PO_4] tetrahedra comprise the 3D framework via corner sharing. The Na atoms can be replaced with Li, forming the $LiM_2(PO_4)_3$ general formula, where M is Ti, Zr or Ge[73] with M = Ti (LTP) demonstrating high chemical and thermal stability along with a ionic conductivity ranging from 10^{-6}-10^{-8} S cm^{-1} due to the high resistance in the grain boundaries.[74] Research into LTP has shown that partial heteroatom

substitution can have a large effect on the ionic conduction in the material.[74] The most successful of which having been substitution with Al^{3+} cations to create $Li_{1+x}Al_xTi_{2-x}(PO_4)_3$ (LATP) (**Figure 2.8(a,b)**). Substituting Ti^{4+} with Al^{3+} creates an additional positive charge allowing for the accommodation of further Li-ions.[75]

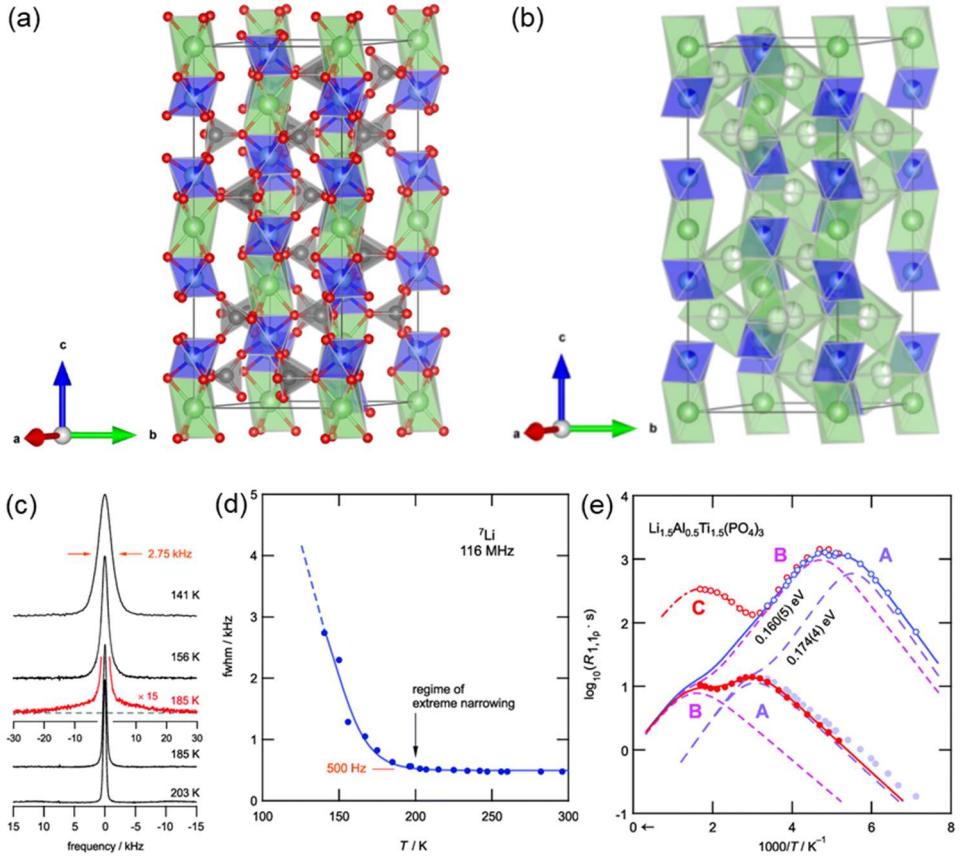

Figure 2.8. Crystal structure of $Li_{1.5}Al_{0.5}Ti_{1.5}(PO_4)_3$ where (a) Li atoms in the 36f position have been omitted for clarity and (b) where P and O atoms and all bonds have been omitted for clarity. Li, Al/Ti, P and O atoms and polyhedra are coloured green, blue, grey and red respectively. Structural parameters were taken from reference[74] and replotted in VESTA. (c) Static ^{7}Li variable temperature NMR spectra (d) FWHM of the ^{7}Li central transition as a function of temperature. (e) Arrhenius plot of the ^{7}Li NMR SLR rate is the laboratory (filled circles) and rotating (empty circle) frame of reference. The spin-lock frequency was $\omega_1/2\pi$ = 30 kHz. Red data points were recorded using a high-temperature probe, while blue points in (d) and (e) were recorded using a cryoprobe. Reproduced from reference[76] with permission from the Royal Society of Chemistry.

^{7}Li solid-state NMR spectroscopy has been utilised in order to monitor the key Li jump processes in LATP on the atomic scale.[76] The Li-ion diffusivity in LATP is extremely high as evidenced from the ^{7}Li line narrowing data (**Figure 2.8(c,d)**) and can compete with that of sulfide-based electrolytes, which suffer from hygroscopic properties that complicate both preparation and processing on a commercial level.

NMR relaxation experiments reveal heterogeneous dynamics comprising distinct ultra-fast and slower diffusion processes (**Figure 2.8(e)**), ^{7}Li NMR relaxometry revealed several distinct diffusion processes pointing to a complex overall diffusion mechanism, with activation energies of 0.16(1) eV. The τ^{-1} values obtained at the temperatures of the diffusion-induced rate peak (see **Chapter 1.4**) maxima are on the order of 10^{8} s^{-1} and 10^{4} s^{-1} depending whether the measurements were performed in the laboratory or rotating frame, respectively. The data seem to suggest three distinct relaxation processes in the accessible temperature range, as evidenced by the number of maxima marked by A, B, and C in the figure. Processes A and B are attributed to long range translational Li-ion mobility, while the process reflected by maximum C is only partially observable in the rotating frame at T ≥ 600 K. The peak might reflect Li motion along a separate diffusion pathway that is activated at elevated temperatures only. Alternatively, it could represent rotational dynamics of the [PO_4] or [TiO_6] polyhedra.

NASICON-type solid electrolytes such as LAGP have high ionic conductivity and good chemical and electrochemical stability. However, one of the LAGP

precursor, GeO_2, is expensive and can significantly increase cost of LAGP based ASSBs. It is necessary to develop cost effective new NASICON.

2.2.3 Perovskites

Perovskite materials have grown rapid interest in the energy storage materials community for their potential use in solar cells and LEDs[77-79] as well as solid electrolytes[80,81] and electrodes.[82-84] The perovskite structure has the basic formula of ABX_3 where A and B are different sized cations and X is the anion. The B cation is octahedrally coordinated to six X anions. Each X anion bridges with another B cation, forming a 3D lattice of corner shared BX_6 octahedra. The A site cation resides in a 12-coordination hole made by the octahedral lattice. This growth in interest in perovskites in various materials communities, including the battery community, is due to their flexible nature in replacing both A- and B-site cations, and their ability to not only dope into the cation sites but also the anion sites.[85]

The most highly conducting perovskite to date is the $Li_{3x}La_{2/3-x}TiO_3$ (LLTO) family[86] and is composed of TiO_6 octahedra on the B-site and La^{3+} and Li^+ on the A-site, with alternating La^{3+} rich and poor layers (**Figure 2.9(a)**). The bulk conductivity of LLTO (x = 0.11) is high with a value of 10^{-3} S cm^{-1} at room temperature and an activation barrier of 0.40 eV. Many materials based on LLTO have been made, both by altering the Li^+ content and cations on both sites, with bulk conductivities and activation barriers of 10^{-3}–10^{-5} S cm^{-1} and 0.25–0.40 eV.[87]

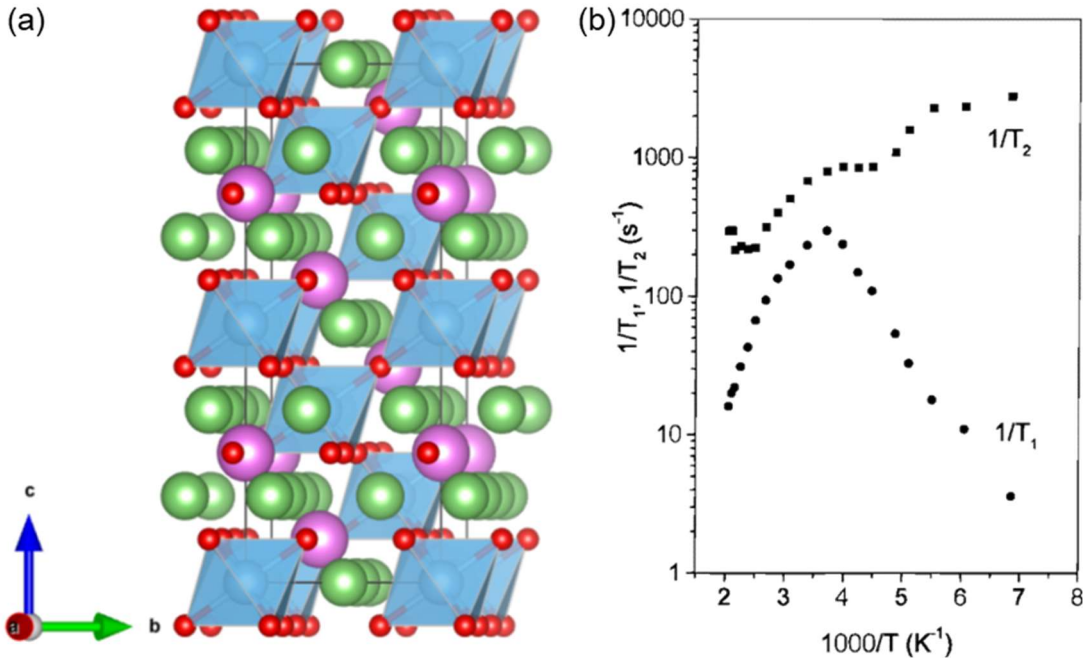

Figure 2.13. (a) Crystal structure of $Li_{3x}La_{2/3-x}TiO_3$ (x = 0.11) with corner sharing TiO_6 octahedra. Atoms and polyhedra colours: La (pink), Li (green), Ti (blue), O (red). Structural model taken from reference[88] and is replotted in VESTA. (b) Evolution of the T_1^{-1} (black circles) and T_2^{-1} (black squares) relaxation rates as a function of inverse temperature for $Li_{0.18}La_{0.61}TiO_3$. Adapted with permission from reference[89]. Copyright 2000 American Chemical Society.

Two main properties make LLTO a good Li^+ ion conductor. First, the A-site cations in LLTO have different charges and defects must therefore be introduced to balance the charge. In the case of LLTO, vacant A-sites are formed. Secondly, due to the small ionic radii of Li^+ (0.59 Å),[90] it is displaced from the centre of the A-site and displays a fourfold coordination.[91] The ionic radii of Li^+ in this coordination sphere is significantly smaller than La^{3+} (1.36

Å),[90] allowing Li^+ to travel through the bottleneck between A-sites (~1.07 Å for an ideal perovskite cell,[92] corresponding to Li^+ diffusion through the material. Solid-state NMR has been used extensively to understand the Li^+ dynamics in LLTO. The change in spin-lattice relaxation time T_1 of $Li_{0.18}La_{0.61}TiO_3$ with temperature showed a maximum of T_1^{-1} curve at 275 K (**Figure 2.9(b)**), the correlation time τ of the Li motion satisfies the relation $\omega_0\tau \approx 1$. From this fact, the correlation time is calculated to be $\approx 10^{-8}$ s at 275 K. A more comprehensive analysis of the T_1^{-1} curve shows that a second maximum with a lower intensity could be present at 333 K, confirming the existence of two stages in Li motion deduced from T_2^{-1} data. The presence of these two rate maxima was also observed in other LLTO phases.[93] Activation energies deduced from both sides of the maximum are 0.16 eV (low temperatures flank) and 0.25 eV (high temperatures flank).

Perovskite-type solid electrolytes are promising for application in ASSBs. However, preparation conditions are very harsh and ionic conductivity is less than other families of materials.

2.2.4 Anti-perovskites

Whereas the perovskite structure has a basic formula of ABX_3 where A and B are different sized cations and X is the anion, the anti-perovskite structure contains the same basic formula with the anion and cation sites reversed. Lithium rich anti-perovskites (LiRAPs) have been widely researched[94-97] due to their high reported room temperature ionic conductivities ($>10^{-3}$ S cm^{-1}),

however the preparation, structures, ionic conductivities and ion mobility mechanisms in LiRAPs have been the subject of considerable debate in recent years.[98]

One example of such a material is the hydrated phase, Li_2OHCl, in which two phases have been confirmed.[99] Below ~310 K, Li_2OHCl is reported to exist as an orthorhombic structure whilst above this temperature, Li_2OHCl undergoes a phase transition to the cubic anti-perovskite phase. This phase transition, which is observed via both ^2H VT measurements and ^7Li and ^1H relaxometry (**Figure 2.10(a-c)**), is known to increase the Li-ion conductivity by several orders of magnitude. The ^2H VT measurements between −19 and 63 °C display a classic, axially symmetric lineshape MAS pattern indicative of the absence of motion and, hence, static OH^-/OD^- groups. The ^2H NMR data presented indicates that even at 63 °C, when Li_2ODCl is known to be in the cubic phase, the OH^-/OD^- groups are still static, indicating that even though the phase transition has occurred, the OH^-/OD^- groups are not yet mobile. Hence, the phase transition alone is not responsible for mobility of the OH^-/OD^- groups. As the temperature is increased to 95 and 110 °C, a single resonance is observed, confirming mobility of the OH^-/OD^- groups. There is a strong correlation between the Li motion and OH^- group rotation in $Li_{3-x}OH_xCl$, with the OH^- groups being able to freely rotate in the cubic phase, whereas they are believed to be static in the orthorhombic phase as a result of the reduced Li motion.[100]

Extensive studies combining NMR and computational methods have been undertaken in order to investigate the local and long range ionic diffusion in Li_2OHCl.[99-101] The rotation of the OH^- group determines ion dynamics of Li^+ and H^+ as evidenced by the ^2H NMR as well as the ^7Li and ^1H spin-lattice T_1 relaxation experiments (**Figure 2.10(b,c)**). Variable temperature ^2H and ^1H relaxometry NMR data indicates that proton movement is limited to rotation of the OH^- groups while Li-ion mobility is long range. The presence of both static and locally mobile OH^- groups in the cubic phase of Li_2OHCl was confirmed using ^2H NMR. The NMR experiments show that the protons point towards Li vacancy sites and that there is a strong correlation between long-range Li-ion transport and OH^- rotation (**Figure 2.10(d)**).

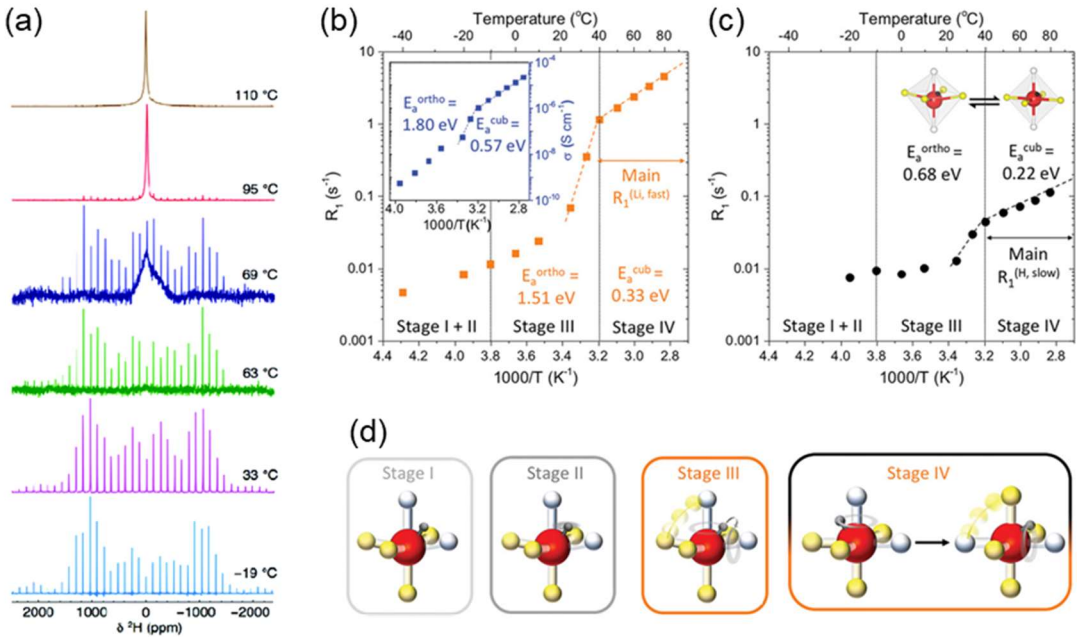

Figure 2.14. (a) Variable temperature ^{2}H MAS NMR spectra of Li_2ODCl collected at ν_r = 10 kHz. Spin lattice relaxation rate for (b) ^{7}Li and (c) ^{1}H. Inset shows the Li ionic conductivity measured by electrical impedance spectroscopy (EIS). (d) Li and H motion in Li_2OHCl at various stages (Li: yellow, Li vacancy: white, H: dark grey, O: red). (a) Figure adapted from reference[100] with permission from the Royal Society of Chemistry. (b-d) Figure adapted from reference[101] with permission from Wiley Ltd.

Below −40 °C (Stage I), no large-angle motions are observed for both H^+ and Li^+. The proton movement is first detected as librational motion of the OH group in the temperature range between −40 °C and −10 °C (Stage II), in which Li-ions are still immobile. At higher temperature range of −10 to +40 °C thermally activated re-orientational motion of the OH group between two adjacent vacancy sites enables Li^+ diffusion within a unit cell. At above 40 °C

the rapid hopping of Li^+ that represents the change from apical to adjacent Li vacancy sites enabling Li^+ diffusion between unit cells. In the (orthorhombic symmetry) unit cell the Li/H-rearrangements are sluggish and random in different conformations. As the crystal structure changes to tetragonal and then to cubic symmetry at higher temperatures, the exchange rates and thus the translation Li^+ diffusion rapidly increases.

Anti-perovskite-type of solid electrolytes have the benefit of high ionic conductivities and can be applied in bulk and thin-film ASSBs. However, they are very hygroscopic and operation in an inert atmosphere is required, limiting their usage in ASSBs.

2.2.5 LISICON

The first lithium superionic conductor (LISICON) $Li_{14}Zn(GeO_4)_4$ was reported during the study of the $Li_{16-2x}M^{II}_x(M^{IV}O_4)_4$ compositions (M^{2+} = Mg^{2+}, Zn^{2+}; M^{4+} = Si^{4+}, Ge^{4+}) ($1 < x < 3$) and has a conductivity value of 0.13 S cm^{-1} at 300 ^oC.[102] The framework of LISICONs is the same as γ-Li_3PO_4 (**Figure 2.11(a)**) and consists of a hexagonal closed packed array of corner sharing $M^{2+}O_4$ and $M^{4+}O_4$ tetrahedra. However Li_3PO_4 has been shown to have a very limiting Li-ion conductivity of 10^{-9} S cm^{-1}.[103]

Nitridation of γ-Li_3PO_4 proceeds by the substitution of two atoms of N^{3-} for every three atoms of O^{2-}, giving rise to an oxynitride glass with formula $MPO_{3-3x/2}N_x$. The network structure of this new glass will then be composed of some remaining PO_4 groups and new PO_3N and PO_2N_2 ones. Due to this nitridation

process, the properties of the resulting materials are greatly enhanced, notably mechanical and chemical resistance and ionic conductivity. This class of solid-ion conductors is referred to as LiPON. Solid-state NMR has been utilised in the investigation of LiPON in both the Li-ion mobility as well as the role of the PO_4 units in the ion migration.[104,105] The ^{7}Li NMR investigations on LiPON thin films evidenced that only part of the Li-ions are mobile and participate in the diffusion process. In addition, the number of mobile Li-ions decreases in conjunction with the total number of lithium ions as nitridation increases.[104] ^{31}P MAS NMR spectra as a function of temperature (**Figure 2.11(b)**) of $LiPON_{0.42}$ in conjunction with the mapping of the ^{31}P signals obtained through various 2D correlation experiments such as rotation echo double resonance (REDOR), heteronuclear correlation (HETCOR) and incredible natural abundance double quantum transfer experiment (INADEQUATE) NMR experiments[105] allowed for the investigation of the structural arrangement of the building units and its evolution with temperature. The results evidenced that the network organization adopted by the glasses distinctively depends on the nature of the modifier cation (Li or Na). However, the results excluded any significant phase separation or segregation of oxide and oxynitride regions, despite some clustering of nitride species may be occurring, mostly in the lithium-containing glasses.

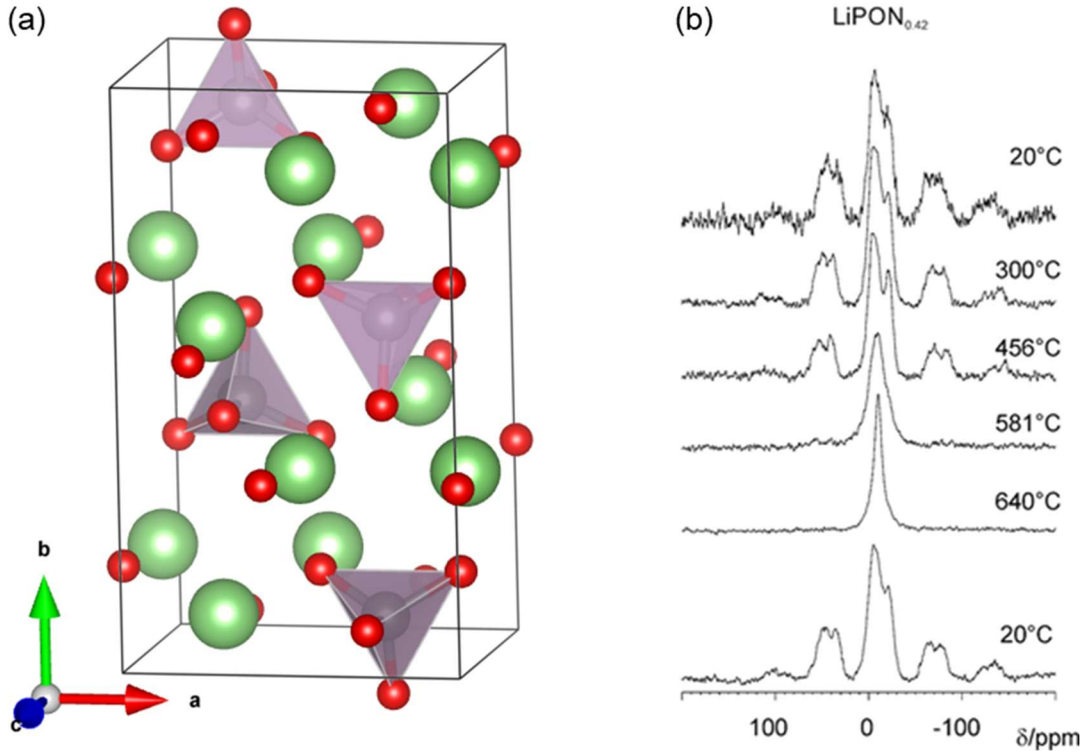

Figure 2.8. (a) Crystal structure of γ-Li_3PO_4. Atom colours: lithium (green), phosphorus (grey), O (red). Structural model was taken from reference[106] and is plotted in VESTA. (b) Variable temperature ^{31}P MAS NMR spectra for a glass sample of LiPON. The lowest spectrum is taken at ambient temperature after heating to check for permanent structural changes. Figure reprinted with permission from reference[105]. Copyright 2021 American Chemical Society.

LISICON solid electrolytes generally have good chemical and electrochemical stability, but low ionic conductivities compared with other oxide solid electrolytes. LiPON-type solid electrolytes have been applied and are suitable in thin-film ASSBs, but are not suitable for bulk ASSBs due to their low ionic conductivities of 10^{-6}-10^{-5} S cm^{-1} at room temperature.

2.2.6 Thio-LISICONs

Thio-LISICONs are a structural group based on the LISICON group, where O^{2-} is replaced with S^{2-} to improve ionic conductivity due to its larger ionic radii (152 and 170 pm, respectively) and higher polarizability characteristics.[107-110] This anion replacement reduces the Li^{+} interaction with the framework and increases the channel size, easing ion transport in the material.[109]

The most well-known and high performance best thio-LISICON reported is $Li_{10}GeP_2S_{12}$ (LGPS), which exhibits a very high conductivity of 1.2×10^{-2} S cm^{-1} at room temperature,[111] surpassing liquid-state electrolytes.[112] The structure consists of two isolated tetrahedra residing in two different crystallographic sites – one fully occupied with PS_4 and the other with a 1:1 ratio of PS_4 and GeS_4 (**Figure 2.12(a,b)**).[111,112] Further analogues of LGPS have been synthesised by replacing Ge with Si and Sn, which have shown similar conductivity values.[113,114]

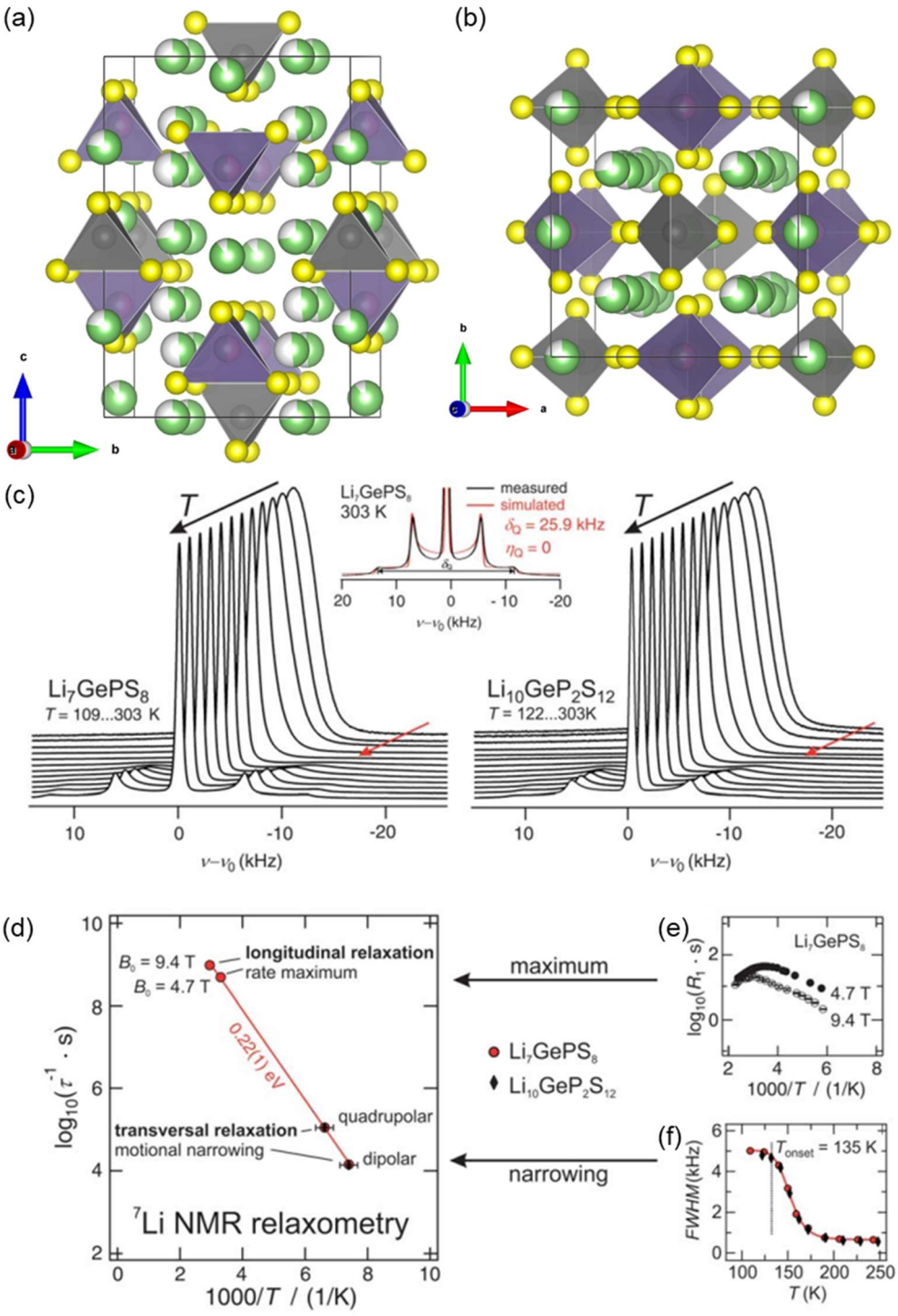

Figure 2.12. (a) Crystal structure of $Li_{10}GeP_2S_{12}$ along the (a) ***a***-axis and (b) ***c***-axis. Atom colours: Li (green), Ge (purple), P (grey), S (yellow). Purple tetrahedra denote the (Ge/P)S_4 tetrahedra site. Vacancies are shown in white.

Structural model taken from reference[115] and is plotted in VESTA. (c) Static ^{7}Li NMR spectra as a function of temperature of Li_7GePS_8 (left) and $Li_{10}GeP_2S_{12}$ (right) measured at 9.4 T. The red arrow indicates the averaging of the quadrupolar interaction. Inset: measured and simulated quadrupolar coupling of the ^{7}Li NMR spectrum of Li_7GePS_8 at 303 K. (d) Arrhenius plot of the τ^{-1} values obtained from the relaxometry and line narrowing measurements. The τ^{-1} values obtained for Li_7GePS_8 and $Li_{10}GeP_2S_{12}$ are represented by red and black circles respectively. (e) Longitudinal ^{7}Li relaxation rates measured as a function of inverse temperature of Li_7GePS_8 at 9.4 and 4.7 T. (f) Motional narrowing of the FWHM of the central transition of Li_7GePS_8 and $Li_{10}GeP_2S_{12}$. Reproduced from reference[116] with permission from the Royal Society of Chemistry.

The LGPS family has been investigated extensively through solid-state NMR spectroscopy.[116-119] The Li^+ dynamics of multiple compositions of LGPS and its Si/Sn variants have been studied using NMR relaxometry and pulse-field gradient (PFG) NMR.[116,118] It is reported that $Li_{11}Si_2PS_{12}$ has the lowest activation barrier of the series studied (0.19(1) eV), followed by $Li_{10}GeP_2S_{12}$ (0.21(1) eV), then $Li_{10}SnP_2S_{12}$ (0.23(1) eV), which are in agreement with computational studies of these phases.[120] ^{6}Li, ^{7}Li and ^{31}P NMR relaxometry and PFG NMR have been used to study the Li^+ diffusive pathway in both Li_7GePS_8 and $L_{10}GeP_2S_{12}$[117] and $Li_{10}SnP_2S_{12}$.[121] ^{7}Li line narrowing and T_1 relaxometry of Li_7GePS_8 and $Li_{10}GeP_2S_{12}$ (**Figure 2.12(d-f)**) reveal an

exceptionally high ionic conductivity of tetragonal LGPS of ~10^{-2} S cm^{-1} due to a nearly isotropic Li hopping processes in the bulk lattice of LGPS. Further investigations identify an anisotropic 3D Li^+ diffusion network, consisting of a combination of an ultrafast 1D diffusion channel of 0.16 eV probed by ^{7}Li line width and the frequency dependence on the high temperature flank of the $T_{1\rho}$-^{1} BPP curve (**Chapter 1 section 1.4.2**) relaxometry and an in-plane 2D pathway of 0.26 eV by various NMR methods. The authors also suggest the activation barriers obtained by other NMR such as PFG and non-NMR methods such as EIS are an average of the 1D and 2D processes as the timescales probed via these methods are significantly longer than for relaxometry.

Thio-LISICON solid electrolytes have the highest ionic conductivities in the magnitude of 10^{-2} S cm^{-1} at room temperature. However, they are not stable in the ambient atmosphere due to reacting with moisture. Hence they have to be used in a controlled atmosphere for bulk batteries.

2.2.7 Argyrodites

Argyrodites are a family of Li^+ ion conductors with general formula of Li_6PS_5X (X = Cl, Br, I) based on the mineral on the argyrodite Ag_8GeS_6 and has high ionic conductivities ranging between 10^{-2} and 10^{-3} S cm^{-1}.[122] The structure consists of layers of isolated PS_4 tetrahedra and X^-, with layer of isolated S^{2-} and Li^+ sites in between (**Figure 2.13(a)**).

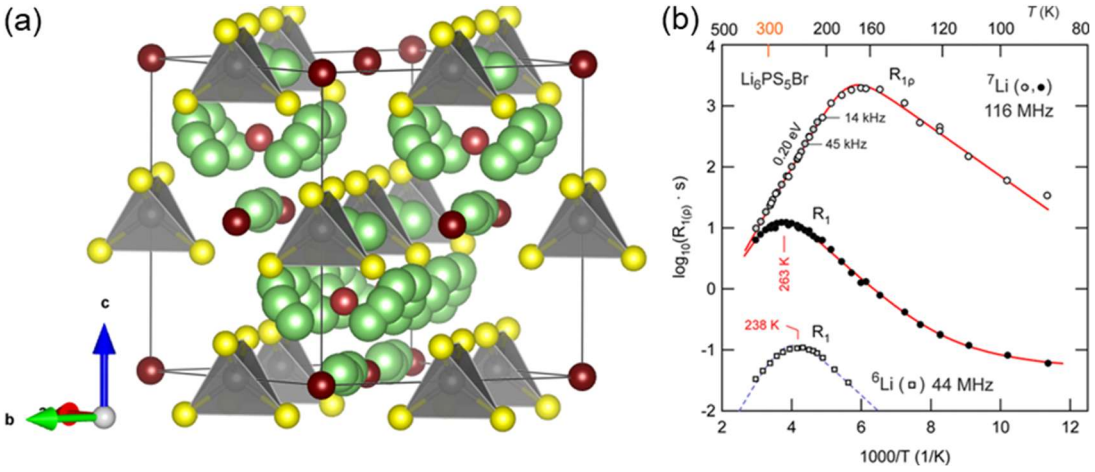

Figure 2.13. (a) Crystal structure of Li_6PS_5I. Atom colours: Li (green), P (purple), S (yellow), I (violet). Vacancies are shown in white. Structural model taken from reference[122] and is plotted in VESTA. (b) Arrhenius plot of ^6Li and ^7Li NMR relaxation rates T_1^{-1} and $T_{1\rho}^{-1}$ of Li_6PS_5Br. Reprinted with permission from reference[123]. Copyright 2013 American Chemical Society.

Variable temperature static ^7Li NMR were performed on these samples to study their Li^+ dynamics.[122-124] The bromine sample was identified as having the highest Li^+ mobility out of the halide compounds using ^7Li line width analysis,[122] which were complemented by impedance studies.[125] ^7Li NMR relaxometry on Li_6PS_5Br showed a small activation barrier for 3D Li^+ long range diffusion of 0.20(2) eV and a $T_{1\rho}^{-1}$ and T_1^{-1} maximum at 167 and 263 K, respectively (**Figure 2.13(b)**). The Li^+ jump rate derived here is converted into conductivity values by the Einstein-Smolchowski and Nernst-Einstein equations, and was found to be on the order of 10^{-2} S cm^{-1}, illustrating extremely fast Li^+ diffusion in Li_6PS_5Br.[123]

Further investigations into the dynamic processes in the iodide phase and the Ge doped derivatives $Li_{6+x}P_{1-x}Ge_xS_5I$ demonstrated that while Li_6PS_5I is a rather poor ionic conductor (10^{-6} S cm^{-1}, 298 K), the Ge-containing samples show specific conductivities on the order of 10^{-2} S cm^{-1} (330 K). Substituting P^{5+} with Ge^{4+} not only causes S^{2-}/I^- anion site disorder but also reveals via neutron diffraction that the Li-ions do occupy several originally empty sites between the Li rich cages in the argyrodite framework. As the Ge and subsequently the Li content increases the population of interstitial sites is increased and the extent of anion site disorder also increases, however, to a much lesser extent. At 25 at. % Ge, Li-ions start to occupy the new site T2 (Wyckoff 48h); at 60 at. % Ge, they also reside on the T4 position (Wyckoff 16e). The occupation of these originally empty sites forms an interconnected Li^+ sublattice offering a larger variety of jump processes. Consequently, in samples with high Ge-contents, the Li^+ ions have access to an interconnected network of pathways allowing for rapid exchange processes between the Li cages, as evidenced by the ^{7}Li line narrowing data (**Figure 2.14(a)**). Using ^{7}Li and ^{31}P SLR NMR (**Figure 2.14(b)**) it was possible to quantify and differentiate between the local intracage dynamics and the intercage jumps. The population of interstitial Li sites in $Li_{6+x}P_{1-x}Ge_xS_5I$, forming a variety of Li pathways connecting the Li-rich cages is responsible for the significant increase in Li-ion conductivity in this class of argyrodite-type materials (**Figure 2.14(c)**).

Argyrodite-type solid electrolytes possess high ionic conductivities, similar to sulfide-type solid electrolytes, however they are not stable in the ambient

atmosphere. Suitable encapsulation of cells using argyrodite-type solid electrolytes is essential, otherwise this will likely lead to safety concerns.

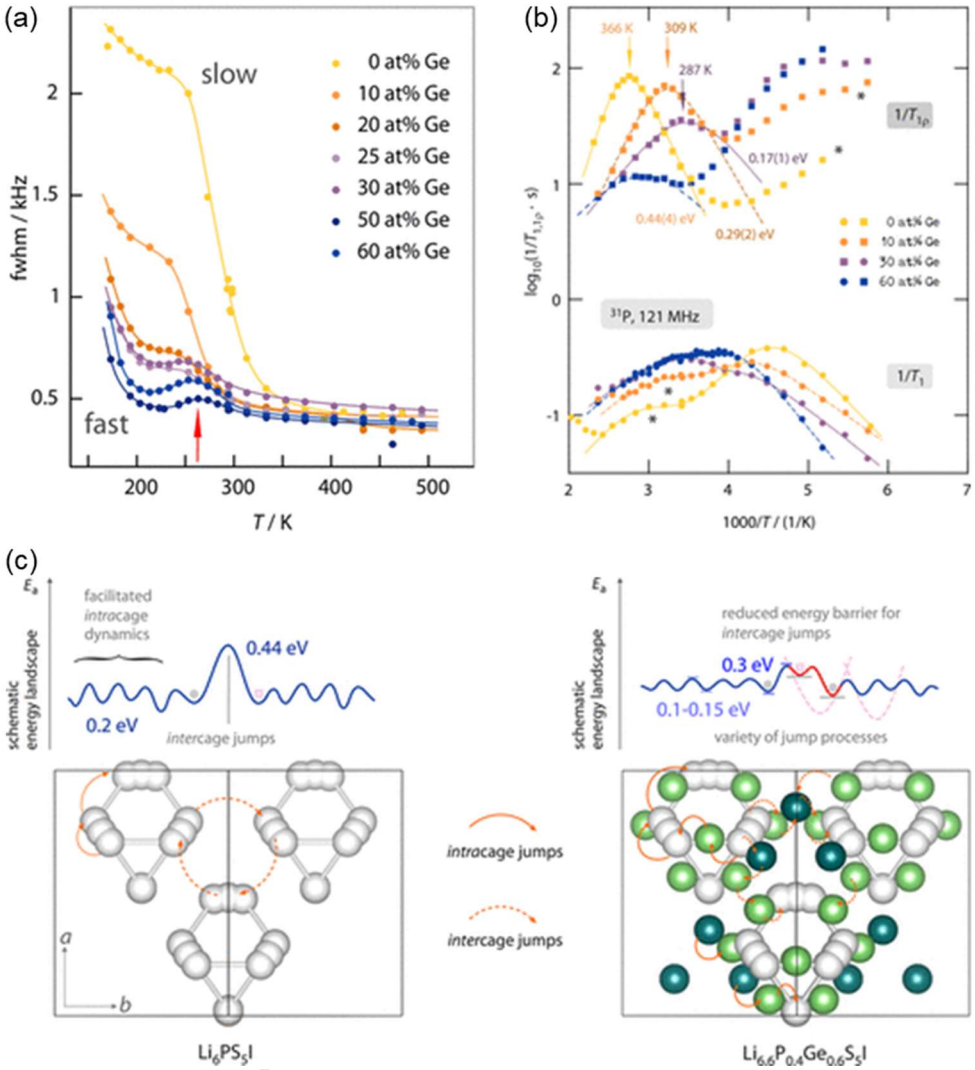

Figure 2.14. (a) Static ^{7}Li FWHM linewidths for $Li_{6+x}P_{1-x}Ge_xS_5I$ with x ranging from 0-0.6. The vertical arrow points to a local maximum that is caused by interactions of the mobile Li spins with paramagnetic centres. (b) Arrhenius plot of the diffusion induced ^{7}Li SLR rates in the laboratory (circles) and rotating (squares) frame of the x = 0.25 sample. Solid lines represent BPP global fits; dotted lines show the separate contributions to the overall response. For $T_{1\rho}^{-1}$, the two different fits including error bars are shown: Orange squares refer to the rate when fitting the transients by a simple exponential decay function, and blue squares indicate the two rates from using

a bi-exponential expression. (c) Distribution of Li^+ ions in the crystal structure of $Li_{6+x}P_{1-x}Ge_xS_5I$ with 0 at. % Ge (left) and 60 at. % Ge (right). Arrows indicate the available jump processes for the cations. A schematic energy landscape is also shown for each structure. Adapted with permission from reference[126]. Copyright 2022 American Chemical Society.

2.3 Summary and Outlook

Reported conductivities of representative Li-ion conductors of the main structural families discussed in this chapter are reported in Table 2.1. Sulfide Li-ion conductors generally have higher conductivities compared with oxide based conductors, as expected due to their higher polarizability. LGPS, $Li_{9.54}Si_{1.74}P_{1.44}S_{11.7}Cl_{0.3}$ $Li_{6.25}La_3Zr_2Al_{0.25}O_{12}$ and $Li_3OCl_{0.5}Br_{0.5}$ have comparable ionic conductivities to liquid electrolytes, however atmospheric and electrode stability limit their application in ASSBs.

Table 2.1 Reported Li-ion conductivities of solid ion conductors for the various electrolyte families discussed in this chapter at room temperature.

Family	Composition	σ / S cm^{-1}	Ref
Garnet	$Li_7La_3Zr_2O_{12}$	5×10^{-4}	64
	$Li_{6.55}Ga_{0.15}La_3Zr_2O_{12}$	2.06×10^{-3}	127
	$Li_{6.5}La_3Zr_{1.5}Ta_{0.5}O_{12}$	7.5×10^{-2}	128
	$Li_{6.25}La_3Zr_2Al_{0.25}O_{12}$	6.8×10^{-2}	128
	$Li_{6.25}La_3Zr_2Ta_{0.25}Ga_{0.2}O_{12}$	1.04×10^{-3}	128
NASICON	$Li_{1.5}Al_{0.5}Ti_{1.5}(PO_4)_3$	3×10^{-3}	76
	$Li_{1.4}Al_{0.4}Ti_{1.6}(PO_4)_3$	1.12×10^{-3}	129
	$Li_{1.3}Al_{0.3}Ti_{1.7}(PO_4)_3$	7×10^{-4}	130
	$LiTi_2(PO_4)_3$	2×10^{-6}	131
Perovskite	$Li_{0.18}La_{0.61}TiO_3$	$\sim 10^{-4}$	89
	$Li_{0.34}La_{0.51}TiO_{2.94}$	2×10^{-5}	132
	$Li_{3/8}Sr_{7/16}Ta_{3/4}Hf_{1/4}O_3$	3.8×10^{-4}	133
	$Li_{0.25}La_{0.583}TiO_3$	4.53×10^{-4}	134
Anti-perovskite	Li_2OHCl	$\sim 10^{-3}$	100
	$Li_3OCl_{0.5}Br_{0.5}$	$\sim 10^{-2}$	94
LISICON	γ-Li_3PO_4	$\sim 10^{-9}$	103
	$LiPON_{0.42}$	$\sim 10^{-6}$	105
	γ-$Li_{14.4}V_{1.6}Ge_{2.4}O_{16}$	$\sim 10^{-6}$	110
	$Li_{3.53}(Ge_{0.75}P_{0.25})_{0.7}V_{0.3}O_4$	5.1×10^{-5}	135
	$Li_{3.6}Ge_{0.6}V_{0.4}O_4$	4×10^{-5}	136
Thio-LISICON	$Li_{10}GeP_2S_{12}$	1.2×10^{-2}	111
	$Li_{4.275}Ge_{0.61}Ga_{0.25}S_4$	6.5×10^{-5}	108
	$Li_{9.54}Si_{1.74}P_{1.44}S_{11.7}Cl_{0.3}$	2.5×10^{-2}	59
	$Li_{3.25}Si_{0.25}P_{0.75}S_4$	1.22×10^{-3}	137
Argyrodite	Li_6PS_5Br	2.5×10^{-4}	138
	Li_6PS_5Cl	1.4×10^{-5}	138
	Li_6PS_5I	1.9×10^{-5}	138
	$Li_{6.6}P_{0.4}Ge_{0.6}S_5I$	5.4×10^{-3}	139
Liquid	1M $LiPF_6$ (50:50 EC/PC)	6.8×10^{-2}	140

Whilst the field of solid-electrolytes further advances, an increasing number of materials are reaching and exceeding the ionic conductivity of liquid electrolytes. However, understanding the local structure and Li-ion pathways in these materials is paramount in the further increasing the ionic conductivity

and enhancing stability against electrodes. Solid-state NMR is well suited to this task, an inherently local characterisation technique, allowing for the acquisition of information vital to the understanding of solid-electrolyte candidates. NMR can be used in conjunction (or isolated) with x-ray diffraction and impedance spectroscopy, in order to gain insights on both the local and long range structures and ion mobility pathways in these types of material.

2.4 References

1. Youngman, R., NMR Spectroscopy in Glass Science: A Review of the Elements. *Materials (Basel, Switzerland)* **2018,** *11* (4).
2. Munoz, S.; Greenbaum, S., Review of Recent Nuclear Magnetic Resonance Studies of Ion Transport in Polymer Electrolytes. *Membranes* **2018,** *8* (4), 120.
3. Morales, D. J.; Greenbaum, S., NMR Investigations of Crystalline and Glassy Solid Electrolytes for Lithium Batteries: A Brief Review. *International Journal of Molecular Sciences* **2020,** *21* (9), 3402.
4. Foran, G.; Verdier, N.; Lepage, D.; Malveau, C.; Dupré, N.; Dollé, M., Use of Solid-State NMR Spectroscopy for the Characterization of Molecular Structure and Dynamics in Solid Polymer and Hybrid Electrolytes. *Polymers* **2021,** *13* (8), 1207.
5. Tarascon, J. M.; Armand, M., Issues and challenges facing rechargeable lithium batteries. *Nature 2001 414:6861* **2001,** *414* (6861), 359.
6. Mizushima, K.; Jones, P. C.; Wiseman, P. J.; Goodenough, J. B., Li_xCoO_2 ($0<x\leqslant1$): A new cathode material for batteries of high energy density. *Solid State Ionics* **1981,** *3-4* (C), 171.
7. Goodenough, J. B., Rechargeable batteries: challenges old and new. *Journal of Solid State Electrochemistry* **2012,** *16* (6), 2019.
8. A.Robert Armstrong, A. D. R., Robert Gitzendanner, Peter G Bruce,, The Layered Intercalation Compounds $Li(Mn_{1-y}Co_y)O_2$: Positive Electrode Materials for Lithium–Ion Batteries. *Journal of Solid State Chemistry* **1999,** *145* (2), 549.
9. Thackeray, M. M.; David, W. I. F.; Bruce, P. G.; Goodenough, J. B., Lithium Insertion into Manganese Spinels. *Materials Research Bulletin* **1983,** *18* (4), 461.
10. Märker, K.; Xu, C.; Grey, C. P., Operando NMR of NMC811/Graphite Lithium-Ion Batteries: Structure, Dynamics, and Lithium Metal Deposition. *Journal of the American Chemical Society* **2020,** *142* (41), 17447.

11. Guilmard, M.; Pouillerie, C.; Croguennec, L.; Delmas, C., Structural and electrochemical properties of $LiNi_{0.70}Co_{0.15}Al_{0.15}O_2$. *Solid State Ionics* **2003,** *160* (1), 39.

12. Armand, M.; Tarascon, J. M., Building better batteries. *Nature* **2008,** *451* (7179), 652.

13. Liu, W. M.; Hu, G. R.; Peng, Z. D.; Du, K.; Cao, Y. B.; Liu, Q., Synthesis of spherical $LiNi_{0.8}Co_{0.15}Al_{0.05}O_2$ cathode materials for lithium-ion batteries by a co-oxidation-controlled crystallization method. *Chinese Chemical Letters* **2011,** *22* (9), 1099.

14. Liu, W.; Oh, P.; Liu, X.; Lee, M.-J.; Cho, W.; Chae, S.; Kim, Y.; Cho, J., Nickel-Rich Layered Lithium Transition-Metal Oxide for High-Energy Lithium-Ion Batteries. *Angewandte Chemie International Edition* **2015,** *54* (15), 4440.

15. Duan, J.; Wu, C.; Cao, Y.; Du, K.; Peng, Z.; Hu, G., Enhanced electrochemical performance and thermal stability of $LiNi_{0.80}Co_{0.15}Al_{0.05}O_2$ via nano-sized $LiMnPO_4$ coating. *Electrochimica Acta* **2016,** *221*, 14.

16. Noh, H.-J.; Youn, S.; Yoon, C. S.; Sun, Y.-K., Comparison of the structural and electrochemical properties of layered $Li[Ni_xCo_yMn_z]O_2$ (x = 1/3, 0.5, 0.6, 0.7, 0.8 and 0.85) cathode material for lithium-ion batteries. *Journal of Power Sources* **2013,** *233*, 121.

17. Li, J.; Camardese, J.; Glazier, S.; Dahn, J. R., Structural and Electrochemical Study of the Li–Mn–Ni Oxide System within the Layered Single Phase Region. *Chemistry of Materials* **2014,** *26* (24), 7059.

18. Li, J.; Downie, L. E.; Ma, L.; Qiu, W.; Dahn, J. R., Study of the Failure Mechanisms of $LiNi_{0.8}Mn_{0.1}Co_{0.1}O_2$ Cathode Material for Lithium Ion Batteries. *Journal of The Electrochemical Society* **2015,** *162* (7), A1401.

19. Manthiram, A.; Song, B.; Li, W., A perspective on nickel-rich layered oxide cathodes for lithium-ion batteries. *Energy Storage Materials* **2017,** *6*, 125.

20. Tang, M.; Sarou-Kanian, V.; Melin, P.; Leriche, J.-B.; Ménétrier, M.; Tarascon, J.-M.; Deschamps, M.; Salager, E., Following lithiation fronts in

paramagnetic electrodes with in situ magnetic resonance spectroscopic imaging. *Nature Communications* **2016,** *7* (1), 13284.

21. Bassey, E. N.; Reeves, P. J.; Seymour, I. D.; Grey, C. P., ^{17}O NMR Spectroscopy in Lithium-Ion Battery Cathode Materials: Challenges and Interpretation. *Journal of the American Chemical Society* **2022,** *144* (41), 18714.

22. Haworth, A. R.; Cook, C. W.; Griffin, J. M., Solid-state NMR studies of coatings and interfaces in batteries. *Current Opinion in Colloid & Interface Science* **2022,** *62*, 101638.

23. Märker, K.; Reeves, P. J.; Xu, C.; Griffith, K. J.; Grey, C. P., Evolution of Structure and Lithium Dynamics in $LiNi_{0.8}Mn_{0.1}Co_{0.1}O_2$ (NMC811) Cathodes during Electrochemical Cycling. *Chemistry of Materials* **2019,** *31* (7), 2545.

24. Hérold, A., Insertion compounds of graphite with bromine and alkali metals. *Bull. Soc. Chim. Fr.* **1955,** *7* (8999), 1012.

25. Armand, M.; Touzain, P., Graphite intercalation compounds as cathode materials. *Materials Science and Engineering* **1977,** *31* (C), 319.

26. Colbow, K. M.; Dahn, J. R.; Haering, R. R., Structure and electrochemistry of the spinel oxides $LiTi_2O_4$ and $Li_4Ti_5O_4$. *Journal of Power Sources* **1989,** *26* (3), 397.

27. Ferg, E.; Gummow, R. J.; de Kock, A.; Thackeray, M. M., Spinel Anodes for Lithium-Ion Batteries. *Journal of The Electrochemical Society* **1994,** *141* (11), L147.

28. Ohzuku, T.; Ueda, A.; Yamamoto, N., Zero-Strain Insertion Material of $Li[Li_{1/3}Ti_{5/3}]O_4$ for Rechargeable Lithium Cells. *Journal of The Electrochemical Society* **1995,** *142* (5), 1431.

29. Deschanvres, A.; Raveau, B.; Sekkal, Z., Mise en evidence et etude cristallographique d'une nouvelle solution solide de type spinelle $Li_{1+x}Ti_{2-x}O_4$ $0 \leqslant x \leqslant 0, 333$. *Materials Research Bulletin* **1971,** *6* (8), 699.

30. Zhang, H.; Yang, Y.; Xu, H.; Wang, L.; Lu, X.; He, X., $Li_4Ti_5O_{12}$ spinel anode: Fundamentals and advances in rechargeable batteries. *InfoMat* **2022,** *4* (4).

31. Szczech, J. R.; Jin, S., Nanostructured silicon for high capacity lithium battery anodes. *Energy Environ. Sci.* **2011,** *4* (1), 56.

32. Wu, H.; Zheng, G.; Liu, N.; Carney, T. J.; Yang, Y.; Cui, Y., Engineering Empty Space between Si Nanoparticles for Lithium-Ion Battery Anodes. *Nano Letters* **2012,** *12* (2), 904.

33. Obrovac, M. N.; Chevrier, V. L., Alloy Negative Electrodes for Li-Ion Batteries. *Chemical Reviews* **2014,** *114* (23), 11444.

34. Kitada, K.; Pecher, O.; Magusin, P. C. M. M.; Groh, M. F.; Weatherup, R. S.; Grey, C. P., Unraveling the Reaction Mechanisms of SiO Anodes for Li-Ion Batteries by Combining *in Situ* ^{7}Li and *ex Situ* ^{7}Li/^{29}Si Solid-State NMR Spectroscopy. *Journal of the American Chemical Society* **2019,** *141* (17), 7014.

35. Lee, B. S.; Oh, S.-H.; Choi, Y. J.; Yi, M.-J.; Kim, S. H.; Kim, S.-Y.; Sung, Y.-E.; Shin, S. Y.; Lee, Y.; Yu, S.-H., SiO-induced thermal instability and interplay between graphite and SiO in graphite/SiO composite anode. *Nature Communications* **2023,** *14* (1).

36. Guerard, D.; Herold, A., Intercalation of lithium into graphite and other carbons. *Carbon* **1975,** *13* (4), 337.

37. Colin, J.-F.; Godbole, V.; Novák, P., In situ neutron diffraction study of Li insertion in $Li_4Ti_5O_{12}$. *Electrochemistry Communications* **2010,** *12* (6), 804.

38. Wilkening, M.; Amade, R.; Iwaniak, W.; Heitjans, P., Ultraslow Li diffusion in spinel-type structured $Li_4Ti_5O_{12}$—A comparison of results from solid state NMR and impedance spectroscopy. *Physical Chemistry Chemical Physics* **2007,** *9* (10), 1239.

39. Wagemaker, M.; Simon, D. R.; Kelder, E. M.; Schoonman, J.; Ringpfeil, C.; Haake, U.; Lützenkirchen-Hecht, D.; Frahm, R.; Mulder, F. M., A Kinetic Two-Phase and Equilibrium Solid Solution in Spinel $Li_{4+x}Ti_5O_{12}$. *Advanced Materials* **2006,** *18* (23), 3169.

40. Wagemaker, M.; van Eck, E. R. H.; Kentgens, A. P. M.; Mulder, F. M., Li-Ion Diffusion in the Equilibrium Nanomorphology of Spinel $Li_{4+x}Ti_5O_{12}$. *The Journal of Physical Chemistry B* **2009,** *113* (1), 224.

41. Weydanz, W. J.; Wohlfahrt-Mehrens, M.; Huggins, R. A., A room temperature study of the binary lithium–silicon and the ternary lithium–chromium–silicon system for use in rechargeable lithium batteries. *Journal of Power Sources* **1999,** *81-82*, 237.

42. Chan, C. K.; Peng, H.; Liu, G.; McIlwrath, K.; Zhang, X. F.; Huggins, R. A.; Cui, Y., High-performance lithium battery anodes using silicon nanowires. *Nature Nanotechnology* **2008,** *3* (1), 31.

43. Key, B.; Bhattacharyya, R.; Morcrette, M.; Seznéc, V.; Tarascon, J.-M.; Grey, C. P., Real-Time NMR Investigations of Structural Changes in Silicon Electrodes for Lithium-Ion Batteries. *Journal of the American Chemical Society* **2009,** *131* (26), 9239.

44. Hertzberg, B.; Alexeev, A.; Yushin, G., Deformations in Si−Li Anodes Upon Electrochemical Alloying in Nano-Confined Space. *Journal of the American Chemical Society* **2010,** *132* (25), 8548.

45. Kuhn, A.; Sreeraj, P.; Pöttgen, R.; Wiemhöfer, H.-D.; Wilkening, M.; Heitjans, P.; Pöttgen, R.; Wiemhöfer, H. D.; Wilkening, M.; Heitjans, P.; Pöttgen, R.; Wiemhöfer, H.-D.; Wilkening, M.; Heitjans, P., Li Ion Diffusion in the Anode Material $Li_{12}Si_7$: Ultrafast Quasi-1D Diffusion and Two Distinct Fast 3D Jump Processes Separately Revealed by ^{7}Li NMR Relaxometry. *Journal of the American Chemical Society* **2011,** *133* (29), 11018.

46. Sholl, C. A., Nuclear spin relaxation by translational diffusion in liquids and solids: high- and low-frequency limits. *Journal of Physics C: Solid State Physics* **1981,** *14* (4), 447.

47. Goodenough, J. B.; Kim, Y., Challenges for rechargeable Li batteries. *Chemistry of Materials* **2010,** *22* (3), 587.

48. Goodenough, J. B.; Park, K. S., The Li-ion rechargeable battery: A perspective. *Journal of the American Chemical Society* **2013,** *135* (4), 1167.

49. Famprikis, T.; Canepa, P.; Dawson, J. A.; Islam, M. S.; Masquelier, C., Fundamentals of inorganic solid-state electrolytes for batteries. *Nature Materials* **2019,** *18* (12), 1278.

50. Takada, K.; Yamada, Y.; Yamada, A., Optimized Nonflammable Concentrated Electrolytes by Introducing a Low-Dielectric Diluent. *ACS Applied Materials & Interfaces* **2019,** *11* (39), 35770.

51. Zhang, L.; Huang, Y.; Fan, H.; Wang, H., Flame-Retardant Electrolyte Solution for Dual-Ion Batteries. *ACS Applied Energy Materials* **2019,** *2* (2), 1363.

52. Wang, W.; Hu, H.; Zeng, X.; Fan, W.; Yang, T.; Zhao, X.; Fan, C.; Zuo, X.; Nan, J., Comprehensive Insight into the Probability of Cyclotriphosphazene Derivatives as the Functional Electrolyte Additives in Lithium-Ion Batteries: Which Is Better and Why? *ACS Applied Energy Materials* **2021,** *4* (7), 7101.

53. Zhao, Q.; Stalin, S.; Zhao, C.-Z.; Archer, L. A., Designing solid-state electrolytes for safe, energy-dense batteries. *Nature Reviews Materials* **2020,** *5* (3), 229.

54. Ding, Z.; Li, J.; Li, J.; An, C., Review—Interfaces: Key Issue to Be Solved for All Solid-State Lithium Battery Technologies. *Journal of The Electrochemical Society* **2020,** *167* (7), 070541.

55. Yao, P.; Yu, H.; Ding, Z.; Liu, Y.; Lu, J.; Lavorgna, M.; Wu, J.; Liu, X., Review on Polymer-Based Composite Electrolytes for Lithium Batteries. *Frontiers in Chemistry* **2019,** *7*, 522.

56. Méry, A.; Rousselot, S.; Lepage, D.; Dollé, M., A Critical Review for an Accurate Electrochemical Stability Window Measurement of Solid Polymer and Composite Electrolytes. *Materials* **2021,** *14* (14), 3840.

57. Buannic, L.; Orayech, B.; López Del Amo, J. M.; Carrasco, J.; Katcho, N. A.; Aguesse, F.; Manalastas, W.; Zhang, W.; Kilner, J.; Llordés, A., Dual Substitution Strategy to Enhance Li+ Ionic Conductivity in $Li_7La_3Zr_2O_{12}$ Solid Electrolyte. *Chemistry of Materials* **2017,** *29* (4), 1769.

58. Seino, Y.; Ota, T.; Takada, K.; Hayashi, A.; Tatsumisago, M., A sulphide lithium super ion conductor is superior to liquid ion conductors for use in rechargeable batteries. *Energy & Environmental Science* **2014,** *7* (2), 627.

59. Kato, Y.; Hori, S.; Saito, T.; Suzuki, K.; Hirayama, M.; Mitsui, A.; Yonemura, M.; Iba, H.; Kanno, R., High-power all-solid-state batteries using sulfide superionic conductors. *Nature Energy* **2016,** *1* (4).

60. Asano, T.; Sakai, A.; Ouchi, S.; Sakaida, M.; Miyazaki, A.; Hasegawa, S., Solid Halide Electrolytes with High Lithium-Ion Conductivity for Application in 4 V Class Bulk-Type All-Solid-State Batteries. *Advanced Materials* **2018,** *30* (44), 1803075.

61. Zhou, L.; Assoud, A.; Zhang, Q.; Wu, X.; Nazar, L. F., New Family of Argyrodite Thioantimonate Lithium Superionic Conductors. *Journal of the American Chemical Society* **2019,** *141* (48), 19002.

62. Wang, Y.; Richards, W. D.; Ong, S. P.; Miara, L. J.; Kim, J. C.; Mo, Y.; Ceder, G., Design principles for solid-state lithium superionic conductors. *Nature Materials* **2015,** *14* (10), 1026.

63. Thangadurai, V.; Kaack, H.; Weppner, W. J. F., Novel Fast Lithium Ion Conduction in Garnet-Type $Li_5La_3M_2O_{12}$ (M = Nb, Ta). *Journal of the American Ceramic Society* **2003,** *86* (3), 437.

64. Murugan, R.; Thangadurai, V.; Weppner, W., Fast Lithium Ion Conduction in Garnet-Type $Li_7La_3Zr_2O_{12}$. *Angewandte Chemie International Edition* **2007,** *46* (41), 7778.

65. Awaka, J.; Kijima, N.; Hayakawa, H.; Akimoto, J., Synthesis and structure analysis of tetragonal $Li_7La_3Zr_2O_{12}$ with the garnet-related type structure. *Journal of Solid State Chemistry* **2009,** *182* (8), 2046.

66. Geiger, C. A.; Alekseev, E.; Lazic, B.; Fisch, M.; Armbruster, T.; Langner, R.; Fechtelkord, M.; Kim, N.; Pettke, T.; Weppner, W., Crystal Chemistry and Stability of "$Li_7La_3Zr_2O_{12}$ " Garnet: A Fast Lithium-Ion Conductor. *Inorganic Chemistry* **2011,** *50* (3), 1089.

67. Düvel, A.; Kuhn, A.; Robben, L.; Wilkening, M.; Heitjans, P., Mechanosynthesis of solid electrolytes: Preparation, characterization, and li ion transport properties of garnet-type Al-doped $Li_7La_3Zr_2O_{12}$ crystallizing with cubic symmetry. *Journal of Physical Chemistry C* **2012,** *116* (29), 15192.

68. Buschmann, H.; Dölle, J.; Berendts, S.; Kuhn, A.; Bottke, P.; Wilkening, M.; Heitjans, P.; Senyshyn, A.; Ehrenberg, H.; Lotnyk, A.; Duppel, V.; Kienle, L.; Janek, J., Structure and dynamics of the fast lithium ion conductor "$Li_7La_3Zr_2O_{12}$". *Physical Chemistry Chemical Physics* **2011,** *13* (43), 19378.

69. Lee, J.-M.; Kim, T.; Baek, S.-W.; Aihara, Y.; Park, Y.; Kim, Y.-I.; Doo, S.-G., High lithium ion conductivity of $Li_7La_3Zr_2O_{12}$ synthesized by solid state reaction. *Solid State Ionics* **2014,** *258*, 13.

70. Awaka, J.; Takashima, A.; Kataoka, K.; Kijima, N.; Idemoto, Y.; Akimoto, J., Crystal Structure of Fast Lithium-ion-conducting Cubic $Li_7La_3Zr_2O_{12}$. *Chemistry Letters* **2011,** *40* (1), 60.

71. Hayamizu, K.; Seki, S.; Haishi, T., Lithium ion micrometer diffusion in a garnet-type cubic $Li_7La_3Zr_2O_{12}$(LLZO) studied using ^7Li NMR spectroscopy. *The Journal of Chemical Physics* **2017,** *146* (2), 024701.

72. Bernuy-Lopez, C.; Manalastas, W.; Lopez Del Amo, J. M.; Aguadero, A.; Aguesse, F.; Kilner, J. A., Atmosphere Controlled Processing of Ga-Substituted Garnets for High Li-Ion Conductivity Ceramics. *Chemistry of Materials* **2014,** *26* (12), 3610.

73. Xiao, W.; Wang, J.; Fan, L.; Zhang, J.; Li, X., Recent advances in $Li_{1+x}Al_xTi_{2-x}(PO_4)_3$ solid-state electrolyte for safe lithium batteries. *Energy Storage Materials* **2019,** *19*, 379.

74. Aono, H.; Sugimoto, E.; Sadaoka, Y.; Imanaka, N.; Adachi, G. Y., Ionic Conductivity of Solid Electrolytes Based on Lithium Titanium Phosphate. *Journal of the Electrochemical Society* **1990,** *137* (4), 1023.

75. Arbi, K.; Lazarraga, M. G.; Ben Hassen Chehimi, D.; Ayadi-Trabelsi, M.; Rojo, J. M.; Sanz, J., Lithium Mobility in $Li_{1.2}Ti_{1.8}R_{0.2}(PO_4)_3$ Compounds (R = Al, Ga, Sc, In) as Followed by NMR and Impedance Spectroscopy. *Chemistry of Materials* **2004,** *16* (2), 255.

76. Epp, V.; Ma, Q.; Hammer, E.-M.; Tietz, F.; Wilkening, M., Very fast bulk Li ion diffusivity in crystalline $Li_{-1.5}Al_{0.5}Ti_{1.5}(PO_4)_3$ as seen using NMR relaxometry. **2015,** *17* (48).

77. Gao, P.; Grätzel, M.; Nazeeruddin, M. K., Organohalide lead perovskites for photovoltaic applications. *Energy Environ. Sci.* **2014,** *7* (8), 2448.
78. Grätzel, M., The light and shade of perovskite solar cells. *Nature Materials* **2014,** *13* (9), 838.
79. Manser, J. S.; Christians, J. A.; Kamat, P. V., Intriguing Optoelectronic Properties of Metal Halide Perovskites. *Chemical Reviews* **2016,** *116* (21), 12956.
80. Bonanos, N.; Knight, K. S.; Ellis, B., Perovskite solid electrolytes: Structure, transport properties and fuel cell applications. *Solid State Ionics* **1995,** *79*, 161.
81. Lu, J.; Li, Y., Perovskite-type Li-ion solid electrolytes: a review. *Journal of Materials Science: Materials in Electronics* **2021,** *32* (8), 9736.
82. Alcock, C. B.; Doshi, R. C.; Shen, Y., Perovskite electrodes for sensors. *Solid State Ionics* **1992,** *51* (3), 281.
83. Beall, C. E.; Fabbri, E.; Schmidt, T. J., Perovskite Oxide Based Electrodes for the Oxygen Reduction and Evolution Reactions: The Underlying Mechanism. *ACS Catalysis* **2021,** *11* (5), 3094.
84. Zhang, C.; Lu, B.; Xiong, H.; Lin, C.; Fang, L.; Fu, J.; Deng, D.; Fan, X.; Li, Y.; Wu, Q.-H., Cobalt-Based Perovskite Electrodes for Solid Oxide Electrolysis Cells. *Inorganics* **2022,** *10* (11).
85. Zhang, Z.; Zhu, Y.; Zhong, Y.; Zhou, W.; Shao, Z., Anion Doping: A New Strategy for Developing High-Performance Perovskite-Type Cathode Materials of Solid Oxide Fuel Cells. *Advanced Energy Materials* **2017,** *7* (17), 1700242.
86. Inaguma, Y.; Liquan, C.; Itoh, M.; Nakamura, T.; Uchida, T.; Ikuta, H.; Wakihara, M., High ionic conductivity in lithium lanthanum titanate. *Solid State Communications* **1993,** *86* (10), 689.
87. Stramare, S.; Thangadurai, V.; Weppner, W., Lithium Lanthanum Titanates: A Review. *Chemistry of Materials* **2003,** *15* (21), 3974.

88. Fourquet, J. L.; Duroy, H.; Crosnier-Lopez, M. P., Structural and Microstructural Studies of the Series $La_{2/3-x}Li_{3x}\square_{1/3-2x}TiO_3$. *Journal of Solid State Chemistry* **1996,** *127* (2), 283.

89. París, M. A.; Sanz, J.; León, C.; Santamaría, J.; Ibarra, J.; Várez, A., Li Mobility in the Orthorhombic $Li_{0.18}La_{0.61}TiO_3$ Perovskite Studied by NMR and Impedance Spectroscopies. *Chemistry of Materials* **2000,** *12* (6), 1694.

90. Shannon, R. D. t. D., Revised effective ionic radii and systematic studies of interatomic distances in halides and chalcogenides. **1976,** *32* (5).

91. Rivera, A.; Sanz, J., Lithium dynamics in the fast ionic conductor $Li_{0.18}La_{0.61}TiO_3$ probed by ^7Li NMR spectroscopy. *Phys. Rev. B* **2004,** *70* (9), 94301.

92. Inaguma, Y.; Yu, J.; Shan, Y. J.; Itoh, M.; Nakamuraa, T., The Effect of the Hydrostatic Pressure on the Ionic Conductivity in a Perovskite Lanthanum Lithium Titanate. *Journal of The Electrochemical Society* **1995,** *142* (1), L8.

93. Emery, J.; Bohnke, O.; Fourquet, J. L.; Buzaré, J. Y.; Florian, P.; Massiot, D., Polaronic effects on lithium motion in intercalated perovskitelithium lanthanum titanate observed by ^7Li NMR andimpedance spectroscopy. *Journal of Physics: Condensed Matter* **1999,** *11* (50), 10401.

94. Zhao, Y.; Daemen, L. L., Superionic Conductivity in Lithium-Rich Anti-Perovskites. *Journal of the American Chemical Society* **2012,** *134* (36), 15042.

95. Mouta, R.; Diniz, E. M.; Paschoal, C. W. A., Li+ interstitials as the charge carriers in superionic lithium-rich anti-perovskites. *Journal of Materials Chemistry A* **2016,** *4* (5), 1586.

96. Hanghofer, I.; Redhammer, G. J.; Rohde, S.; Hanzu, I.; Senyshyn, A.; Wilkening, H. M. R.; Rettenwander, D., Untangling the Structure and Dynamics of Lithium-Rich Anti-Perovskites Envisaged as Solid Electrolytes for Batteries. *Chemistry of Materials* **2018,** *30* (22), 8134.

97. Feng, W.; Zhu, L.; Dong, X.; Wang, Y.; Xia, Y.; Wang, F., Enhanced Moisture Stability of Lithium Rich Anti-perovskites for Sustainable All Solid-State Lithium Batteries. *Advanced Materials* **2022**, 2210365.

98. Dawson, J. A.; Famprikis, T.; Johnston, K. E., Anti-perovskites for solid-state batteries: recent developments, current challenges and future prospects. *Journal of Materials Chemistry A* **2021,** *9* (35), 18746.

99. Wang, F.; Evans, H. A.; Kim, K.; Yin, L.; Li, Y.; Tsai, P.-C.; Liu, J.; Lapidus, S. H.; Brown, C. M.; Siegel, D. J.; Chiang, Y.-M., Dynamics of Hydroxyl Anions Promotes Lithium Ion Conduction in Antiperovskite Li_2OHCl. *Chemistry of Materials* **2020,** *32* (19), 8481.

100. Dawson, J. A.; Attari, T. S.; Chen, H.; Emge, S. P.; Johnston, K. E.; Islam, M. S., Elucidating lithium-ion and proton dynamics in anti-perovskite solid electrolytes. *Energy and Environmental Science* **2018,** *11* (10), 2993.

101. Song, A. Y.; Turcheniuk, K.; Leisen, J.; Xiao, Y.; Meda, L.; Borodin, O.; Yushin, G., Understanding Li-Ion Dynamics in Lithium Hydroxychloride (Li_2OHCl) Solid State Electrolyte via Addressing the Role of Protons. *Advanced Energy Materials* **2020,** *10* (8), 1903480.

102. Hong, H. Y. P., Crystal structure and ionic conductivity of $Li_{14}Zn(GeO_4)_4$ and other new Li+ superionic conductors. *Materials Research Bulletin* **1978,** *13*, 117.

103. Ivanov-Shitz, A. K.; Kireev, V. V.; Mel'Nikov, O. K.; Demianets, L. N., Growth and ionic conductivity of γ-Li_3PO_4. *Crystallography Reports* **2001,** *46* (5), 864.

104. Fleutot, B.; Pecquenard, B.; Martinez, H.; Letellier, M.; Levasseur, A., Investigation of the local structure of LiPON thin films to better understand the role of nitrogen on their performance. *Solid State Ionics* **2011,** *186* (1), 29.

105. Muñoz, F.; Ren, J.; van Wüllen, L.; Zhao, T.; Kirchhain, H.; Rehfuß, U.; Uesbeck, T., Structure and Dynamics of LiPON and NaPON Oxynitride Phosphate Glasses by Solid-State NMR. *The Journal of Physical Chemistry C* **2021,** *125* (7), 4077.

106. Zemann, J., Die Kristallstruktur von Lithiumphosphat, Li_3PO_4. *Acta Crystallographica* **1960,** *13* (11), 863.

107. Kanno, R.; Murayama, M., Lithium Ionic Conductor Thio-LISICON: The Li_2S-GeS_2-P_2S_5 System. *Journal of The Electrochemical Society* **2001,** *148* (7), A742.

108. Kanno, R.; Hata, T.; Kawamoto, Y.; Irie, M., Synthesis of a new lithium ionic conductor, thio-LISICON–lithium germanium sulfide system. *Solid State Ionics* **2000,** *130*, 97.

109. Chen, R.; Qu, W.; Guo, X.; Li, L.; Wu, F., The pursuit of solid-state electrolytes for lithium batteries: from comprehensive insight to emerging horizons. *Mater. Horiz* **2016,** *3* (3), 487.

110. Knauth, P., Inorganic solid Li ion conductors: An overview. *Solid State Ionics* **2009,** *180* (14), 911.

111. Kamaya, N.; Homma, K.; Yamakawa, Y.; Hirayama, M.; Kanno, R.; Yonemura, M.; Kamiyama, T.; Kato, Y.; Hama, S.; Kawamoto, K.; Mitsui, A., A lithium superionic conductor. *Nature Materials* **2011,** *10* (9), 682.

112. Bachman, J. C.; Muy, S.; Grimaud, A.; Chang, H.-H.; Pour, N.; Lux, S. F.; Paschos, O.; Maglia, F.; Lupart, S.; Lamp, P.; Giordano, L.; Shao-Horn, Y., Inorganic Solid-State Electrolytes for Lithium Batteries: Mechanisms and Properties Governing Ion Conduction. *Chemical Reviews* **2016,** *116* (1), 140.

113. Bron, P.; Johansson, S.; Zick, K.; Schmedt auf der Günne, J.; Dehnen, S.; Roling, B.; Der Günne, J. S. A.; Dehnen, S.; Roling, B., $Li_{10}SnP_2S_{12}$: An Affordable Lithium Superionic Conductor. *Journal of the American Chemical Society* **2013,** *135* (42), 15694.

114. Whiteley, J. M.; Woo, J. H.; Hu, E.; Nam, K. W.; Lee, S. H., Empowering the Lithium Metal Battery through a Silicon-Based Superionic Conductor. *Journal of the Electrochemical Society* **2014,** *161* (12), A1812.

115. Weber, D. A.; Senyshyn, A.; Weldert, K. S.; Wenzel, S.; Zhang, W.; Kaiser, R.; Berendts, S.; Janek, J.; Zeier, W. G., Structural Insights and 3D Diffusion Pathways within the Lithium Superionic Conductor $Li_{10}GeP_2S_{12}$. *Chemistry of Materials* **2016,** *28* (16), 5905.

116. Kuhn, A.; Duppel, V.; Lotsch, B. V., Tetragonal $Li_{10}GeP_2S_{12}$ and Li_7GePS_8 – exploring the Li ion dynamics in LGPS Li electrolytes. *Energy & Environmental Science* **2013,** *6* (12), 3548.

117. Liang, X.; Wang, L.; Jiang, Y.; Wang, J.; Luo, H.; Liu, C.; Feng, J., In-Channel and In-Plane Li Ion Diffusions in the Superionic Conductor $Li_{10}GeP_2S_{12}$ Probed by Solid-State NMR. *Chemistry of Materials* **2015,** *27* (16), 5503.

118. Kuhn, A.; Gerbig, O.; Zhu, C.; Falkenberg, F.; Maier, J.; Lotsch, B. V., A new ultrafast superionic Li-conductor: ion dynamics in $Li_{11}Si_2PS_{12}$ and comparison with other tetragonal LGPS-type electrolytes. *Phys. Chem. Chem. Phys.* **2014,** *16* (28), 14669.

119. Paulus, M. C.; Graf, M. F.; Harks, P. P. R. M. L.; Paulus, A.; Schleker, P. P. M.; Notten, P. H. L.; Eichel, R. A.; Granwehr, J., Investigation of the Li-ion conduction behavior in the $Li_{10}GeP_2S_{12}$ solid electrolyte by two-dimensional T_1 -spin alignment echo correlation NMR. *Journal of Magnetic Resonance* **2018,** *294*, 133.

120. Ong, S. P.; Mo, Y.; Richards, W. D.; Miara, L.; Lee, H. S.; Ceder, G., Phase stability, electrochemical stability and ionic conductivity of the $Li_{10\pm1}MP_2X_{12}$ (M = Ge, Si, Sn, Al or P, and X = O, S or Se) family of superionic conductors. *Energy & Environmental Science* **2013,** *6* (1), 148.

121. Liang, X.; Yang, L.; Lei, Y.; Qu, L.; Wang, L.; Cai, W.; Xu, K.; Jiang, Y.; Liu, B.; Feng, J., Selective Blockage of Li-Ion Diffusion Pathways in $Li_{10}SnP_2S_{12}$: Insights from Nuclear Magnetic Resonance. *Journal of Physical Chemistry C* **2021,** *125* (50), 27884.

122. Deiseroth, H.-J.; Kong, S.-T.; Eckert, H.; Vannahme, J.; Reiner, C.; Zaiß, T.; Schlosser, M., Li_6PS_5X: A Class of Crystalline Li-Rich Solids With an Unusually High Li+ Mobility. *Angewandte Chemie International Edition* **2008,** *47* (4), 755.

123. Epp, V.; Gün, Ö.; Deiseroth, H.-J.; Wilkening, M., Highly Mobile Ions: Low Temperature NMR Directly Probes Extremely Fast Li+ Hopping in

Argyrodite-Type Li_6PS_5Br. *The Journal of Physical Chemistry Letters* **2013,** *4*, 2118.

124. Pecher, O.; Kong, S.-T.; Goebel, T.; Nickel, V.; Weichert, K.; Reiner, C.; Deiseroth, H.-J.; Maier, J.; Haarmann, F.; Zahn, D., Atomistic Characterisation of Li+ Mobility and Conductivity in $Li_{7-x}PS_{6-x}I_x$ Argyrodites from Molecular Dynamics Simulations, Solid-State NMR, and Impedance Spectroscopy. *Chemistry - A European Journal* **2010,** *16* (28), 8347.

125. Rao, R. P.; Adams, S., Studies of lithium argyrodite solid electrolytes for all-solid-state batteries. *Physica Status Solidi* **2011,** *208* (8), 1804.

126. Hogrefe, K.; Minafra, N.; Hanghofer, I.; Banik, A.; Zeier, W. G.; Wilkening, H. M. R., Opening Diffusion Pathways through Site Disorder: The Interplay of Local Structure and Ion Dynamics in the Solid Electrolyte $Li_{6+x}P_{1-x}Ge_xS_5I$ as Probed by Neutron Diffraction and NMR. *Journal of the American Chemical Society* **2022,** *144* (4), 1795.

127. Ramzy, A.; Thangadurai, V., Tailor-Made Development of Fast Li Ion Conducting Garnet-Like Solid Electrolytes. *ACS Applied Materials & Interfaces* **2010,** *2* (2), 385.

128. Han, G.; Kinzer, B.; Garcia-Mendez, R.; Choe, H.; Wolfenstine, J.; Sakamoto, J., Correlating the effect of dopant type (Al, Ga, Ta) on the mechanical and electrical properties of hot-pressed Li-garnet electrolyte. *Journal of the European Ceramic Society* **2020,** *40* (5), 1999.

129. Wen, Z.; Xu, X.; Li, J., Preparation, microstructure and electrical properties of $Li_{1.4}Al_{0.4}Ti_{1.6}(PO_4)_3$ nanoceramics. *Journal of Electroceramics* **2009,** *22* (1), 342.

130. Aono, H.; Sugimoto, E.; Sadaoka, Y.; Imanaka, N.; Adachi, G.-y., Electrical property and sinterability of $LiTi_2(PO_4)_3$ mixed with lithium salt (Li_3PO_4 or Li_3BO_3). *Solid State Ionics* **1991,** *47* (3), 257.

131. Aono, H.; Sugimoto, E.; Sadaoka, Y.; Imanaka, N.; Adachi, G.-y., Ionic conductivity and sinterability of lithium titanium phosphate system. *Solid State Ionics* **1990,** *40*, 38.

132. Li, C.; Soh, K. C. K.; Wu, P., Formability of ABO_3 perovskites. *Journal of Alloys and Compounds* **2004,** *372* (1), 40.

133. Huang, B.; Xu, B.; Li, Y.; Zhou, W.; You, Y.; Zhong, S.; Wang, C.-A.; Goodenough, J. B., Li-Ion Conduction and Stability of Perovskite $Li_{3/8}Sr_{7/16}Hf_{1/4}Ta_{3/4}O_3$. *ACS Applied Materials & Interfaces* **2016,** *8* (23), 14552.

134. Lu, J.; Li, Y.; Ding, Y., Li-ion conductivity and electrochemical stability of A-site deficient perovskite-structured $Li_{3x-y}La_{1-x}Al_{1-y}Ti_yO_3$ electrolytes. *Materials Research Bulletin* **2021,** *133*, 111019.

135. Zhao, G.; Suzuki, K.; Yonemura, M.; Hirayama, M.; Kanno, R., Enhancing Fast Lithium Ion Conduction in Li_4GeO_4–Li_3PO_4 Solid Electrolytes. *ACS Applied Energy Materials* **2019,** *2* (9), 6608.

136. Kuwano, J.; West, A. R., New Li+ ion conductors in the system, Li_4GeO_4-Li_3VO_4. *Materials Research Bulletin* **1980,** *15* (11), 1661.

137. Zhou, L.; Assoud, A.; Shyamsunder, A.; Huq, A.; Zhang, Q.; Hartmann, P.; Kulisch, J.; Nazar, L. F., An Entropically Stabilized Fast-Ion Conductor: $Li_{3.25}[Si_{0.25}P_{0.75}]S_4$. *Chemistry of Materials* **2019,** *31* (19), 7801.

138. Yubuchi, S.; Uematsu, M.; Deguchi, M.; Hayashi, A.; Tatsumisago, M., Lithium-Ion-Conducting Argyrodite-Type Li_6PS_5X (X = Cl, Br, I) Solid Electrolytes Prepared by a Liquid-Phase Technique Using Ethanol as a Solvent. *ACS Applied Energy Materials* **2018,** *1* (8), 3622.

139. Kraft, M. A.; Ohno, S.; Zinkevich, T.; Koerver, R.; Culver, S. P.; Fuchs, T.; Senyshyn, A.; Indris, S.; Morgan, B. J.; Zeier, W. G., Inducing High Ionic Conductivity in the Lithium Superionic Argyrodites $Li_{6+x}P_{1-x}Ge_xS_5I$ for All-Solid-State Batteries. *Journal of the American Chemical Society* **2018,** *140* (47), 16330.

140. Stallworth, P. E.; Fontanella, J. J.; Wintersgill, M. C.; Scheidler, C. D.; Immel, J. J.; Greenbaum, S. G.; Gozdz, A. S., NMR, DSC and high pressure electrical conductivity studies of liquid and hybrid electrolytes. *Journal of Power Sources* **1999,** *81-82*, 739.

3. Toward Understanding of the Li-Ion Migration Pathways in the Lithium Aluminium Sulfides Li_3AlS_3 and $Li_{4.3}AlS_{3.3}Cl_{0.7}$ via $^{6,7}Li$ Solid-State Nuclear Magnetic Resonance Spectroscopy

3.1 Overview

The first new materials of interest reported in this thesis are the lithium aluminium sulfides Li_3AlS_3 and the chlorine-doped analogue $Li_{4.3}AlS_{3.3}Cl_{0.7}$. These materials were first reported in Chemistry of Materials in 2019[1] and 2021[2] respectively, with a follow-up NMR focussed paper published in 2023[3] from which this chapter is largely extracted from.

The paper reporting the Li_3AlS_3 and $Li_{4.3}AlS_{3.3}Cl_{0.7}$ materials were entitled "Computationally Guided Discovery of the Sulfide Li_3AlS_3 in the Li–Al–S Phase Field: Structure and Lithium Conductivity" by Jacinthe Gamon, Benjamin B. Duff, Matthew S. Dyer, Christopher Collins, Luke M. Daniels, T. Wesley Surta, Paul M. Sharp, Michael W. Gaultois, Frédéric Blanc, John Bleddyn Claridge, and Matthew J. Rosseinsky and "$Li_{4.3}AlS_{3.3}Cl_{0.7}$: A Sulfide–Chloride Lithium Ion Conductor with Highly Disordered Structure and Increased Conductivity" by Jacinthe Gamon, Matthew S. Dyer, Benjamin B. Duff, Andrij Vasylenko, Luke M. Daniels, Marco Zanella, Michael W. Gaultois, Frédéric Blanc, John B. Claridge, and Matthew J. Rosseinsky. The author contributions are as follows, M.J.R devised the project, L.M.D, M.W.G and J.B.C assisted in supervising

the project, M.S.D, C.C, T.W.S, A.V, M.Z and P.M.S performed the computational calculations, J.G synthesised the material, performed the diffraction experiments/analysis and conducted the EIS measurements. B.D conducted the NMR experiments and analysis, with support from F.B. This chapter combines the NMR contribution to these collaborative works with the NMR focussed paper entitled “Towards Understanding of the Li-Ion Migration Pathways in the Lithium Aluminium Sulphides Li_3AlS_3 and $Li_{4.3}AlS_{3.3}Cl_{0.7}$ via ^{6,7}Li Solid-State Nuclear Magnetic Resonance Spectroscopy” by Benjamin B. Duff, Stuart J. Elliott, Jacinthe Gamon, Luke M. Daniels, Matthew J. Rosseinsky, and Frédéric Blanc. The authors’ contributions are as follows, F.B devised the project, M.J.R and L.M.D assisted in supervising the project, J.G synthesised the original materials as well as the 6Li-enriched samples and performed diffraction experiments S.J.E assisted with the simulation of the relaxation profiles, B.D collected all the NMR experiments and performed their analysis.

3.2 Abstract

Li-containing materials providing fast ion transport pathways are fundamental in Li solid electrolytes and the future of all-solid-state batteries. Understanding the structures as well as the Li-ion pathways; which usually benefit from structural disorder and cation/anion substitution, is paramount for further developments in next-generation Li solid electrolytes. Here, we exploit ^{6}Li and ^{27}Al MAS techniques in conjunction with DFT and XRD in order to derive the structures of Li_3AlS_3 and $Li_{4.3}AlS_{3.3}Cl_{0.7}$, as well as a use a range of variable temperature ^{6}Li and ^{7}Li nuclear magnetic resonance approaches to determine Li-ion mobility pathways, quantify Li-ion jump rates, and subsequently identify the limiting factors for Li-ion diffusion in Li_3AlS_3 and chlorine-doped analogue $Li_{4.3}AlS_{3.3}Cl_{0.7}$. Static ^{7}Li NMR line narrowing spectra of Li_3AlS_3 show the existence of both mobile and immobile Li-ions, with the latter limiting long-range translational ion diffusion, while in $Li_{4.3}AlS_{3.3}Cl_{0.7}$, a single type of fast-moving ion is present and responsible for the higher conductivity of this phase. ^{6}Li-^{6}Li exchange spectroscopy spectra of Li_3AlS_3 reveal that the slower moving ions hop between non-equivalent Li positions in different structural layers. The absence of the immobile ions in $Li_{4.3}AlS_{3.3}Cl_{0.7}$, as revealed from ^{7}Li line narrowing experiments, suggests an increased rate of ion exchange between the layers in this phase compared with Li_3AlS_3. Detailed analysis of spin-lattice relaxation data allows extraction of Li-ion jump rates that are significantly increased for the doped material and identify Li mobility pathways in both materials to be three-dimensional. The identification of factors limiting long-range translational Li diffusion and understanding the effects of structural

modification (such as anion substitution) on Li-ion mobility provide a framework for the further development of more highly conductive Li solid electrolytes.

3.3 Introduction

Higher symmetry structures with mixed site occupancy have been shown to lead to significant improvements in ionic conductivity, the reason for which remains somewhat uncertain.[4,5] Anion substitution in order to produce mixed anion materials has been commonly utilised in solid-state chemistry to achieve improved electrolyte stability against electrodes. In particular halides present the advantage of being highly stable against Li metal with increased conductivities compared to pure sulphide analogues and comparatively higher oxidation potentials leading to a lower likelihood of halide oxidation.[6,7] Moreover, as halide anions have a lower charge compared to sulphide anions, halide-sulphide substitution enables cation off-stoichiometry, which is favourable for conductivity. In particular, the Cl^- anion, which has a similar ionic radius to S^{2-} (167 and 170 pm, respectively),[8] favours mixed occupancy on the anionic sites, and hence disorder, leading to increased performance as shown in disordered argyrodites[9] and the previously mentioned $Li_{9.54}Si_{1.74}P_{1.44}S_{11.7}Cl_{0.3}$.[7]

Solid-state nuclear magnetic resonance (NMR) spectroscopy is an extremely powerful tool for the investigation of disordered materials, as unlike diffraction-based methods the technique does not depend on long-range structural order.[10] NMR is widely used for structural determination purposes,[10] yet can also be very effectively employed for the assessment of ion dynamics and diffusion processes,[11] complementing, for example, conductivity measurements from electrical impedance spectroscopy (EIS)[8] or Muon spectroscopy.[12] In particular, NMR spectroscopy offers a direct, non-

destructive method to probe the mobility of Li^+ specifically[13-17] because of its unique inherent isotope specificity exploiting both NMR-active isotopes of lithium (^6Li, 7.59% natural abundance, spin I = 1 and ^7Li, 92.41%, I = 3/2) whilst also being suitable for powdered samples. The key to the study of dynamics by NMR lies in the wide range of timescales that can be accessed. These range from very fast motional processes in the order of 10^{-12} s^{-1} probed by measuring spin-lattice relaxation (SLR) time constants to much slower motion on the timescale of 10^{-3} s^{-1} from lineshape analysis or s^{-1} in exchange spectroscopy (EXSY). NMR also allows for the extraction of site selective dynamics information which is highly complementary to the mean structure with average occupancies of particular sites accessible by diffraction-based methods.

Static ^7Li variable temperature (VT) NMR has been widely used to probe lithium ion dynamics in ionic conductors, allowing for extraction of activation energies (E_a) and correlation rates (τ_c^{-1}) of the Li-ion jump processes (τ_c^{-1} is basically the jump rate τ^{-1}).[13] ^7Li VT NMR spectra can also provide qualitative insights into ion mobility in solids by identifying the sites contributing to long range ion mobility and the pathways involved. For instance, a number of previous works[18-20] have shown that static VT NMR spectra can support the presence of both mobile and immobile ions on the NMR timescale which is evidenced by the superposition of resonances with different linewidths from ions moving at different rates. VT diffusion-induced ^7Li NMR SLR rate constants in both the laboratory (T_1^{-1}) and rotating ($T_{1\rho}^{-1}$) frames allow access to quantitative information on the Li diffusion process. Additionally, the

dimensionality of Li-ion mobility within the material can be extracted from the frequency-dependence of the SLR rate constants as initially postulated based on theoretical calculations[21] and recent experimental verification for $Li_{12}Si_7$.[22] Two-dimensional (2D) EXSY NMR experiments are a powerful method for investigating chemical exchange in ionic conductors and allow for both qualitative observation of which inequivalent sites are involved in the ionic exchange and quantitative extraction of site-specific jump rates.[23-26]

We discovered two lithium aluminium sulphide phases, Li_3AlS_3[1] and $Li_{4.3}AlS_{3.3}Cl_{0.7}$,[2] through a computational approach involving the screening and identification of new materials in the Li-Al-S phase field. We utilised ^6Li magic angle spinning (MAS) and ^{27}Al (I = 5/2) multiple quantum MAS (MQMAS) NMR for structure determination. Here, we report a comprehensive understanding of the lithium-ion dynamics of these phases from ^7Li line narrowing, relaxation, EXSY data and site specific ^6Li exchange. The results identify the limiting factors for Li-ion mobility in Li_3AlS_3 and rationalise the increased ion mobility observed in the $Li_{4.3}AlS_{3.3}Cl_{0.7}$ disordered mixed anion structure.

3.4 Experimental

Li_3AlS_3[1] and $Li_{4.3}AlS_{3.3}Cl_{0.7}$[2] at natural abundance were synthesised according to reported solid-state synthesis procedures. ^6Li enriched Li_3AlS_3 and $Li_{4.3}AlS_{3.3}Cl_{0.7}$ were prepared using the same procedure with ^6Li enriched Li_2S (prepared from 95% ^6Li enriched Li_2CO_3,[5] CortecNet, 99.7% purity) as the lithium precursor. Routine analysis of phase purity and lattice parameters were performed on a Bruker D8 Advance diffractometer with a monochromated Cu source (Kα1, λ = 1.54060 Å) in powder transmission Debye Scherrer geometry (capillary) with sample rotation. Powder X-ray diffraction patterns of the ^6Li enriched samples are shown in **Figure 3.15** and are in agreement with the literature.[1,2]

The ^{27}Al MAS NMR data of Li_3AlS_3 were recorded at 9.4 T on a Bruker Avance III HD under MAS at a rate of $\omega_r/2\pi$ = 12 kHz using a 4 mm HXY MAS probe (in double resonance mode) and at 20 T on a Bruker NEO spectrometer using a 3.2 mm HXY MAS probe (in triple resonance mode). The ^{27}Al spectra of Li_3AlS_3 were obtained at 9.4 T with a short pulse angle of 30° of 0.33 μs duration at an rf amplitude of $\omega_1/2\pi$ = 83 kHz and at 20 T with a short pulse angle of 30° of 0.55 μs duration at an rf amplitude of $\omega_1/2\pi$ = 50 kHz. The ^{27}Al spectra of $Li_{4.3}AlS_{3.3}Cl_{0.7}$ were obtained using a 3.2 mm HXY MAS probe in double resonance mode on a 20 T Bruker NEO solid-state NMR spectrometer under MAS at a rate of $\omega_r/2\pi$ = 20 kHz. The ^{27}Al triple quantum magic-angle spinning (MQMAS)[27] for both phases were obtained at 9.4 T with a z-filtered sequence[28] and using rf field amplitudes of $\omega_1/2\pi$ = 83 kHz for the excitation

and reconversion pulses and 4 kHz for the selective 90° pulse. The ^{27}Al shifts were referenced to 0.1 M $Al(NO_3)_3$ in H_2O at 0 ppm.

Static ^{7}Li VT NMR experiments were recorded on a 9.4 T Bruker Avance III HD spectrometer equipped with a 4 mm HX high temperature MAS probe with the X channel tuned to ^{7}Li at $\omega_0/2\pi(^7Li)$ = 156 MHz. All ^{7}Li one pulse NMR spectra were obtained with a hard 90° pulse at a radiofrequency (rf) field amplitude of $\omega_1/2\pi(^7Li)$ = 83 kHz. ^{7}Li quantum filtered NMR experiments were performed using the multiple-quantum filter pulse sequence $\pi/2 - \tau_1 - \pi - \tau_1 - \theta - \tau_2 - \theta$ - acq with suitable phase cycling depending on whether double (θ = 54.7°) or triple (θ = 90°) quantum coherence was targeted for filtration.[29-31] Delays τ_1 and τ_2 were optimised for maximum signal intensity. Hahn-echo experiments were performed using the sequence $\pi/2 - \tau - \pi - \tau$ - acq with hard pulses at rf field amplitudes of $\omega_1/2\pi(^7Li)$ = 83 kHz, τ delays varied from 9 to 90 μs. All NMR spectra were obtained under quantitative recycle delays of more than 5 times the T_1 time constants at each temperature. T_1 time constants were measured using the saturation recovery pulse sequence $(\pi/2)_{x100} - \tau - \pi/2$ - acq with increasing recovery delay values τ. For Li_3AlS_3, data were fitted with a bi-exponential recovery of the form $1 - a\cdot\exp[-(\tau/T_{1,slow})] + b\cdot\exp[-(\tau/T_{1,fast})]$ where $T_{1,slow}$ and $T_{1,fast}$ are the time constants and a and b are the proportional contributions associated with the slow and fast components of the build up curves, respectively. For $Li_{4.3}AlS_{3.3}Cl_{0.7}$, data were fitted with a stretch exponential function of the form $1 - \exp[-(\tau/T_1)^{\alpha}]$ (with α ranging from 0.9 to 1). $T_{1\rho}$ time constants were recorded using a standard spin-lock pulse sequence $\pi/2$ – spin lock – acq (where the duration of the spin-lock pulse is incremented)

at frequencies of $\omega_1/2\pi(^7Li)$ = 10, 30, and 80 kHz and the data were fitted to a stretch exponential function of the form $\exp[-(\tau/T_{1\rho})^{\beta}]$ (with β ranging from 0.5 to 1). The stretch exponential was used in order to account for a distribution of τ_c values, temperature gradients across the sample (see below) and the inherent multi-exponential behaviour for relaxation of I = 3/2 nuclei.[32-34] Static ^7Li NMR lineshapes obtained at various temperatures were simulated with the solid lineshape analysis tool “Sola” in Topspin to determine the ratio of the two components contributing to the lineshapes as well as the quadrupolar coupling constant C_Q and the asymmetry parameter η_Q values. All samples for static experiments were flame-sealed in Pyrex inserts under an Ar atmosphere.

^6Li MAS NMR experiments were performed on a 9.4 T Bruker DSX spectrometer using a 4 mm HXY MAS probe (in double resonance mode) with the X channel tuned to ^6Li at $\omega_0/2\pi(^6Li)$ = 59 MHz. A 90° pulse of duration 3 μs at a rf amplitude of $\omega_1/2\pi(^6Li)$ = 83 kHz was used. The MAS frequency $\omega_r/2\pi$ was set to 10 kHz. ^6Li MAS NMR spectra were acquired under quantitative recycle delays of more than 5 times the ^6Li T_1, measured via the saturation recovery pulse sequence. Static ^6Li T_1 time constants were also recorded using the same pulse sequence. Additionally, ^6Li MAS NMR spectra were also collected on a 20 T Bruker NEO spectrometer using a 3.2 mm HXY probe with the X channel tuned to ^6Li at $\omega_0/2\pi(^6Li)$ = 126 MHz and at $\omega_r/2\pi$ = 20 kHz with a 90° pulse duration 4.5 μs at an rf amplitude of $\omega_1/2\pi(^6Li)$ = 56 kHz for Li_3AlS_3 and a 90° pulse duration 3 μs at an rf amplitude of $\omega_1/2\pi(^6Li)$ = 83 kHz for $Li_{4.3}AlS_{3.3}Cl_{0.7}$.

^6Li-^6Li EXSY NMR experiments were performed on an 18.8 T Bruker NEO

spectrometer equipped with a 1.3 mm HX MAS probe with the X channel tuned to ^{6}Li at $\omega_0/2\pi(^{6}\text{Li})$ = 118 MHz, a 90° pulse of duration 3 μs at an rf amplitude of $\omega_1/2\pi(^{6}\text{Li})$ = 83 kHz and under $\omega_r/2\pi$ = 15 and 45 kHz. Diagonal and cross peak intensities I_d and I_c, respectively, were extracted using Topspin. The sample temperature increase due to frictional heating at faster MAS frequencies was calibrated via ^{79}Br T_1 measurement on the chemical shift thermometer KBr.[35]

Temperature calibrations of the 9.4 T NMR probes were performed with the chemical shift thermometers $Pb(NO_3)_2$ using ^{207}Pb NMR[36,37] and CuI and CuBr using ^{63}Cu NMR.[38,39] The errors associated with this method were calculated using the line broadening of the isotropic peak and are in the 5-20 K range. The ^{6}Li and ^{7}Li shifts were referenced to 10 M LiCl in D_2O.

3.5 Results and Discussion

3.5.1 Structure determination and description

NMR spectroscopy at various fields was deployed in conjunction with diffraction techniques in order to confirm the overall pattern of site occupancy of the lithium atoms in Li_3AlS_3. The ^6Li MAS NMR spectra at 9.4 and 20 T for Li_3AlS_3 are shown in **Figure 3.1(a)** and display three well-resolved resonances at 1.7, 1.3, and −0.2 ppm, which fit yield signals of equal integration. A small shoulder is also observed at 1 ppm and corresponds to the Li_5AlS_4 impurity seen in the diffraction and ^{27}Al NMR data (**Figure 3.2**);[40] this signal was found to integrate 3.0(5) mol % Li_3AlS_3, in agreement with the 3.3(5) mol % value from diffraction. Based on the well-established semi-empirical correlations relating the lithium coordination environment and ^6Li NMR shifts,[41] further aided by calculations of the NMR parameters using the GIPAW approach[42,43] as implemented in CASTEP[44] (**Table 3.1**), the signal at −0.2 ppm has been attributed to the octahedrally coordinated Li2/Li2b and Li3 sites while the resonances at 1.3 and 1.7 ppm correspond to Li4 and Li1, respectively. These assignments agree well with the structural refinement from diffraction, which identified the sum of the contents of the three octahedrally coordinated sites Li2 (0.8(3)), Li2b (3.2(3)), and Li3 (4.0(4)) to 8.0(7) Li per unit cell and the contents of the two tetrahedrally coordinated Li4 and Li1 to 7.8(3) and 8.00 per unit cell, respectively.

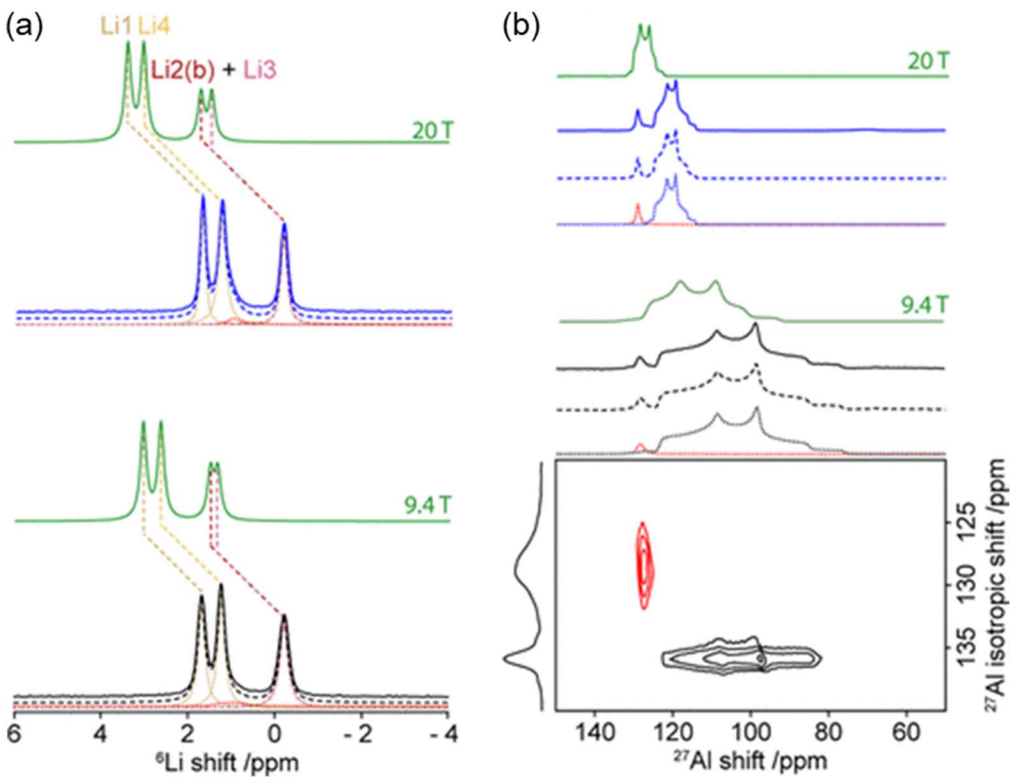

Figure 3.1 (a) ^{6}Li MAS spectrum of Li_3AlS_3 obtained at magnetic fields of 9.4 T (black) and 20 T (blue). The experimental spectrum (full lines), total fit (dashed lines) spectral deconvolution (dotted lines), Li_5AlS_4 impurity (red dotted lines), and GIPAW-simulated spectrum (green lines) are shown. (b) ^{27}Al MQMAS NMR spectrum of Li_3AlS_3 recorded at a magnetic field of 9.4 T and 20 T. The dotted lines (black for a field of 9.4 T and blue for 20 T) and the red dotted lines represent the spectral deconvolution of Li_3AlS_3 and Li_5AlS_4, respectively. The dashed lines show the total fit for the sample, and the solid lines show the anisotropic one-dimensional ^{27}Al spectrum, while the vertical spectrum shows the non-quantitative isotropic ^{27}Al spectrum. The solid green line shows the GIPAW-simulated spectrum with an isotropic chemical shift of 117 ppm, a quadrupolar coupling constant of 5.1 MHz and an asymmetry parameter of 0.44 (**Table 3.1**).

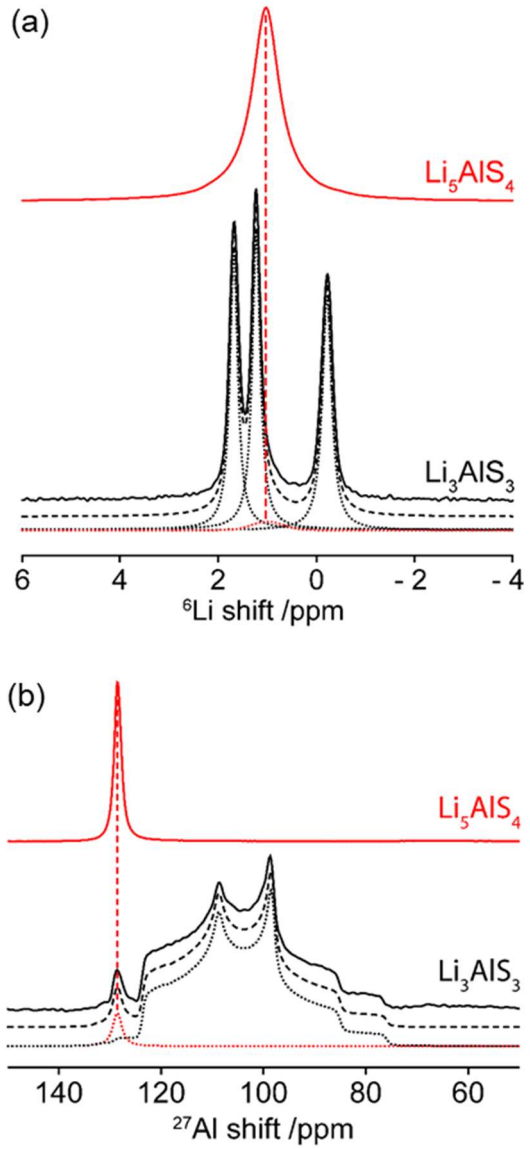

Figure 3.2 (a) ^{6}Li MAS NMR spectra of Li_3AlS_3 and Li_5AlS_4 recorded at a magnetic field of 9.4 T and under MAS at 10 kHz demonstrating the correlation between the resonance observed in the spectral deconvolution of Li_3AlS_3 and the signal in in the spectrum of pure Li_5AlS_4. (b) ^{27}Al MAS NMR spectra of Li_3AlS_3 and Li_5AlS_4 obtained at a magnetic field of 9.4 T and under MAS at 10 kHz demonstrating the correlation between the ^{27}Al shift observed at approximately 130 ppm in the spectrum of Li_3AlS_3 with the only resonance observed in the spectrum of Li_5AlS_4.

The ^{27}Al one-dimensional MAS spectra for Li_3AlS_3 at 9.4 and 20 T are shown in **Figure 3.2(b)** and reveal a second order quadrupolar line shape that resonates at ~100 ppm (at 9.4 T) and ~120 ppm (at 20 T), typical of tetrahedrally coordinated Al sites, and a very sharp signal, which is field-independent, at ~130 ppm, corresponding to the small amount of Li_5AlS_4 impurity (**Figure 3.2(b)**). Note that no signal in the octahedral region (around 0 ppm) of the ^{27}Al MAS NMR spectrum is present as expected. The z-filtered triple quantum MAS[43,45] NMR spectrum of Li_3AlS_3 is also shown in **Figure 3.1(b)** and demonstrates that the ~100 ppm signal corresponds to one resonance only with an isotropic chemical shift of 117 ppm and a quadrupolar coupling constant (C_Q) of 5.8 MHz in close agreement with the computed value of 5.1 MHz (**Table 3.1**).

3.5.2 Calculation and conversion of NMR parameters

For comparison with experiment, NMR parameters were calculated for the experimentally refined crystal structure of Li_3AlS_3 considering occupancy of the high symmetry sites for Li2 and Li3 atoms instead of the split sites due the results found in phonon calculation stated above. For this model, both sites are in the 4e Wyckoff position along the two fold axis. Following geometry optimisation in VASP, the geometry was optimised again using GIPAW[42,43] in CASTEP[44] with the same parameters as VASP, except for a higher plane wave cut-off of 800 eV. On-the-fly generated pseudopotentials were used to treat core electrons in CASTEP. NMR parameters were then calculated using the GIPAW method as implemented in CASTEP. The method used for conversion

of the chemical shieldings to the calculated isotropic chemical shifts is presented in the supplementary information.

Conversion of the chemical shieldings, σ_{iso}, directly obtained from the calculations, to the isotropic chemical shifts, $\delta_{iso,cs}$, is obtained with the expression:[43]

$$\delta_{iso,cs} = \sigma_{iso,ref} + m_{ref}\,\sigma_{iso} \qquad \text{(Eq. 3.1)}$$

where m_{ref} and $\sigma_{iso,ref}$ are a gradient close to -1 and a reference shielding, respectively. For ^{6}Li, m_{ref} and $\sigma_{iso,ref}$ were taken from our own calculations of Li_2O, LiOH and Li_2CO_3 and compared with shifts from the literature[46] yielding $\sigma_{iso,ref}$ = 89.6 ppm and m_{ref} = - 0.961. For ^{27}Al, $\sigma_{iso,ref}$ = 555.4 ppm, m_{ref} = - 0.996 were taken from the literature.[47]

It is well known that for quadrupolar nuclei (such as ^{6}Li and ^{27}Al), the NMR shift δ (or centre of gravity of the line) is shifted from $\delta_{iso,cs}$ by the quadrupolar induced shift $\delta_{iso,Q}$ according to:[48]

$$\delta = \delta_{iso,cs} + \delta_{iso,Q} \qquad \text{(Eq. 3.2)}$$

with

$$\delta_{iso,Q} = -\frac{3}{40}\frac{C_Q^2\left(I(I+1) - {}^{3}/_{4}\right)}{{\nu_0}^2 I^2 (2I-1)^2}\left(1 + \frac{\eta_Q^2}{3}\right)10^6 \qquad \text{(Eq. 3.3)}$$

where C_Q, η_Q, ν_0, and I are the quadrupolar coupling constant, asymmetry parameter, Larmor frequency and the nuclear spin quantum number, respectively. For ^{6}Li and other spin 1 nuclei **equation 3.3** becomes:

$$\delta_{iso,Q} = -\frac{3}{32}\frac{C_Q^2}{{\nu_0}^2}\left(1+\frac{\eta_Q^2}{3}\right)10^6 \quad \text{(Eq. 3.4)}$$

For ^{27}Al and other spin 5/2 nuclei **equation 3.3** takes the form of:

$$\delta_{iso,Q} = -\frac{3}{500}\frac{C_Q^2}{{\nu_0}^2}\left(1+\frac{\eta_Q^2}{3}\right)10^6 \quad \text{(Eq. 3.5)}$$

All experimentally determined and computed NMR parameters for Li_3AlS_3 are given in **Table** .

3.5.3 Calculation of isotropic chemical shift for ^{27}Al MQMAS

The experimental isotropic chemical shift for the ^{27}Al resonance can be extracted from the measurements using the following equation:

$$\delta_{iso,cs} = \frac{10}{27}\delta_{F2}^{Obs} + \frac{17}{27}\delta_{F1}^{Obs} \quad \text{(Eq. 3.6)}$$

where δ_{F2}^{Obs} and δ_{F1}^{Obs} are the observed chemical shifts in the anisotropic (horizontal F_2) and isotopic (vertical F_1) dimensions, respectively from the ^{27}Al MQMAS NMR spectrum of Li_3AlS_3 (**Figure 3.1(b)**).

The calculations predict a resonance at 1.5 ppm linked to Li3, a resonance at 1.7 ppm associated with Li2 and two resonances at 3.1 and 3.5 ppm each with double the intensity (4 times Li1 and 4 times Li4).

Table 3.1 Summary of the NMR parameters for Li_3AlS_3 obtained experimentally (in bold at 9.4 T and bold italics at 20 T) and calculated (in plain text at 9.4 T and italics at 20 T) using the GIPAW method as implemented in CASTEP. The experimental ^{27}Al $\delta_{iso,cs}$, C_Q and η_Q values were extracted from fits of the ^{27}Al MQMAS and MAS spectra. The $\delta_{iso,Q}$ values were obtained as described above.

Environment	Coordination	σ_{iso} / ppm	δ / ppm	$\delta_{iso,cs}$ / ppm	$\lvert C_Q \rvert$ / kHz	η_Q	$\delta_{iso,Q}$ at 9.4 T / ppm	$\delta_{iso,Q}$ at 20 T / ppm
Li1	VI	89.6	3.1/*3.4* **1.7/*1.7***	3.5	124	0.2	-0.4	-0.09
Li2	IV	87.8	1.5/*1.7* **-0.2/*-0.2***	1.7	72	0.3	-0.2	-0.03
Li3	IV	87.6	1.4/*1.5* **-0.2/*-0.2***	1.5	85	0.6	-0.1	-0.05
Li4	VI	89.2	2.6/*3.0* **1.2/*1.1***	3.1	133	0.1	-0.5	-0.11
Al	IV	422.8	119/*131* **95/*111***	134 **116**	5125 **5850**	0.4 **0.6**	-15 **-21**	-3 **-5**

The structure of Li_3AlS_3[1] consists of a *hcp* arrangement of sulphur atoms with an A B A* B* stacking of anion layers, giving rise to the four layer repeat (**Figure 3.3(a) (i)**) where B is the equivalent of A through the *c* glide plane and 2-fold axis symmetry operations. A* and B* are the equivalent of A and B through the C centering translation. The two different polyhedral layers are stacked alternately perpendicular to the *bc* plane (**Figure 3.3(a)**). In the tetrahedral layers (between A and B and between A* and B*), Li1 and Al atoms

occupy 2/3 of the tetrahedral interstices between a pair of sulphur atom layers to form edge sharing tetrahedra. Between the second pairs of sulphur layers (between B and A* and between B* and A), Li2 and Li3 occupy octahedral interstices, whereas Li4 occupies a tetrahedral interstice, generating a mixed polyhedral (octahedral-tetrahedral) layer (Li-only layer). In the tetrahedral layer, Al, Li1 and vacancies are ordered in a 1:1:1 arrangement, and 2/3 of the octahedral interstices are occupied in the Li-only layer, resulting in edge sharing Li2 and Li3 octahedra, so that this structure presents a high proportion of ordered vacancies in both the tetrahedral and Li-only layer.

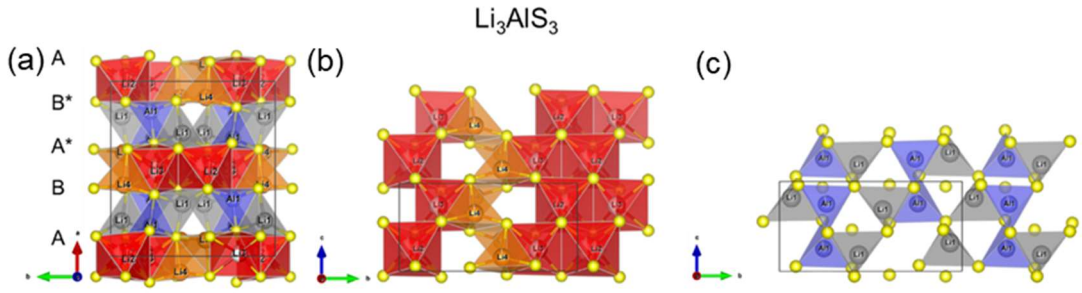

Figure 3.3 Crystal structures of Li_3AlS_3 showing the *hcp* arrangement of sulphur atoms, and the alternating mixed cation polyhedral layer and Li-only layer stacked perpendicular to the (*bc*) plane. (a) Layered view, (b) Li only polyhedral layer and (c) mixed cation tetrahedral layer in the (*bc*) plane. The A B A* B* stacking of anion layers leads to a 4 layer repeat (A* and B* being the equivalent of A and B through the C centering translation). Blue, orange and red polyhedra correspond to Al tetrahedra, Li tetrahedra and Li octahedra, respectively. Grey polyhedra correspond to Li tetrahedra from the mixed cation tetrahedral layer in Li_3AlS_3

Multinuclear ^{6}Li and ^{27}Al NMR spectra were recorded to further support the structural refinement of $Li_{4.3}AlS_{3.3}Cl_{0.7}$. The ^{6}Li MAS NMR spectrum (**Figure 3.4(a)**) displays an intense resonance at 1 ppm assigned to tetrahedral and octahedral sites from the $Li_{4.3}AlS_{3.3}Cl_{0.7}$ phase and a small peak at ~−0.3 ppm, which could potentially be attributed to small amounts of octahedral lithium sites from the ordered Li_3AlS_3 phase.[1] A smaller peak at −1.1 ppm is also visible and corresponds to solid LiCl[49] (observed in XRD). The main signal is narrow (50 Hz) at room temperature and suggests the presence of a motionally averaged NMR signal arising from fast Li+ hops and preventing the spectral resolution of Li sites with various coordination numbers. The ^{27}Al MAS NMR spectrum (**Figure 3.4(b)**) shows the presence of two asymmetrically broadened and overlapping peaks around 125 ppm which are assigned to Al tetrahedra based on the shift value (note that the quadrupolar induced shift[48] is likely smaller than 5 ppm at this magnetic field). Less intense resonances at 70 and 16 ppm (**Figure 3.5**) are assigned to a small amount of more highly coordinated Al. Most importantly, the second-order quadrupolar line shape observed for an AlS_4 tetrahedron in the parent Li_3AlS_3[1] is not observed and further supports that $Li_{4.3}AlS_{3.3}Cl_{0.7}$ cannot be described by distinct $AlCl_4$ and AlS_4 tetrahedra but by a random distribution of the S and Cl atoms. The asymmetrically broadened lines arise from second-order quadrupolar interaction coming from deviation from the perfect tetrahedral site symmetry while the low frequency tail is cause by a distribution of quadrupolar couplings stemming from local structural disorder. An attempt to resolve the main resonances using a ^{27}Al MQMAS NMR experiment only yields the typical 2D

line shape from distribution of quadrupolar couplings, and no improvement in the resolution of the corresponding ^{27}Al isotropic spectrum is observed.

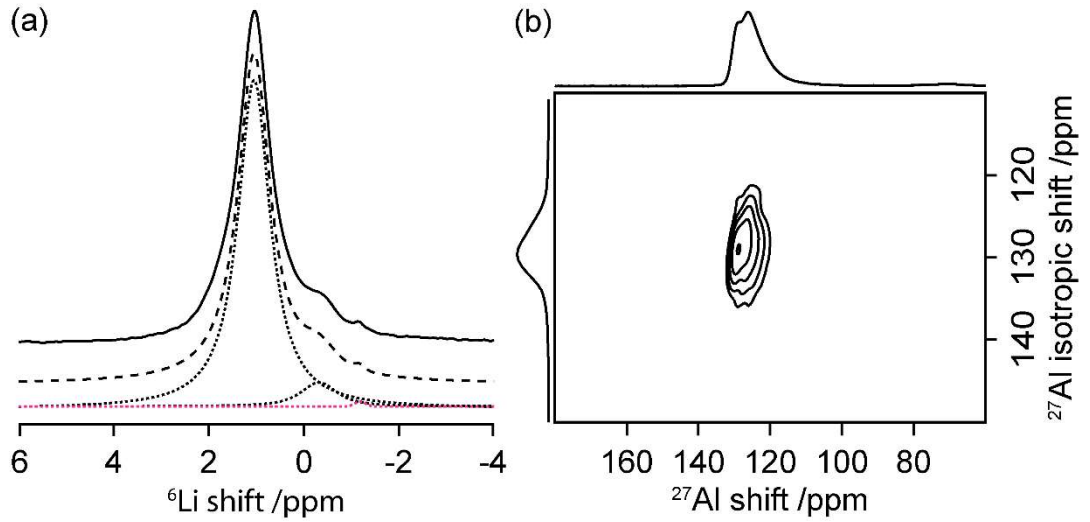

Figure 3.4 (a) ^{6}Li MAS spectrum of $Li_{4.3}AlS_{3.3}Cl_{0.7}$. The experimental spectrum (full line), total fit (dashed line), and spectral deconvolution (dotted lines) are also shown. (b) ^{27}Al MQMAS spectrum of $Li_{4.3}AlS_{3.3}Cl_{0.7}$. The spectrum on the top is the ^{27}Al MAS NMR spectrum, while the one on the left is the isotropic ^{27}Al spectrum free of anisotropic broadening.

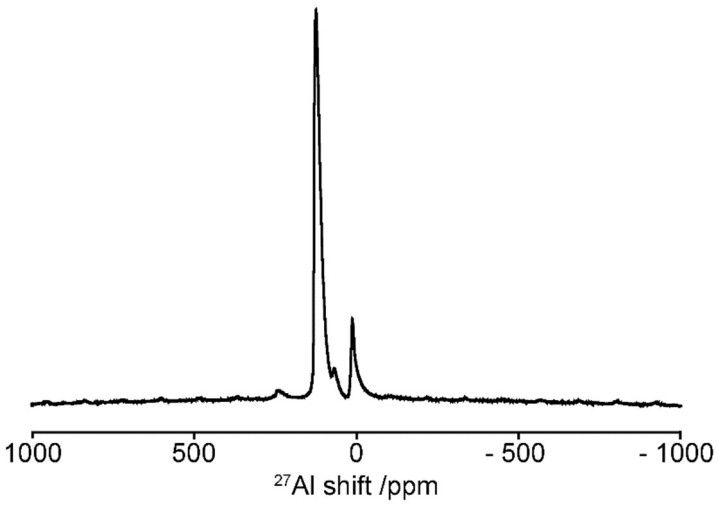

Figure 3.5 One-dimensional ^{27}Al MAS NMR spectrum of $Li_{4.3}AlS_{3.3}Cl_{0.7}$ obtained at a magnetic field of 20 T and under MAS at 20 kHz showing the full spectral width.

The substitution of Cl onto the *hcp* sulphur sites in Li_3AlS_3 gives the new $Li_{4.3}AlS_{3.3}Cl_{0.7}$[2] phase (**Figure 3.6**), which retains the *hcp* arrangement of Li_3AlS_3, as well as the alternating tetrahedral and Li-only layer, while leading to a strong cation site disorder within the polyhedral interstices, so that Li_3AlS_3 is a superstructure of $Li_{4.3}AlS_{3.3}Cl_{0.7}$. In the latter, the anion stacking motif is A B with only a two layer repeat. Within the tetrahedral layer, lithium (Li1, site occupancy factor: sof_{Li1}= 0.50(1)) and aluminium (sof_{Al} = 0.25) are disordered among all the tetrahedral interstices. Within the Li-only layer, lithium and vacancies are disordered among all the octahedral (Li3, sof_{Li3}=0.644(2)) and tetrahedral (Li2, sof_{Li2}=0.260(2)) sites. Li1/Al and Li2 tetrahedra of the adjacent layer share a common base and form a polyhedral unit which can only host one cation. Indeed, the small hypothetical interatomic distances $d_{Al\text{-}Li2}$ = 1.543(13) Å and $d_{Li1\text{-}Li2}$ = 1.274(14) Å) renders the occupation of both the Li1/Al and Li2 sites of the same unit very unlikely. A summary of the various Li interatomic distances is available in **Table 3.2**.

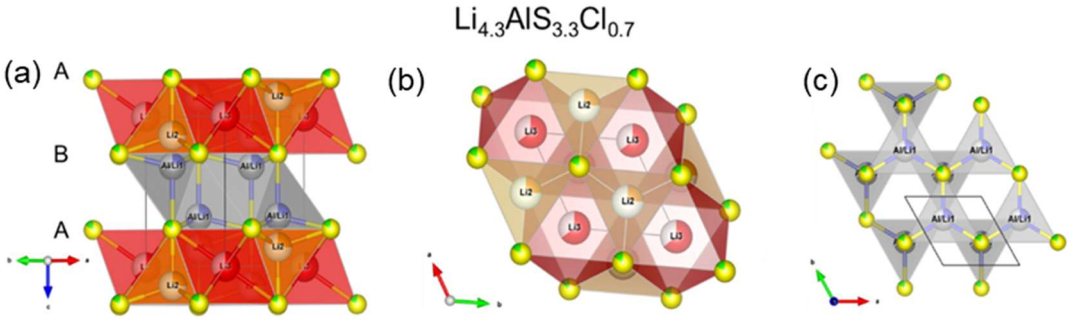

Figure 3.6 Crystal structures of $Li_{4.3}AlS_{3.3}Cl_{0.7}$ showing the similar *hcp* arrangement of sulphur atoms to Li_3AlS_3, and the alternating mixed cation polyhedral layer and Li-only layer stacked perpendicular to the (*ab*) plane. (a) Layered view, (b) Li only polyhedral layer and (c) mixed cation tetrahedral layer in the (*ab*) plane. In Li_3AlS_3, the A B A* B* stacking of anion layers leads to a 4 layer repeat (A* and B* being the equivalent of A and B through the C centering translation). In $Li_{4.3}AlS_{3.3}Cl_{0.7}$, only a two layer repeat is occurring with an A B stacking of the anion layers. Orange and red polyhedra correspond to Al tetrahedra, Li tetrahedra and Li octahedra, respectively. Grey polyhedra correspond to mixed Al/Li occupied tetrahedra in $Li_{4.3}AlS_{3.3}Cl_{0.7}$.

Table 3.2 Summary of the shortest interatomic distances between the various crystallographic Li sites in Li_3AlS_3 and $Li_{4.3}AlS_{3.3}Cl_{0.7}$ extracted from diffraction data.[1,2] Note the labelling of the Li sites varies between the two materials, with Li2 referring to octahedral Li in Li_3AlS_3, while Li2 corresponds to tetrahedral Li in $Li_{4.3}AlS_{3.3}Cl_{0.7}$.

Sample	Interatomic distance / Å					
	Li1-Li2	Li1-Li3	Li1-Li4	Li2-Li3	Li2-Li4	Li3-Li4
Li_3AlS_3	4.07(13)	3.12(3)	3.322(13)	3.3(3)	4.49(8)	2.83(3)
$Li_{4.3}AlS_{3.3}Cl_{0.7}$	1.274(14)	3.074(4)	N/A	2.406(5)	N/A	N/A

3.5.4 Static ^{7}Li VT line narrowing NMR

Static ^{7}Li NMR spectra of Li_3AlS_3 and $Li_{4.3}AlS_{3.3}Cl_{0.7}$ were collected in the 130-450 K temperature range (**Figure 3.7**) to provide information on the Li-ion dynamics on the kHz timescale. At low temperatures (<250 K and <200 K for Li_3AlS_3 and $Li_{4.3}AlS_{3.3}Cl_{0.7}$, respectively), the lineshape of the 1/2 ↔ -1/2 central transition strongly suggests that the linewidth is dominated by the strong ^{7}Li - ^{7}Li homonuclear dipolar broadening of the ^{7}Li spins with a static ^{7}Li NMR linewidth $\omega/2\pi$ at half-height of ~6.7 kHz for Li_3AlS_3 and ~7.0 kHz for $Li_{4.3}AlS_{3.3}Cl_{0.7}$. This broadening is significant given that it is proportional to the square of the gyromagnetic ratio γ of the nuclear spins which is large for ^{7}Li ($\gamma(^7Li)$ = 16.5 MHz T^{-1}). At these low temperatures, the materials reside in the so-called rigid lattice regime and the corresponding Li^+ ion τ^{-1} values are smaller than $\omega/2\pi$. As the sample temperature is increased, the central transition linewidths of both phases significantly decrease at the onset

temperatures T_{onset} of motional narrowing, which occur at around 270 K and 220 K for Li_3AlS_3 and $Li_{4.3}AlS_{3.3}Cl_{0.7}$, respectively (**Figure 3.8**). This narrowing effect arises from the continuous averaging of the ^7Li - ^7Li homonuclear dipolar coupling due to the increasing motion of the Li^+ ions at frequencies larger than $\omega/2\pi$. Importantly, the significantly lower T_{onset} observed for $Li_{4.3}AlS_{3.3}Cl_{0.7}$ *vs.* Li_3AlS_3 indicates higher Li^+ ion mobility in the former phase, supporting the previously reported results obtained via EIS[1,2] where room temperature conductivity values in the order of 10^{-6} and 10^{-9} S cm^{-1} were extracted for the respective samples.

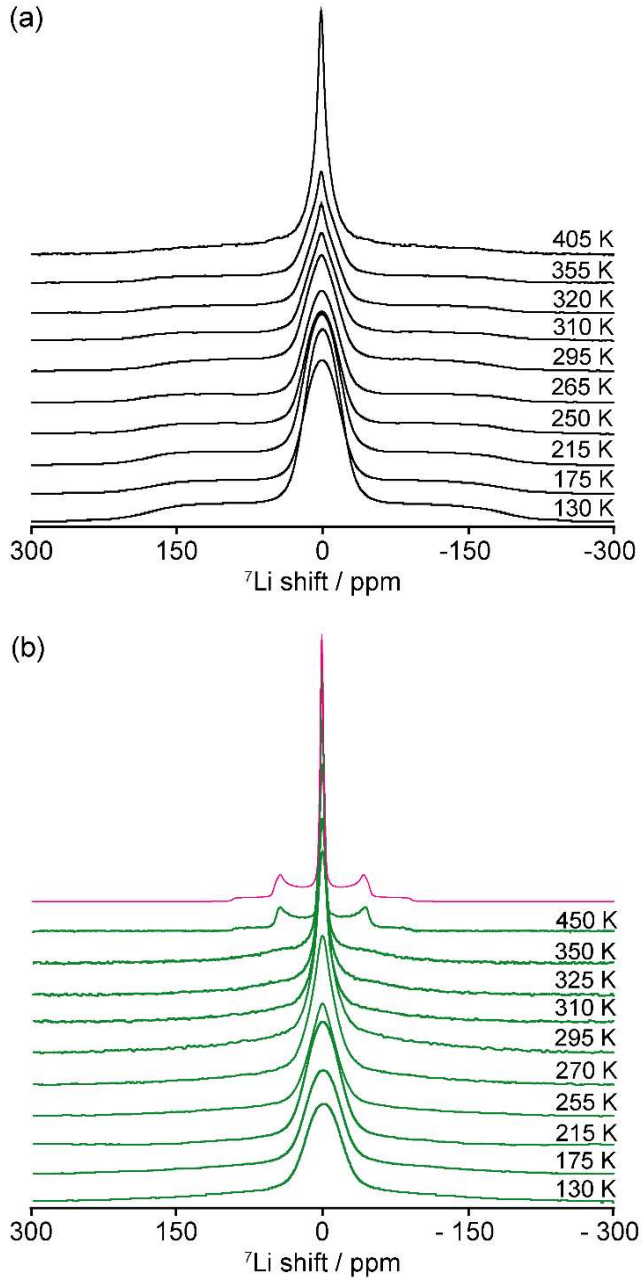

Figure 3.7 Static ^{7}Li one pulse NMR spectra of (a) Li_3AlS_3 and (b) $Li_{4.3}AlS_{3.3}Cl_{0.7}$ as a function of temperature. The pink line displays a simulation of the static ^{7}Li NMR spectrum of $Li_{4.3}AlS_{3.3}Cl_{0.7}$ at 450 K using a single set of parameters describing the quadrupolar powder pattern for a spin 3/2 nucleus with a shift δ of 0 ppm, a quadrupolar coupling constant C_Q of 30 kHz and a quadrupolar asymmetry η_Q of 0.1.

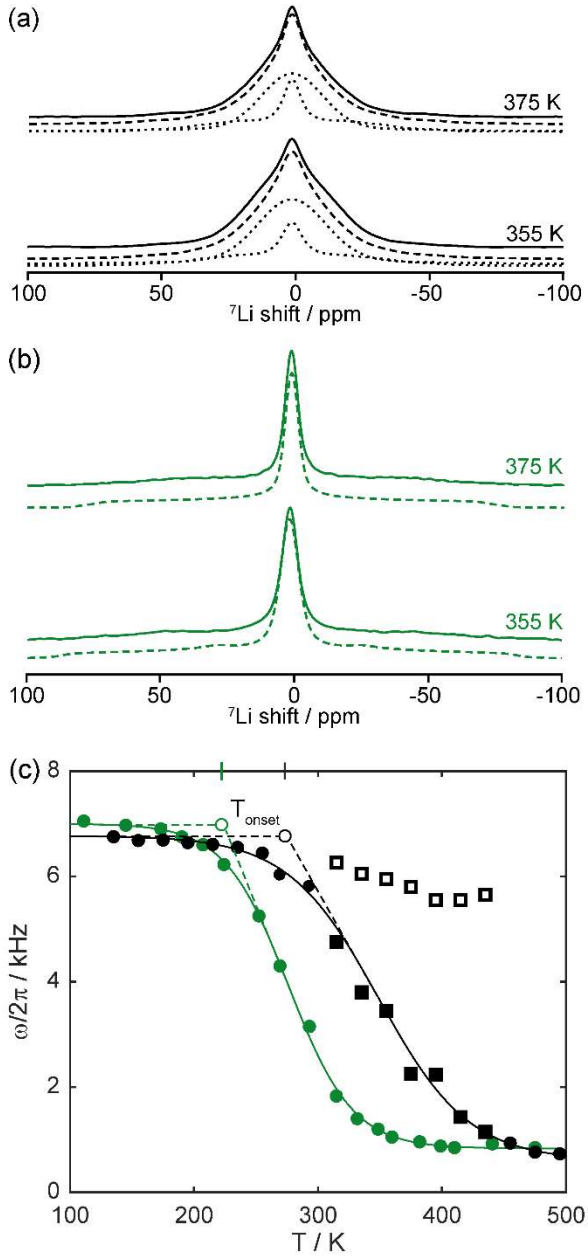

Figure 3.8 Representative static ^{7}Li one pulse NMR spectra of (a) Li_3AlS_3 and (b) $Li_{4.3}AlS_{3.3}Cl_{0.7}$ illustrating the broad and motionally narrowed components of the NMR lineshape associated with Li-ion diffusion. The experimental spectra (solid lines), total fit (dashed lines) and spectral deconvolution (dotted lines) are shown. (c) Temperature dependence of ^{7}Li NMR linewidth $\omega(T)/2\pi$ of Li_3AlS_3 (black) and $Li_{4.3}AlS_{3.3}Cl_{0.7}$ (green). In Li_3AlS_3, the empty and filled squares represent the broad and narrow components of the lineshape

observed in (a), respectively, while circles for $Li_{4.3}AlS_{3.3}Cl_{0.7}$ correspond to the total lineshape in (b). The onset temperatures of line narrowing T_{onset} are given with double length ticks on the upper vertical axis, with dashed lines showing the tangents of curve used to extract T_{onset}. The solid black and green lines are fit to the data based on the sigmoidal regression given in **equation 3.8** and are used to determine the inflection points of the respective curves.

Further sample heating above room temperature yields significantly narrower lines with $\omega/2\pi$ on the order of 750 Hz and a multicomponent lineshape for Li_3AlS_3 (see below). This corresponds to $\tau^{-1} >> \omega/2\pi$ in the static regime, with ^7Li - ^7Li homonuclear dipolar coupling (fast motional regime) that are largely averaged out and residual linewidth is mainly governed by non-homonuclear dipolar interactions and inhomogeneities of the external magnetic field B_0.[50] The ^7Li NMR spectrum of $Li_{4.3}AlS_{3.3}Cl_{0.7}$ at 450 K displays the typical quadrupolar powder pattern of this spin I = 3/2 nucleus with a quadrupolar tensor in (or close to) axial symmetry, consisting of a central transition at 0 ppm and quadrupolar satellite transitions at approximately ± 50 ppm corresponding to a quadrupolar coupling constant C_Q of ~30 kHz (**Figure 3.7(b)**). The axial symmetry suggests Li^+ ions exchange between axially symmetric sites of similar orientation, or between sites with different orientations averaging out two of the three components of the quadrupolar tensors. Accessing these orientations is beyond the scope of the work as this would require significant computational work[51] capturing the complex site disorder of $Li_{4.3}AlS_{3.3}Cl_{0.7}$.

Close inspection of the ^7Li NMR spectra for Li_3AlS_3 between 315 and 435 K

(**Figure 3.8(a)**) for representative spectra in the middle of this temperature range) clearly reveal two contributions to the lineshape. This consists of a motionally narrowed line, corresponding to highly mobile Li^+ ions ($\tau^{-1} < \omega/2\pi$), superimposed on a much broader one for slower moving ions ($\tau^{-1} > \omega/2\pi$). The two components display significantly different C_Q values of 58 and 15 kHz for the broad and narrow components, respectively (**Figure 3.9**). It is postulated that this two-component NMR lineshape arises from ions moving along the faster diffusion pathways present in the layered structure (see below). At 315 K, approximately 12% of the Li-ions present are mobile, with this percentage increasing as a function of temperature (**Figure 3.10**). This two-component lineshape is not observed in the ^7Li NMR spectra of $Li_{4.3}AlS_{3.3}Cl_{0.7}$ (**Figure 3.8(b)**) which is ascribed to the improved mobility of the Li^+ species facilitated by the presence of more favourable ion mobility pathways due to the introduction of disordered vacancies. In order to confirm the presence of two superimposed quadrupolar lineshapes in the ^7Li NMR spectra of Li_3AlS_3, double- and triple-quantum filtration and Hahn-echo experiments were performed (**Figure 3.11**). In the double-quantum filtered spectrum, the central transition is suppressed while the quadrupolar satellites associated with transitions between the ±3/2 <-> ±1/2 energy levels have opposite phase to one another. In **Figure 3.11(a)**, the presence of two sets of satellite peaks with inverted phase can be seen. In the triple-quantum filtered spectrum, the central transition remains while the quadrupolar satellites have inverted phase. The triple-quantum filtered spectrum in **Figure 3.11(b)** displays two sets of satellite transitions with opposite phase to the central transition, with corresponding C_Q values matching well the ones obtained from the static ^7Li one pulse spectra

obtained at VT (**Figure 3.9**). Two static ^{7}Li NMR Hahn-echo experiments with different echo delays (**Figure 3.11(c)**) reveal efficient T_2 filtering to observe a lineshape dominated by a broad component at short dephasing time which is then largely removed at longer dephasing time where the narrower component is isolated.

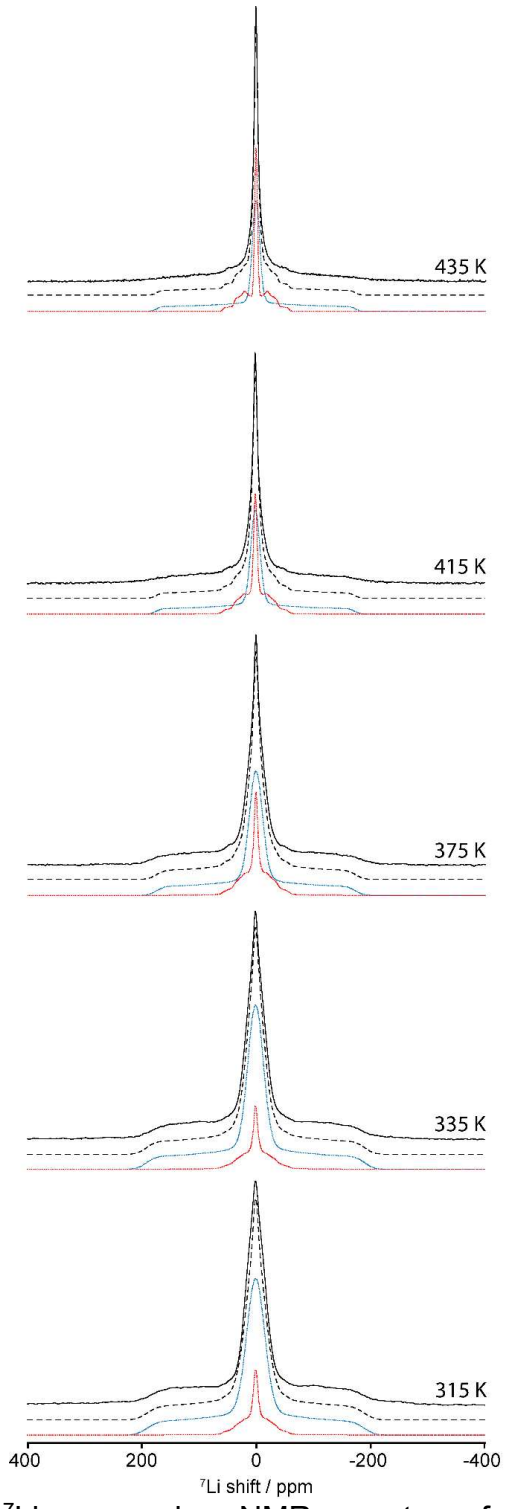

Figure 3.9 Static ^{7}Li one pulse NMR spectra of Li_3AlS_3 at selected temperatures demonstrating how the two components of the lineshape vary as a function of temperature. Experimental spectra (full black line), total fit (dashed black line) and spectral deconvolution for the broad (blue dotted line) and narrow (red dotted line) are shown.

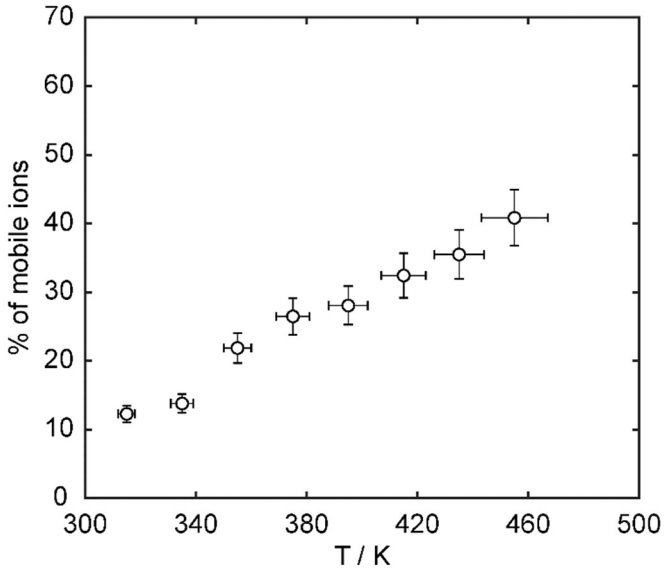

Figure 3.10 Percentage of mobile ions present in Li_3AlS_3 as a function of temperature. The percentage of mobile ions was taken as the contribution from the narrow component to the overall integration of the static ^7Li resonance.

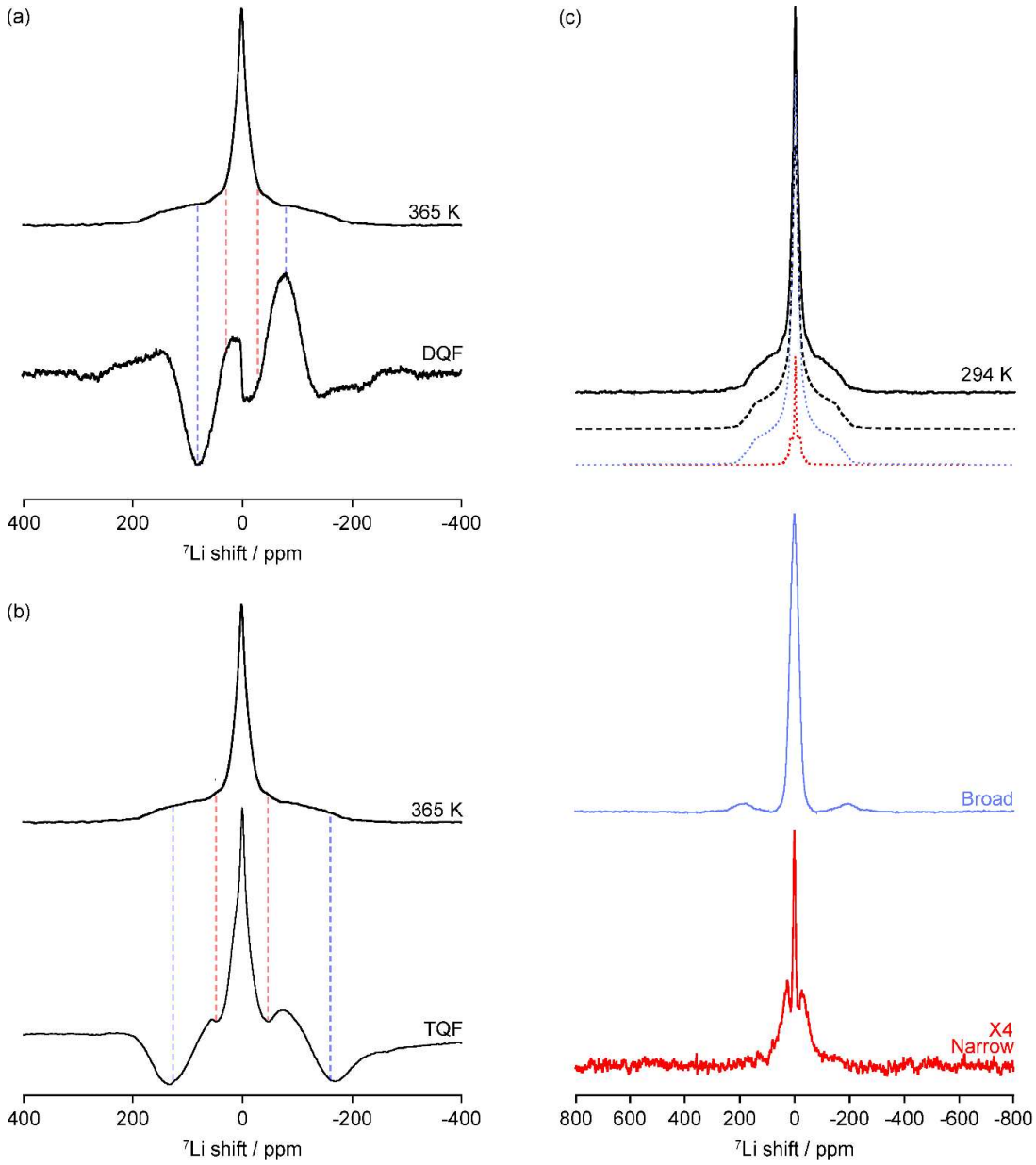

Figure 3.11 ^{7}Li NMR spectra of Li_3AlS_3 recorded at 9.4 T under static conditions. (a) Double-quantum filtered (DQF)[29,30,34] spectrum at 365 K, where the central transition is supressed and the quadrupolar satellite transitions associated with the ± 3/2 <-> ± 1/2 transitions have opposite phase. (b) Triple-quantum filtered (TQF) spectrum at 365 K in which the quadrupolar satellites have inverted phase. The coloured dashed lines highlight the satellite transitions associated with the broad component (blue) and narrow component (red), respectively. (c) Hahn-echo pulse sequence at room temperature with

two different dephasing delays (9 and 90 μs in the blue and red spectra, respectively), allowing for the observation of the two separate components. The ^{7}Li one pulse spectra at the corresponding temperatures are also shown, where in panel (c) the experimental spectrum (full black lines), total fit (dashed black lines) and spectral deconvolution of the broad component (blue dotted line) and narrow component (red dotted line) are given.

Using a simple expression introduced by Waugh and Fedin[52] correlating T_{onset} to E_a of the diffusion process:

$$E_a = 1.67 \times 10^{-3} \cdot T_{onset} \qquad \text{(Eq. 3.7)}$$

approximate E_a values of 0.5 and 0.4 eV were estimated for Li_3AlS_3 and $Li_{4.3}AlS_{3.3}Cl_{0.7}$, respectively, suggesting more favourable local Li^+ ion mobility in $Li_{4.3}AlS_{3.3}Cl_{0.7}$ than in the non-doped parent material as previously indicated. Moreover, the inflection points of the line narrowing curves $T_{inflection}$ (**Figure 3.8(c)**) define the Li^+ τ^{-1}, which is of the order of $(\omega/2\pi)_{rl}$ (linewidth in the rigid lattice regime), and yield comparable values of ~4.2(3) × 10^4 s^{-1} for Li_3AlS_3 and ~4.4(4) × 10^4 s^{-1} for $Li_{4.3}AlS_{3.3}Cl_{0.7}$. $T_{inflection}$ values were determined from fitting the $\omega/2\pi$ data in **Figure 3.8(c)** to a Boltzmann sigmoid regression curve of the form:

$$\frac{\omega(T)}{2\pi} = \left(\frac{\left(\frac{\omega}{2\pi}\right)_{\infty} - \left(\frac{\omega}{2\pi}\right)_{rl}}{1 + \exp\left(\frac{T_{inflection} - T}{a}\right)} \right) \qquad \text{(Eq. 3.8)}$$

where $\omega(T)/2\pi$ is the linewidth of the central transition at temperature T, $(\omega/2\pi)_{\infty}$ is the residual linewidth at high temperature in the fast motional regime and a

is a fitting parameter. Importantly, the lower $T_{inflection}$ value obtained for $Li_{4.3}AlS_{3.3}Cl_{0.7}$ (276(6) K) than for Li_3AlS_3 (371(9) K) clearly indicates a faster Li^+ ion diffusion process in the former phase.

3.5.5 ^{6}Li MAS NMR

Figure 3.12 compares the room temperature ^{6}Li MAS NMR spectra of Li_3AlS_3[1] and $Li_{4.3}AlS_{3.3}Cl_{0.7}$.[2] Li_3AlS_3 displays resonances at -0.2 ppm attributed to octahedrally coordinated Li2 and Li3 sites, 1.3 ppm for tetrahedral Li4 and 1.7 ppm corresponding to tetrahedral Li1,[1] while $Li_{4.3}AlS_{3.3}Cl_{0.7}$ shows an intense resonance at 1 ppm and a smaller peak at ~-0.3 ppm assigned to the tetrahedral Li1/Li2 and octahedral Li3 sites, respectively[2] (a smaller peak at -1.1 ppm is also visible and corresponds to residual solid LiCl).[49] In $Li_{4.3}AlS_{3.3}Cl_{0.7}$, the main signal at 1 ppm is narrow, with a peak width at half-height of $\omega/2\pi$ = 50 Hz at room temperature, and suggests the presence of a motionally averaged NMR signal arising from fast Li^+ hops between the two tetrahedral Li sites. This is not observed in the ^{6}Li MAS spectrum of Li_3AlS_3 as Li-ion exchange between non-equivalent Li1-Li4 sites are comparatively slow on the NMR timescale. Reduced motional averaging from decreasing the Li^+ ion mobility at 230 K revealed three different Li sites at 1.4, 0.9 and -0.55 ppm in $Li_{4.3}AlS_{3.3}Cl_{0.7}$ (**Figure 3.12(c)**). These are assigned to tetrahedral Li2 in the Li only layer (**Figure 3.6(b)**), tetrahedral Li1 in the Li/Al tetrahedral layer and octahedral Li3 in the Li only polyhedral layer, respectively, based on the semi-empirical correlation between lithium coordination environment and ^{6}Li NMR shift.[41] The higher resonance frequency of Li2 than Li1 arises from the large degree of bond length distortion present at Li1 (3 × 2.392(4) Å, 2.615(6) Å and

3.625(6) Å), which can be considered pseudo trigonal-bipyramidal as the Li positions are strongly displaced towards one face of the tetrahedron[1] and lead to a greater degree of chemical shielding for Li1. Note that the assignment of the tetrahedral sites in $Li_{4.3}AlS_{3.3}Cl_{0.7}$ is the inverse of the spectral assignments in Li_3AlS_3 and this is due to the added polyhedral distortion of the Li1 position in the former, compared with the more tetrahedral Li1 in the latter. Note also that the signal intensity of the Li3 site seems to differ from the site occupancy refined against neutron powder diffraction data[2] as at 230 K, the ^{6}Li MAS NMR spectrum is in the intermediate motional regime where there is a strong interplay between signal intensity and broadening (see below).

The relative rates of site exchange occurring in $Li_{4.3}AlS_{3.3}Cl_{0.7}$ can be qualitatively determined from the comparison of ^{6}Li MAS spectra obtained at two different temperatures (**Figure 3.12(b,c)**). While at 230 K, three resonances can be observed and upon heating to room temperature, the Li1 and Li2 resonances have completely coalesced at a weighted shift average of 1 ppm. The following expression relating the frequency separation between resonances $\Delta\omega/2\pi$ with the ion jump rate τ^{-1}:

$$\tau^{-1} = \frac{\Delta\omega}{2\sqrt{2}} \qquad \text{(Eq. 3.9)}$$

yields a Li^+ ion exchange rate on the timescale of $\tau^{-1} > 66$ s^{-1} (*i.e.*, (1.4-0.9) ppm × 59 · 10^6 × $\pi/\sqrt{2}$) occurring between Li1 and Li2. Additionally, the intensity of the resonance associated with Li3 has decreased at room temperature and indicates that some exchange is occurring between this octahedrally coordinated Li3 and the two tetrahedral Li1/Li2 sites at a rate of <203 s^{-1} (*i.e.*,

(1.0-(-0.55)) ppm × 59 · 10^6 × $\pi/\sqrt{2}$).

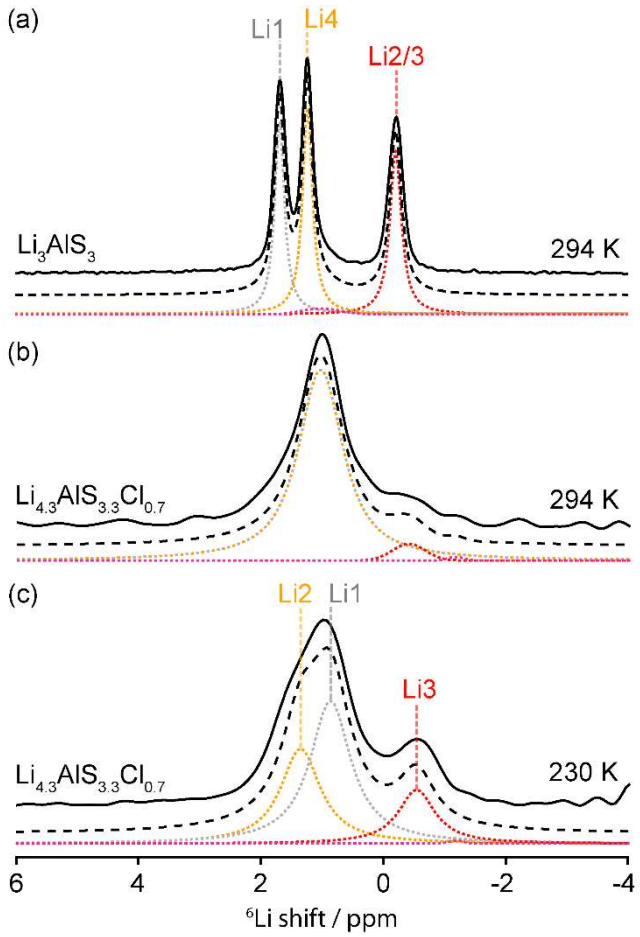

Figure 3.12 ^{6}Li MAS one pulse NMR spectra collected at 9.4 T and $\omega_r/2\pi$ = 10 kHz of (a) Li_3AlS_3 at 294 K, and $Li_{4.3}AlS_{3.3}Cl_{0.7}$ at (b) 294 K and (c) 230 K. The experimental spectra (full lines), total fit (dashed lines), spectral deconvolution of each Li1/Li2/Li3/Li4 signal (dotted lines), impurities Li_5AlS_4 in Li_3AlS_3 and solid LiCl in $Li_{4.3}AlS_{3.3}Cl_{0.7}$ as observed in the powder X-ray diffraction patterns (pink dotted line) and spectral assignments are shown. Room temperature data at 20 T for both phases are shown in **Figure 3.13** and have the same resolution.

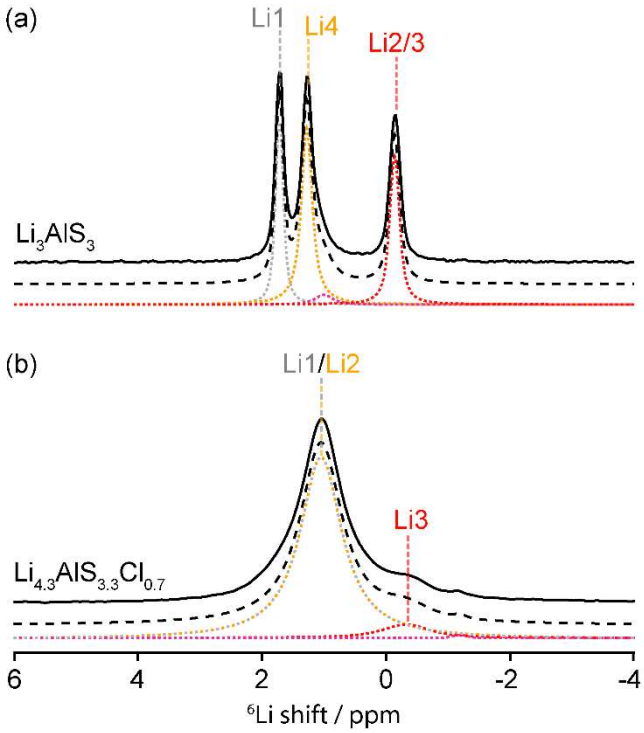

Figure 3.13 Room temperature ^{6}Li MAS one pulse NMR spectra collected at 20 T and $\omega_r/2\pi$ = 20 kHz of (a) Li_3AlS_3 and (b) $Li_{4.3}AlS_{3.3}Cl_{0.7}$. The experimental spectra (full lines), total fit (dashed lines), spectral deconvolution of each Li1/Li2/Li3/Li4 signals (dotted lines), impurities (Li_5AlS_4[40] in Li_3AlS_3 and solid LiCl[49] in $Li_{4.3}AlS_{3.3}Cl_{0.7}$ as per the powder X-ray-diffraction patterns in **Figure 3.15**, pink dotted lines) and spectral assignments are shown.

The room temperature ^{6}Li MAS spectra of the parent material reveals that the exchange between tetrahedral Li4 and octahedral Li2/3 in the mixed polyhedral layer is < 197 s^{-1} (*i.e.*, (1.3-(-0.2)) ppm × 59 · 10^6 × $\pi/\sqrt{2}$) while exchange between tetrahedral Li1 and Li4 is < 52 s^{-1} *(i.e.*, (1.7-1.3) ppm × 59 · 10^6 × $\pi/\sqrt{2}$). The upper bound of this exchange rate is lower compared to the ones in the halide substituted analogue at low temperatures and highlights increased mobility of ions exchanging between the two distinct layers in $Li_{4.3}AlS_{3.3}Cl_{0.7}$. **Figure 3.14** provides a summary of the various τ^{-1} extracted

and visualizes the interlayer Li-ion migration pathway superposed on to schematics of the crystal structures.

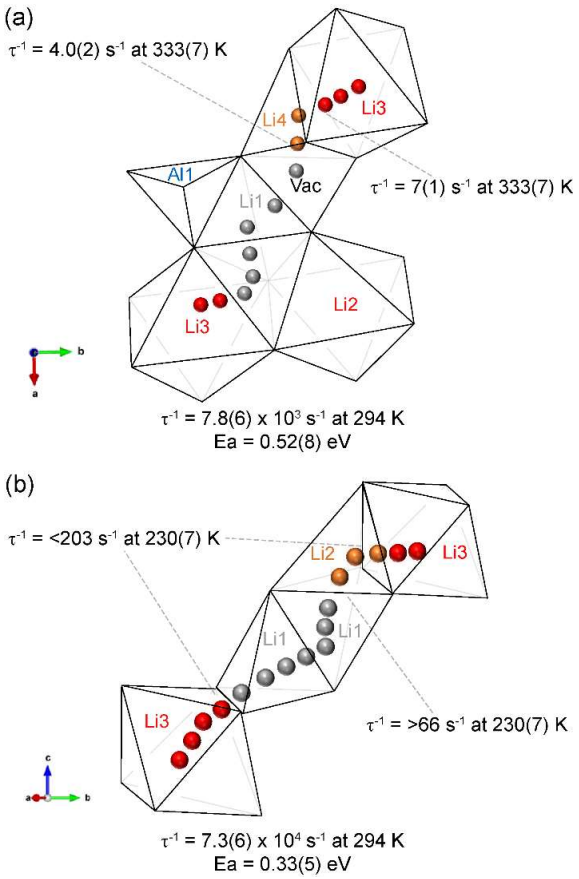

Figure 3.14 Visualization of the interlayer Li-ion migration pathway for (a) Li_3AlS_3 and (b) $Li_{4.3}AlS_{3.3}Cl_{0.7}$ showing a schematic of the polyhedral arrangement of both phases as well as the τ^{-1} values associated with the corresponding Li-ion jumps. These values are obtained from the magnetization build up of the 2D ^{6}Li-^{6}Li EXSY spectra (**Figure 3.16**) and line shape analysis of the variable temperature one pulse ^{6}Li NMR spectra (**Figure 3.12**) for Li_3AlS_3 and $Li_{4.3}AlS_{3.3}Cl_{0.7}$, respectively. Coloured spheres correspond to tetrahedral Li in the tetrahedral layer (grey), octahedral Li (red) and tetrahedral Li in the mixed polyhedral layer (orange), respectively. τ^{-1} values underneath the schematics are derived from the linear fits to the data points in **Figure 3.24** and correspond to average jump rate values across the entire sample. Activation energies quoted are taken from the linear fit of the

high temperature data in **Figure 3.22**.

3.5.6 ^{6}Li-^{6}Li EXSY NMR

Further insights into this pathway in Li_3AlS_3 were obtained from homonuclear ^{6}Li - ^{6}Li 2D EXSY spectra of ^{6}Li-enriched Li_3AlS_3 (XRD patterns shown in **Figure 3.15**) as a function of mixing time τ_m (**Figure 3.16(a-c)**) which exploit the high spectral resolution of the one-dimensional ^{6}Li MAS spectrum of this phase. Exchange is observed experimentally in the form of off-diagonal cross peaks in the 2D EXSY spectra at the corresponding shifts and start to emerge at around τ_m = 30 ms (**Figure 3.16(b)**) between all the sites of ^{6}Li enriched Li_3AlS_3. These cross peaks arise from either chemical exchange or spin diffusion from ^{6}Li - ^{6}Li homonuclear coupling (as the sample is 95% ^{6}Li enriched) at a rate that is governed by the rate of exchange occurring during τ_m (**Figure 3.17**). Site specific Li-ion correlation rates τ_c^{-1} (and jump rates τ^{-1}) can be extracted by fitting the relative intensities of diagonal (I_d) and cross peaks (I_c) as a function of τ_m to the following expression:[23]

$$\frac{I_c}{I_d} = 1 - \exp\left(\frac{\tau_m}{\tau_c}\right) \qquad \text{(Eq. 3.10)}$$

as shown in **Figure 3.16(d-f)** with the extracted Li^+ τ^{-1} values summarised in **Table 3.3**. Chemical exchange and spin diffusion processes can be differentiated by performing EXSY experiments at different MAS rates since faster MAS averages dipole-dipole interactions more efficiently and hence reduces spin diffusion. Faster cross peak build up rates are observed for Li2/3-Li4 and Li4-Li1 when increasing the MAS rate from 15 to 45 kHz (**Figures 3.16**

and **3.18, Table 3.3**), which rules out spin diffusion in favour of supporting chemical exchange and jumps between the magnetically inequivalent sites (note that the increased rates of cross peak build up are likely due to temperature increase from frictional heating). However, the opposite trend is observed for the Li1-Li2/3 cross peaks (*i.e.*, slower rate at a faster MAS frequency) and is evidence for spin-diffusion between these two sites. This is unsurprising as in order for Li-ions to exchange between these two sites a 3-step jump process is required along the Li1-tetrahedral vacancy-Li4-Li2/3 pathway, which would be less favoured than dipolar coupling driven spin diffusion between Li1 and Li2/3 (**Figure 3.14**).

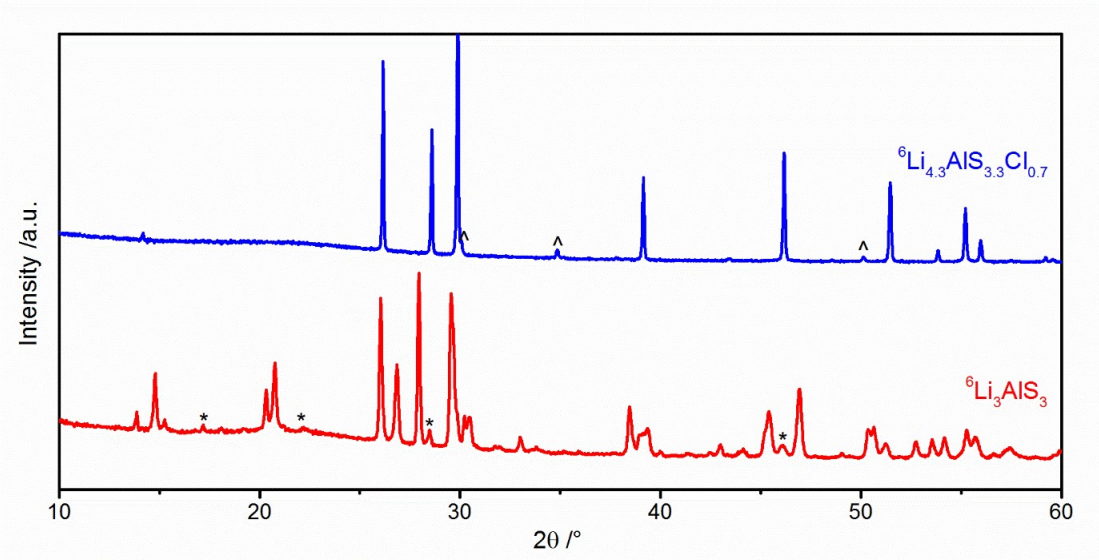

Figure 3.15 Laboratory XRD patterns of ^{6}Li enriched samples $^6Li_3AlS_3$ (red line) and $^6Li_{4.3}AlS_{3.3}Cl_{0.7}$ (blue line) obtained with λ = 1.5406 Å. The phases contain small amounts of impurities: Li_5AlS_4 for Li_3AlS_3 (*) and LiCl for $Li_{4.3}AlS_{3.3}Cl_{0.7}$ (^).

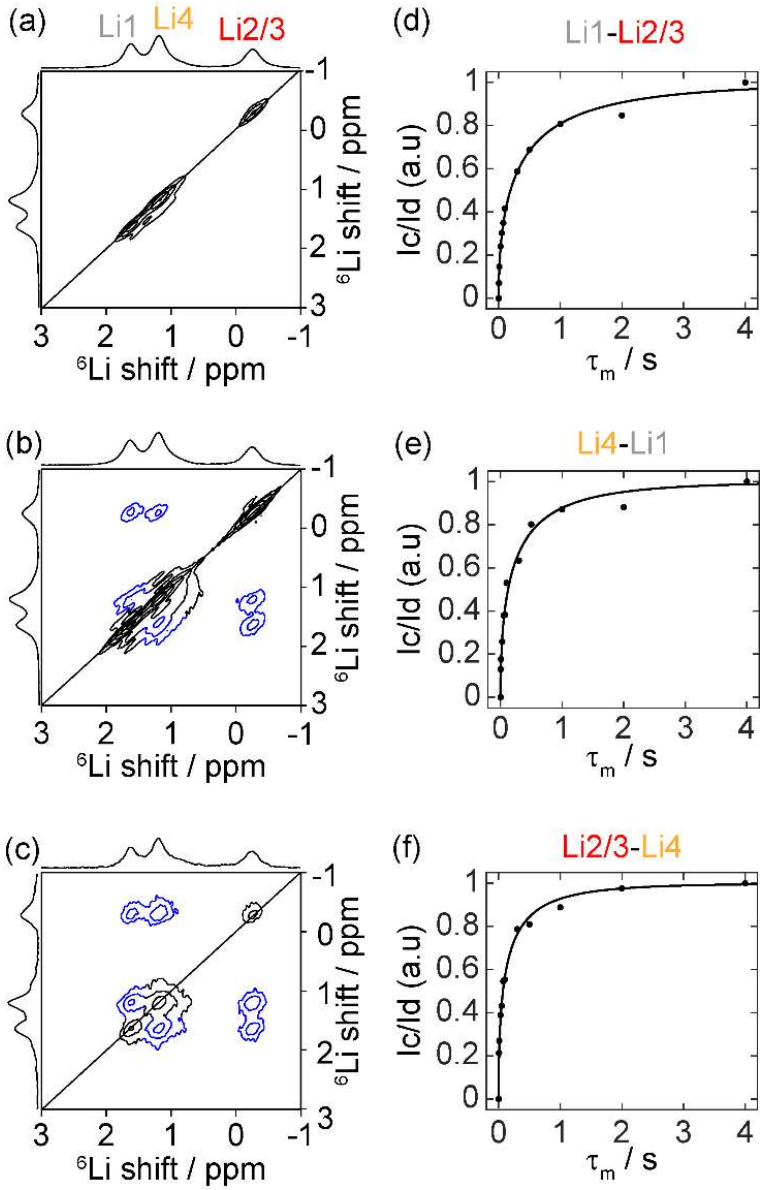

Figure 3.16 2D ^{6}Li-^{6}Li EXSY NMR spectra of ^{6}Li enriched Li_3AlS_3 recorded at $\omega_r/2\pi$ = 45 kHz and mixing times τ_m of (a) 0, (b) 0.03, and (c) 4 s with diagonal and cross peaks shown in black and blue, respectively. The solid black lines outline the position of the diagonal. 2D ^{6}Li-^{6}Li EXSY NMR spectra of ^{6}Li enriched $Li_{4.3}AlS_{3.3}Cl_{0.7}$ are available in **Figure 3.19**. (d-f) plots of the cross peak build up curves at $\omega_r/2\pi$ = 45 kHz. The solid lines show the accompanying fits to **equation 3.10**, where I_c and I_d are the intensities of the observed cross and diagonal peaks, respectively.

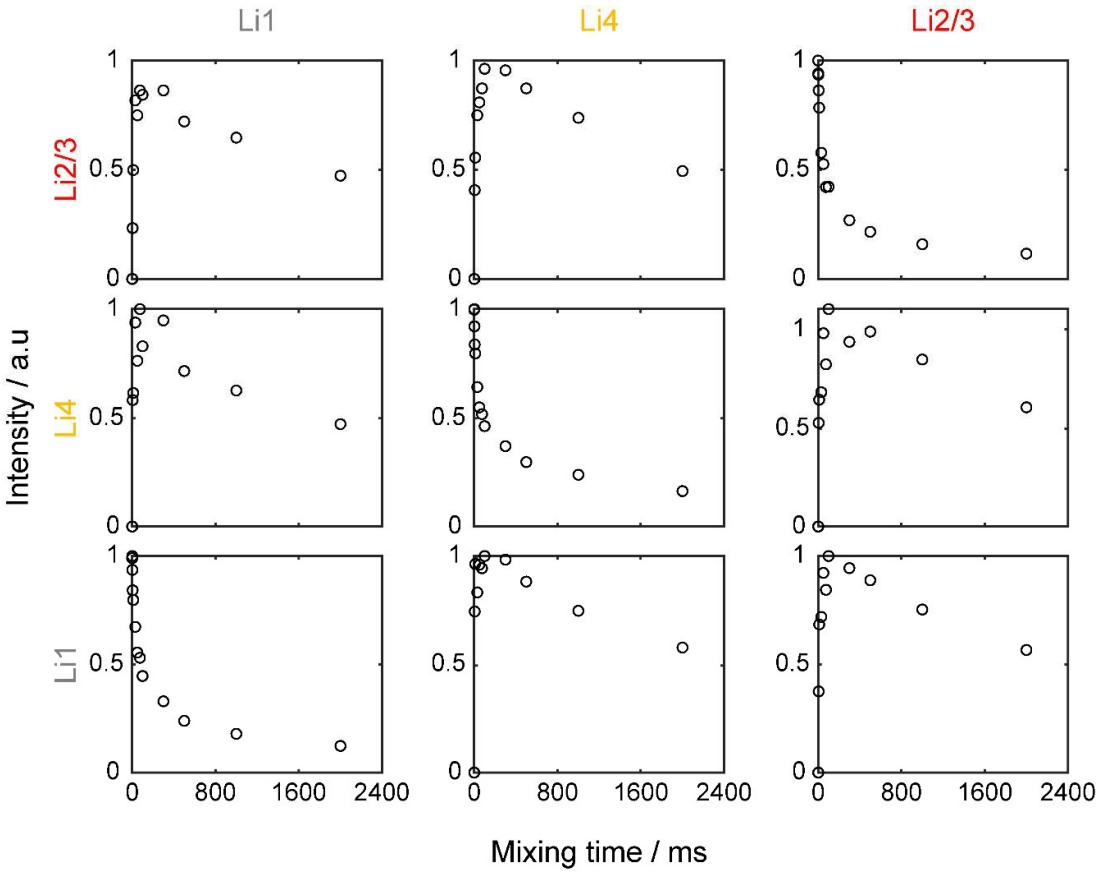

Figure 3.17 Intensity of the diagonal and cross-peaks in the ^{6}Li-^{6}Li EXSY NMR spectra of Li_3AlS_3 at $\omega_r/2\pi$ = 45 kHz as a function of the mixing time τ_m. The columns and rows are labelled on the left and the top according to the different resonances.

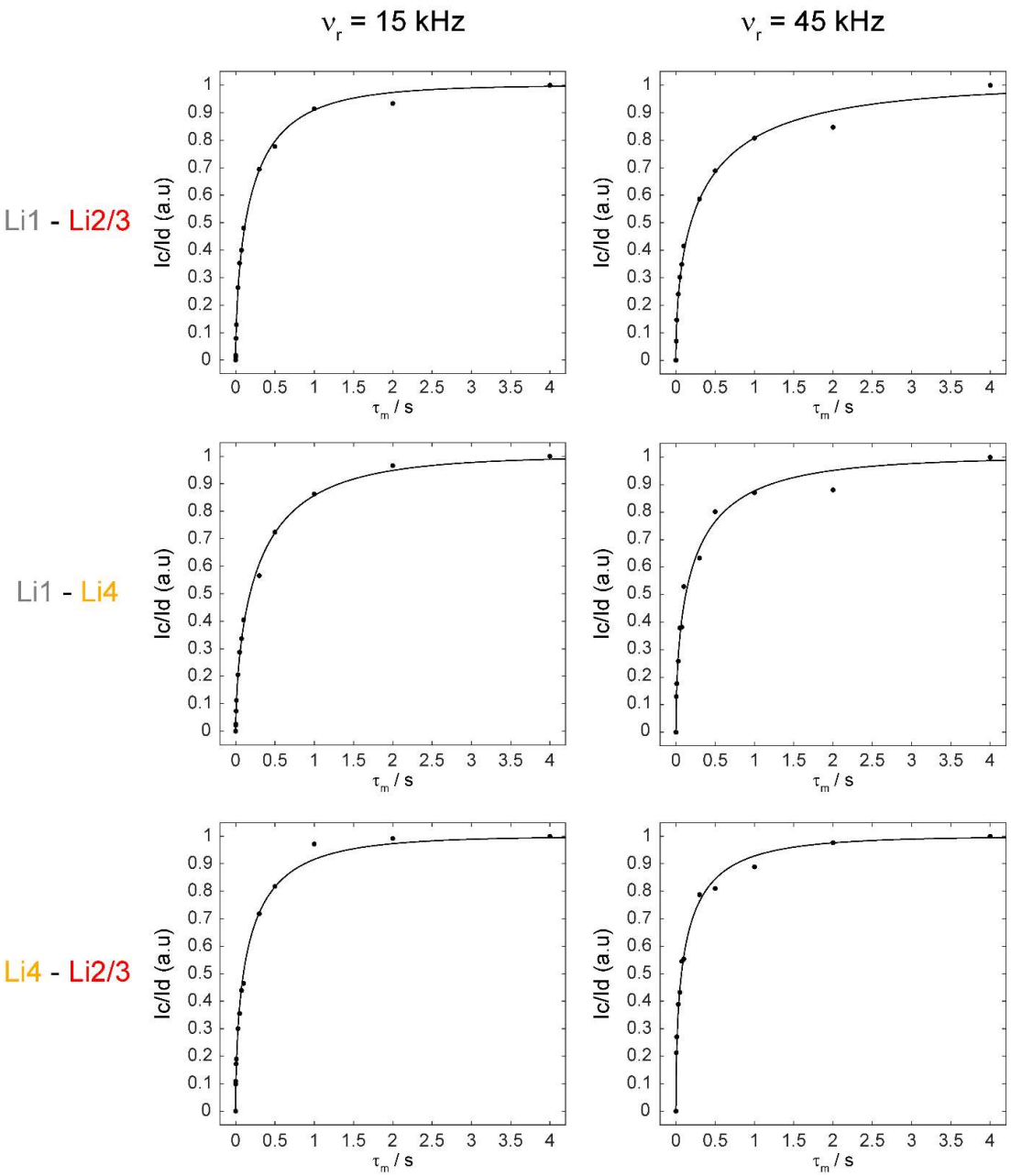

Figure 3.18 Plots of the ratio of the cross-peaks (Ic) *vs.* diagonal intensities (Id) in the ^{6}Li-^{6}Li EXSY NMR spectra of Li_3AlS_3 at MAS frequencies $\omega_r/2\pi$ = 15 (left) and 45 kHz (right) as a function of τ_m. The solid lines correspond to fits of the data according to **equation 3.10**.

Table 3.3 Site specific Li-ion jump rates τ^{-1} for Li_3AlS_3 extracted from ^6Li-^6Li EXSY data at two different MAS frequencies.

$\omega_r/2\pi$ / kHz	T / K	τ^{-1}/s^{-1}		
		Li1-Li2/3	Li2/3-Li4	Li4-Li1
15	309(5)	4.4(4)	5.2(6)	3.0(2)
45	333(7)	2.6(4)	7(1)	4.0(7)

The extracted τ^{-1} values clearly show the highest ion migration rates for inequivalent site exchange between Li2/3 and Li4 ($d_{Li2\text{-}Li4}$ = 4.49(8) Å, $d_{Li3\text{-}Li4}$ = 2.83(3) Å), which correspond to Li^+ mobility between the tetrahedral and octahedral sites in the mixed polyhedral layer occurring through a shared face. Note that due to the lack of resolution between Li2 and Li3 it is not possible to quantify the ion migration between these two octahedral sites in the mixed polyhedral layer that form chains running along the *c*-axis. Exchange also exists between the tetrahedral Li4 and Li1 ($d_{Li1\text{-}Li4}$ = 3.322(13) Å) in mixed polyhedral and tetrahedral layers, respectively, and occurs via a mutually shared face of a vacant tetrahedral site.

The lack of resolution observed in the room temperature ^6Li MAS spectrum of $Li_{4.3}AlS_{3.3}Cl_{0.7}$ between Li1 and Li2 sites due to motional averaging, coupled with the low intensity of the Li3 resonance discussed above, prevents access to τ^{-1} values from the 2D EXSY spectra. Nevertheless, these data provide supporting evidence for the assignment of the one-dimensional ^6Li MAS spectrum as cross peaks can be observed between the motionally averaged

Li1/L2 site at ~1 ppm and the octahedral Li3 site at ~ -0.3 ppm (**Figure 3.19**).

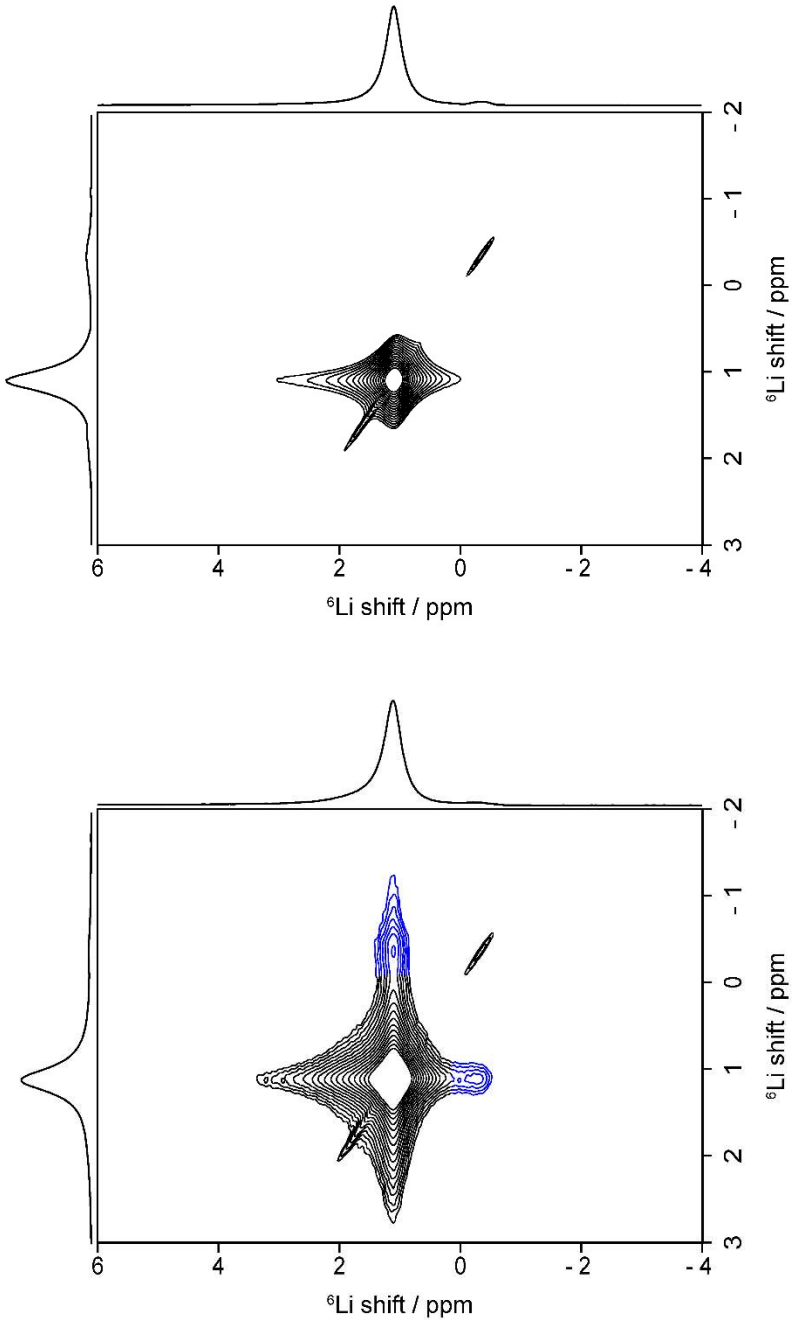

Figure 3.19 Examples of ^{6}Li-^{6}Li EXSY NMR spectra of ^{6}Li enriched $Li_{4.3}AlS_{3.3}Cl_{0.7}$ recorded at $\omega_r/2\pi$ = 45 kHz and τ_m of 0 (top) and 0.5 s (bottom) with diagonal and cross peaks shown in black and blue, respectively.

3.5.7 ^{7}Li relaxometry

SLR rate constants in the laboratory frame T_1^{-1} and the rotating frame $T_{1\rho}^{-1}$ were also obtained to provide further information on Li^+ dynamics on the MHz and kHz frequency scales, respectively. Relaxation is dependent on the random fluctuation of local magnetic fields caused by the motion of atoms or functional groups. These microscopic fluctuating fields are captured by the time-dependent correlation function G(t) that contains quantitative information on the diffusion process. τ_c describes the timescale of these fluctuations and, in the Bloembergen-Purcell-Pound (BPP) theory, the increased mobility of ^{7}Li nuclei with increasing temperatures is the primary factor affecting the reorientation of the local magnetic fields, the correlation function decays exponentially and follows the equation:

$$G(t) = G(0)\exp\left(-\frac{|t|}{\tau_c}\right) \qquad \text{(Eq. 3.11)}$$

where G(0) is the value of the correlation function at time t = 0, and is equal to the mean square of the local magnetic fields. Fourier transformation of G(t) gives the spectral density function $J(\omega_0)$ which quantifies the motion at the Larmor frequency ω_0:[53,54]

$$J(\omega_0) = G(0)\left(\frac{2\tau_c}{1+\omega_0^2\tau_c^2}\right) \qquad \text{(Eq. 3.12)}$$

where, in this work, changes in τ_c are solely induced by the diffusion and motion of the spins as the increased mobility of ^{7}Li nuclei with increasing temperature is the primary factor affecting the reorientation of the local

magnetic fields and hence temperature dependent and follow an Arrhenius relation of the type:

$$\tau_c^{-1} = \tau_{c,0}^{-1} \exp\left(-\frac{E_a}{k_B T}\right) \qquad \text{(Eq. 3.13)}$$

where $\tau_{c,0}^{-1}$ is the Arrhenius pre-exponential factor, T is the temperature and k_B is the Boltzmann constant. The temperature dependence of the ^{7}Li SLR rate constants under static conditions were collected and exploited to access the activation energy, conductivity and dimensionality of the Li diffusion processes.

In the case of Li_3AlS_3, the SLR T_1^{-1} build up rate was best fitted to a bi-exponential function (**Figure 3.20**) with slow and fast relaxing components $T_{1,slow}$ and $T_{1,fast}$, respectively. There are two possible explanations for this behaviour. Firstly, quadrupolar nuclei with spin 3/2 such as ^{7}Li will inherently relax bi-exponentially with a theoretical percentage contribution of 80% and 20% for the fast (satellite transition) and slow (central transition) relaxing contributions,[32-34] respectively. Therefore, it is possible that the superimposed lineshapes observed in the static ^{7}Li VT NMR (**Figure 3.8(a)**) may be due to quadrupolar satellite transitions. However, if this was the case the percentage contributions of $T_{1,slow}$ and $T_{1,fast}$ would be expected to remain fairly constant with temperature. In the case of Li_3AlS_3, the percentage contribution is 40% and 60% for $T_{1,slow}$ and $T_{1,fast}$, respectively, with the percentage contribution of $T_{1,slow}$ increasing to 50% as temperature increases. The second possibility is the presence of two batches of Li-ions with differing τ_c values, giving rise to two differing values of T_1. This explanation is supported by the two superimposed ^{7}Li lineshapes mentioned previously, as the double- and triple-

quantum filtration and Hahn-echo experiments (**Figure 3.11**) display two sets of quadrupolar satellite transitions, arising from the two differing batches of Li-ions. Therefore, we attribute the bi-exponentiality in Li_3AlS_3 to the presence of at least two batches of differing Li-ions, which are governed by the same relaxation process but with differing values of τ_c. In the case of $Li_{4.3}AlS_{3.3}Cl_{0.7}$, the T_1 build up was a mono-exponential as evidenced by the high stretch exponential factors α of around 0.9. Upon heating from room temperature to 490 K, the SLR T_1^{-1} rate constants for Li_3AlS_3 increase from 0.22(3) to 9.4(6) s^{-1} and from 1.0(3) to 28(3) s^{-1} for the slow and fast relaxing components, respectively, while heating $Li_{4.3}AlS_{3.3}Cl_{0.7}$ from 250 to 505 K results in a T_1^{-1} increase from 0.46(1) to 13.6(5) s^{-1} (**Figure 3.22**). Both materials largely follow an Arrhenius behaviour from which E_a barriers of 0.22(6) and 0.25(6) eV for the fast and slow components of T_1^{-1} in Li_3AlS_3 and 0.15(5) eV for $Li_{4.3}AlS_{3.3}Cl_{0.7}$ could be obtained and illustrate a significant difference between both phases. The increase in SLR T_1^{-1} rate constants with higher T imply data in the low temperature flank of the SLR rate constants, which are indicative of short-range motional processes, and demonstrate more energetically favourable short-range Li-ion diffusion in the more disordered Cl-doped phase.

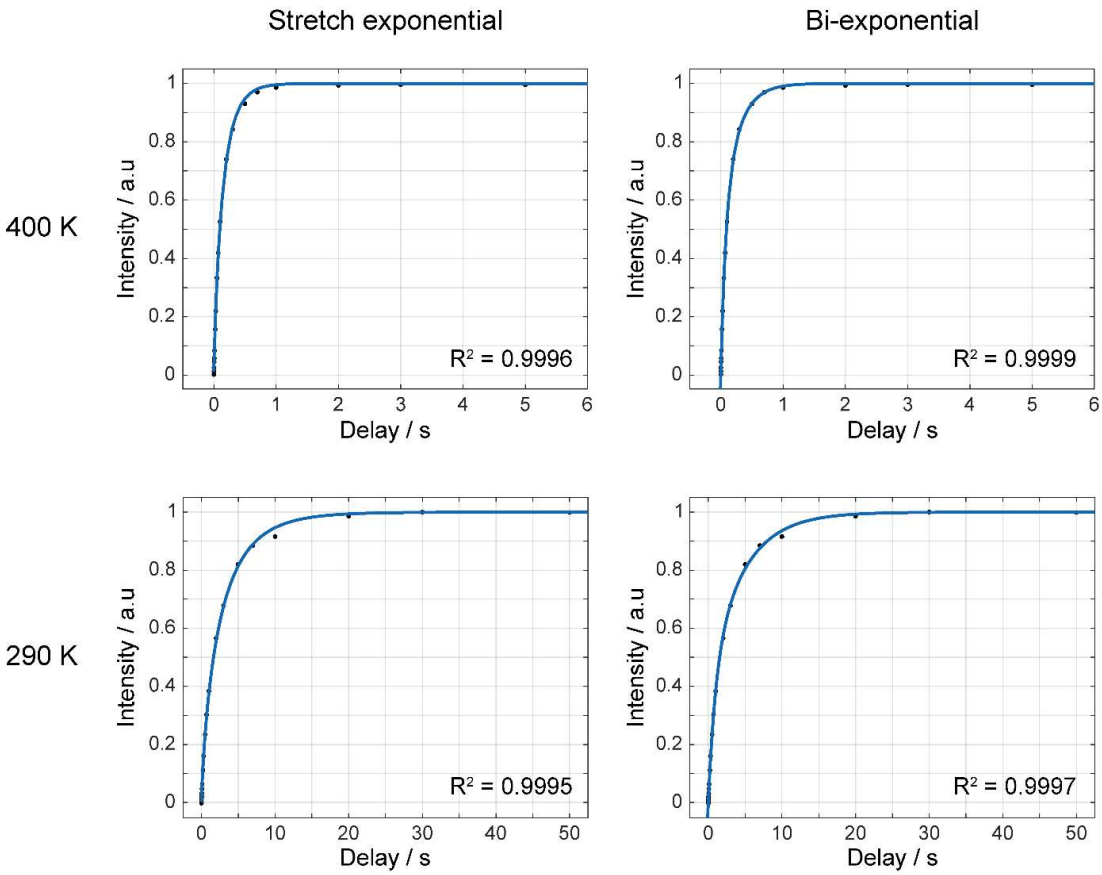

Figure 3.20 Comparison of methods to fit ^{7}Li T_1 build up curves of Li_3AlS_3 at representative temperatures of 290 and 400 K, where the data was fit with a stretch exponential of the form $1-\exp[-(\tau/T_1)^{\alpha}]$ (left) and a bi-exponential of the form $1-a\cdot\exp[-(\tau/T_{1,slow})]+b\cdot\exp[-(\tau/T_{1,fast})]$ (right). The goodness of fit (R^2 values) are given in the figure and illustrate slightly better fit in the case of a bi-exponential.

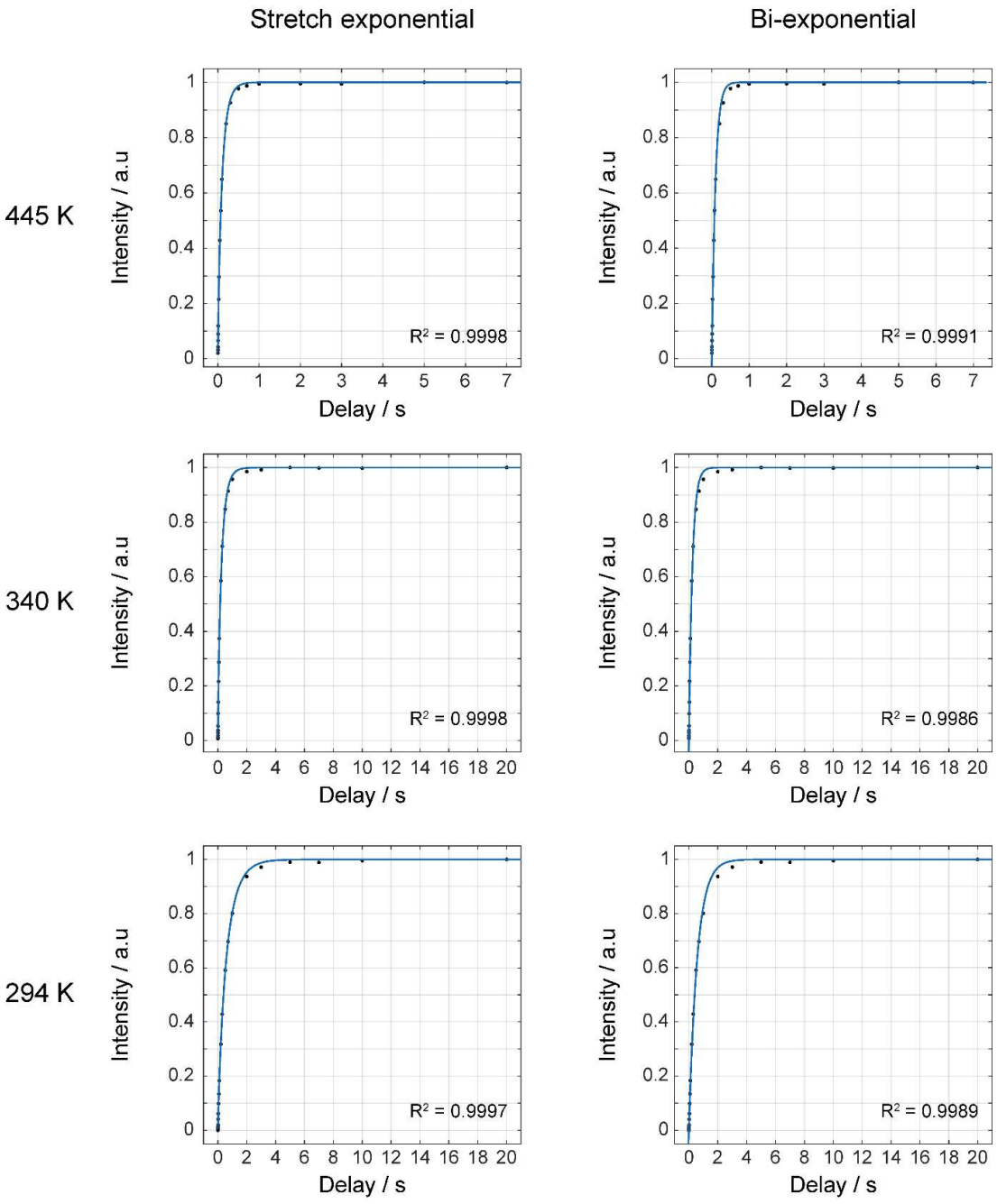

Figure 3.21 Comparison of methods to fit ^{7}Li T_1 build up curves of $Li_{4.3}AlS_{3.3}Cl_{0.7}$ at representative temperatures of 294, 340 and 445 K, where the data was fit with a stretch exponential of the form $1-\exp[-(\tau/T1)^{\alpha}]$ (left) and a bi-exponential of the form $1-a\cdot\exp[-(\tau/T_{1,slow})]+b\cdot\exp[-(\tau/T_{1,fast})]$ (right). The goodness of fit (R^2 values) are given in the figure and illustrate slightly better fit in the case of a stretch exponential.

The SLR $T_{1\rho}^{-1}$ data recorded at three different spin-lock frequencies $\omega_1/2\pi$ are given in **Figure 3.22** The rates initially increase with temperatures above room temperature (*i.e.*, low temperature flank) and activation barriers indicative of more accessible local Li^+ jump processes for $Li_{4.3}AlS_{3.3}Cl_{0.7}$ (E_a = 0.19(4) eV) than for Li_3AlS_3 (E_a = 0.42(8) eV) are extracted. Upon heating further, the SLR $T_{1\rho}^{-1}$ rate constants pass through maxima (in the 325-495 K temperature range) before decreasing (*i.e.*, high temperature flank) with activation barrier values for translational diffusion of 0.52(8) and 0.33(5) eV for Li_3AlS_3 and $Li_{4.3}AlS_{3.3}Cl_{0.7}$, respectively, indicating that long-range Li^+ diffusion is also more favourable in $Li_{4.3}AlS_{3.3}Cl_{0.7}$.

SLR $T_{1\rho}^{-1}$ rate constants at different frequencies provide information on the dimensionality of the Li^+ diffusion process and, for diffusion-induced rates in solids, the high temperature limits of the spectral density function $J(\omega_1)$ have the following frequency dependence to $(\tau_c/\omega_1)^{0.5}$, $\tau_c\ln(1/\omega_1\tau_c)$ and τ_c for one, two and three-dimensional diffusion processes, respectively.[21,22] Both Li_3AlS_3 and $Li_{4.3}AlS_{3.3}Cl_{0.7}$ materials show $T_{1\rho}^{-1}$ rate constants that are independent of the probe frequencies $\omega_1/2\pi$ (**Figure 3.22**), which is strong evidence for the presence of three-dimensional Li^+ mobility within both materials. This is an experimental validation of the computational prediction from ab initio molecular dynamics simulations and further evidence of the diffusion pathway revealed by the scattering density of the diffraction data, although via the direct detection of the Li^+ ions as they proceed along the determined pathway. It is therefore postulated that Li-ion mobility occurs both between the layers and within the layers, which is in agreement with the observation of cross peaks

for all Li sites in the ^{6}Li-^{6}Li EXSY spectra of Li_3AlS_3.

At the temperatures of the $T_{1\rho}^{-1}$ maxima, the Li^+ τ^{-1} values are on the order of the spin-lock probe frequency ω_1 and satisfy the following relationship:[50]

$$2\omega_1\tau_c \approx 1 \qquad \text{(Eq. 3.14)}$$

Li^+ τ^{-1} values in the order of 1.3×10^5 - 1.0×10^6 s^{-1} are therefore obtained in the 420-495 K and 325-380 K temperature range for Li_3AlS_3 and $Li_{4.3}AlS_{3.3}Cl_{0.7}$, which lower temperatures in the latter again demonstrate increased Li^+ mobility.

The SLR values can be further parameterized using the following expression to extract τ_c from T_1^{-1} rates:

$$\frac{1}{T_1} = K\left(\frac{\tau_c}{1+\omega_0^2\tau_c^2} + \frac{\tau_c}{1+4\omega_0^2\tau_c^2}\right) \qquad \text{(Eq. 3.15)}$$

and from $T_{1\rho}^{-1}$:

$$\frac{1}{T_{1\rho}} = K\left(\frac{3}{2}\frac{\tau_c}{1+4\omega_1^2\tau_c^2} + \frac{5}{2}\frac{\tau_c}{1+\omega_0^2\tau_c^2} + \frac{\tau_c}{1+4\omega_0^2\tau_c^2}\right) \qquad \text{(Eq. 3.16)}$$

where K is the local fluctuating magnetic field term in these expressions and depends on the relaxation mechanism.

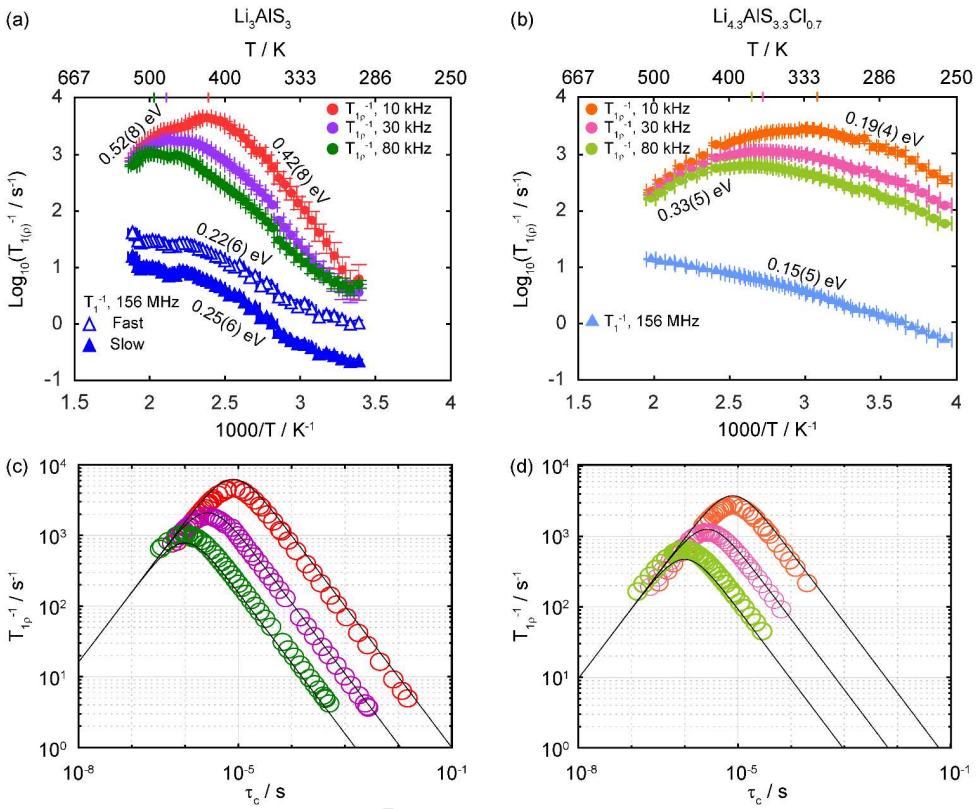

Figure 3.22 Arrhenius plots of ^{7}Li NMR SLR rate constants in the laboratory frame (T_1^{-1}) at $\omega_0/2\pi$ = 156 MHz and rotating frame ($T_{1\rho}^{-1}$) at $\omega_1/2\pi$ = 10, 30 and 80 kHz for (a) Li_3AlS_3, where the filled blue triangles and empty blue triangles are the T_1^{-1} SLR rate constants associated with the slow and fast components of the build up curves, respectively, and (b) $Li_{4.3}AlS_{3.3}Cl_{0.7}$. The coloured ticks on the temperature scale represent the position of $T_{1\rho}^{-1}$ maxima. ^{7}Li $T_{1\rho}^{-1}$ versus τ_c for (c) Li_3AlS_3 and (d) $Li_{4.3}AlS_{3.3}Cl_{0.7}$. Data were collected at spin-lock frequencies of $\omega_1/2\pi$ of 10 kHz (red and orange), 30 kHz (purple and pink) and 80 kHz (green and olive) and the solid lines are those obtained from **equation 3.16** using the experimentally determined local magnetic field fluctuation terms of 1.1(6) × 10^9 and 6.3(8) × 10^8 Hz^2 for Li_3AlS_3 and $Li_{4.3}AlS_{3.3}Cl_{0.7}$, respectively. Averaged values over the three $\omega_1/2\pi$ were used resulting in the slight offsets observed at high τ_c. ^{7}Li $T_{1\rho}^{-1}$ versus τ_c data for both phases for each $\omega_1/2\pi$ are given in **Figure 3.23** for clarity.

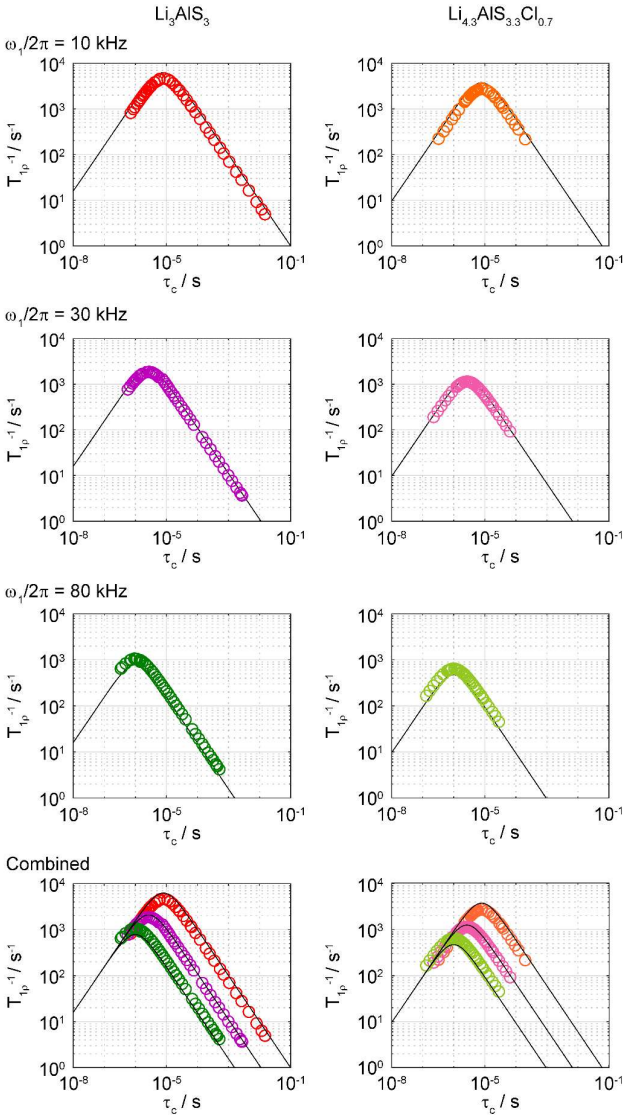

Figure 3.23 ^{7}Li $T_{1\rho}^{-1}$ versus τ_c for Li_3AlS_3 (left) and $Li_{4.3}AlS_{3.3}Cl_{0.7}$ (right). Data were collected at spin-lock frequencies of $\omega_1/2\pi$ of 10 kHz (red and orange), 30 kHz (purple and pink) and 80 kHz (green and olive) and the solid lines are those obtained from **equation 3.16** using the experimentally determined local field fluctuation terms of 1.1(6) x 10^9 and 6.3(8) x 10^8 Hz^2 for Li_3AlS_3 and $Li_{4.3}AlS_{3.3}Cl_{0.7}$ respectively. Averaged values over the three $\omega_1/2\pi$ were used resulting in the slight offsets observed at high τ_c.

For homonuclear dipolar relaxation involving spin 3/2 nuclei such as ^{7}Li, K is proportional to the square of the dipolar coupling constant and is given by:[55]

$$K = \frac{3}{2}\left(\frac{\mu_0}{4\pi}\right)^2 \frac{\gamma^4 \hbar^2}{r^6} \qquad \text{(Eq. 3.17)}$$

where μ_0 is the permeability of free space, $\hbar$ is the reduced Planck's constant, γ is the gyromagnetic ratio of the nuclear spins and r is the distance between the two nuclear spins, while for quadrupolar relaxation, K is proportional to the quadrupolar tensor parameters and expressed as:

$$K = \frac{1}{50} C_Q^2 \left(1 + \left(\frac{\eta_Q^2}{3}\right)\right) \qquad \text{(Eq. 3.18)}$$

where η_Q is the asymmetry parameter. Accessing τ_c from T_1^{-1} and $T_{1\rho}^{-1}$ data first requires a dominant relaxation mechanism to be postulated which for ^{6,7}Li NMR is best obtained from comparing ^{6}Li and ^{7}Li T_1 time constants under static conditions.[56]

Given the power law of 4 and quadratic dependencies of T_1^{-1} rate constants on γ and the quadrupolar moment Q in the dipolar and quadrupolar relaxation mechanisms, respectively, a ratio of

$$\frac{T_1(^7\mathrm{Li})}{T_1(^6\mathrm{Li})} \propto \frac{\gamma^4(^7\mathrm{Li})}{\gamma^2(^6\mathrm{Li})\gamma^2(^7\mathrm{Li})(^7\mathrm{Li})[(^6\mathrm{Li}) + \frac{3}{2}(^7\mathrm{Li})]} \sim 0.5 \qquad \text{(Eq. 3.19)}$$

is expected in the case of dipolar relaxation, while a ratio of

$$\frac{T_1(^7Li)}{T_1(^6Li)} \propto \frac{Q^2(^7Li)}{Q^2(^6Li)} \sim 3 \times 10^{-4} \qquad \text{(Eq. 3.20)}$$

is anticipated for a quadrupolar relaxation mechanism. Experimental $T_1(^7Li)/T_1(^6Li)$ ratios of 0.10(3) for Li_3AlS_3 and 0.48(8) for $Li_{4.3}AlS_{3.3}Cl_{0.7}$ were obtained at room temperature, which suggests that either cross relaxation mechanisms or a mixture of the two mechanisms contribute to the overall SLR for Li_3AlS_3 while dipolar relaxation mechanisms dominate for $Li_{4.3}AlS_{3.3}Cl_{0.7}$. The origin of this difference and of the cross relaxation may be due to a rather complex situation where the dominant relaxation mechanism changes between low and high temperatures or that the SLR rate constant measured correspond to an average across the whole sample. Therefore, it is possible that the slow and fast moving ions observed in **Figure 3.8(a)** for Li_3AlS_3 may have these different relaxation mechanisms, as previously observed in other systems.[57,58] Additionally, the presence of ^{27}Al (a 100% abundant spin 5/2 nucleus) in close proximity with lithium ions may introduce additional heteronuclear dipolar coupling and dipolar-quadrupolar cross relaxation terms.

At the ^7Li $T_{1\rho}^{-1}$ maxima, substituting **equation 3.14** into **equation 3.16** enables experimental determination of the local fluctuating magnetic field term K. A value of 1.1(6) × 10^9 Hz^2 (averaged over the three consistent values of K for the three different $\omega_1/2\pi$ frequencies used) was extracted for Li_3AlS_3 and lies between the calculated K terms for the dipolar (2 × 10^7 Hz^2 using **equation 3.17** and the closest Li−Li jump distance of 3.3 Å at room temperature for Li_3AlS_3 based on the crystal structure) and quadrupolar (4 × 10^9 Hz^2, **equation 3.17**) relaxation mechanisms as one would expect for cross relaxation. In

$Li_{4.3}AlS_{3.3}Cl_{0.7}$, the experimental (averaged) K value is 6.3(8) × 10^8 Hz^2 compares favourably with the dipolar dominated relaxation value of 5 × 10^7 Hz^2 (using a static 2.4 Å Li−Li jump distance for $Li_{4.3}AlS_{3.3}Cl_{0.7}$). These experimentally determined K values are then used to convert experimental $T_{1\rho}^{-1}$ values to τ_c estimates at each temperature using **equation 3.16** (**Figure 3.23**) and allows access to τ_c and NMR-derived jump rates τ^{-1} at all temperatures (**Figure 3.24**).

3.5.8 NMR-derived Li^+ ion τ^{-1} values

NMR-derived jump rates τ^{-1} obtained from NMR line narrowing experiments (**Figure 3.8**), EXSYs (**Figure 3.16**) and relaxometry experiments (**Figure 3.22**) are plotted against reciprocal temperature in **Figure 3.24** for $\omega_1/2\pi$ = 30 kHz (data for $\omega_1/2\pi$ = 10 and 80 kHz are given in **Figures 3.25** and **3.26**, respectively). Overall, Li-ion jump rates τ^{-1} are significantly lower for Li_3AlS_3 than $Li_{4.3}AlS_{3.3}Cl_{0.7}$ and reinforce the increased Li-ion mobility in the latter phase as revealed from the known EIS impedance data.[1,2] For both phases, there is an excellent agreement between τ^{-1} obtained from ^7Li line narrowing spectra and relaxometry data, and fitting those to an Arrhenius equation yields activation barriers of 0.29 (0.21-0.41) and 0.29 (0.25-0.37) eV for Li_3AlS_3 and $Li_{4.3}AlS_{3.3}Cl_{0.7}$, respectively. The values of the activation energies here are lower than the previously reported values from bulk conductivity observed by EIS (0.48(1) and 0.33(1) eV) which is a common experimental observation[59-62] due to the largely different approaches used where NMR spectroscopy determines the activation barrier for Li-ion mobility to neighbouring sites over

a much shorter length scale, whereas impedance measurements probe longer range translational Li diffusion. Additionally, NMR also accesses unsuccessful Li-ion hops which is likely prevalent in Li_3AlS_3 and $Li_{4.3}AlS_{3.3}Cl_{0.7}$ as the Li^+ sites are partially occupied. While the same activation energy is extracted from **Figure 3.24** for both phases, the errors are particularly large due to the combination of various methods used. Hence, the energy barriers obtained from ^7Li line narrowing and SLR experiments are likely to be more informative. A summary of the activation energies obtained via the various spectroscopic methods is available in **Table 3.4**.

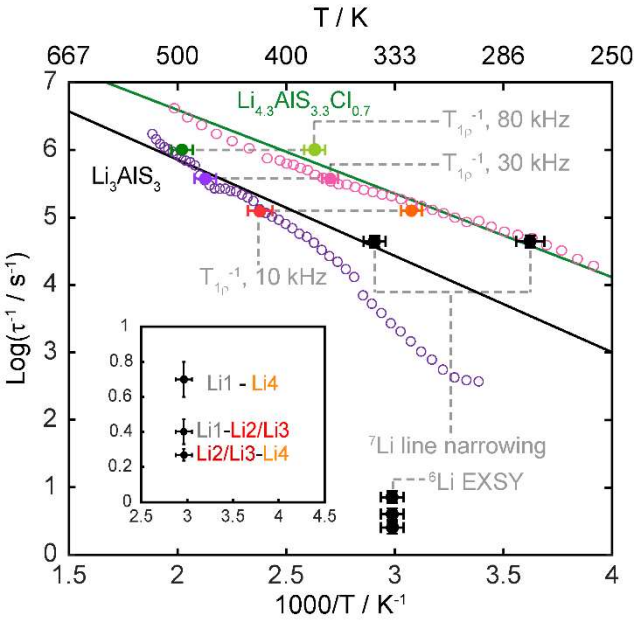

Figure 2.24 Arrhenius plot of Li-ion jump rates τ^{-1} extracted from ^{7}Li linewidth, 2D ^{6}Li-^{6}Li EXSY experiments and ^{7}Li SLR $T_{1\rho}^{-1}$ rate constants. Purple and pink open circles are data points from ^{7}Li SLR $T_{1\rho}^{-1}$ rate constants at $\omega_1/2\pi$ = 30 kHz for Li_3AlS_3 and $Li_{4.3}AlS_{3.3}Cl_{0.7}$, respectively. Red/orange (for Li_3AlS_3) and green/olive (for $Li_{4.3}AlS_{3.3}Cl_{0.7}$) are τ^{-1} extracted from ^{7}Li SLR $T_{1\rho}^{-1}$ maxima at $\omega_1/2\pi$ = 10 and 80 kHz, respectively. The complete datasets at these frequencies have been omitted for clarity and can be found in **Figures 3.25** and **3.26**. Solid lines correspond to the fits to **equation 3.13** for the experimentally determined SLR $T_{1\rho}^{-1}$ maxima and the value of τ^{-1} extracted from ^{7}Li linewidth experiments for Li_3AlS_3 (black) and $Li_{4.3}AlS_{3.3}Cl_{0.7}$ (green). The inset demonstrates a magnified view of the region at which τ^{-1} values extracted from 2D ^{6}Li-^{6}Li EXSY experiments of Li_3AlS_3 reside.

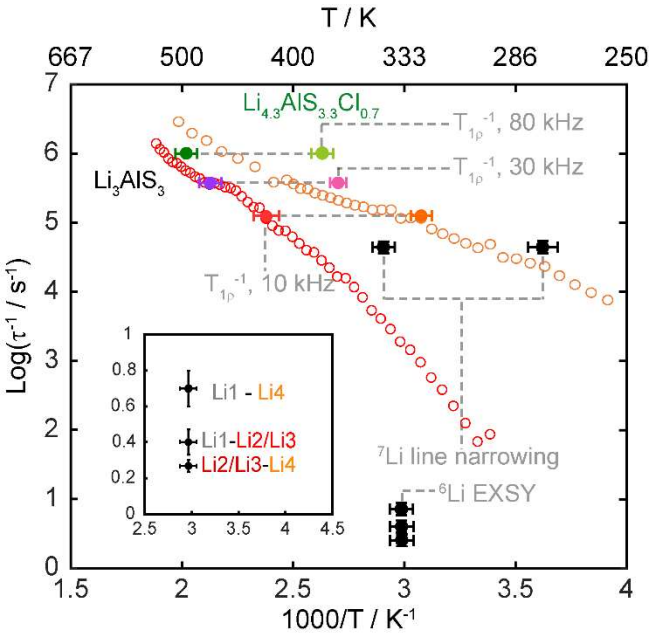

Figure 2.25 Arrhenius plot of Li-ion jump rates extracted from ^{7}Li linewidth, ^{7}Li SLR in the rotating frame and 2D ^{6}Li-^{6}Li EXSY experiments and Bloembergen-Purcell-Pound (BPP) simulations red and orange open circles (10 kHz), for Li_3AlS_3 and $Li_{4.3}AlS_{3.3}Cl_{0.7}$, respectively. Solid lines correspond to the fits to **equation 3.13** for the experimentally determined SLR $T_{1\rho}^{-1}$ maxima and the value of τ^{-1} extracted from ^{7}Li linewidth experiments for Li_3AlS_3 (black) and $Li_{4.3}AlS_{3.3}Cl_{0.7}$ (green). The inset demonstrates a magnified view of the region at which τ^{-1} values extracted from 2D ^{6}Li-^{6}Li EXSY experiments of Li_3AlS_3 reside.

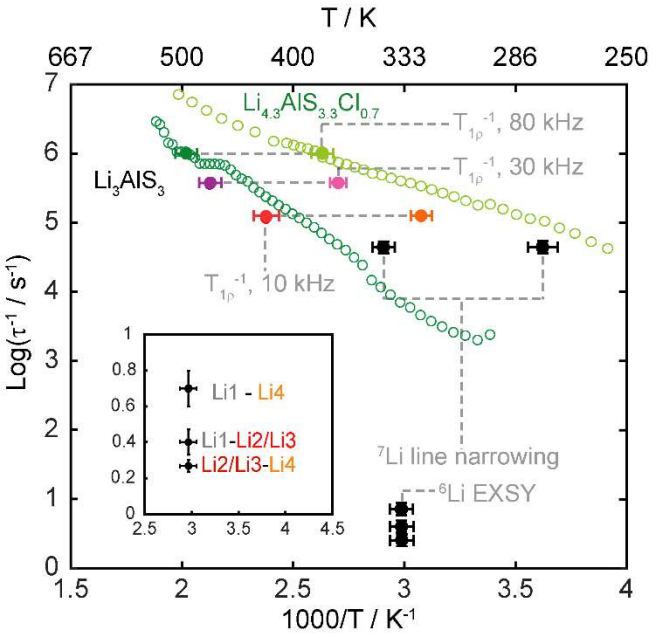

Figure 2.26 Arrhenius plot of Li-ion jump rates extracted from ^{7}Li linewidth, ^{7}Li SLR in the rotating frame and 2D ^{6}Li-^{6}Li EXSY experiments and BPP simulations green and olive open circles (80 kHz), for Li_3AlS_3 and $Li_{4.3}AlS_{3.3}Cl_{0.7}$, respectively. Solid lines correspond to the fits to **equation 3.13** for the experimentally determined SLR $T_{1\rho}^{-1}$ maxima and the value of τ^{-1} extracted from ^{7}Li linewidth experiments for Li_3AlS_3 (black) and $Li_{4.3}AlS_{3.3}Cl_{0.7}$ (green). The inset demonstrates a magnified view of the region at which τ^{-1} values extracted from 2D ^{6}Li-^{6}Li EXSY experiments of Li_3AlS_3 reside.

Table 3.4 Summary of the activation energies for Li_3AlS_3 and $Li_{4.3}AlS_{3.3}Cl_{0.7}$ extracted from electrical impedance spectroscopy (EIS),[1,2] ^7Li motional narrowing[52] from **Figure 3.8**, spin-lattice relaxation data in the laboratory frame (T_1) and the rotating frame ($T_{1\rho}$) from **Figure 3.22**. Activation energies on both the high and low temperature flanks are quoted as well as the activation energy obtained from the jump rate plot (**Figure 3.24**).

Sample	Activation Energy /eV					
	EIS	Waugh-Fedin	T_1	$T_{1\rho,LT}$	$T_{1\rho,HT}$	Jump rate
Li_3AlS_3	0.48(1)	~0.5	0.32(6)	0.42(8)	0.52(8)	0.29 (0.15-0.41)
$Li_{4.3}AlS_{3.3}Cl_{0.7}$	0.33(1)	~0.4	0.15(5)	0.19(4)	0.33(5)	0.29 (0.25-0.37)

The Li_3AlS_3 τ^{-1} values obtained from the EXSYs are notably lower than those extracted from the other approaches used. This is attributed to site-specific diffusion processes captured by the EXSY experiments compared to the information averaged across all Li sites only accessible from ^7Li line narrowing and SLR measurements. The two components of the static ^7Li NMR lineshape observed in line narrowing experiments of Li_3AlS_3 can therefore be attributed to slow moving ions ($\tau^{-1} << \omega/2\pi$, broad component in ^7Li static NMR spectra) associated with non-equivalent site exchange occurring between the layers ($d_{Li1-Li2}$ = 4.07(13) Å, $d_{Li1-Li3}$ = 3.12(3) Å, $d_{Li1-Li4}$ = 3.322(13) Å) and between tetrahedral Li4 and octahedral Li2/3 sites in the mixed polyhedral layer ($d_{Li2-Li4}$ = 4.49(8) Å, $d_{Li3-Li4}$ = 2.83(3) Å), while the fast moving ions ($\tau^{-1} >> \omega/2\pi$, narrow component) can be assigned to exchange occurring within the layers

themselves along the *c*-axis between equivalent sites. Since the ion mobility mechanism is three-dimensional, migration between the layers is crucial for long range translational diffusion since it connects the different diffusion channels along the *c*-axis so as to avoid any blockages that may occur in the diffusion pathways. We note that the calculated τ^{-1} values for Li_3AlS_3 derived from BPP theory, deviate from the expected trend observed from the experimentally determined τ^{-1} (through ^{7}Li line narrowing and $T_{1\rho}^{-1}$ maxima) at low temperatures. A possible explanation for this observation is that since the Li-ion τ^{-1} for the various different sites in Li_3AlS_3 are expected to differ, it seems that the dependence of τ^{-1} on the temperature should also differ for the different sites. Additionally, it is possible that there is a significant number of unsuccessful Li-ion jumps given that ion mobility between non-equivalent sites is limited. The large distribution of Li-ion τ^{-1} values, originating from both fast and slow Li-ion mobility, likely results in a complex relaxation profile that deviates from the single τ^{-1} approach in the BPP model used and the potential use of other models such as the Cole-Cole,[33] Cole-Davidson[34] or a related model[63] could potentially further rationalise this behaviour. However, these models are used in order to account for a distribution of τ_c values across various sites and pathways, while in the case of Li_3AlS_3 we are probing one Li-ion pathway with two largely different τ_c values. Moreover, in this work we are interested in comparing the diffusion pathways in Li_3AlS_3 and $Li_{4.3}AlS_{3.3}Cl_{0.7}$, two closely related phases with connected chemistries, we have chosen to exploit the BPP model as the relaxation behaviour of $Li_{4.3}AlS_{3.3}Cl_{0.7}$ is close to being mono exponential.

τ^{-1} can then be used to derive conductivities σ_{NMR} from NMR data using the combined Nernst−Einstein and Einstein−Smoluchowski equations:

$$\sigma = \frac{f}{H_R}\frac{N_{cc}q^2r^2}{N_{NN}k_BT}\frac{1}{\tau} \qquad \text{(Eq. 3.21)}$$

where f and H_R are the correlation factor and Haven ratio respectively (f/H_R is assumed to be smaller than 1 for correlated motion as per our previous ab initio calculations on $Li_{4.3}AlS_{3.3}Cl_{0.7}$[2]), N_{CC} is the number of charge carriers per unit cell volume (based on unit cell volumes obtained from diffraction of 1014 $Å^3$ for Li_3AlS_3[1] and 83.5 $Å^3$ for $Li_{4.3}AlS_{3.3}Cl_{0.7}$[2]), q is the ionic charge of Li, r is the closest Li−Li jump distance as given above and N_{NN} is the number of neighbouring Li sites (6 for the three-dimensional diffusion here). Obtaining f and H_R is beyond the scope of this work as exemplified for the extremely well studied Li garnet,[64] and we have therefore chosen to provide the upper boundary of the extrapolated conductivity values. At 303 K, these are 4(3) × 10^{-8} and 3(2) × 10^{-6} S cm^{-1} for Li_3AlS_3 and $Li_{4.3}AlS_{3.3}Cl_{0.7}$, respectively, which are in cautious agreement with the values determined by EIS (10^{-9} and 10^{-6} S cm^{-1} for Li_3AlS_3[1] and $Li_{4.3}AlS_{3.3}Cl_{0.7}$,[2] respectively).

3.6 Conclusions and Outlook

In this chapter the identification and characterisation of both the structure and ion dynamics in two new aluminium sulfide materials have been reported. The local structures of the two materials were characterised using ^{6}Li and ^{27}Al NMR (with the long range order having been analysed via synchrotron X-ray diffraction and neutron powder diffraction by Jacinthe Gamon). We employed a range of advanced NMR approaches focusing on both ^{6}Li and ^{7}Li nuclear spins to capture the Li^{+} dynamics of two newly discovered Li-containing materials, Li_3AlS_3 and $Li_{4.3}AlS_{3.3}Cl_{0.7}$. In the parent Li_3AlS_3 phase, the two component lineshapes of the ^{7}Li static NMR spectra demonstrate the existence of fast and slow-moving Li^{+}. The slow-moving ions were identified to diffuse between non-equivalent sites and are located between the two distinct tetrahedral and mixed polyhedral layers of the material, as captured by 2D ^{6}Li-^{6}Li EXSY spectra on ^{6}Li enriched Li_3AlS_3. In $Li_{4.3}AlS_{3.3}Cl_{0.7}$, the single component observed in the static ^{7}Li NMR spectra and the absence of the broad component contribution to the ^{7}Li lineshape indicate that the exchange of Li-ions between the layers facilitates an overall increase in conductivity, as confirmed by the NMR-derived conductivities, and is associated with accelerated Li^{+} diffusion of the immobile ions of the parent Li_3AlS_3 material. This arises from the introduction of disordered octahedral lithium vacancies in the mixed polyhedral layer of $Li_{4.3}AlS_{3.3}Cl_{0.7}$ that opens up Li-ion diffusion pathways not available by the presence of ordered vacancies in the tetrahedral layer of Li_3AlS_3. The frequency dependence of the SLR rate constants provides direct experimental evidence of the three-dimensional Li^{+} diffusion

previously proposed. This dimensionality is, therefore, an important factor to increase ion mobility by accelerating ion exchange between layers to avoid any bottlenecks that occur via faster diffusion pathways along the *c*-axis for Li_3AlS_3 and the *ab* plane for $Li_{4.3}AlS_{3.3}Cl_{0.7}$. Overall, this work illustrates the importance of ^6Li and ^7Li NMR data in accessing dynamics to understand Li-ion mobility pathways in structures that are structurally related by order/disorder.

3.7 References

1. Gamon, J.; Duff, B. B.; Dyer, M. S.; Collins, C.; Daniels, L. M.; Surta, T. W.; Sharp, P. M.; Gaultois, M. W.; Blanc, F.; Claridge, J. B.; Rosseinsky, M. J., Computationally Guided Discovery of the Sulfide Li_3AlS_3 in the Li–Al–S Phase Field: Structure and Lithium Conductivity. *Chemistry of Materials* **2019,** *31* (23), 9699.

2. Gamon, J.; Dyer, M. S.; Duff, B. B.; Vasylenko, A.; Daniels, L. M.; Zanella, M.; Gaultois, M. W.; Blanc, F.; Claridge, J. B.; Rosseinsky, M. J., $Li_{4.3}AlS_{3.3}Cl_{0.7}$: A Sulfide-Chloride Lithium Ion Conductor with Highly Disordered Structure and Increased Conductivity. *Chemistry of Materials* **2021,** *33* (22), 8733.

3. Duff, B. B.; Elliott, S. J.; Gamon, J.; Daniels, L. M.; Rosseinsky, M. J.; Blanc, F., Toward Understanding of the Li-Ion Migration Pathways in the Lithium Aluminum Sulfides Li_3AlS_3 and $Li_{4.3}AlS_{3.3}Cl_{0.7}$ via $^{6,7}Li$ Solid-State Nuclear Magnetic Resonance Spectroscopy. *Chemistry of Materials* **2023,** *35* (1), 27.

4. Hanghofer, I.; Brinek, M.; Eisbacher, S. L.; Bitschnau, B.; Volck, M.; Hennige, V.; Hanzu, I.; Rettenwander, D.; Wilkening, H. M. R., Substitutional disorder: structure and ion dynamics of the argyrodites Li_6PS_5Cl, Li_6PS_5Br and Li_6PS_5I. *Phys. Chem. Chem. Phys* **2019,** *21*, 8489.

5. Leube, B. T.; Inglis, K. K.; Carrington, E. J.; Sharp, P. M.; Shin, J. F.; Neale, A. R.; Manning, T. D.; Pitcher, M. J.; Hardwick, L. J.; Dyer, M. S.; Blanc, F.; Claridge, J. B.; Rosseinsky, M. J., Lithium Transport in $Li_{4.4}M_{0.4}M'_{0.6}S_4$ (M = Al^{3+}, Ga^{3+}, and M ′ = Ge^{4+}, Sn^{4+}): Combined Crystallographic, Conductivity, Solid State NMR, and Computational Studies. *Chemistry of Materials* **2018,** *30* (20), 7183.

6. Lau, J.; DeBlock, R. H.; Butts, D. M.; Ashby, D. S.; Choi, C. S.; Dunn, B. S., Sulfide Solid Electrolytes for Lithium Battery Applications. *Advanced Energy Materials* **2018,** *8* (27), 1800933.

7. Kato, Y.; Hori, S.; Saito, T.; Suzuki, K.; Hirayama, M.; Mitsui, A.; Yonemura, M.; Iba, H.; Kanno, R., High-power all-solid-state batteries using sulfide superionic conductors. *Nature Energy* **2016,** *1* (4).

8. Chang, B. Y.; Park, S. M., Electrochemical Impedance Spectroscopy. *Annual Review of Analytical Chemistry* **2010,** *3* (1), 207.

9. Minafra, N.; Kraft, M. A.; Bernges, T.; Li, C.; Schlem, R.; Morgan, B. J.; Zeier, W. G., Local Charge Inhomogeneity and Lithium Distribution in the Superionic Argyrodites Li_6PS_5X (X = Cl, Br, I). *Inorganic Chemistry* **2020,** *59* (15), 11009.

10. Ashbrook, S. E. D. D.; Griffin, J., *Local Structure Characterisation*. John Wiley & Sons Ltd, Ed.: 2013; p 1.

11. O'Dell, L. A.; Ratcliffe, C. I., Quadrupolar NMR to Investigate Dynamics in Solid Materials. *eMagRes* **1996**, 1.

12. McClelland, I.; Johnston, B.; Baker, P. J.; Amores, M.; Cussen, E. J.; Corr, S. A., Muon Spectroscopy for Investigating Diffusion in Energy Storage Materials. *Annual Review of Materials Research* **2020,** *50*, 371.

13. Böhmer, R.; Jeffrey, K. R. R.; Vogel, M., Solid-state Li NMR with applications to the translational dynamics in ion conductors. *Progress in Nuclear Magnetic Resonance Spectroscopy* **2007,** *50* (2-3), 87.

14. Vinod Chandran, C.; Heitjans, P., Solid-State NMR Studies of Lithium Ion Dynamics Across Materials Classes. *Annual Reports on NMR Spectroscopy* **2016,** *89*, 1.

15. Munoz, S.; Greenbaum, S., Review of Recent Nuclear Magnetic Resonance Studies of Ion Transport in Polymer Electrolytes. *Membranes* **2018,** *8* (4), 120.

16. Morales, D. J.; Greenbaum, S., NMR Investigations of Crystalline and Glassy Solid Electrolytes for Lithium Batteries: A Brief Review. *International Journal of Molecular Sciences* **2020,** *21* (9), 3402.

17. Foran, G.; Verdier, N.; Lepage, D.; Malveau, C.; Dupré, N.; Dollé, M., Use of Solid-State NMR Spectroscopy for the Characterization of Molecular Structure and Dynamics in Solid Polymer and Hybrid Electrolytes. *Polymers* **2021,** *13* (8), 1207.

18. Epp, V.; Gün, Ö.; Deiseroth, H. J.; Wilkening, M., Long-range Li+ dynamics in the lithium argyrodite Li_7PSe_6 as probed by rotating-frame spin–lattice relaxation NMR. *Physical Chemistry Chemical Physics* **2013,** *15* (19), 7123.

19. Gombotz, M.; Rettenwander, D.; Wilkening, H. M. R., Lithium-Ion Transport in Nanocrystalline Spinel-Type $Li[In_xLi_y]Br_4$ as Seen by Conductivity Spectroscopy and NMR. *Frontiers in Chemistry* **2020,** *8*, 100.

20. Hogrefe, K.; Minafra, N.; Zeier, W. G.; Wilkening, H. M. R., Tracking Ions the Direct Way: Long-Range Li+ Dynamics in the Thio-LISICON Family Li_4MCh_4 (M = Sn, Ge; Ch = S, Se) as Probed by ^7Li NMR Relaxometry and ^7Li Spin-Alignment Echo NMR. *Journal of Physical Chemistry C* **2021,** *125* (4), 2306.

21. Sholl, C. A., Nuclear spin relaxation by translational diffusion in liquids and solids: high- and low-frequency limits. *Journal of Physics C: Solid State Physics* **1981,** *14* (4), 447.

22. Kuhn, A.; Sreeraj, P.; Pöttgen, R.; Wiemhöfer, H.-D.; Wilkening, M.; Heitjans, P.; Pöttgen, R.; Wiemhöfer, H. D.; Wilkening, M.; Heitjans, P.; Pöttgen, R.; Wiemhöfer, H.-D.; Wilkening, M.; Heitjans, P., Li Ion Diffusion in the Anode Material $Li_{12}Si_7$: Ultrafast Quasi-1D Diffusion and Two Distinct Fast 3D Jump Processes Separately Revealed by ^7Li NMR Relaxometry. *Journal of the American Chemical Society* **2011,** *133* (29), 11018.

23. Xu, Z.; Stebbins, J. F., Cation Dynamics and Diffusion in Lithium Orthosilicate: Two-Dimensional Lithium-6 NMR. *Science* **1995,** *270* (5240), 1332.

24. Chaudhuri, S.; Wang, F.; Grey, C. P., Resolving the different dynamics of the fluorine sublattices in the anionic conductor $BaSnF_4$ by using high-resolution MAS NMR techniques. *Journal of the American Chemical Society* **2002,** *124* (39), 11746.

25. Davis, L. J. M.; Ellis, B. L.; Ramesh, T. N.; Nazar, L. F.; Bain, A. D.; Goward, G. R., ^6Li 1D EXSY NMR Spectroscopy: A New Tool for Studying Lithium Dynamics in Paramagnetic Materials Applied to Monoclinic Li_2VPO_4F. *Journal of Physical Chemistry C* **2011,** *115* (45), 22603.

26. Vinod Chandran, C.; Pristat, S.; Witt, E.; Tietz, F.; Heitjans, P., Solid-State NMR Investigations on the Structure and Dynamics of the Ionic Conductor Li1+xAlxTi2–x(PO4)3 (0.0 ≤ x ≤ 1.0). *Journal of Physical Chemistry C* **2016,** *120* (16), 8436.

27. Medek, A.; Harwood, J. S.; Frydman, L., Multiple-Quantum Magic-Angle Spinning NMR: A New Method for the Study of Quadrupolar Nuclei in Solids. *Journal of the American Chemical Society* **1995,** *117* (51), 12779.

28. Amoureux, J. P.; Fernandez, C.; Steuernagel, S., Z Filtering in MQMAS NMR. *Journal of Magnetic Resonance - Series A* **1996,** *123* (1), 116.

29. Jaccard, G.; Wimperis, S.; Bodenhausen, G., Multiple-quantum NMR spectroscopy of S=3/2 spins in isotropic phase: A new probe for multiexponential relaxation. *Interactions The Journal of Chemical Physics* **1986,** *85*, 4546.

30. Eliav, U.; Navon, G., Measurement of dipolar interaction of quadrupolar nuclei in solution using multiple-quantum NMR spectroscopy. *Journal of Magnetic Resonance - Series A* **1996,** *123* (1), 32.

31. Deschamps, M.; Burghardt, I.; Derouet, C.; Bodenhausen, G., Nuclear magnetic resonance study of xenon-131 interacting with surfaces: Effective Liouvillian and spectral analysis. *The Journal of Chemical Physics* **2000,** *113*, 6923.

32. Gordon, M. I.; Hoch, M. J. R., Quadrupolar spin-lattice relaxation in solids. *Journal of Physics C: Solid State Physics* **1978,** *11* (4), 783.

33. Gabriel, J.; Petrov, O. V.; Kim, Y.; Martin, S. W.; Vogel, M., Lithium ion dynamics in Li_2S+GeS_2+GeO_2 glasses studied using ^{7}Li NMR field-cycling relaxometry and line-shape analysis. *Solid State Nuclear Magnetic Resonance* **2015,** *70*, 53.

34. Huynh, T. V.; Messinger, R. J.; Sarou-Kanian, V.; Fayon, F.; Bouchet, R.; Deschamps, M., Restricted lithium ion dynamics in PEO-based block copolymer electrolytes measured by high-field nuclear magnetic resonance relaxation. *The Journal of Chemical Physics* **2017,** *147* (13), 134902.

35. Thurber, K. R.; Tycko, R., Measurement of sample temperatures under magic-angle spinning from the chemical shift and spin-lattice relaxation rate of

^{79}Br in KBr powder. *Journal of magnetic resonance (San Diego, Calif. : 1997)* **2009,** *196* (1), 84.

36. Bielecki, A.; Burum, D. P. D. P., Temperature Dependence of ^{207}Pb MAS Spectra of Solid Lead Nitrate. An Accurate, Sensitive Thermometer for Variable-Temperature MAS. *Journal of Magnetic Resonance, Series A* **1995,** *116* (2), 215.

37. Beckmann, P. A.; Dybowski, C., A Thermometer for Nonspinning Solid-State NMR Spectroscopy. *Journal of Magnetic Resonance* **2000,** *146* (2), 379.

38. Becker, K. D., Temperature dependence of NMR chemical shifts in cuprous halides. *The Journal of Chemical Physics* **1978,** *68* (8), 3785.

39. Wu, J.; Kim, N.; Stebbins, J. F., Temperature calibration for high-temperature MAS NMR to 913 K: ^{63}Cu MAS NMR of CuBr and CuI, and ^{23}Na MAS NMR of $NaNbO_3$. *Solid State Nuclear Magnetic Resonance* **2011,** *40* (2), 45.

40. Lim, H.; Kim, S.-C.; Kim, J.; Kim, Y.-I.; Kim, S.-J., Structure of Li_5AlS_4 and comparison with other lithium-containing metal sulfides. *Journal of Solid State Chemistry* **2018,** *257*, 19.

41. Xu, Z.; Stebbins, J. F., ^{6}Li nuclear magnetic resonance chemical shifts, coordination number and relaxation in crystalline and glassy silicates. *Solid State Nuclear Magnetic Resonance* **1995,** *5* (1), 103.

42. Pickard, C. J.; Mauri, F., All-electron magnetic response with pseudopotentials: NMR chemical shifts. *Physical Review B* **2001,** *63* (24), 245101.

43. Yates, J. R.; Pickard, C. J.; Mauri, F., Calculation of NMR chemical shifts for extended systems using ultrasoft pseudopotentials. *Physical Review B* **2007,** *76* (2), 024401.

44. Clark, S. J.; Segall, M. D.; Pickard, C. J.; Hasnip, P. J.; Probert, M. I. J.; Refson, K.; Payne, M. C., First principles methods using CASTEP. *Zeitschrift für Kristallographie - Crystalline Materials* **2005,** *220* (5/6), 567.

45. Finger, L. W.; Cox, D. E.; Jephcoat, A. P., A correction for powder diffraction peak asymmetry due to axial divergence. *Journal of Applied Crystallography* **1994,** *27* (6), 892.

46. Santibáñez-Mendieta, A. B.; Didier, C.; Inglis, K. K.; Corkett, A. J.; Pitcher, M. J.; Zanella, M.; Shin, J. F.; Daniels, L. M.; Rakhmatullin, A.; Li, M.; Dyer, M. S.; Claridge, J. B.; Blanc, F.; Rosseinsky, M. J., $La_3Li_3W_2O_{12}$: Ionic Diffusion in a Perovskite with Lithium on both A- and B-Sites. *Chemistry of Materials* **2016,** *28* (21), 7833.

47. Tu, B.; Liu, X.; Wang, H.; Wang, W.; Zhai, P.; Fu, Z., Combining ^{27}Al Solid-State NMR and First-Principles Simulations To Explore Crystal Structure in Disordered Aluminum Oxynitride. *Inorganic Chemistry* **2016,** *55* (24), 12930.

48. Smith, M. E.; van Eck, E. R. H., Recent advances in experimental solid state NMR methodology for half-integer spin quadrupolar nuclei. *Progress in Nuclear Magnetic Resonance Spectroscopy* **1999,** *34* (2), 159.

49. Meyer, B. M.; Leifer, N.; Sakamoto, S.; Greenbaum, S. G.; Grey, C. P., High Field Multinuclear NMR Investigation of the SEI Layer in Lithium Rechargeable Batteries. *Electrochemical and Solid-State Letters* **2005,** *8* (3), 145.

50. Abragam, A., *The principles of nuclear magnetism*. Clarendon Press: 1983.

51. Moran, R. F.; McKay, D.; Tornstrom, P. C.; Aziz, A.; Fernandes, A.; Grau-Crespo, R.; Ashbrook, S. E., Ensemble-Based Modeling of the NMR Spectra of Solid Solutions: Cation Disorder in $Y_2(Sn,Ti)_2O_7$. *Journal of the American Chemical Society* **2019,** *141* (44), 17838.

52. Waugh, J. S.; Fedin, E. I., Determination of hindered-rotation barriers in solids. *Soviet Phsics-Solid State* **1963,** *4* (8), 1633.

53. Heitjans, P.; Kärger, J. r., *Diffusion in condensed matter : methods, materials, models*. Springer: 2005.

54. Levitt, M. E., *Spin Dynamics: Basics of Nuclear Magnetic Resonance*. 2nd ed.; Wiley: 2008; p 740.

55. Stiegel, A.; Spiess, H. W., *Dynamic NMR spectroscopy*. Springer: Berlin Heidelberg, 1978.

56. Pietrass, T.; Taulelle, F.; Lavela, P.; Olivier-Fourcade, J.; Jumas, J.-C.; Steuernagel, S., Structure and Dynamics of Lithium-Intercalated SnS_2. ^{6,7}Li and ^{119}Sn Solid State NMR. *J. Phys. Chem. B* **1997,** *101* (34), 6715.

57. Bohnke, O.; Emery, J.; Veron, A.; Fourquet, J. L.; Buzare, J. Y.; Florian, P.; Massiot, D., A distribution of activation energies for the local and long-range ionic motion is consistent with the disordered structure of the perovskite $Li_{3x}La_{2/3-x}TiO_3$. *Solid State Ionics* **1998,** *109* (1-2), 25.

58. Berger, S.; Roos, J.; Brinkmann, D.; Chowdari, B. V. R., ^{6,7}Li and ^{19}F NMR studies of xLiF· (1 − x)$LiPO_3$ glasses. *Solid State Ionics* **1996,** *86-88* (1), 475.

59. Kim, N.; Hsieh, C. H.; Huang, H.; Prinz, F. B.; Stebbins, J. F., High temperature ^{17}O MAS NMR study of calcia, magnesia, scandia and yttria stabilized zirconia. *Solid State Ionics* **2007,** *178* (27-28), 1499.

60. Yu, C.; Ganapathy, S.; De Klerk, N. J. J.; Van Eck, E. R. H.; Wagemaker, M., Na-ion dynamics in tetragonal and cubic Na_3PS_4, a Na-ion conductor for solid state Na-ion batteries. *Journal of Materials Chemistry A* **2016,** *4* (39), 15095.

61. Deng, Y.; Eames, C.; Chotard, J. N.; Laleìre, F.; Seznec, V.; Emge, S.; Pecher, O.; Grey, C. P.; Masquelier, C.; Islam, M. S., Structural and Mechanistic Insights into Fast Lithium-Ion Conduction in Li_4SiO_4-Li_3PO_4 Solid Electrolytes. *Journal of the American Chemical Society* **2015,** *137* (28), 9136.

62. Han, G.; Vasylenko, A.; Neale, A. R.; Duff, B. B.; Chen, R.; Dyer, M. S.; Dang, Y.; Daniels, L. M.; Zanella, M.; Robertson, C. M.; Kershaw Cook, L. J.; Hansen, A. L.; Knapp, M.; Hardwick, L. J.; Blanc, F.; Claridge, J. B.; Rosseinsky, M. J., Extended Condensed Ultraphosphate Frameworks with Monovalent Ions Combine Lithium Mobility with High Computed Electrochemical Stability. *Journal of the American Chemical Society* **2021,** *143* (43), 18216.

63. Porion, P.; Faugère, M. P.; Lécolier, E.; Gherardi, B.; Delville, A., ^{23}Na nuclear quadrupolar relaxation as a probe of the microstructure and dynamics of aqueous clay dispersions: An application to laponite gels. *Journal of Physical Chemistry B* **1998,** *102* (18), 3477.

64. Morgan, B. J., Lattice-geometry effects in garnet solid electrolytes: a lattice-gas Monte Carlo simulation study. *Royal Society Open Science* **2017,** *4* (11).

4. Understanding the Li-Ion Diffusion Pathways in the Defect Stuffed Wurtzite $Li_{3.3}Sn_{3.3}Cl_{0.7}$ via Solid-State NMR

4.1 Overview

The second new material of interest reported in this thesis is the Li-Sn-S-Cl phase, $Li_{3.3}SnS_{3.3}Cl_{0.7}$. This material was first reported in Nature Communication in 2021,[1] where in this highly collaborative work, an unsupervised machine learning technique was reported for the first time. The material in question was identified through this new model and subsequently synthesised and characterised via a range of techniques such as diffraction, EIS and NMR. The paper reporting this model and material was entitled "Element selection for crystalline inorganic solid discovery guided by unsupervised machine learning of experimentally explored chemistry" by Andrij Vasylenko, Jacinthe Gamon, Benjamin B. Duff, Vladimir V. Gusev, Luke M. Daniels, Marco Zanella, J. Felix Shin, Paul M. Sharp, Alexandra Morscher, Ruiyong Chen, Alex R. Neale, Laurence J. Hardwick, John B. Claridge, Frédéric Blanc, Michael W. Gaultois, Matthew S. Dyer & Matthew J. Rosseinsky. The author contributions are as follows, M.J.R directed the whole project and F.B. the NMR component, A.V. identified, developed, and implemented the variational autoencoder (VAE) model in discussion with V.G., M.W.G., and M.S.D. and performed all the CSP. J.G. performed all synthetic work on the Li-Sn-S-Cl phases, solved and analysed the structure in collaboration with L.M.D. and J.B.C. and performed the impedance characterization, with assistance from A.M. B.B.D. designed, performed, and

analysed all the NMR experiments, assisted by F.B. R.C., A.R.N., and L.J.H. designed and performed the symmetrical cell and interface evaluation experiments. M.Z. performed all the electron microscopy. J.F.S. performed all the experimental work on the Li-Mg-S-Cl phases, and evaluated all the data in collaboration with L.M.D. and J.B.C.; P.M.S. and M.S.D. performed all the computational work on these phases. This chapter focusses on the NMR component of this work with a brief background and context of the computational and diffraction data.

4.2 Abstract

In order to further develop the field of Li solid electrolytes for use in all-solid-state batteries, the understanding of the Li-ion pathways is paramount. Here, we exploit ^{6}Li MAS in conjunction with diffraction techniques in order to derive the structure of the anion substituted $Li_{3.3}SnS_{3.3}Cl_{0.7}$ phase that was identified through an unsupervised machine learning approach. ^{7}Li line narrowing and relaxation measurements allowed for the quantification of Li-ion jump rates which were extrapolated and converted to a room temperature conductivity value of 2.6(7) x 10^{-5} S cm^{-1} in excellent agreement with the bulk conductivity value of 3.2(3) x 10^{-5} S cm^{-1} with an activation energy of 0.23(5) eV. Detailed analysis of the frequency dependence of the NMR relaxation rates indicated low-dimensional Li-ion diffusion, which when combined with the results from the nuclear density obtained from the maximum entropy method, revealed the Li-ion pathway to be one-dimensional. This pathway was identified to occur between one Li octahedra to another through a common face along the *c*-axis. The understanding of the effects of structural modifications of ternary materials through anion substitution on the Li-ion mobility pathways provides a framework for developing improved solid ion conductors.

4.3 Introduction

There has been a surge of machine learning (ML) studies that aim to extract the underlying patterns of chemistry available from ICSD[2-5] based on the knowledge of the composition and structure at the level of an individual material. Supervised learning[3, 6-8] infers relationships between materials' features and materials' properties, and requires large hand-labelled datasets for training. Unsupervised ML, on the other hand, infers underlying patterns of chemical knowledge in the absence of human-labelled data.[9, 10] Collaborators at the University of Liverpool developed an unsupervised ML approach in order to rank unexplored quaternary two anion phase fields for experimental investigation as solid electrolyte candidates through the method summarised in **Figure 4.1**.[1] Machine learning-assisted researcher assessment of the candidate element combinations then identified the Li-Sn-S-Cl field. Probe structure computation[11, 12] targeted a region within this field for synthetic exploration that afforded the defect stuffed wurtzite $Li_{3.3}SnS_{3.3}Cl_{0.7}$.

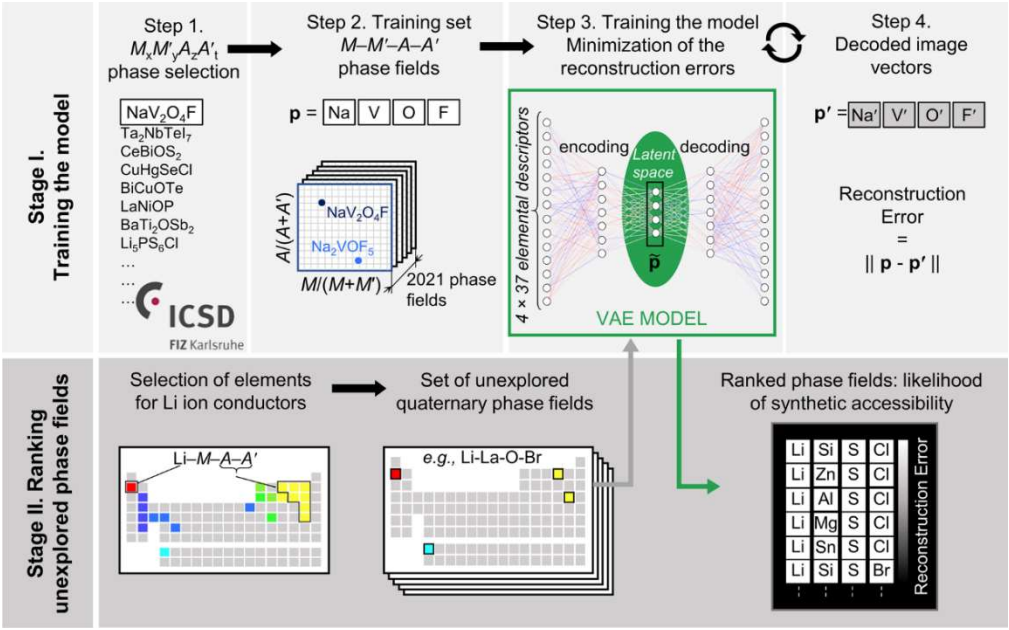

Figure 4.1 Summary of the ML model Stage I: ML model training from ICSD data of reported chemical systems in four steps: **1** quaternary phases with two anions are collected, for example, NaV_2O_4F.; **2** The individual phases (e.g., NaV_2O_4F and Na_2VOF_5) are aggregated to define those phase fields containing reported two anions quaternaries. Each phase field is represented as a 148-dimensional (four elements × 37 elemental features) vector **p**; **3** the VAE[13] is used to reduce (encode) **p** into a four-dimensional latent vector, p~; **4** the VAE decodes p~ back to a 148-dimensional image vector, **p′**. During training the VAE tunes the weights and biases of its neural networks to minimize the reconstruction errors, the Euclidean distances between the original, **p**, and decoded, **p′**, vectors. When exploring a new quaternary phase field with two anions (Stage II), e.g., Li-La-O-Br, the trained VAE model encodes the phase field into the latent space and decodes it while measuring its reconstruction error. The reconstruction error of a candidate phase field captures the degree of its deviation from reported chemical systems, enabling the ranking of unexplored phase fields for synthetic exploration. Figure was created by A.V all computations performed by A.V., V.G., M.W.G., and M.S.D.

The diffraction-derived average structure is a defect stuffed wurtzite, where Cl and S atoms are randomly distributed on the fully occupied anionic site in a hexagonal closed packed (*hcp*) lattice and the Sn and Li atoms on the fully occupied tetrahedral T^+ interstices, with the T^- sites empty, while the remaining 0.3 lithium atoms per formula unit are located on the octahedral site, O (**Figure 4.2(a)**). Refinement of the site occupancy factors (sof) reveals full occupancy of the anionic and the tetrahedral sites with S/Cl and Sn/Li atomic ratios of 0.823(8)/0.175(8) and 0.242(3)/0.760(3), respectively.

The Li1 position is slightly displaced towards the base of the tetrahedron compared to Sn, which presents a much more regular coordination environment (**Figure 4.2(b)**) that can be associated with a predominant S-only single anion first coordination sphere driven by the higher formal cation charge. The less regular geometry around Li1 would then be associated with the presence of both S and Cl anions in its first coordination sphere, as seen in the computed probe structure, driven by the lower formal charges of Li and Cl.

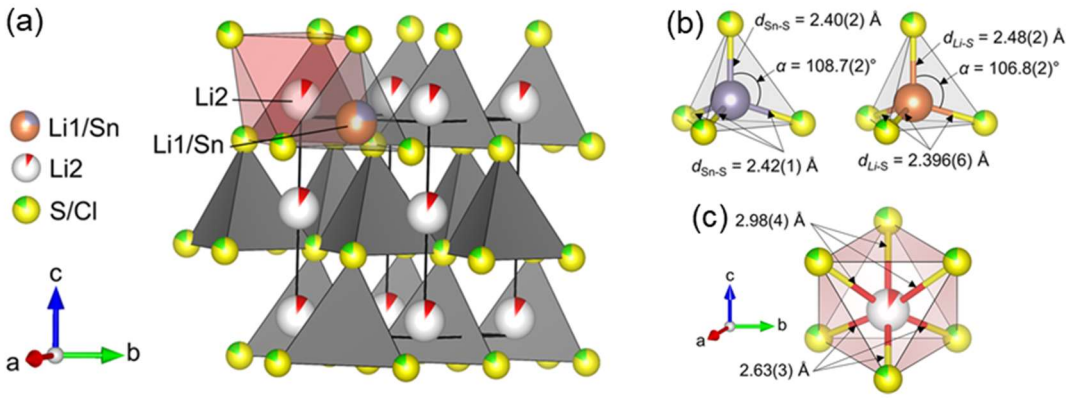

Figure 4.2 The defect stuffed wurtzite average structure of $Li_{3.3}SnS_{3.3}Cl_{0.7}$ with Li1 (orange) and Sn (purple) occupying the tetrahedral site (grey) and Li2 the octahedral site (red) along with the polyhedral environments for (b) Sn and Li1 as well as (c) Li2. The *hcp* anion sublattice is shown by the mixed S (yellow) and Cl (green) sites.

4.4 Experimental

Computational details as well as information on sample synthesis and analytical methods other than NMR can be found in reference [14]. All NMR data were recorded at 9.4 T on a Bruker AVIII HD spectrometer. ^{6}Li Magic Angle Spinning (MAS) NMR experiments were obtained with a 4 mm HXY MAS probe (in double resonance mode) with the X channel tuned to ^{7}Li at $\omega_0/2\pi$ (^{6}Li) = 58.9 MHz and under MAS at a rate of $\omega_r/2\pi$ = 10 kHz. Spectra were obtained with a pulse length of 3 μs at a radiofrequency (rf) field amplitude of $\omega_1/2\pi$ = 83 kHz. The sample was packed into a 4 mm MAS rotor under an argon atmosphere. Variable temperature ^{7}Li static NMR experiments were recorded on a 4 mm HXY MAS probe (in double resonance mode) at and below room temperature and on a 4 mm HX High-Temperature MAS Probe above room temperature with the X channel tuned to ^{7}Li at $\omega_0/2\pi$(^{7}Li) = 156 MHz. The ^{7}Li spectra were recorded with a pulse length of 1.5 μs at an rf field amplitude of $\omega_1/2\pi$ = 83 kHz. The sample was flame sealed in glass inserts under an Argon atmosphere of 10^{-3} mbar. All ^{6,7}Li spectra were referenced to 10 M LiCl in D_2O at 0 ppm.

SLR rates in the laboratory frame (T_1^{-1}) were obtained using a saturation recovery pulse sequence and the data were fitted to a stretch exponential function of the form:

$$1 - \exp[-(\tau/T_1^{-1})^{\alpha}] \qquad \text{(Eq. 4.1)}$$

where τ are the variable delays and α is the stretch exponential (values between 0.4 and 1). SLR rates in the rotating frame ($T_{1\rho}^{-1}$) were recorded using

a standard spin-lock pulse sequence at frequencies of $\omega_1/2\pi$ (^{7}Li) = 15, 45, and 80 kHz, and data were fitted to a stretch exponential function of the form:

$$1 - \exp\left[-\left(\tau/T_{1\rho}^{-1}\right)^{\beta}\right] \qquad \text{(Eq. 4.2)}$$

where β values are between 0.3 and 1. Temperature calibrations were performed using the chemical shift thermometers $Pb(NO_3)_2$, CuI and CuBr using ^{207}Pb NMR[15, 16] and ^{63}Cu NMR.[17, 18] The errors associated with this method were calculated using the broadening of the isotropic peak and ranged from 5 - 20 K.

4.5 Results and Discussion

4.5.1 ^{6}Li MAS

In order to gain insights into the local Li environments in $Li_{3.3}SnS_{3.3}Cl_{0.7}$, ^{6}Li MAS NMR was performed. The spectrum shown in **Figure 4.3** reveals a single resonance associated with $Li_{3.3}SnS_{3.3}Cl_{0.7}$ centred at 1.4 ppm, in agreement with the majority of Li occupying the tetrahedral interstices (**Figure 4.2**, octahedral sites are typically located near 0 ppm),[19] as well as a small shoulder at 1.8 ppm attributed to a small amount (~10 mol%) of orthorhombic Li_4SnS_4.[20] It is likely that the resonance associated with Li residing in the octahedral interstices is not observed in this case, because of the high Li-ion mobility in $Li_{3.3}SnS_{3.3}Cl_{0.7}$ leading to a single motionally averaged signal at the weighted average of the two resonances.

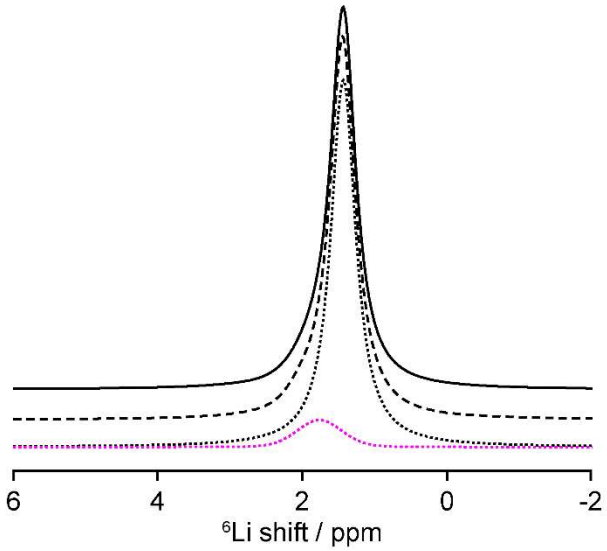

Figure 4.3 ^{6}Li MAS NMR spectrum of $Li_{3.3}SnS_{3.3}Cl_{0.7}$ recorded at 9.4 T and MAS rate of 10 kHz. The experimental spectrum (full line), total fit (dashed line), spectral deconvolution (dotted lines) and orthorhombic Li_4SnS_4 impurity[20] (pink dotted line) are also shown.

4.5.2 Static ^{7}Li VT Line Narrowing NMR

In static ^{7}Li solid-state NMR spectra, the absence of mobility is displayed through a broadening of the 1/2 ↔ −1/2 central transition arising from the strong homonuclear ^{7}Li-^{7}Li dipolar coupling interactions. At low temperatures, the material is said to be in the rigid lattice regime, in this regime spectra dominated by dipolar broadening are observed. This effect is present at approximately 165 K, where the line width of the central transition, $\omega/2\pi$, is approximately 5.2 kHz for $Li_{3.3}SnS_{3.3}Cl_{0.7}$. As the temperature is increased the dipolar interactions are continuously averaged due to the increasing motion of the Li spins causing the spectra to narrow significantly (**Figure 4.4**). This effect can be seen by plotting the full width half maximum of the peak as a function of the temperature (**Figure 4.4(b)**), where the onset of motional narrowing, T_{onset} occurs at around 200 K. Using an expression introduced by Waugh and Fedin[21] relating the onset temperature of motional narrowing with the activation energy of the diffusion process, given by:

$$E_a = 1.67 \times 10^{-3}\, T_{onset} \qquad \text{(Eq. 4.3)}$$

an activation energy of approximately 0.35 eV can be estimated for $Li_{3.3}SnS_{3.3}Cl_{0.7}$. The peak width then decreases significantly as the temperature is increased above ~ 220 K, down to a minimum line width of approximately 750 Hz where the homonuclear dipolar interactions are completely averaged out. The inflection point of this temperature-dependent linewidth, $T_{inflection}$ defines the Li-ion jump rate, τ^{-1}, which is of the order of the linewidth in the rigid lattice regime (~5 kHz), yielding a value of ~ 3.3(2) x 10^{4} s^{-1} at a temperature of ~ 250 K.

$T_{inflection}$ values were determined from fitting the $\omega/2\pi$ data in **Figure 4.4(b)** to a Boltzmann sigmoid regression curve of the form:

$$\frac{\omega(T)}{2\pi} = \left(\frac{\left(\frac{\omega}{2\pi}\right)_{\infty} - \left(\frac{\omega}{2\pi}\right)_{rl}}{1 + \exp\left(\frac{T_{inflection} - T}{a}\right)} \right) \qquad \text{(Eq. 4.4)}$$

where $\omega(T)/2\pi$ is the linewidth of the central transition at temperature T, $(\omega/2\pi)_{\infty}$ is the residual linewidth at high temperature in the fast motional regime and a is a fitting parameter.

As $Li_{3.3}SnS_{3.3}Cl_{0.7}$ appears to be in the fast-motional regime at room temperature, this is a reasonable explanation for the absence of two distinct resonances attributed to the material in the ^{6}Li MAS NMR spectrum (**Figure 4.3**). At room temperature, rapid exchange between tetrahedral and octahedral Li sites will occur on the NMR timescale leading to the observation of a single resonance.

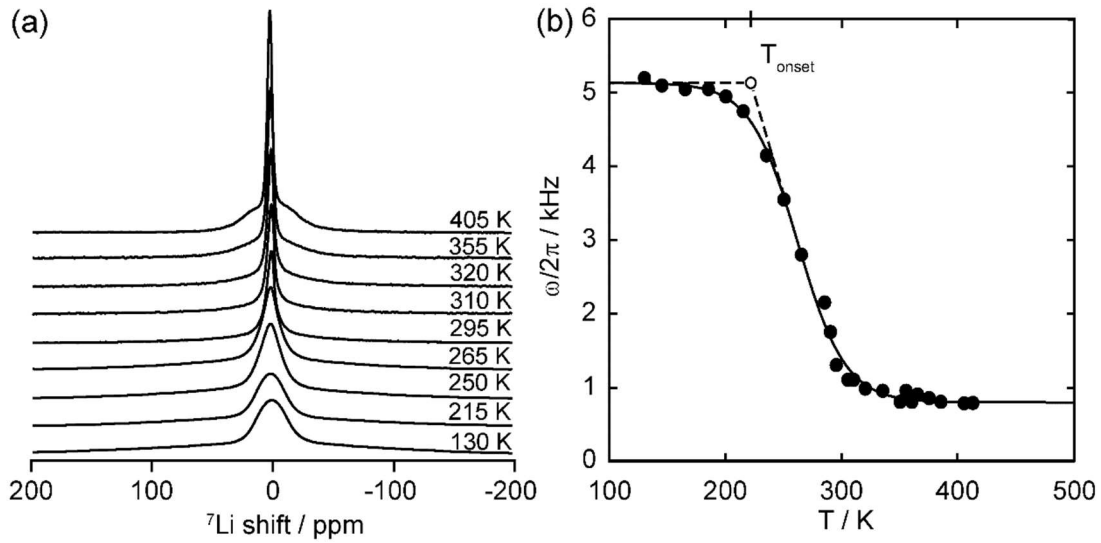

Figure 4.4 (a) Representative static ^{7}Li VT NMR spectra of $Li_{3.3}SnS_{3.3}Cl_{0.7}$. (b) Temperature dependence of the ^{7}Li NMR linewidth $\omega(T)/2\pi$ of $Li_{3.3}SnS_{3.3}Cl_{0.7}$ where the onset temperature of line narrowing T_{onset} is given with a double length tick on the upper axis, with dashed lines showing the tangents of the curve used to extract T_{onset}. The solid black line is a fit to the data based on the sigmoidal regression given in **equation 4.4** and is used to determine the inflection point of the curve.

4.5.3 ^{7}Li Relaxometry

The temperature dependence of the ^{7}Li SLR in the laboratory (T_1^{-1}) and rotating frame ($T_{1\rho}^{-1}$) under static conditions were monitored using the saturation recovery and spin lock pulse sequences, respectively. These measurements were performed in order to obtain values for the activation energy, conductivity and dimensionality of the Li diffusion. The SLR $T_{1\rho}^{-1}$ rates are purely induced by diffusion processes initially increasing with temperatures above room temperature before decreasing thereby passing through a maximum at temperatures that are characteristic of the Li correlation rates τ_c^{-1} (that is the average Li jump rates τ^{-1}) being equal to the spin-lock frequencies ω_1, i.e. $2\omega_1 \approx \tau_c^{-1} = \tau^{-1}$. Accessing these maxima at different ω_1 enables different NMR-derived jump rates τ^{-1} to be obtained at different temperatures (**Figure 4.5**), giving jump rate values of the order of 1.8×10^5 - 1×10^6 s^{-1} in the 330–355 K temperature range.

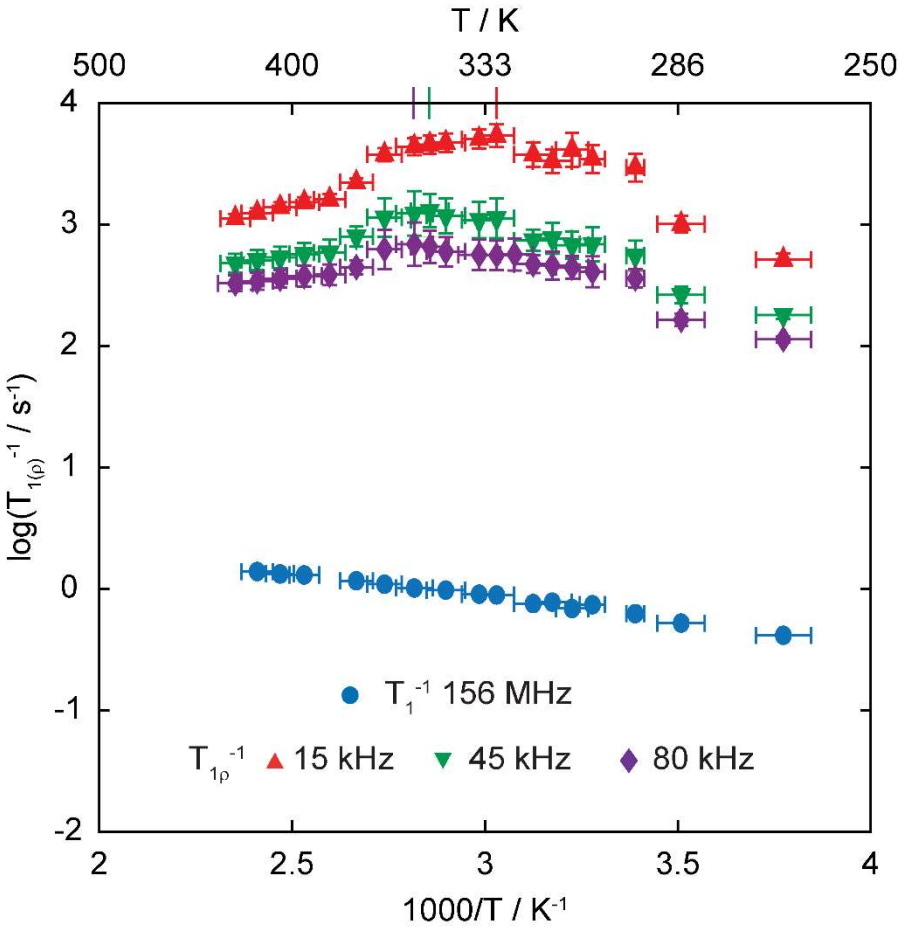

Figure 4.5 Arrhenius plot of spin-lattice relaxation (SLR) rates in the laboratory frame (T_1^{-1}) at a Larmor frequency of 156 MHz (blue circle) and in the rotating frame ($T_{1\rho}^{-1}$) at spin-lock frequencies $\omega_1/2\pi$ of 15 (red triangle), 45 (green inverted triangle) and 80 kHz (purple diamond). The coloured ticks on the upper x-axis represent the temperatures of the $T_{1\rho}^{-1}$ maxima. The error bars associated with the temperature are calculated from the broadening of the isotropic peak of the chemical shift thermometer $Pb(NO_3)_2$, while the errors in T_1^{-1} and $T_{1\rho}^{-1}$ are obtained from the output of the fittings of Supplementary **Equations 4.1** and **4.2** respectively.

As previously discussed in **Chapter 1 section 1.3.3**, the dimensionality of the Li^+ ion diffusion can be accessed from the frequency-dependence of the high temperature limits of the SLR $T_{1\rho}^{-1}$ values and follows characteristic relationships with one, two, and three-dimensional diffusion in solids being proportional to $(\tau/\omega)^{0.5}$, $\tau\ln(1/\omega\tau)$, or τ, respectively[22, 23] (where τ and ω are the correlation times and probe frequencies, respectively) for which the corresponding fit is shown at various temperatures in **Figure 4.6**.

Figure 4.7(a) shows the frequency dependence of the SLR rate at 425 K, in which there is a clear dependence of the SLR rate with ω_1, ruling out the possibility of 3D Li diffusion. However the models for 1D and 2D Li-ion mobility fit well the experimentally recorded SLR data (also shown in **Figure 4.5**).

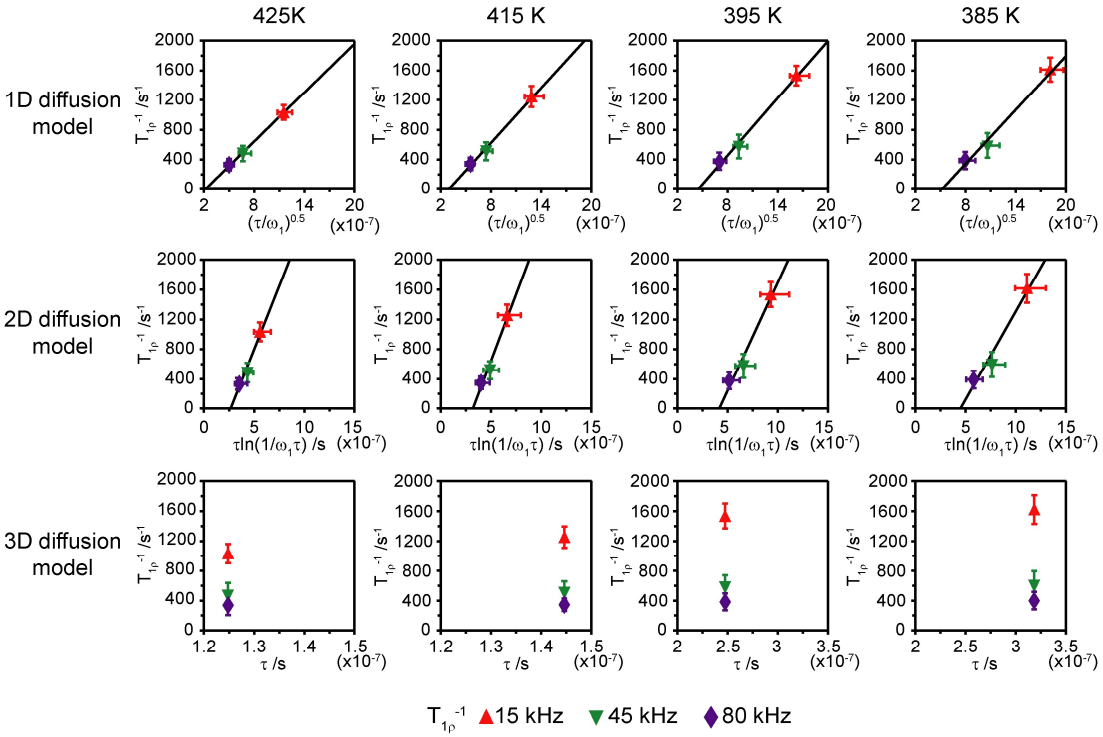

Figure 4.6 Frequency dependence of the NMR SLR $T_{1\rho}^{-1}$ rates at 425, 415, 395 and 385 K for one, two and three-dimensional models, at spin lock frequencies $\omega_1/2\pi$ of 15 (red triangle), 45 (green inverted triangle), 80 kHz (purple diamond), and average Li^+ jump times τ from $T_{1\rho}^{-1}$ maxima (**Figure 4.5**). The solid lines correspond to linear fits of $(\tau/\omega)^{0.5}$ and $\tau\ln(1/\omega\tau)$ for one and two-dimensional diffusion, respectively. The frequency dependence of the SLR $T_{1\rho}^{-1}$ rates (also shown in **Figure 4.5**) clearly rules out the possibility of three-dimensional diffusion. Errors in the spinlock frequencies ω_1 are estimated to be 10% while the errors in the correlation time τ are extracted from the fit in **Figure 4.8**. Errors in $T_{1\rho}^{-1}$ are obtained from the outputs of the fits to **equation 4.2**.

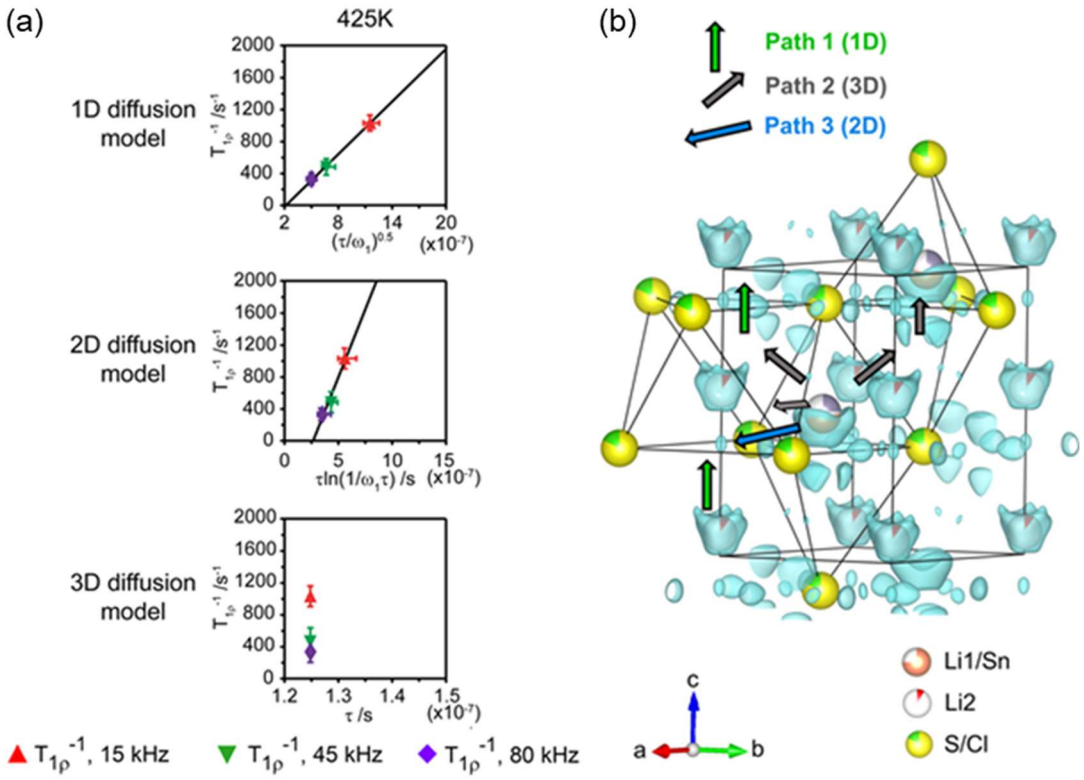

Figure 4.7 (a) Frequency dependence of the NMR SLR $T_{1\rho}^{-1}$ rates at 425 K for one-dimensional, two-dimensional and three-dimensional diffusion models, as a function of spin-lock frequencies $\omega_1/2\pi$ of 15 (red triangle), 45 (green inverted triangle), 80 kHz (purple diamond) and average Li^+ jump times τ from $T_{1\rho}^{-1}$ maxima (**Figure 4.5**). The black lines correspond to linear fits with regression factor r^2 of 0.99 for 1D and 0.98 for 2D diffusion. Data for other temperatures are given in **Figure 4.6**. Errors in the spin-lock frequencies ω_1 are estimated to be 10% while the errors in the correlation time τ are extracted from the fit in **Figure 4.9**. Errors in $T_{1\rho}^{-1}$ are obtained from the outputs of the fits to **equation 4.2**. (b) Nuclear density reconstructed by the maximum entropy method and highlighted potential diffusion pathways (path 1 (1D): green arrow, path 2 (3D): gray arrows and path 3 (2D): blue arrows).

Analysis of the periodic distribution of the scattering density provides further important experimental evidence for possible diffusion pathways and their dimensionality.[24] **Figure 4.8** shows the nuclear density obtained by the maximum entropy method (MEM). Three potential diffusion pathways are highlighted: i) path 1 Octahedral (O) to Octahedral (O-O)): 1D diffusion from one Li2 octahedron to another through their common face along the *c*-axis (green arrows, **Figure 4.8(a)**), ii) path 2 (T^+ - T^- - T^+): 3D diffusion from the Li1 (T^+) tetrahedra to one of the vacant T^- tetrahedra of the same layer via their common edge (3 possibilities spanning the whole (ab) plane, grey arrows on **Figure 4.8(a)**), followed by diffusion to the T^+ site in the layer above through their common face (along c, grey arrows Fig. 5b, c) and iii) path 3 (T^+ - O - T^+): 2D diffusion in the sulfide slab from one Li1 tetrahedron to another by passing through the edge of the T^+ base, via the octahedral interstice and again through the edge of the adjacent Li1 tetrahedron (blue arrows, **Figure 4.8(c)**).

MEM analysis (**Figure 4.8(a,c)**)shows path 3 has much higher energy barriers compared to paths 1 and 2 indicating that 2D diffusion is not dominant (**Figure 4.8(b,d)**). As NMR also dismisses possible 3D conductivity, path 2 with its three-dimensional nature can also be discarded. This is further reinforced by the absence of vacancies on the Li1 site preventing direct Li1-Li1 jumps as described in paths 2 and 3. By combining NMR and MEM data, we thus demonstrate 1D diffusion in the defect stuffed mixed anion wurtzite, involving Li2-Li2 jumps between the partially occupied O sites along the *c*-axis described by path 1. O–O was indeed identified as the lower energy barrier pathway in a model sulfide *hcp* lattice.[25]

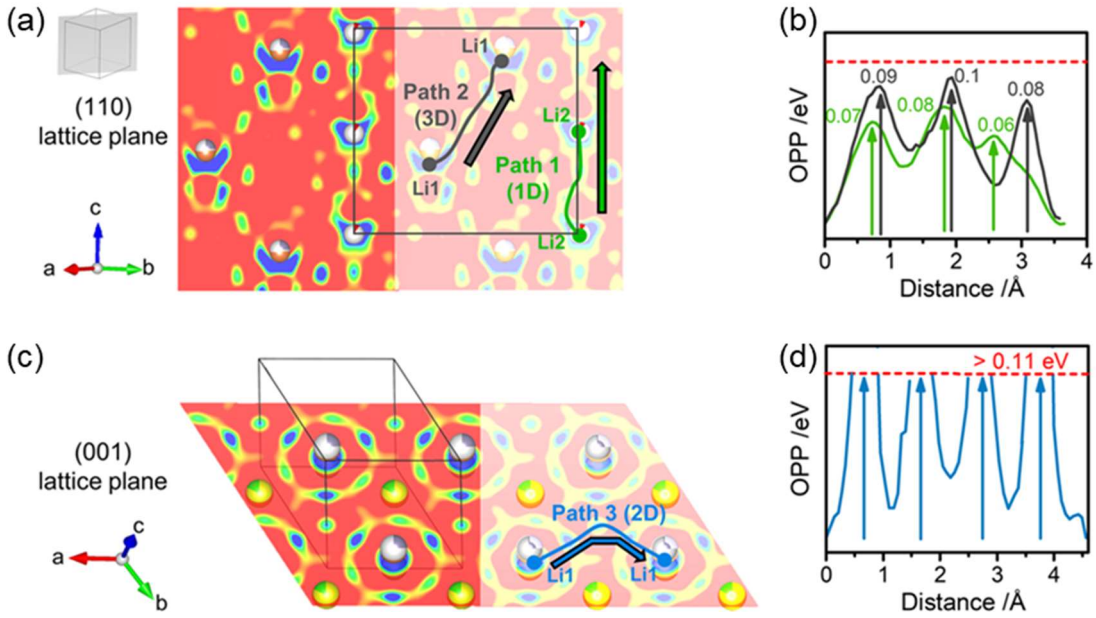

Figure 4.8 (a) Nuclear density in the (110) lattice plane and (b) estimated one particle potential (OPP) along the two diffusion pathways in this plane (Path 1: green line; Path 2: gray line), energy barriers are indicated on the plot in eV. (c) Nuclear density in the (001) lattice plane and (d) OPP estimated along Path 3 in this plane. The dashed red line on (b) and (d) corresponds to the maximum OPP that can be calculated given the background level of the nuclear density. Density levels on (a) and (c) are plotted in the [-0.02 fm $Å^{-3}$; 0 fm $Å^{-3}$] range to identify scattering from Li. Figure created and analysis performed by J.G.

However, near the wurtzite structure, as O is a nonstable site, it is often left vacant when composition allows, and the limiting mechanism is defined by diffusion through T–O shared faces with higher activation energy, therefore hindering conductivity. By using two anions to stabilize Li cation excess with both O and T sites occupied, we show that defect stuffed wurtzites should be considered as promising Li ionic conductor candidates by locating the Li cations and resolving their conduction pathways. The cation stuffing onto the

O site opens the lower energy barrier O–O diffusion pathway as the main limiting transport mechanism, in contrast to tetrahedral-only materials.

4.5.4 Li-Ion Mobility

τ^{-1} from NMR line narrowing experiments and relaxometry experiments are plotted against reciprocal temperature **Figure 4.9**. Fitting this data to:

$$\tau^{-1} = \tau_0^{-1}\exp[-(E_a/RT)] \quad \text{(Eq. 4.5)}$$

yields an activation barrier of 0.26(5) eV for $Li_{3.3}SnS_{3.3}Cl_{0.7}$.

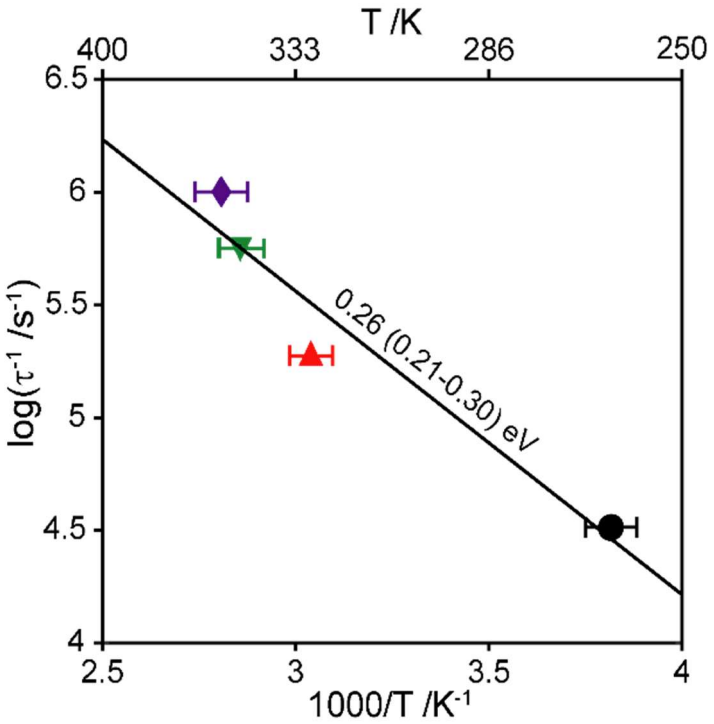

Figure 4.9 Arrhenius plot of Li jump rates τ^{-1}. Data were extracted from the onset of ^{7}Li line narrowing of the variable temperature ^{7}Li NMR spectra (black circle, **Figure 4.4**) and SLR rates in the rotating frame ($T_{1\rho}^{-1}$) experiments (**Figure 4.5**) at spin lock frequencies $\omega_1/2\pi$ of 15 (red triangle), 45 (green inverted triangle) and 80 kHz (purple diamond), respectively. The horizontal error bar associated with the temperature is calculated from the broadening of the isotropic peak of the chemical shift thermometer $Pb(NO_3)_2$ as explained above. Errors in the jump rate τ^{-1} are within the data points.

NMR conductivity σ_{NMR} can be estimated from the Li jump rates τ^{-1} using the combined Nernst-Einstein and Einstein-Smoluchowski equations:

$$\sigma_{NMR} = \frac{f}{H_R}\frac{N_{cc}q^2a^2}{N_{NN}k_BT}\frac{1}{\tau_c} \qquad \text{(Eq. 4.6)}$$

where f/H_R is the correlation factor and Haven ratio (1 for uncorrelated motion), N_{CC}/N_{NN} is the number of charge carriers per unit cell volume (0.092 Å^{-3}), q is

the ionic charge of Li, a is the closest Li-Li jump distance at room temperature (2.4 Å), extracted from the crystal structure determined via diffraction experiments. We estimate the NMR conductivity σ_{NMR} from combined Nernst-Einstein and Einstein-Smoluchowski equations (**Equation 4.6**) and extract an NMR activation barrier of 0.23(6) eV for Li-ion diffusion (**Figure 4.9**). This value is lower than that determined by electrical impedance spectroscopy (EIS) (0.38(3)eV) (performed by Jacinthe Gamon, details of which can be found in reference[1]) as NMR spectroscopy determines the barrier of diffusion of Li to its neighbouring site, whereas EIS probes longer-range translational diffusion. The extrapolated conductivity value at 303 K is $2.6(7) \times 10^{-5}$ S cm^{-1}, in good agreement with the bulk conductivity value of $3.2(3) \times 10^{-5}$ S cm^{-1} obtained from EIS.

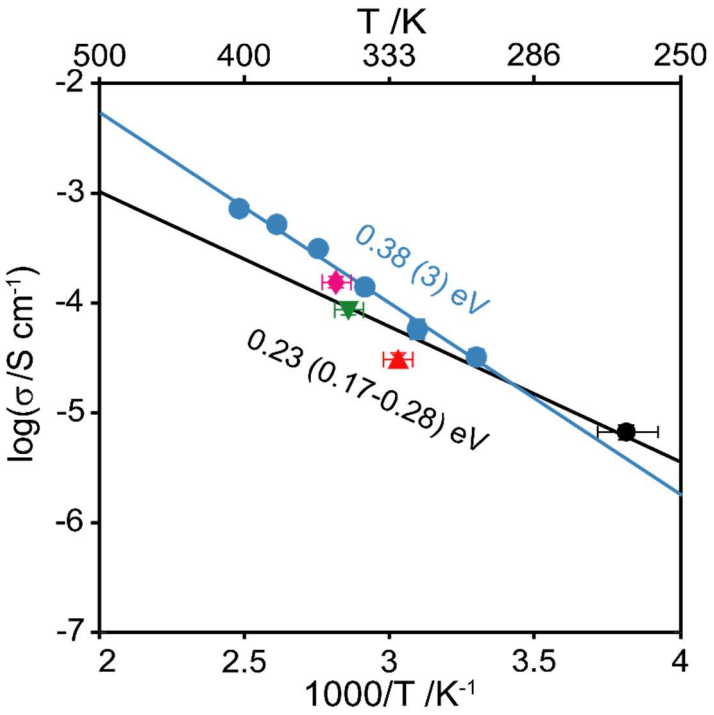

Figure 4.10 Arrhenius plot of the bulk conductivity measured by EIS (blue circles) and calculated from NMR jump rates using **equation 4.6** from line narrowing experiments (black circle, **Figure 4.3**) and SLR rates $T_{1\rho}^{-1}$ (**Figure 4.4**) using the same colour coding. The corresponding linear fits using an Arrhenius law are given in blue and black lines. The errors obtained in σ_{NMR} were derived from the propagation of the various errors associated with **equation 4.6**.

4.6 Conclusion and Outlook

In this chapter, the identification and characterisation of the structure and ion mobility pathway in the new solid ion conductor $Li_{3.3}SnS_{3.3}Cl_{0.7}$ has been reported. The Li-Sn-S-Cl phase field was probed through an unsupervised ML technique, the new material $Li_{3.3}SnS_{3.3}Cl_{0.7}$ was synthesised in this highly collaborative work and the structure derived through a combination of NMR and diffraction techniques. Through ^{7}Li line narrowing and relaxation experiments, the ion dynamics were quantified and in conjunction with MEM analysis the ion mobility pathway was identified to occur in one dimension, occurring between the octahedral Li2 site in 1D channels. This 1D diffusion pathway previously unseen in *hcp* anion arrays and inaccessible to date with monoanionic chemistry. 1D diffusion channels are favourable for accessing liquid-like ionic conductivity behaviour, as in $Li_{10}GeP_2S_{12}$,[26] and further tuning of the composition to increase octahedral occupancy in stuffed wurtzites would increase carrier density. More generally, O–O pathways along the *c*-axis, involving face sharing of octahedra, have not yet been experimentally reported in other *hcp* sulfide materials

4.7 References

(1) Vasylenko, A.; Gamon, J.; Duff, B. B.; Gusev, V. V.; Daniels, L. M.; Zanella, M.; Shin, J. F.; Sharp, P. M.; Morscher, A.; Chen, R.; Neale, A. R.; Hardwick, L. J.; Claridge, J. B.; Blanc, F.; Gaultois, M. W.; Dyer, M. S.; Rosseinsky, M. J. Element selection for crystalline inorganic solid discovery guided by unsupervised machine learning of experimentally explored chemistry. *Nature Communications* **2021**, *12*, 5561.

(2) Ward, L.; Agrawal, A.; Choudhary, A.; Wolverton, C. A general-purpose machine learning framework for predicting properties of inorganic materials. *npj Computational Materials* **2016**, *2*, 16028.

(3) Schmidt, J.; Shi, J.; Borlido, P.; Chen, L.; Botti, S.; Marques, M. A. L. Predicting the Thermodynamic Stability of Solids Combining Density Functional Theory and Machine Learning. *Chem. Mater.* **2017**, *29*, 5090.

(4) Liu, Y.; Zhao, T.; Ju, W.; Shi, S. Materials discovery and design using machine learning. *Journal of Materiomics* **2017**, *3*, 159.

(5) Butler, K. T.; Davies, D. W.; Cartwright, H.; Isayev, O.; Walsh, A. Machine learning for molecular and materials science. *Nature* **2018**, *559*, 547.

(6) Oliynyk, A. O.; Adutwum, L. A.; Rudyk, B. W.; Pisavadia, H.; Lotfi, S.; Hlukhyy, V.; Harynuk, J. J.; Mar, A.; Brgoch, J. Disentangling Structural Confusion through Machine Learning: Structure Prediction and Polymorphism of Equiatomic Ternary Phases ABC. *J. Am. Chem. Soc.* **2017**, *139*, 17870.

(7) Zhuo, Y.; Mansouri Tehrani, A.; Brgoch, J. Predicting the Band Gaps of Inorganic Solids by Machine Learning. *The Journal of Physical Chemistry Letters* **2018**, *9*, 1668.

(8) Sendek, A. D.; Cubuk, E. D.; Antoniuk, E. R.; Cheon, G.; Cui, Y.; Reed, E. J. Machine Learning-Assisted Discovery of Solid Li-Ion Conducting Materials. *Chem. Mater.* **2019**, *31*, 342.

(9) Zhang, Y.; He, X.; Chen, Z.; Bai, Q.; Nolan, A. M.; Roberts, C. A.; Banerjee, D.; Matsunaga, T.; Mo, Y.; Ling, C. Unsupervised discovery of solid-state lithium ion conductors. *Nature Communications* **2019**, *10*, 5260.

(10) Tshitoyan, V.; Dagdelen, J.; Weston, L.; Dunn, A.; Rong, Z.; Kononova, O.; Persson, K. A.; Ceder, G.; Jain, A. Unsupervised word embeddings

capture latent knowledge from materials science literature. *Nature* **2019**, *571*, 95.

(11) Collins, C.; Dyer, M. S.; Pitcher, M. J.; Whitehead, G. F. S.; Zanella, M.; Mandal, P.; Claridge, J. B.; Darling, G. R.; Rosseinsky, M. J. Accelerated discovery of two crystal structure types in a complex inorganic phase field. *Nature* **2017**, *546*, 280.

(12) Gamon, J.; Duff, B. B.; Dyer, M. S.; Collins, C.; Daniels, L. M.; Surta, T. W.; Sharp, P. M.; Gaultois, M. W.; Blanc, F.; Claridge, J. B.; Rosseinsky, M. J. Computationally Guided Discovery of the Sulfide Li_3AlS_3 in the Li–Al–S Phase Field: Structure and Lithium Conductivity. *Chem. Mater.* **2019**, *31*, 9699.

(13) Kingma, D., P; Welling, M. Auto-Encoding Variational Bayes. *arXiv pre-print server* **2014**.

(14) Gamon, J.; Dyer, M. S.; Duff, B. B.; Vasylenko, A.; Daniels, L. M.; Zanella, M.; Gaultois, M. W.; Blanc, F.; Claridge, J. B.; Rosseinsky, M. J. $Li_{4.3}AlS_{3.3}Cl_{0.7}$: A Sulfide-Chloride Lithium Ion Conductor with Highly Disordered Structure and Increased Conductivity. *Chem. Mater.* **2021**, *33*, 8733.

(15) Bielecki, A.; Burum, D. P. D. P. Temperature Dependence of ^{207}Pb MAS Spectra of Solid Lead Nitrate. An Accurate, Sensitive Thermometer for Variable-Temperature MAS. *Journal of Magnetic Resonance, Series A* **1995**, *116*, 215.

(16) Beckmann, P. A.; Dybowski, C. A Thermometer for Nonspinning Solid-State NMR Spectroscopy. *Journal of Magnetic Resonance* **2000**, *146*, 379.

(17) Becker, K. D. Temperature dependence of NMR chemical shifts in cuprous halides. *The Journal of Chemical Physics* **1978**, *68*, 3785.

(18) Wu, J.; Kim, N.; Stebbins, J. F. Temperature calibration for high-temperature MAS NMR to 913 K: ^{63}Cu MAS NMR of CuBr and CuI, and ^{23}Na MAS NMR of $NaNbO_3$. *Solid State Nucl. Magn. Reson.* **2011**, *40*, 45.

(19) MacKenzie, K. J. D.; Smith, M. E. *Multinuclear Solid-State Nuclear Magnetic Resonance of Inorganic Materials*; Elsevier, 2002.

(20) Kaib, T.; Haddadpour, S.; Kapitein, M.; Bron, P.; Schröder, C.; Eckert, H.; Roling, B.; Dehnen, S. New Lithium Chalcogenidotetrelates, LiChT: Synthesis and Characterization of the Li^+-Conducting Tetralithium ortho-Sulfidostannate Li_4SnS_4. *Chem. Mater.* **2012**, *24*, 2211.

(21) Waugh, J. S.; Fedin, E. I. Determination of hindered-rotation barriers in solids. *Soviet Phsics-Solid State* **1963**, *4*, 1633.
(22) Sholl, C. A. Nuclear spin relaxation by translational diffusion in liquids and solids: high- and low-frequency limits. *Journal of Physics C: Solid State Physics* **1981**, *14*, 447.
(23) Kuhn, A.; Sreeraj, P.; Pöttgen, R.; Wiemhöfer, H.-D.; Wilkening, M.; Heitjans, P.; Pöttgen, R.; Wiemhöfer, H. D.; Wilkening, M.; Heitjans, P.; Pöttgen, R.; Wiemhöfer, H.-D.; Wilkening, M.; Heitjans, P. Li Ion Diffusion in the Anode Material $Li_{12}Si_7$: Ultrafast Quasi-1D Diffusion and Two Distinct Fast 3D Jump Processes Separately Revealed by ^{7}Li NMR Relaxometry. *J. Am. Chem. Soc.* **2011**, *133*, 11018.
(24) Zhang, Z.; Zhang, J.; Sun, Y.; Jia, H.; Peng, L.; Zhang, Y.; Xie, J. $Li_{4-x}Sb_xSn_{1-x}S_4$ solid solutions for air-stable solid electrolytes. *Journal of Energy Chemistry* **2020**, *41*, 171.
(25) Wang, Y.; Richards, W. D.; Ong, S. P.; Miara, L. J.; Kim, J. C.; Mo, Y.; Ceder, G. Design principles for solid-state lithium superionic conductors. *Nature Materials* **2015**, *14*, 1026.
(26) Kamaya, N.; Homma, K.; Yamakawa, Y.; Hirayama, M.; Kanno, R.; Yonemura, M.; Kamiyama, T.; Kato, Y.; Hama, S.; Kawamoto, K.; Mitsui, A. A lithium superionic conductor. *Nature Materials* **2011**, *10*, 682.

5. A new lithium ion conducting ultraphosphate phase $Li_3P_5O_{14}$ and Understanding the Li-Ion Dynamics via Solid-State Nuclear Magnetic Resonance Spectroscopy

5.1 Overview

The final material of interest in this thesis is the ultraphosphate phase $Li_3P_5O_{14}$. This material was first reported in a paper in the *Journal of the American Chemical Society* in 2021[1] entitled Extended Condensed Ultraphosphate Frameworks with Monovalent Ions Combine Lithium Mobility with High Computed Electrochemical Stability by Guopeng Han, Andrij Vasylenko, Alex R. Neale, Benjamin B. Duff, Ruiyong Chen, Matthew S. Dyer, Yun Dang, Luke M. Daniels, Marco Zanella, Craig M. Robertson, Laurence J. Kershaw Cook, Anna-Lena Hansen, Michael Knapp, Laurence J. Hardwick, Frédéric Blanc, John B. Claridge, and Matthew J. Rosseinsky. The author contributions are as follows: M.J.R devised the project; G.H synthesised the material and performed the powder diffraction measurements and the EIS experiments, with assistance from Y.D; M.S.D, A.V and A.R.N performed the phase field screening and BVS mapping, C.M.R performed the single crystal diffraction measurements, M.Z performed the microscopy measurements and analysis, A.R.N and L.J.H performed the Li plating/stripping experiments, A.L.H and M.K assisted with synchrotron data acquisition, and B.B.D designed, performed, and analysed all the NMR experiments, assisted by F.B.

This chapter focusses on the NMR aspect from this work as well as follow up NMR experiments that are yet unpublished.

5.2 Abstract

The development of fast Li ion conducting materials for use as solid electrolytes that are electrochemically stable against electrodes, are paramount for the future of all-solid-state batteries. Progression of the research into these materials is dependent on the understanding of the structures and ion mobility properties. Here, we exploit a series of nuclear magnetic resonance (NMR) techniques, including ^{6}Li and ^{31}P magic angle spinning (MAS) and ^{31}P-^{31}P spin diffusion NMR in conjunction with density functional theory (DFT) and diffraction techniques in order to characterise the structure of the ultraphosphate $Li_3P_5O_{14}$, a promising candidate for an oxide based Li ion conductor. $Li_3P_5O_{14}$ has been shown previously to be a highly conductive, energetically favourable and electrochemically stable potential solid-electrolyte. We employed a number of complimentary ^{7}Li NMR techniques including, static ^{7}Li variable temperature (VT) line narrowing spectra, spin-alignment echo (SAE) NMR and relaxometry in order to quantify the lithium ion dynamics in $Li_3P_5O_{14}$. Detailed analysis of the diffusion-induced spin-lattice relaxation (SLR) data allowed for the identification of the dimensionality of ion mobility to be three-dimensional. Static ^{31}P VT experiments and relaxation measurements showed that PO_4^{3-} group rotation in the ultraphosphate layer was minimal and does not contribute to translational Li ion mobility. Future work into this material will allow for the experimental verification and experimentally verify the proposed 3D Li ion pathway as well as determine the site specific Li ion jump rates in order to outline further development in phosphate materials, providing a pathway for further increases in the performance of solid electrolytes.

5.3 Introduction

Compared with lithium ion conducting sulfides such as the ones mentioned previously in this thesis, oxide based lithium ion conductors tend to have lower total ionic conductivities but with improved stabilities.[2,3] Phosphates consisting of PO_4^{3-} tetrahedra can adopt isolated, linear, cyclic, and branched anionic substructures, giving rise to orthophosphate, polyphosphate, cyclophosphate, and ultraphosphate structures, respectively.[4,5] In the first three of these families, PO_4^{3-} tetrahedra share zero (isolated tetrahedra), one (terminal tetrahedra), or two (internal tetrahedra) of their oxygens with neighbouring tetrahedra, resulting in unbranched 0-, 2-, or mixed 1,2-connected anions, so only unbranched zero-dimensional (0D) or 1D anions are available, e.g., 0D unbranched 2-connected single $P_6O_{18}^{6-}$ rings in the cyclophosphate $Al_2P_6O_{18}$[6] and 1D 2-connected PO_3^- chains in the polyphosphate $LiPO_3$,[7] as shown in **Figure 5.1(a−c)**. In contrast, ultraphosphates present branched anions that are generated by combining internal tetrahedra with branching PO_4^{3-} tetrahedra that share three of their oxygens with other tetrahedra (**Figure 5.1(d)**) to form a 2D structure of interconnected PO_4^{3-} tetrahedra. This produces richer structural chemistry arising from topologically nonlinear linking, which generates 2,3-connected nets that lie between purely 3-connected phosphoric anhydride P_2O_5 and the 2-connected cyclophosphates. The arising anion geometries are more diverse than in other types of phosphates; e.g., ultraphosphates could adopt 0D (finite $P_8O_{23}^{6-}$ groups in $Na_3FeP_8O_{23}$),[8] 1D (infinite $P_5O_{14}^{3-}$ ribbons in orthorhombic HoP_5O_{14}),[9] 2D ($P_4O_{11}^{2-}$ layers in CaP_4O_{11}),[10] or even 3D (infinite $P_6O_{17}^{4-}$ frameworks in $(UO_2)_2P_6O_{17}$)[11] anionic geometries.

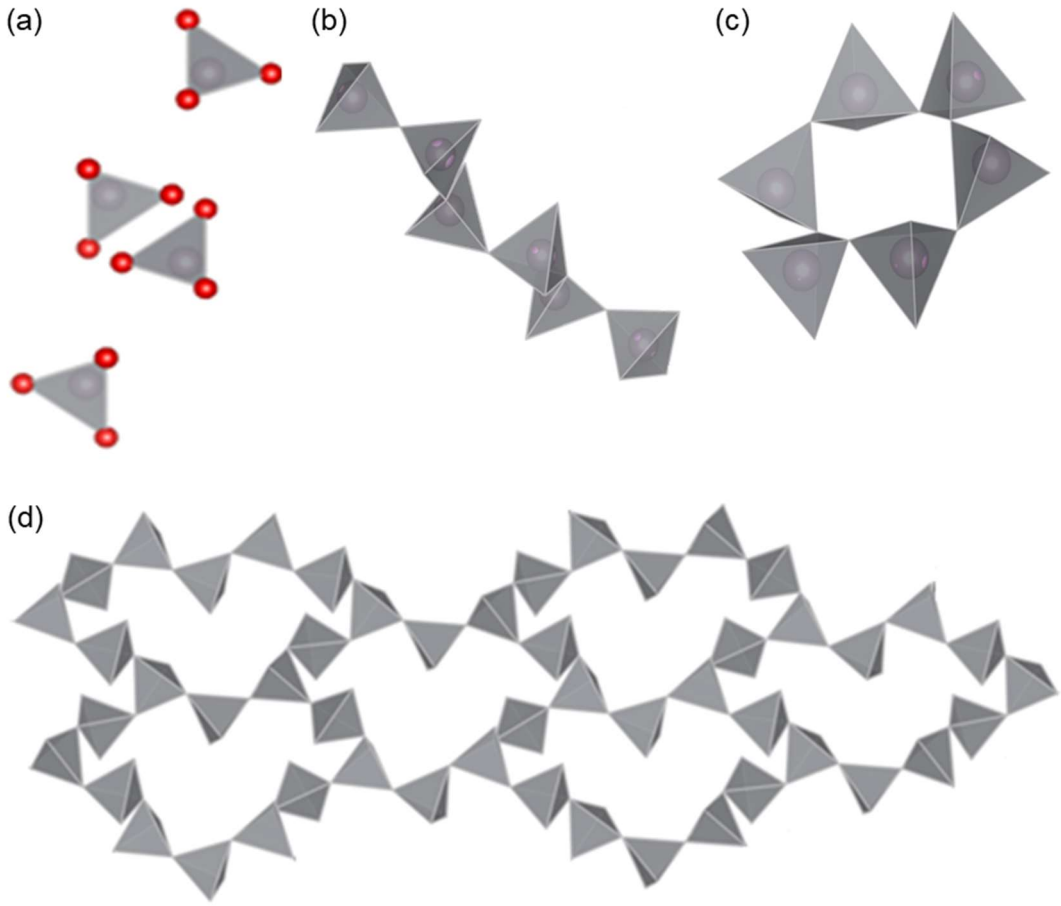

Figure 5.1 Arrangement of PO_4^{3-} tetrahedra in the four types of phosphates. (a) isolated PO_4^{3-} tetrahedra in orthophosphate Li_3PO_4. (b) 1D 2-conneted PO_3^- chain in polyphosphate $LiPO_3$. (c) 2D connected single $P_6O_{18}^{6-}$ ring in the cyclophosphate $Al_2P_6O_{18}$ and (d) $P_{20}O_{56}^{12-}$ chains in $Li_3P_5O_{14}$ form an ultraphosphate layer (this work). O atoms in (a) only are shown in red and PO_4^{3-} tetrahedra are shown in grey. Structural parameters are taken from references [12],[13] and [7] for panels (a-c), respectively, and replotted in VESTA.

The material of interest in this chapter, $Li_3P_5O_{14}$ possesses the aforementioned ultraphosphate motif. These ultraphosphate layers produce a unique topology for the Li sublattices: two types of finite Li polyhedral $Li_6O_{16}^{26-}$ chains with comparatively short Li–Li distances (2.581–3.235 Å in the $Li_6O_{16}^{26-}$ chains) terminated with two distinct vacant tetrahedral sites (**Figure**

5.2(a)). These ordered $Li_6O_{16}^{26-}$ chains are isolated from each other. The type A $Li_6O_{16}^{26-}$ chain is made up of six crystallographically distinct corner- and edge-shared distorted tetrahedra. The type B $Li_6O_{16}^{26-}$ chain consists of five distorted tetrahedra and an Li5 distorted square pyramid connected by corner and edge sharing. These two types of $Li_6O_{16}^{26-}$ chains are alternately arranged parallel to the *ab* plane forming Li polyhedral layers, as shown in **Figure 5.2(b)**. These Li polyhedral layers are further alternately stacked with infinite ultraphosphate layers along the *c*-axis to form a 3D framework. Similar to the Li-occupied sites, the two vacant tetrahedra are coordinated by four PO_4^{3-} tetrahedra by corner sharing (two internal PO_4^{3-} tetrahedra and two branching PO_4^{3-} tetrahedra), and two LiO_4^{7-} tetrahedra by edge sharing.

$Li_3P_5O_{14}$ is a layered structure built from infinite ultraphosphate $P_{20}O_{56}^{12-}$ layers with 12-membered corrugated $P_{12}O_{36}^{12-}$ rings constructed from corner-sharing PO_4^{3-} tetrahedra (**Figure 5.2(c)**) alternately stacked with Li polyhedral layers along the *c*-axis (**Figures 5.2 (d,e)**). The charge compensating Li cations are located between $P_{20}O_{56}^{12-}$ layers, forming bonds to four or five oxide ions in these adjacent layers. The $P_{20}O_{56}^{12-}$ layers provide pathways for ion transport between adjacent Li polyhedral layers. There are four crystallographically distinct $P_{12}O_{36}^{12-}$ rings, which are similar in size and shape, and each is connected to six adjacent rings through branching PO_4^{3-} tetrahedra to form the infinite ultraphosphate layer.

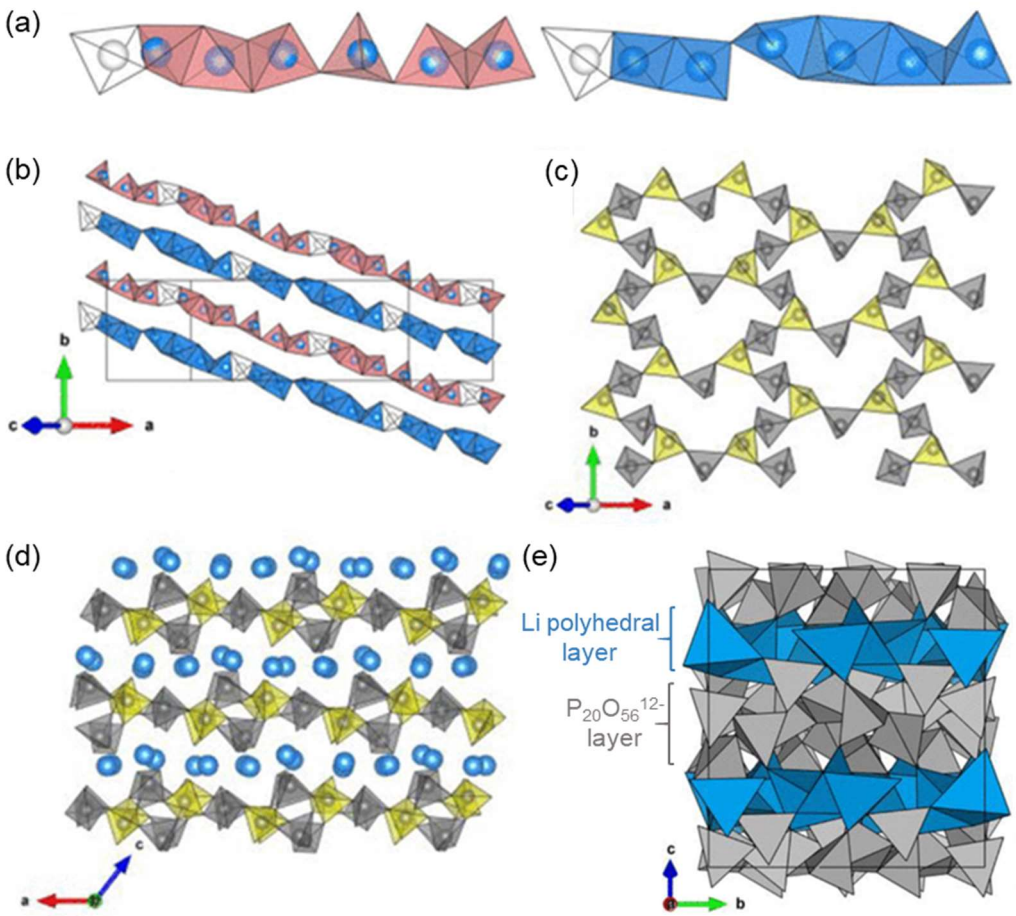

Figure 5.2 Crystal structure of $Li_3P_5O_{14}$ and the polyhedral arrangement of Li and P. (a) Arrangement of lithium in $Li_3P_5O_{14}$, the two types of $Li_6O_{16}^{26-}$ chains, type A (red) and type B (blue), with different connection modes along with two distinct vacant tetrahedral sites at the terminating ends. (b) Stacking of the $Li_6O_{16}^{26-}$ chains along [110]. (c) Arrangement of the infinite $P_{10}O_{56}^{12-}$ ultraphosphate layers in $Li_3P_5O_{14}$. (d) Projection of the atomic arrangement in $Li_3P_5O_{14}$ along the *b*-axis, showing $P_{20}O_{56}^{12-}$ ultraphosphate layers alternately stacked with Li polyhedral layers. Grey and yellow tetrahedra represent internal and branching PO_4^{3-} tetrahedra respectively, Li atoms are represented by blue spheres. (e) Resulting unit cell of $Li_3P_5O_{14}$ projected along the *a*-axis, showing the alternating stacking arrangement of the ultraphosphate layers and the Li polyhedral layers along the *c*-axis. PO_4^{3-} tetrahedra and Li polyhedra are shown in grey and blue respectively.

5.4 Experimental

Details on sample synthesis as well as analytical methods other than NMR can be found in reference[1]. ^{31}P and ^{6}Li MAS NMR experiments were performed on a 9.4 T Bruker Avance III HD spectrometer using a 4 mm HXY MAS probe (in double resonance mode) at an MAS frequency $\omega_r/2\pi$ of 10 kHz with X channel tuned to ^{31}P and ^{6}Li at $\omega_0/2\pi$ (^{31}P and ^{6}Li) = 162 and 59 MHz, respectively. ^{6}Li MAS experiments were recorded via one pulse experiments while ^{31}P MAS experiments were measured via one pulse and Hahn-echo sequences. 90° pulse durations of 3 and 3.8 μs at radio frequency (rf) field amplitudes of $\omega_1/2\pi$ = 83 and 65 kHz were used for ^{6}Li and ^{31}P, respectively. All MAS experiments were performed with quantitative recycle delays of more than 5 times the ^{6}Li and ^{31}P longitudinal relaxation time, T_1 measured via the saturation recovery pulse sequence $(\pi/2)_{x100} - \tau - \pi/2 -$ acq with increasing recovery delay values τ. The data were fitted with a stretch exponential function of the form $1 - \exp[-(\tau/T_1)^{\alpha}]$ (with α ranging from 0.7 to 1). ^{6}Li and ^{31}P shifts were referenced to 10 M LiCl in D_2O and 85% H_3PO_4 in water at 0 ppm, respectively.

^{31}P-^{31}P homonuclear spin diffusion experiments were performed on a 9.4 T Bruker Avance III HD spectrometer equipped with a 4 mm HXY MAS probe (in double resonance mode) with the X channel tuned to $\omega_0/2\pi(^{31}P)$ = 162 MHz with a 90° pulse of duration 3.8 μs at a rf field amplitude of $\omega_1/2\pi(^{31}P)$ = 65 kHz and an MAS rate of $\omega_r/2\pi$ = 10 kHz. The data was measured using the exchange spectroscopy (EXSY) pulse sequence $\pi/2_{(x)} - t_1 - \pi/2_{(y)} - \tau_m - \pi/2_{(x)}$

– acq where τ_m is the mixing time that allows for the spins to diffuse (values of 0, 0.05, 0.25 and 1 s were used).

Variable temperature ^{7}Li NMR experiments were recorded with a 4 mm HX High Temperature (HT) MAS Probe on a 9.4 T Bruker Avance III HD spectrometer under static conditions with the X channel tuned to ^{7}Li at $\omega_0/2\pi$ (^{7}Li) = 156 MHz. The sample was sealed in a glass ampoule, and the spectra were recorded with a pulse length of 1.5 μs at a rf field amplitude of $\omega_1/2\pi$ = 83 kHz and referenced to 10 M LiCl in D_2O at 0 ppm. All ^{7}Li one pulse NMR spectra were obtained under quantitative recycle delays of more than 5 times the T_1 time constants at each temperature. T_1 time constants were measured using the saturation recovery pulse sequence $(\pi/2)_{x100} - \tau - \pi/2$ - acq with increasing recovery delay values τ. The data were fitted with a stretch exponential function of the form $1 - \exp[-(\tau/T_1)^{\alpha}]$ (with α ranging from 0.6 to 1). The ^{6}Li static T_1 time constant was also recorded in this manner. $T_{1\rho}$ time constants were recorded using a spin-lock pulse sequence preceded with pre-saturation block in order to reduce experiment time and ensure all sites were in a steady-state. Hence the pulse sequence used was of the form $(\pi/2)_{x100}$ – d – $\pi/2$ – spin-lock – acq (where the duration of the spin-lock pulse is incremented and the value of the delay, d ranged from 150 to 90 s) at frequencies of $\omega_1/2\pi(^7\text{Li})$ = 25, 50, and 80 kHz and the data were fitted to a stretch exponential function of the form $\exp[-(\tau/T_{1\rho})^{\beta}]$ (with β ranging from 0.4 to 0.8). The stretch exponential was used in order to account for a distribution of τ_c values, temperature gradients across the sample (see below) and the inherent multi-exponential behaviour for relaxation of I = 3/2 nuclei.[14-16] ^{7}Li

SAE decay curves were recorded on the same 9.4 T NMR spectrometer using a 4 mm HX HT MAS probe using the three-pulse Jeener-Broekaert sequence. Due to the extremely long ^{7}Li longitudinal relaxation time in $Li_3P_5O_{14}$, a pre-saturation block was also used in the collection of the SAE NMR spectra so that the pulse sequence implemented was $(\pi/2)_{x100} - d - (\pi/2)_y - t_p - (\pi/4)_x - \tau_m - (\pi/4)_\phi - t_p - acq$; the recycle delay, d used was 260 s, the 90° pulse length was 1.8 μs at a rf field amplitude of $\omega_1/\pi(^{7}Li)$ = 70 kHz. The Jeener-Broekaert sequence generates quadrupolar order[17,18] to create stimulated echoes that decay with the mixing time τ_m. The short preparation time, t_p of only 15 μs ensured the formation of a quadrupolar spin-alignment state whilst simultaneously suppressing the dipolar contributions. A series of 20 echoes were collected with mixing times ranging from 10 μs to 10 s, at three different temperatures (295, 330 and 373 K). The resulting echo decays, $S_2(t_p,\tau_m,\tau_c)$ as a function of τ_m were fitted with a single stretched exponential function of the form:

$$(1 - S_\infty)\exp\left[-\left(\frac{\tau_m}{\tau_c}\right)^{\gamma}\right] + S_0 \qquad \text{(Eq 5.1)}$$

where S_∞, τ_c, S_0 and γ are the echo amplitude at $\tau_m = \infty$, the correlation time, the stretch exponential and the echo amplitude at $\tau_m = 0$, respectively, with γ ranging from 0.2 to 0.6.

Variable temperature ^{31}P NMR experiments were performed with a 4 mm HX HT MAS Probe on a 9.4 T Bruker Avance III HD spectrometer under static conditions with the X channel tuned to ^{31}P at $\omega_0/2\pi(^{31}P)$ = 162 MHz. The spectra were recorded with a pulse length of 5 μs at a rf field amplitude of

$\omega_1/2\pi$ = 50 kHz and all ^{31}P one pulse NMR spectra were obtained under quantitative recycle delays measured using the same methodology as for ^{7}Li and the data fitted with a stretch exponential (with α ranging from 0.8 to 1). $T_{1\rho}$ time constants were measured using spin-lock pulse sequence with a pre-saturation block (where the duration of the recycle delay ranged from 3700 to 4000 s) at a spin-locking frequency of $\omega_1/2\pi(^{31}P)$ = 25 kHz and the data fitted to a stretch exponential (with β ranging from 0.3 to 0.9)

Temperature calibrations were performed using the chemical shift thermometers $Pb(NO_3)_2$ using ^{207}Pb NMR[19,20] and CuI and CuBr using ^{63}Cu NMR.[21,22] The errors associated with this method were calculated using the isotropic peak line broadening and range from 5 to 20 K.

All density functional theory (DFT) calculations were carried out with the CASTEP (version 20.11) package.[23] The geometry optimisation was performed using plane-wave DFT[24] with the PBE[25] exchange-correlation functional and on-the-fly generated ultrasoft pseudopotentials.[26] The Brillouin zone was sampled using a 1 × 1 × 1 Monkhorst-Pack[27] k-point grid with plane-wave cutoff energy of 850 eV (i.e. energy threshold of 1 meV/atom). The electronic energy convergence was set to 1 × 10^{-9} eV/atom. The geometry optimisation was carried out using convergence thresholds of 1 × 10^{-5} eV/atom, 3 × 10^{-2} eV/Å, 5 × 10^{-2} GPa and 1 × 10^{-3} Å respectively for the maximum energy change, maximum force, maximum stress and maximum displacement. All NMR parameters were calculated on the optimized geometry using the GIPAW approach.[28,29] To facilitate the comparison between computational and experimental results, the computed isotropic chemical

shielding, $\sigma_{iso,cs}$, was converted into isotropic chemical shift, $\delta_{iso,cs}$, using $\delta_{iso,cs} = \sigma_{ref} + m\sigma_{iso,cs}$. For ^{6}Li, m and σ_{ref} were taken from our calculations of Li_2O, LiOH and Li_2CO_3 and compared with shifts from the literature[30] yielding σ_{ref} = 89.47 ppm and m = -0.998. For ^{31}P, σ_{ref} = 278 ppm and m = -0.999 were taken from the literature.[31]

5.5 Results and Discussion

5.5.1 ^{31}P MAS NMR

^{31}P MAS NMR was deployed in order to gain insight into the local environment of the PO_4^{3-} tetrahedra (**Figure 5.3**). At short recycle delays (< 20 s) *vs.* the T_1 times of $Li_3P_5O_{14}$ (~1600 s), a broad peak emerges at ~ -25 ppm, corresponding to an amorphous phase that was not detected through diffraction measurements. As the recycle delay is increased a number of narrow resonances appear centred at ~ -40 ppm, typical for ultraphosphate rings[32] corresponding to the crystalline $Li_3P_5O_{14}$ (**Figure 5.3**). The ^{31}P spin-lattice relaxation (SLR) time for the sites in $Li_3P_5O_{14}$ is extremely long (**Table 5.1**) therefore much longer recycle delays are required in order to observe the resonances. The long relaxation times of the ^{31}P resonances of $Li_3P_5O_{14}$ is due to the lack of efficient pathways for relaxation (see **Chapter 1 section 1.4**) with the nearest NMR active nuclei to the P atoms being the low natural abundance ^{17}O (0.038%) any dipolar or quadrupolar relaxation from ^{17}O nuclei will be minimal. The primary mechanisms for ^{31}P SLR will likely come from chemical shift anisotropy (CSA) and homonuclear dipolar to neighbouring ^{31}P nuclei, as well as heteronuclear dipolar relaxation and quadrupolar relaxation from the nearest ^{7}Li nuclei, however these interactions decrease significantly with interatomic distance, hence the most prominent relaxation mechanism will likely be CSA. This conclusion is supported by the extremely long SLR times for ^{31}P, as a predominantly dipolar or quadrupolar relaxation pathway would likely lead to faster relaxation. From the experimental spectrum, at least 18 resonances can be discerned, while 20 crystallographically distinct, equally

populated ^{31}P sites are expected from the crystal structure (**Figure 5.2**). However a number of the resonances are overlapping due to the rather similar chemical environments of the PO_4^{3-} tetrahedra, challenging the assignment of the ^{31}P resonances. In order to support the assignment of the spectrum of $Li_3P_5O_{14}$, calculations of the NMR parameters using the GIPAW[23,28] approach as implemented in CASTEP[23] were performed in order and allowed for the simulation shown in green in **Figure 5.3**. There is a reasonable agreement between the GIPAW simulations with the experimental spectrum of $Li_3P_5O_{14}$, therefore to a good degree of confidence the model used is suitable in order to assign the resonances observed experimentally.

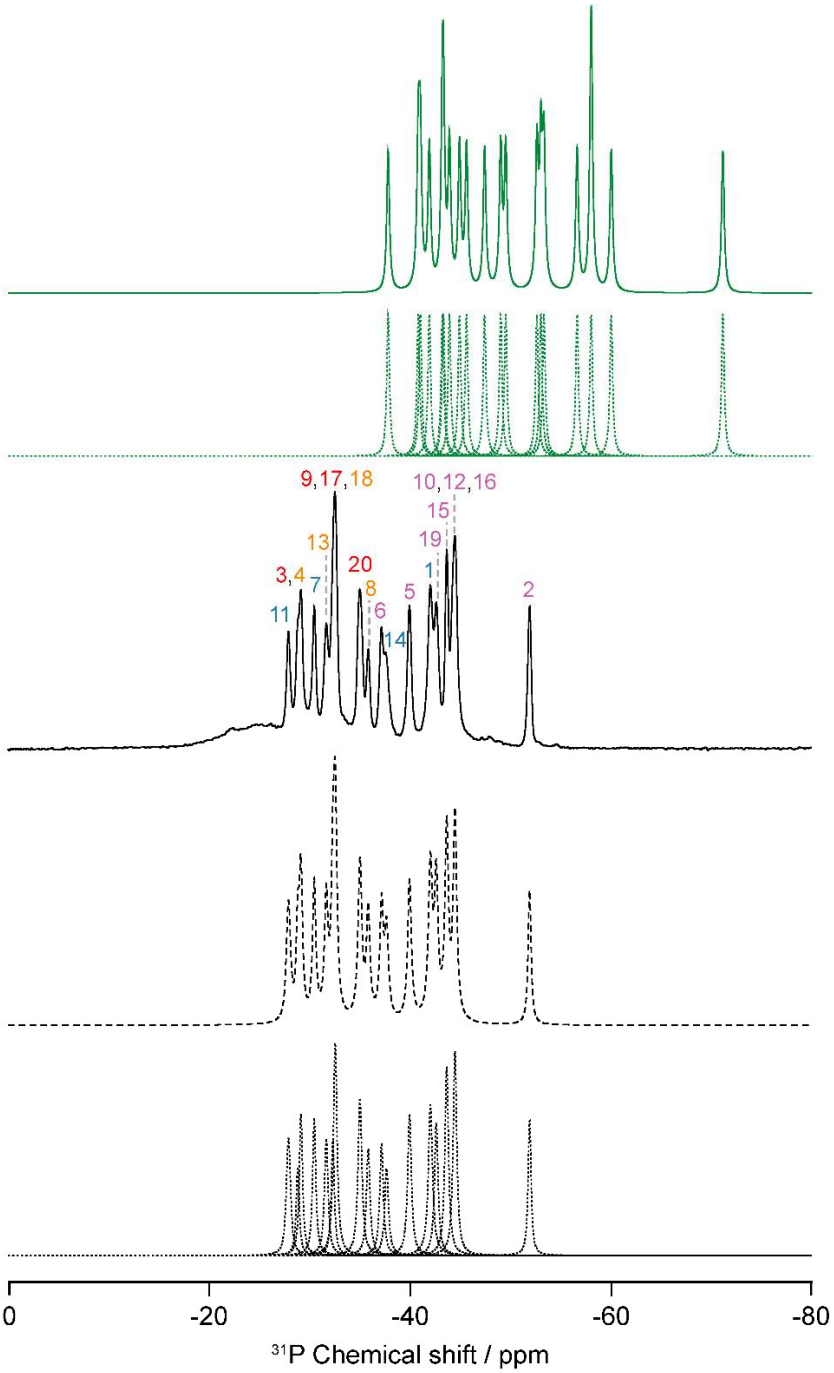

Figure 5.3 ^{31}P MAS spectrum of $Li_3P_5O_{14}$ collected 9.4 T and $\omega_r/2\pi$ = 10 kHz with the spectral assignment based off the DFT simulations. The experimental spectrum (full black line), total fit (dashed black line), spectral deconvolution (dotted lines) and GIPAW-simulated spectrum (green line) are shown. The assignments of the ^{31}P resonances are also shown, where type i, type ii, type iii and type iv PO_4^{3-} groups are coloured in pink, blue, red and orange respectively.

Table 5.1 Summary of the assignment of the ^{31}P MAS NMR spectrum of $Li_3P_5O_{14}$ and SLR times obtained through the saturation recovery pulse sequence.

Type	Assignment	^{31}P chemical shift / ppm	T_1 / s
Type i	P2	-51.9	1938 ± 119
	P5	-40.0	1731 ± 68
	P6	-37.2	1663 ± 86
	P10	-44.5	1758 ± 145
	P12	-44.5	1758 ± 145
	P15	-43.7	1613 ± 63
	P16	-44.5	1758 ± 145
	P19	-42.6	1590 ± 87
Type ii	P1	-42.1	1603 ± 38
	P7	-30.5	1380 ± 160
	P11	-27.9	1580 ± 256
	P14	-37.7	1688 ± 98
Type iii	P3	-28.9	1496 ± 169
	P9	-32.5	1562 ± 77
	P17	-32.5	1562 ± 77
	P20	-35.1	1652 ± 79
Type iv	P4	-28.9	1496 ± 169
	P8	-35.9	1688 ± 181
	P13	-31.7	1553 ± 126
	P18	-32.5	1562 ± 77

Upon close inspection of the crystal structure of the ultraphosphate layer in $Li_3P_5O_{14}$, two types of rings (A and B) repeat along the *b*-axis (**Figure 5.4(a)**). The PO_4^{3-} tetrahedra in these rings can be divided into two categories, PO_4^{3-} groups that have three bridging O atoms to other PO_4^{3-} groups (type i) (shown in pink in **Figure 5.4**) and ones that have two bridging O atoms to other phosphate groups. This second group can be further sub-divided into three more categories, the first corresponds to PO_4^{3-} tetrahedra at the centre of the conjoined rings and are the only P atoms that are not shared between rings A and B, i.e P1, P7, P11 and P14 (type ii) (shown in blue in **Figure 5.4**). The remaining two sub-groups correspond to the remaining PO_4^{3-} tetrahedra that have bridging O atoms with two other phosphate groups and are differentiated from one another by their respective positioning relative to one another along the *c*-axis (**Figure 5.4(b)**). The P atoms that are found at the upper part of ring A or B are shown in red (type iii) and those at the lower part of the ring are shown in orange (type iv).

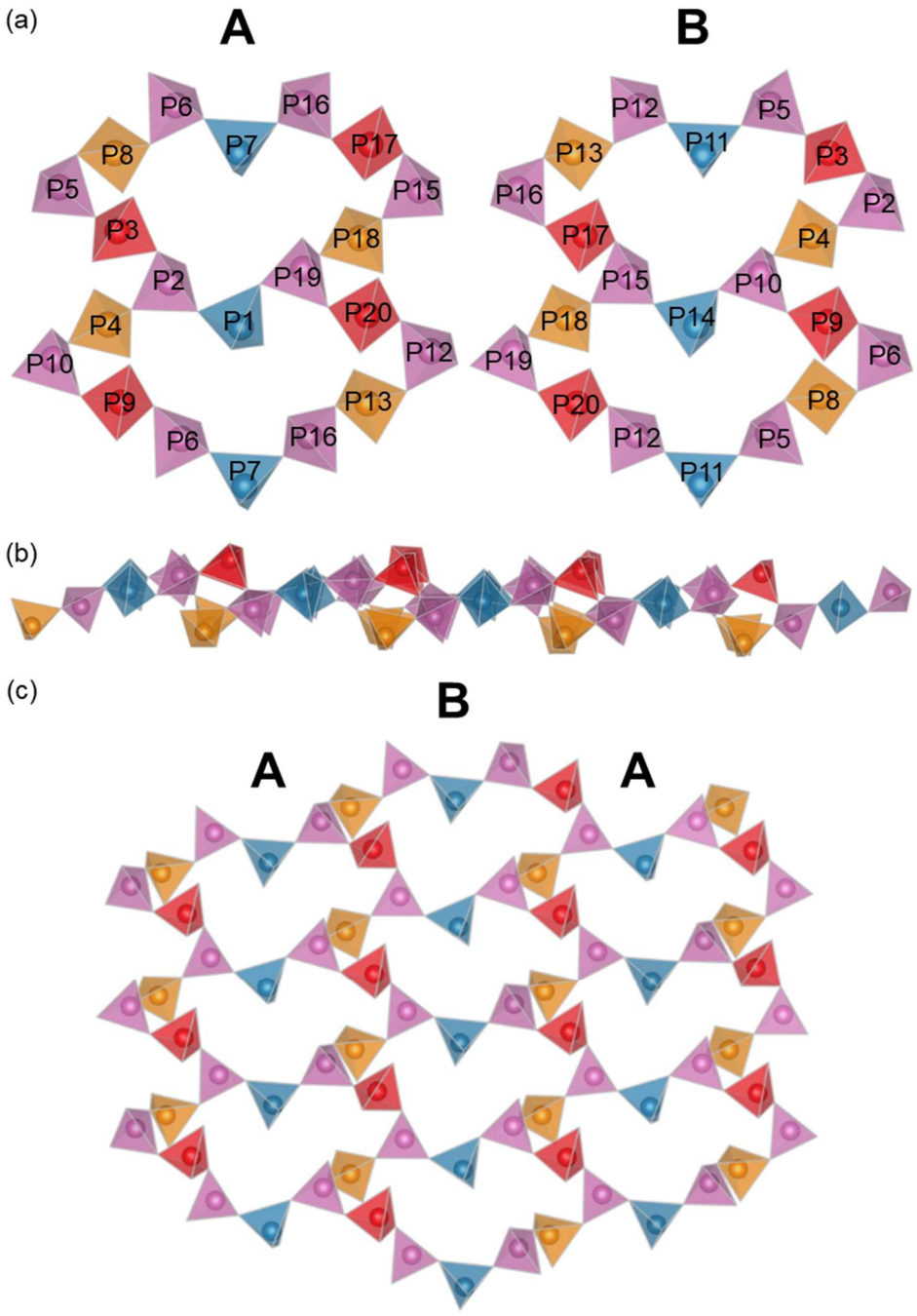

Figure 5.4 Crystal structure of $Li_3P_5O_{14}$ displaying (a) the different crystallographic P sites, (b) view along the *b*-axis highlighting the subtle difference between the orange and red polyhedra and (c) the two types of interconnecting ultraphosphate rings. Chains of ring A and B along the *b*-axis are interconnected through sharing PO_4^{3-} tetrahedra. PO_4^{3-} groups are colour coded according to their type (see text) where type i, type ii, type iii and type iv PO_4^{3-} groups are coloured in pink, blue, red and orange respectively.

GIPAW simulations allow for the resonances in the ^{31}P MAS NMR spectrum of $Li_3P_5O_{14}$ to be rationalised with the crystal structure (**Figure 5.3**). The resonances associated with type i PO_4^{3-} groups tend to appear at lower chemical shift, due to three other phosphate groups in close proximity leading to an increased degree of shielding of these ^{31}P nuclei. There does not appear to be any visible chemical shift trend between type ii-iv phosphate groups, however the overall trend that is observed across all groups is related to the LiO_4 tetrahedra that share bridging O atoms with the corresponding phosphate group. Resonances appear at chemical shifts related to the number of O atoms in the LiO_4 tetrahedra that are bonded to three other atoms. For example, P2 shares a bridging O with a Li atom that has three O atoms that have bonds to three atoms. This Li atom then does not donate as much electron density to these three Li-O bonds and hence a larger degree of electron density remains within the ionic radius of the Li atoms, leading to an increase in shielding of the nearby ^{31}P nucleus. P2 is the only site of type i that possesses this feature, leading to the increased shielding and lower chemical shift. Moreover, since P2 also shares bridging O atoms with three other phosphate groups (which will have inherently more electron density), this increase in shielding of the nearby Li atom will lead to a more spherical distribution of electron density around P2. Subsequently, this causes there to a smaller degree of CSA and a less efficient pathway for SLR, causing P2 have an increased T_1 of 1800 s compared to ~ 1600 s for the other P resonances. This trend is also observed across the rest of the resonances, with the T_1 time increasing with the number of bridging O atoms with three bonds and the resulting increase in symmetry of the electron density distribution leading to a smaller degree of CSA.

^{31}P-^{31}P spin diffusion NMR spectra (**Figure 5.5-5.8**) as a function of mixing time, τ_m were utilised in order to attempt to further rationalise the structural assignment of the ^{31}P NMR spectrum of $Li_3P_5O_{14}$ with the crystal structure obtained through diffraction techniques. Experimentally observed off-diagonal cross peaks in the 2D spin diffusion spectra emerge at the corresponding chemical shifts between sites that undergo chemical exchange or are in close spatial proximity, through dipolar coupling mediated spin diffusion.[33,34] Since it is highly unlikely that the ^{31}P atoms in $Li_3P_5O_{14}$ exchange from one another, it is safe to assume that any observed cross peaks are due to spin diffusion. The number of observed cross peaks is expected to increase with τ_m as during this time the spins are allowed to diffuse throughout the structure, hence a longer τ_m allows for the spins to diffuse to sites further away from their origin. The rate at which cross peaks emerge and build as a function of τ_m can be fitted and corresponding dipolar coupling constants, d_{ij} can be extracted and hence interatomic distances can be calculated, allowing for a full spectral assignment. However, due to time constraints arising from the exceptionally long ^{31}P SLR time, T_1 (~1600 s) a full range of τ_m values was not possible in this case, therefore the acquired spectra are used qualitatively in this case in order to confirm experimentally the assignment proposed by computational prediction of the ^{31}P data. At τ_m = 50 ms (**Figure 5.6**), the emergence of cross peaks can be seen between several sets of sites and as τ_m increases to 250 ms (**Figure 5.7**), further cross peaks are clearly visible and this trend continues as τ_m increases to 1 s (**Figure 5.8**). It is often difficult to observe low intensity cross peaks in the 2D spin diffusion NMR spectra and it is often easier to extract 1D horizontal slices of the 2D spectra at the chemical shifts of the

observed peaks to observe cross peaks. This method was utilised here to observe as many of the cross peaks as possible (**Figure 5.9**).

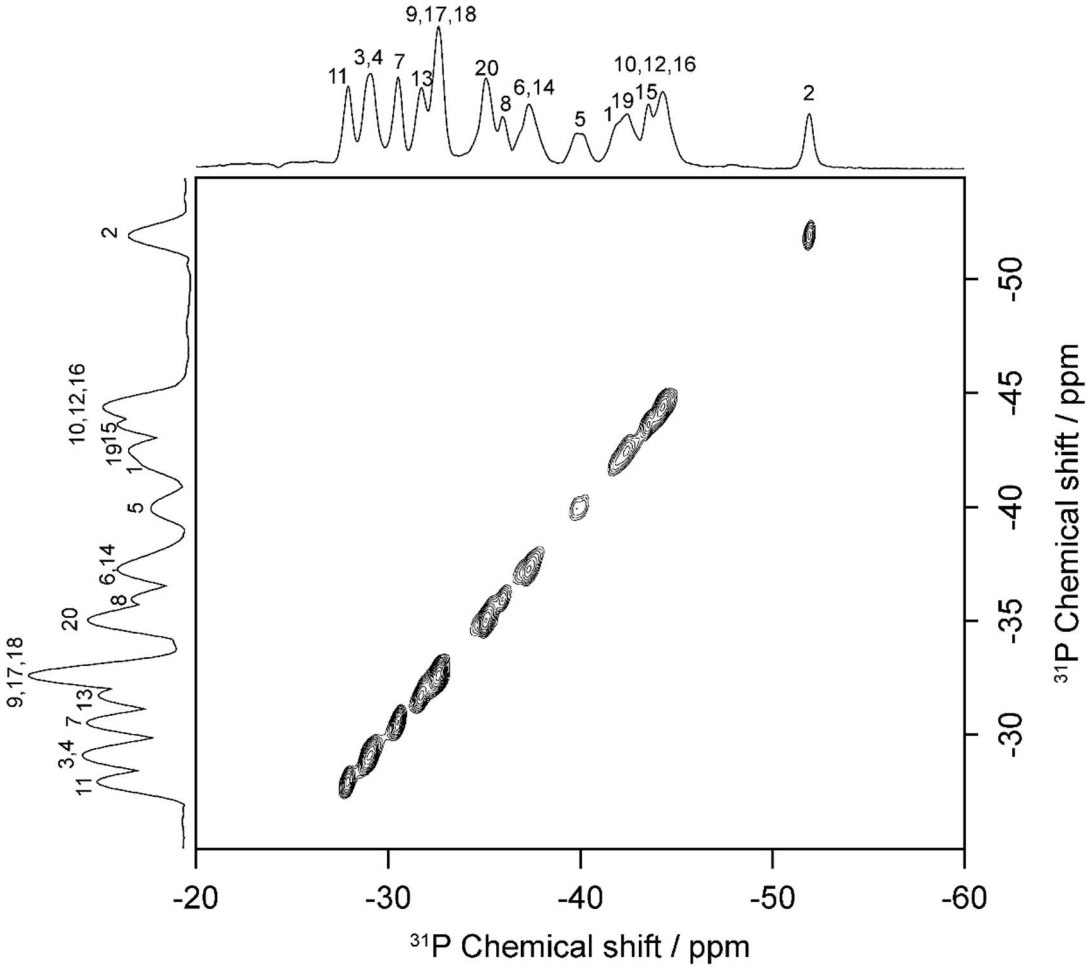

Figure 5.5 2D ^{31}P-^{31}P spin-diffusion NMR spectra of $Li_3P_5O_{14}$ recorded at $\omega_r/2\pi$ = 10 kHz in the absence of exchange (mixing time of 0 s) with diagonal peaks shown in black.

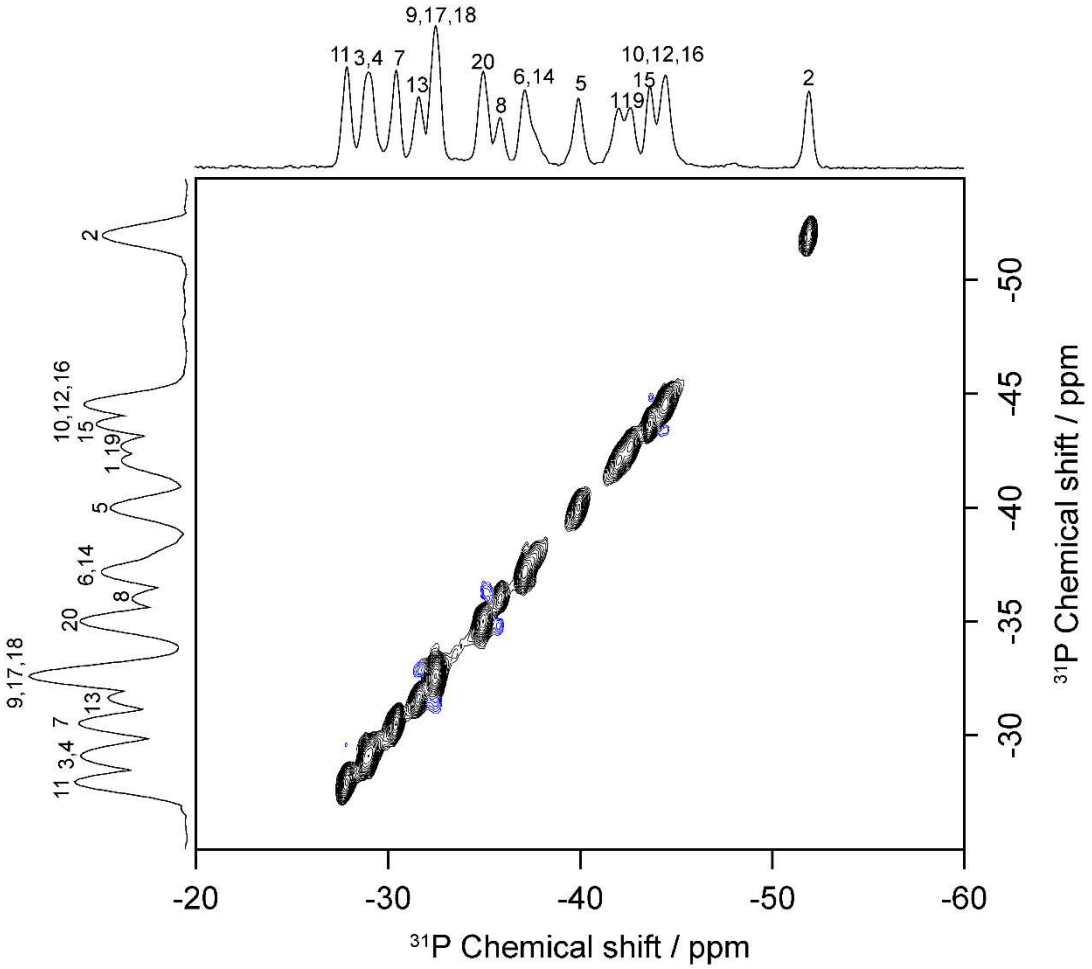

Figure 5.6 2D ^{31}P-^{31}P spin-diffusion NMR spectra of $Li_3P_5O_{14}$ recorded at $\omega_r/2\pi$ = 10 kHz and a mixing time of 50 ms with diagonal and cross peaks shown in black and blue, respectively.

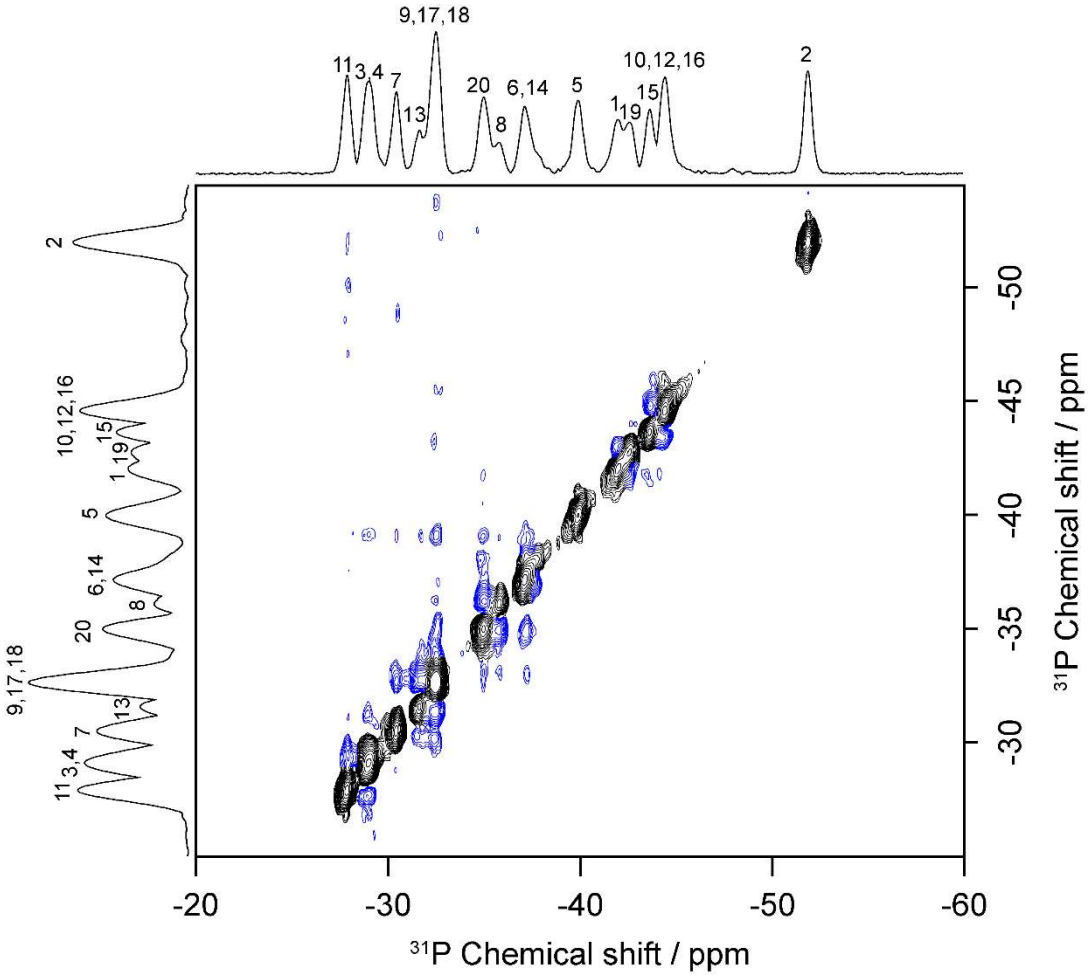

Figure 5.7 2D ^{31}P-^{31}P spin-diffusion NMR spectra of $Li_3P_5O_{14}$ recorded at $\omega_r/2\pi$ = 10 kHz and a mixing time of 250 ms with diagonal and cross peaks shown in black and blue, respectively.

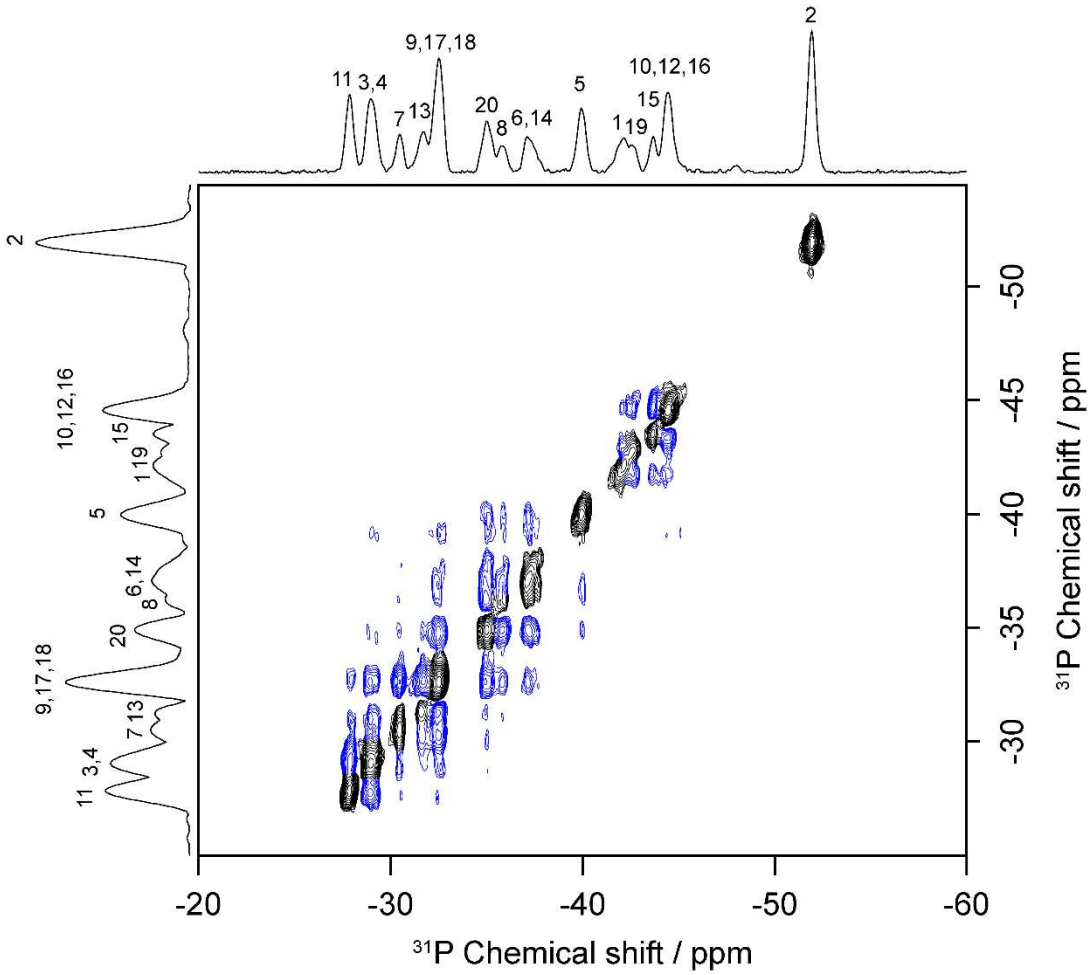

Figure 5.8 2D ^{31}P-^{31}P spin-diffusion NMR spectra of $Li_3P_5O_{14}$ recorded at $\omega_r/2\pi$ = 10 kHz and a mixing time of 1 s with diagonal and cross peaks shown in black and blue, respectively.

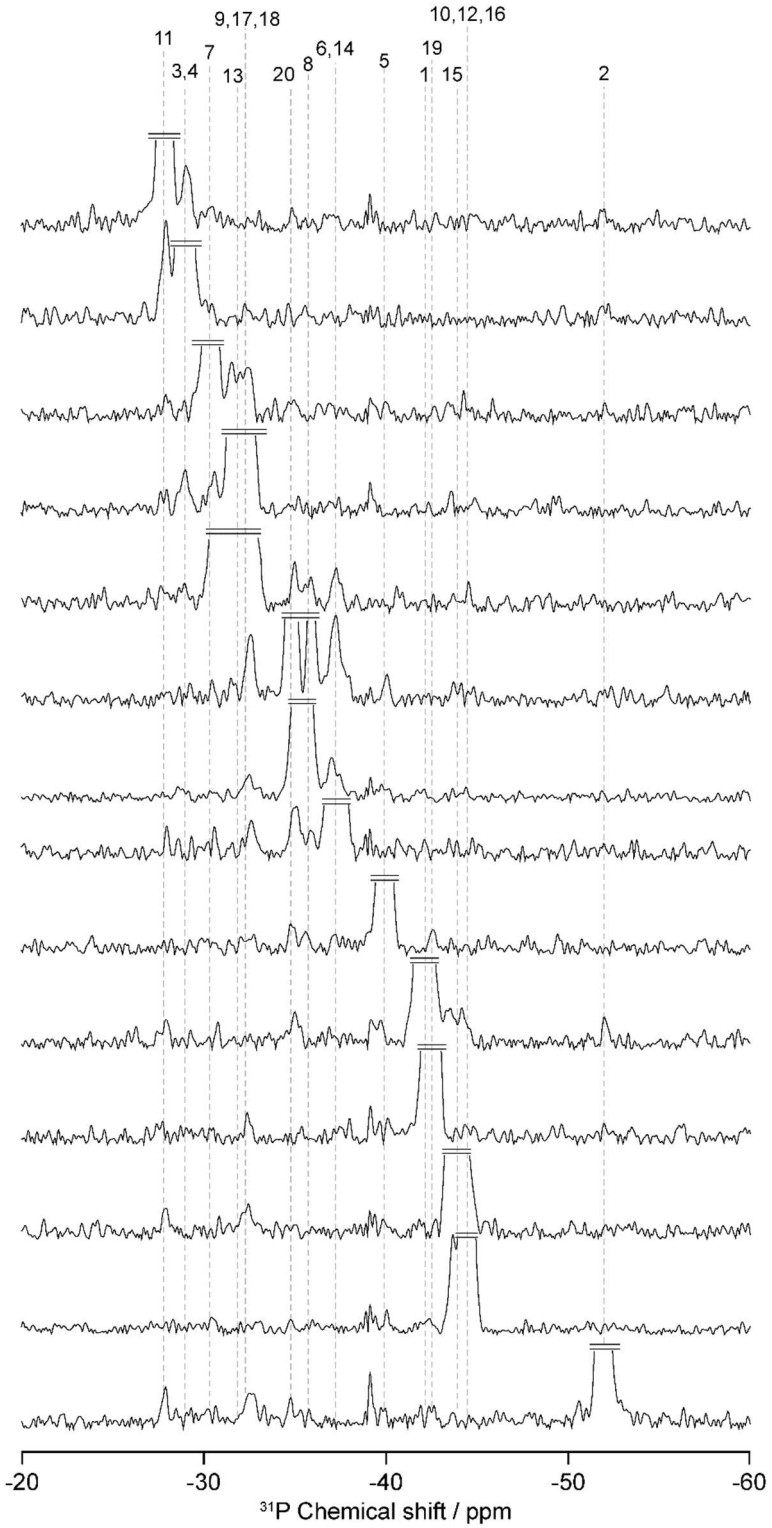

Figure 5.9 Extracted horizontal slices of the 2D spin-diffusion NMR spectra of $Li_3P_5O_{14}$ with τ_m = 1 s, at the positions of the peaks on the diagonal in the 2D spectrum. The assignment and positions of the many different peaks are also shown by grey dashed lines. Double lines show where the intensity of resonances has been cut off for clarity.

A full report of the observed cross peaks (at τ_m = 1 s) is available in **Table 5.2** along with a range of interatomic distances between the P sites in $Li_3P_5O_{14}$ obtained from the assignment of the ^{31}P MAS spectrum based off the GIPAW calculations. P atoms that share bridging O atoms in $Li_3P_5O_{14}$ are separated by an interatomic distance of approximately 2.8 Å. At an interatomic distance of less than 3 Å, it is expected that cross peaks would be clearly visible, at a distance of less than 5 Å a τ_m = 1 s should be sufficient to observe cross peaks. Many of the assigned sites in the ^{31}P spectrum match well with what would be predicted from DFT, for example sites 1,2,6,8,9,17 and 18 all have cross peaks with sites within 3 Å and a number of sites within a distance of 5 Å. However, clearly there are a number of discrepancies in the experimentally observed cross peaks with the assignment of the ^{31}P NMR spectrum using GIPAW computations, namely sites: 10,11,12,13,14 and 20 which do not observe cross peaks with sites within 3 Å as would be predicted. Further work is required in order to rationalise the ^{31}P assignment of the 1D spectrum of $Li_3P_5O_{14}$ based off of DFT calculations with the experimentally observed ^{31}P-^{31}P spin diffusion experiments, one way of addressing this would be through the Incredible Natural Abundance Double Quantum Transfer Experiment (INADEQUATE) in order to further correlate the various P atoms that share bridging O atoms through $^2J_{PP}$ coupling.[35-37]

Table 5.2 Summary of the interatomic distances between different P sites in $Li_3P_5O_{14}$ determined through a combination of diffraction data[1] and DFT, with the cross peaks observed in the ^{31}P-^{31}P EXSY NMR spectra at τ_m = 1 s. Sites listed in brackets are unresolved and are hence grouped together.

Site	Interatomic distance to other P sites/ Å				Cross peaks observed
	≤ 3	≤ 5	≤ 6	> 6	
1	2,19	6, 9, 13, 16, 18, 20	3, 4, 7	5, 8, 10,11,12,14,15, 17	2, (10,12,16),11,19 20
2	1,3, 4	5,7,8,9,10,19	6,11	12,13,14,15,16, 17,18,20	1, (3,4),5,(9,17,18),11,2 0
3	2,5	4,6,7,8,10,11	1,9	12,13,14,15,16, 17,18,19,20	2,11,13,
4	2,10	3,5,6,9,11,14	1,8	7,12,13,15,16,1 7,18,19,20	2,11,13,
5	3,8, 11	2,4,6,9,12,14	10,	1,7,13,15,16,17, 18,19,20	2, (6,14),8, (10,12,16),19,20
6	7,8, 9	1,3,4,5,10,16	2	11,12,13,14,15, 17,18,19,20	5,7,8, (9,17,18),11,20
7	6,16	2,3,8,9,13,17, 18,19	1	4,5,10,11,12,14, 15,20	(6,14), (9,17,18), (10,12,16), 11,13,20,
8	5,6	2,3,7,9,14	4,10 ,11	1,12,13,15,16,1 7,18,19,20	5, (6,14)
9	6,10	1,2,4,5,7,8,14	3	11,12,13,15,16, 17,18,19,20	2,(6,14),7,8, (9,17,18), (10,12,16),15,19,20
10	4,9, 14	2,3,6,7,11,15	8	1,7,12,13,16,17, 18,19,20	1,5,7, (9,17,18),15,19
11	5,12	3,4,13,15,17, 20	2,8, 14	1,6,7,9,16,18,19	1,2, (3,4),7, (6,14),13,15,20
12	11,1 3,20	5,14,16,18,19	15,1 7	1,2,3,4,6,7,8,9	1,5,7, (9,17,18),15,19
13	12,1 6	1,7,11,17,20	18,1 9	2,3,4,5,6,8,9,10, 14,15	(3,4), 7,11,20
14	10,1 5	4,5,8,9,12,17, 20	11,1 8	1,2,3,6,7,13,16, 19	5,7,8, (9,17,18),11,20,7
15	14,1 7,18	10,11,16,19,2 0	12	1,2,3,4,5,6,7,8,9 ,13	(9,17,18), (10,12,16),11
16	7,13 ,17	1,6,12,15,20	18,1 9	2,3,4,5,8,9,10,1 1,14	1,5,7, (9,17,18),15,19
17	15,1 6	7,11,13,14,18 ,19	12,2 0	1,2,3,4,5,6,8,9,1 0	2, (6,14), 7,8, (9,17,18), (10,12,16),15,19,20

18	15,19	1,7,12,17,20	13,14,16	2,3,4,5,6,8,9,10,11	2, (6,14), 7,8, (9,17,18), (10,12,16),15,19,20
19	1,18,20	2,7,12,15,17	13,16	3,4,5,6,8,9,10,11,14	1,5, (9,17,18), (10,12,16)
20	12,19	1,11,13,14,15,16,18	17	2,3,4,5,6,7,8,9,10	1,2,5, (6,14),7, (9,17,18),11,13

5.5.2 Static ^{31}P Variable Temperature NMR

Static ^{31}P NMR spectra as a function of temperature are shown in **Figure 5.10** and display a complex pattern composed of many overlapping CSA powder patterns. The significantly large number of P sites with varying anisotropic chemical shielding, σ_{aniso} and isotropic chemical shifts, δ_{iso} challenges their resolution in a static ^{31}P NMR spectrum. However the primary observation of this set of experiments is that over the 295-520 K temperature range, the observed pattern of resonances remains unchanged. An approximate value of σ_{aniso} can be visually determined from the width of the static ^{31}P NMR spectrum of around 320 ppm. This value compared with the average value of σ_{aniso} obtained from the GIPAW calculations (at 0 K) of 264 ppm, indicates that PO_4^{3-} reorientation occurs at a rate slower than the NMR linewidth of 4.3×10^4 s^{-1}. However, since the large number of P sites challenges the resolution in the spectrum, CSA values for the individual sites cannot be determined. Another reason for the lack of linewidth narrowing is that phosphate reorientation may not occur about the correct PAS, i.e σ_{zz}^{PAS} (**Chapter 1 section 1.1**).

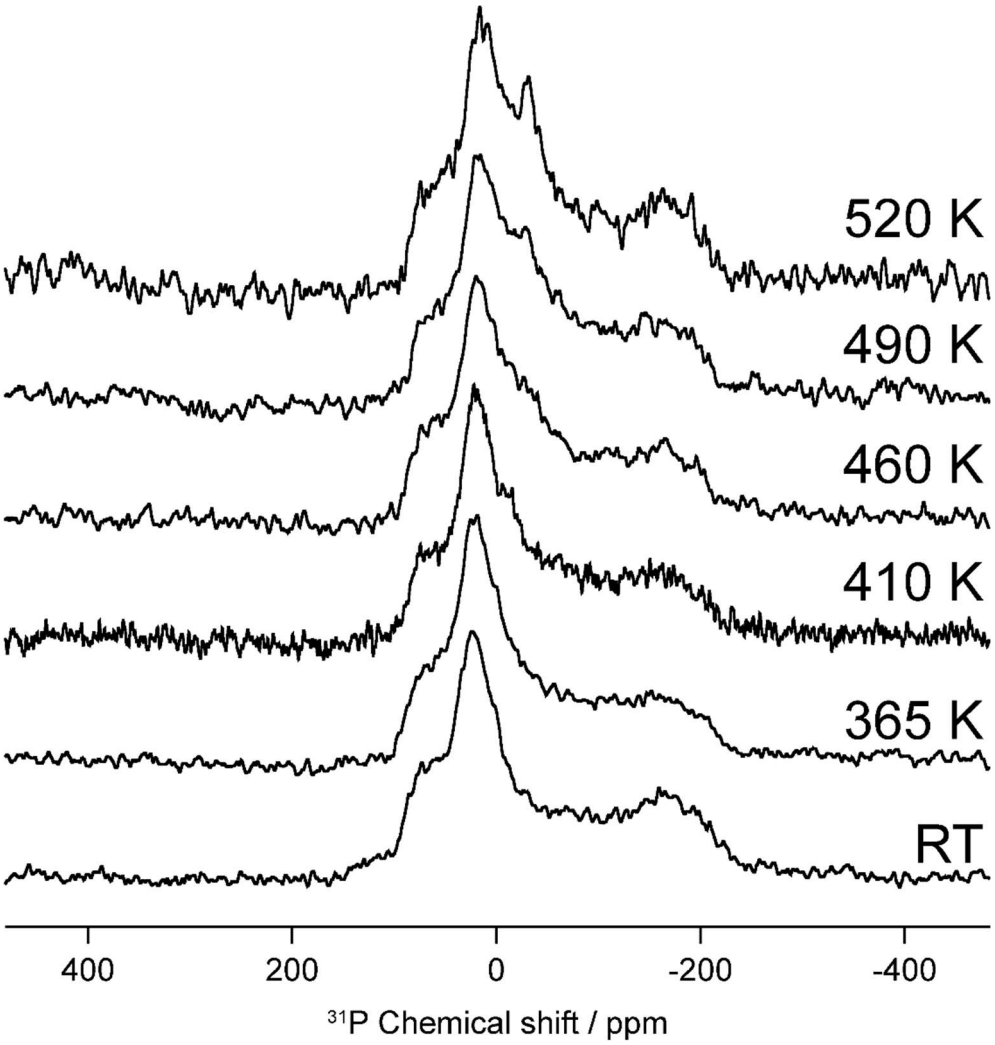

Figure 5.10 Static ^{31}P NMR spectra as a function of temperature for $Li_3P_5O_{14}$, displaying the broad CSA pattern that remains largely the same with temperature, indicating a lack of PO_4^{3-} reorientation motion.

5.5.3 ^{6}Li MAS NMR

Further information on the local arrangement of the atoms in $Li_3P_5O_{14}$ can be obtained through ^{6}Li MAS NMR (**Figure 5.11**). The ^{6}Li MAS NMR spectrum of $Li_3P_5O_{14}$ displays several overlapping resonances centred at ~ -1 ppm, five resonances can be deconvoluted in the observed pattern with integrations of 1 : 2.2 : 4.6 : 2 : 1.9 while 12 resonances of equal intensity expected from diffraction measurements, which corresponds well with the sum of the

integrations obtained from NMR. Due to the large number of expected resonances and the complex nature of the $Li_6O_{16}^{26-}$ chains, GIPAW calculations of $Li_3P_5O_{14}$ were implemented for the assignment of these resonances in the two $Li_6O_{16}^{26-}$ chains (**Figure 5.12**).

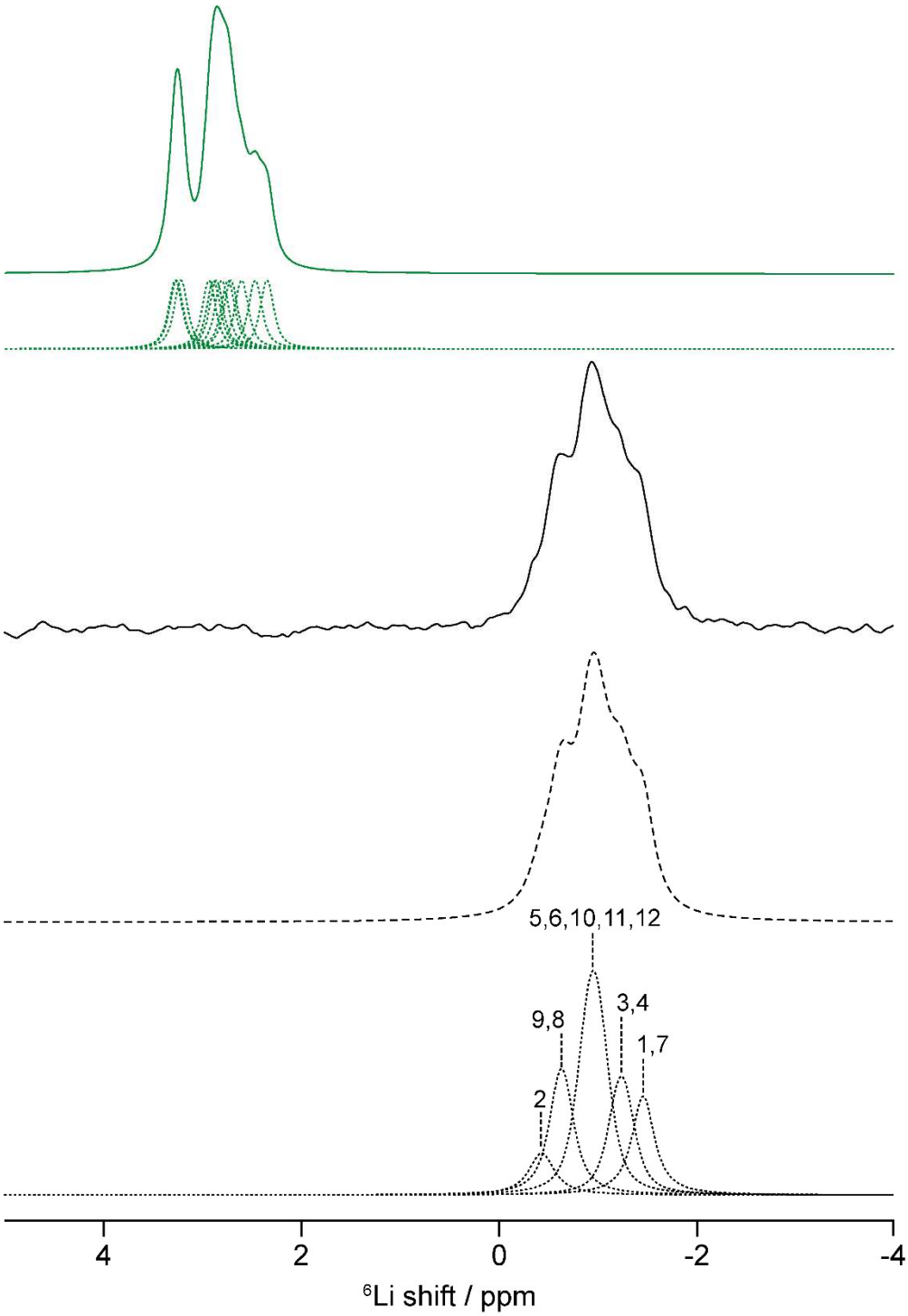

Figure 5.11 ^{6}Li MAS spectrum of $Li_3P_5O_{14}$ along with the spectral assignment based off the DFT calculations. The experimental spectrum (full black lines), total fit (dashed black lines), spectral deconvolution (dotted lines) and GIPAW simulated spectrum (green lines) are shown.

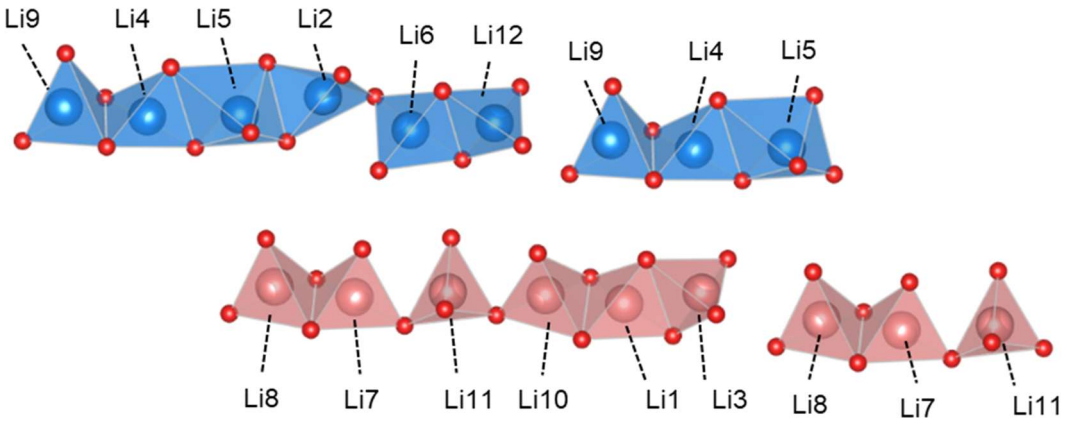

Figure 5.12 Crystal structure of the Li polyhedral layers in $Li_3P_5O_{14}$ displaying the two types of $Li_6O_{16}^{26-}$ chains, type A (red) and type B (blue), with different connection modes along with two distinct vacant tetrahedral sites at the terminating ends.

Upon closer inspection of the Li polyhedra and the assignment of the shifts using the GIPAW calculations, we observe the same trend as observed in the ^{31}P NMR, in that the observed shielding is related to the number of O atoms in the Li polyhedra that are bonded to three other atoms. For example, in the LiO_4 tetrahedra for Li1 and Li7, all of the O atoms in this tetrahedra are shared between three atoms, leading to an increase in electron density around the ^6Li nucleus and a lower shift. These two Li sites also edge share with adjacent LiO_4 tetrahedra, leading to a decrease in the Li-Li interatomic distance (~ 2.5 Å) and additional shielding of this site. The resonances associated with the remaining Li sites also follow this trend, with the observed shift increasing as the number of O atoms in the Li polyhedra that have three bonds decreases. Notably, our assignment seems to disagree with the semi-empirical correlations relating the lithium coordination environment and ^6Li NMR shifts,[38] with the distorted square pyramid site appearing at a higher shift than a

number of the tetrahedral LiO_4 sites. However, this observation is not entirely unexpected as the additional shielding from one additional O atom will be minimal, moreover the extremely narrow chemical shift range of ^6Li means the assignment of a number of Li resonances based off of coordination number is more complex than this first approximation and computational calculations appear to be more reliable.

5.5.4 ^{7}Li Line Narrowing NMR

Insight into the local ionic mobility of $Li_3P_5O_{14}$ was obtained through solid-state NMR. The temperature dependence of the static ^7Li NMR spectra over the 250–560 K temperature range is shown in **Figure 5.13**. At temperatures below ~385 K, ^7Li ion mobility is in the rigid lattice regime; therefore, the 1/2 ↔ −1/2 central transition is broadened by the strong ^7Li–^7Li homonuclear dipolar coupling, as well as ^7Li-^{31}P heteronuclear dipolar coupling and an NMR line width of ~4.5 kHz is observed. As the temperature is increased above 385 K, where the onset of motional narrowing occurs, the line width decreases due to the increasing motion of the ^7Li spins at frequencies larger than $\omega/2\pi$ continuously averaging dipolar interactions. Using an expression introduced by Waugh and Fedin,[39] relating the onset temperature of motional narrowing (T_{onset}) with the activation energy of the diffusion process, given by **equation 5.2**:

$$E_a = 1.67 \times 10^{-3} \cdot T_{onset} \qquad \text{(Eq. 5.2)}$$

an approximate activation energy of 0.6 eV can be estimated for Li_3P5O_{14}. We note that this value is only an estimate (hence no error is quoted) given the

validity of the Waugh and Fedin expression, which does not take into account structural complexity[40,41] ($Li_3P_5O_{14}$ has 12 crystallographically different lithium sites), the fraction of fast moving Li^+ ions,[41] and complete numerical simulations of the ^7Li NMR line shape. As the temperature is increased even further (>500 K), $Li_3P_5O_{15}$ is in the fast motional regime, resulting in averaging of the dipolar interaction through increased mobility, giving rise to narrow spectra with line widths of ~750 Hz. The Li^+ jump rate, τ_c^{-1}, is on the order of the ^7Li central transition NMR line width in the rigid lattice regime and quantified at the temperature of the inflection point, yielding a value of 2.8×10^4 s^{-1} at 424 K.

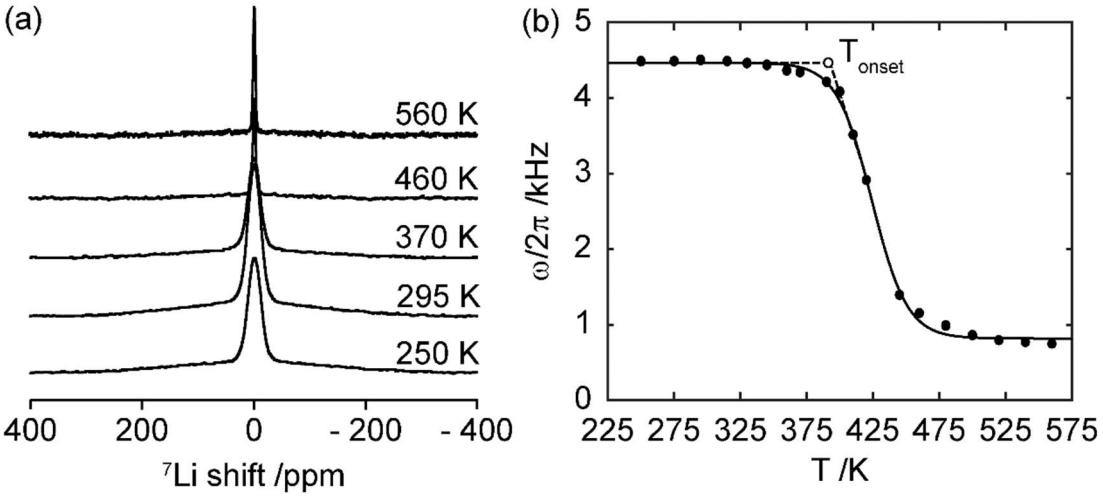

Figure 5.13 (a) ^7Li NMR spectra as a function of temperature for $Li_3P_5O_{14}$. (b) Temperature dependence of static ^7Li NMR line width as a function of temperature. The solid line is a sigmoidal regression fit and is a guide to the eye. The onset temperature of motional narrowing (T_{onset}) is indicated.

The NMR and AC impedance spectroscopy activation energies are cautiously comparable (~0.6 vs 0.43(7) eV) given the largely different approaches used that could potentially lead to contrasting values as observed for a range of

different mobile ionic species,[42-44] the validity of the Waugh and Fedin expression, the measurement uncertainty in the experimentally reported activation barriers based on AC impedance spectroscopy,[45] and the possibility of multiple available pathways for Li^+ hopping processes.

5.5.5 Relaxation Measurements

In order to gain insights into the Li ion mobility in $Li_3P_5O_{14}$, SLR rate constants in the laboratory frame T_1^{-1} and the rotating frame $T_{1\rho}^{-1}$ were measured, through which information on the ion dynamics on the MHz and kHz can be obtained, respectively. The motion of atoms or functional groups causes a random change of the local magnetic fields, which leads to relaxation. Quantitative information on the ion mobility process is contained in these microscopic changing fields and how the Li ions interact with them. τ_c describes the timescale of these fluctuations and Bloembergen-Purcell-Pound (BPP) theory postulates that the main factor influencing the reorientation of the local magnetic fields is the increased mobility of ^7Li nuclei with rising temperatures. The spectral density function $J(\omega_0)$ quantifies the motion at the Larmor frequency ω_0:[46,47]

$$J(\omega_0) = G(0)\left(\frac{2\tau_c}{1+\omega_0^2\tau_c^2}\right) \qquad \text{(Eq. 5.3)}$$

where G(0) is the value of the correlation function at time t = 0, and is equal to the mean square of the local magnetic fields. Since the primary factor affecting the reorientation of the local magnetic fields in this work is the increased

mobility of ^{7}Li nuclei and consequently temperature dependent changes in τ_c are solely induced by the diffusion and follow an Arrhenius relation of the type:

$$\tau_c^{-1} = \tau_{c,0}^{-1} \exp\left(-\frac{E_a}{k_B T}\right) \qquad \text{(Eq. 5.4)}$$

where $\tau_{c,0}^{-1}$ is the Arrhenius pre-exponential factor, T is the temperature and k_B is the Boltzmann constant. In order to gather information on the activation energy, conductivity and dimensionality of the Li diffusion processes, the temperature dependence of the ^{7}Li SLR rate constants under static conditions were collected and exploited.

The SLR T_1^{-1} rate constants for $Li_3P_5O_{14}$ are largely temperature independent in the 250 to 330 K temperature range and vary from 3 to 4 x 10^{-3} s^{-1}. This is to be expected in this regime where the SLR rates are not diffusion-induced due to the absence of (translational) Li ion mobility[48]. Upon heating $Li_3P_5O_{14}$ from 330 to 520 K, T_1^{-1} increases from 4 x 10^{-3} to 0.9 s^{-1} which follows Arrhenius behaviour and hence an E_a of 0.58(7) eV can be extracted (**Figure 5.14**). The increase in SLR T_1^{-1} rate constants with higher T imply data in the low temperature flank of the SLR rate constants, which are indicative of short-range motional processes.

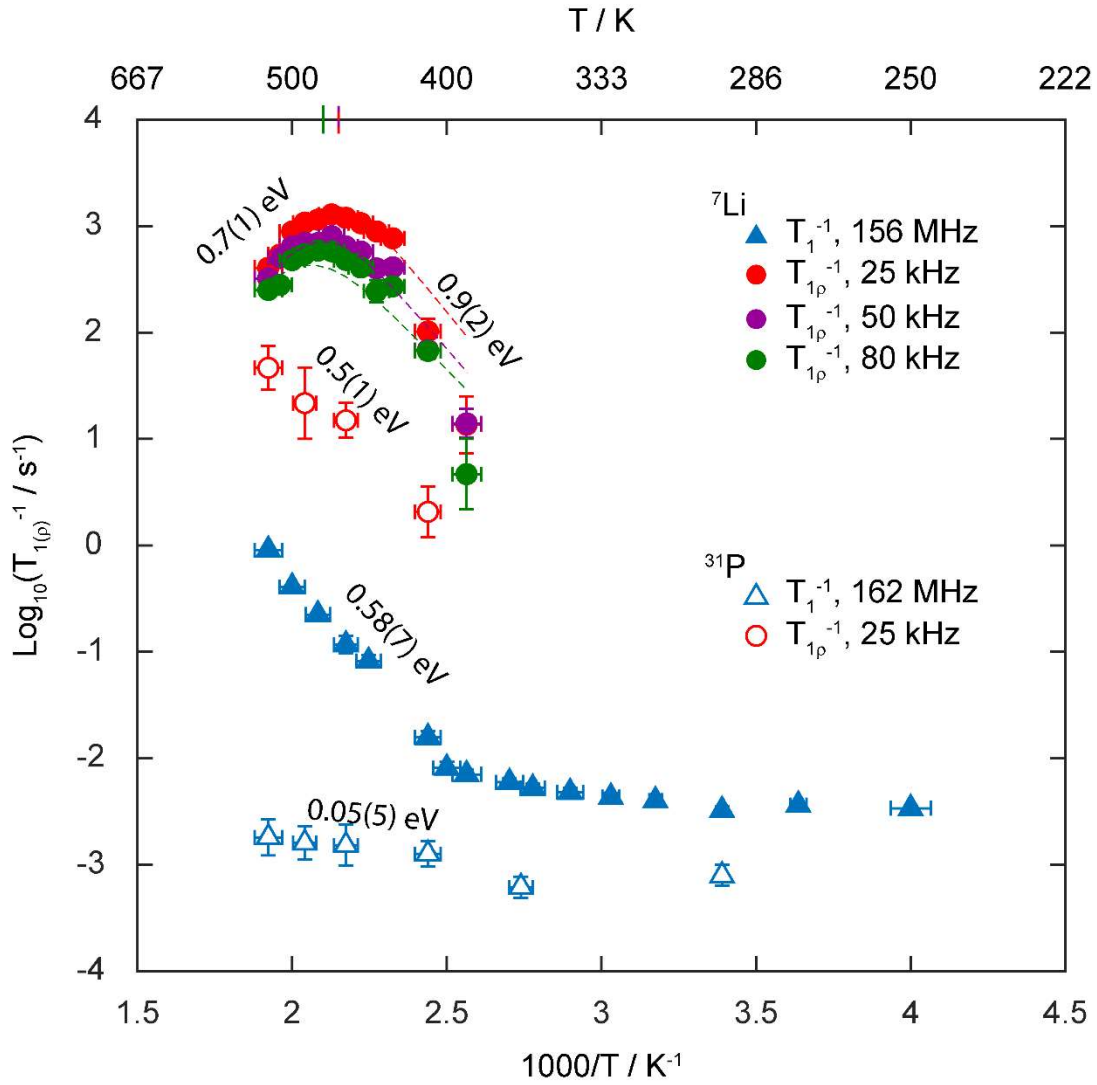

Figure 5.14 Arrhenius plots of ^{7}Li and ^{31}P NMR SLR rate constants in the laboratory (T_1^{-1}) at $\omega_0/2\pi$ = 156 and 162 MHz, respectively (blue triangles) and rotating frame ($T_{1\rho}^{-1}$) at $\omega_1/2\pi$ = 25 (red circles), 50 (purple circles) and 80 kHz (green circles) for ^{7}Li and 25 kHz for ^{31}P. ^{7}Li SLR rate constants are denoted with filled shapes, while ^{31}P SLR rate constants are represented by empty shapes. The coloured ticks on the temperature scale represent the position of the $T_{1\rho}^{-1}$ maxima, note the maxima for $\omega_1/2\pi$ = 25 and 50 kHz occurs at the same temperature and a tick alternating in red and purple is used in this case. Coloured dashed lines outline the fitting of the experimental data to **equation 5.7**.

The SLR rates recorded in the rotating frame were obtained at three different spin-lock frequencies of $\omega_1/2\pi$ = 25, 50 and 80 kHz (**Figure 5.14**). The rates initially increase with temperature (hence the low temperature flank and characterise local short range motional processes) with an activation barrier of 0.9(2) eV. Upon further heating, the SLR $T_{1\rho}^{-1}$ rate constants reach a maximum value (at 470 K for $\omega_1/2\pi$ = 25 and 50 kHz and 480 K for $\omega_1/2\pi$ = 80 kHz) before decreasing once more with an E_a of 0.7(1) eV, this high temperature flank contains information for the long-range Li ion mobility. The ^{31}P SLR rates recorded in the laboratory frame remain consistent over the observed temperature range (~ 10^{-3} s^{-1}), suggesting PO_4^{3-} group rotation is minimal as demonstrated by the ^{31}P CSA data discussed above. The SLR rates in the rotating frame, at a spin-lock frequency of 25 kHz, increase with an activation barrier of 0.5(1) eV. If for instance PO_4^{3-} group rotation was correlated with ion mobility (such as been observed previously in the literature[49,50]) the ^{31}P and ^{7}Li BPP curves would be expected to have the same E_a as well $T_{1\rho}^{-1}$ maxima position. Importantly, both the activation barriers observed on the low temperature flanks of the ^{7}Li and ^{31}P BPP curves are different, and the absence of $T_{1\rho}^{-1}$ maximum for the ^{31}P SLR rates while maxima are observed for ^{7}Li at 470 and 480 K, these observations are indicative of ^{7}Li translational ion mobility not being correlated by PO_4^{3-} rotation.

At the temperatures of the $T_{1\rho}^{-1}$ maxima, the Li^+ τ_c^{-1} values are on the order of the spin-lock probe frequency ω_1 and satisfy the following relationship:[51]

$$2\omega_1\tau_c \approx 1 \qquad \text{(Eq. 5.5)}$$

τ_c^{-1} values on the order of 3.2×10^5 - 1.0×10^6 s^{-1} are therefore obtained at 470 and 480 K (the experimentally collected $T_{1\rho}^{-1}$ rates for $\omega_1/2\pi$ = 25 and 50 kHz have maximum values at the same temperature, smaller intervals in temperature would likely lead to separate maxima) for $Li_3P_5O_{14}$.

The SLR values can be further parameterized using the following expression to extract τ_c from T_1^{-1} rates:

$$\frac{1}{T_1} = K\left(\frac{\tau_c}{1+(\omega_0\tau_c)^{1+\alpha}} + \frac{\tau_c}{1+4(\omega_0\tau_c)^{1+\alpha}}\right) \qquad \text{(Eq. 5.6)}$$

and from $T_{1\rho}^{-1}$:

$$\frac{1}{T_{1\rho}} = K\left(\frac{3}{2}\frac{\tau_c}{1+4(\omega_1\tau_c)^{1+\lambda}} + \frac{5}{2}\frac{\tau_c}{1+(\omega_0\tau_c)^{1+\lambda}} + \frac{\tau_c}{1+4(\omega_0\tau_c)^{1+\lambda}}\right) \qquad \text{(Eq. 5.7)}$$

where K is the local fluctuating magnetic field term in these expressions which depends on the relaxation mechanism and λ in this case is the exponent of the underlying exponential correlation function and ranges from 0 to 1. λ = 1 describes a Lorentizian-shaped $J(\omega)$ and is ascribed to uncorrelated three-dimensional motion, λ < 1 accounts for asymmetry in $J(\omega)$ and often indicates correlated motions when found on the low temperature flank.

In the case of spin 3/2 nuclei such as ^{7}Li, where homonuclear dipolar relaxation is the dominant relaxation mechanism , K is proportional to the square of the dipolar coupling constant and is given by:[52]

$$K = \frac{3}{2}\left(\frac{\mu_0}{4\pi}\right)^2 \frac{\gamma^4\hbar^2}{r^6} \qquad \text{(Eq. 5.8)}$$

where μ_0 is the permeability of free space, $\hbar$ is the reduced Planck's constant, γ is the gyromagnetic ratio of the nuclear spins and r is the interatomic distance between the two nuclear spins. In the case of quadrupolar relaxation being the dominant relaxation mechanism, K is proportional to the quadrupolar tensor parameters and expressed as:

$$K = \frac{1}{50} C_Q^2 \left(1 + \left(\frac{\eta_Q^2}{3}\right)\right) \qquad \text{(Eq. 5.9)}$$

where η_Q is the asymmetry parameter. It is possible to postulate a dominant relaxation mechanism through ^{6,7}Li NMR and is best obtained from comparing ^{6}Li and ^{7}Li T_1 time constants under static conditions.[53]

Given the power law of 4 and quadratic dependencies of T_1^{-1} rate constants on γ as well as the quadrupolar moment Q in the dipolar and quadrupolar relaxation mechanisms, respectively, a ratio of

$$\frac{T_1(^7\mathrm{Li})}{T_1(^6\mathrm{Li})} \propto \frac{\gamma^4(^7\mathrm{Li})}{\gamma^2(^6\mathrm{Li})\gamma^2(^7\mathrm{Li})(^7\mathrm{Li})[(^6\mathrm{Li}) + \frac{3}{2}(^7\mathrm{Li})]} \sim 0.5 \qquad \text{(Eq. 5.10)}$$

is expected in the case of dipolar relaxation, while a ratio of

$$\frac{T_1(^7\mathrm{Li})}{T_1(^6\mathrm{Li})} \propto \frac{Q^2(^7\mathrm{Li})}{Q^2(^6\mathrm{Li})} \sim 3 \times 10^{-4} \qquad \text{(Eq. 5.11)}$$

is anticipated for a quadrupolar relaxation mechanism. In the case of $Li_3P_5O_{14}$, an experimental $T_1(^7\mathrm{Li})/T_1(^6\mathrm{Li})$ ratio of 2(1) x 10^{-2} was obtained at room temperature under static conditions, suggesting that the overall SLR is caused by either cross relaxation processes or a combination of the two mechanisms.

By combining **equations 5.4** and **5.7**, an expression of the SLR rate in the rotating frame $T_{1\rho}^{-1}$ dependent on T can be extracted in order to determine the parameters K, $\tau_{c,0}^{-1}$, E_a and λ. Corresponding fits to the experimental data are shown in **Figure 5.15** with the fitting parameters summarised in **Table 5.3**.

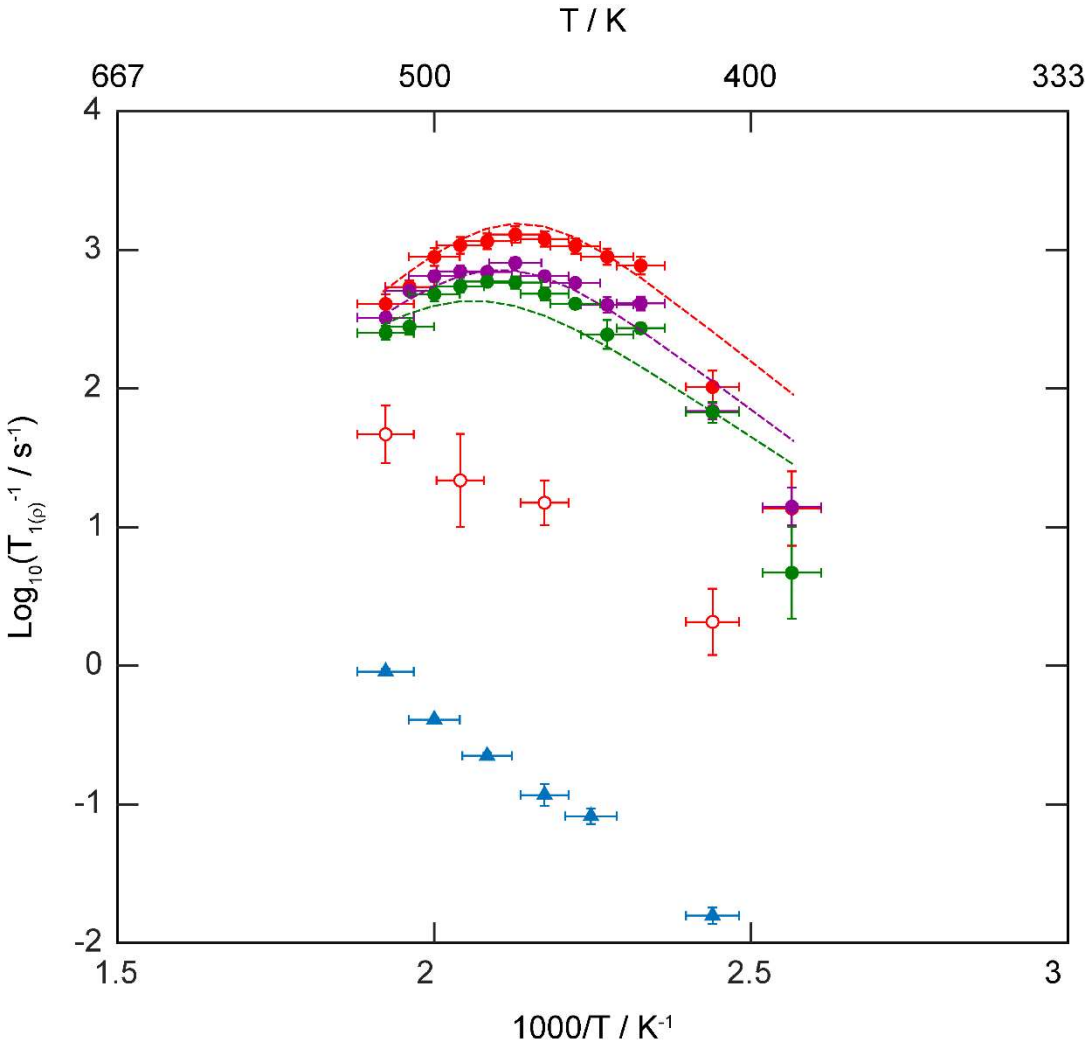

Figure 5.15 Zoom of the Arrhenius plots focussing on the ^{7}Li NMR SLR rate constants in the rotating frame ($T_{1\rho}^{-1}$) at $\omega_1/2\pi$ = 25 (red circles), 50 (purple circles) and 80 kHz (green circles). Coloured dashed lines outline the fitting of the experimental data to **equation 5.7**.

Table 5.3 Summary of the parameters obtained from $T_{1\rho}^{-1}$ relaxation measurements via the experimental $T_{1\rho}^{-1}$ maxima (**equation 5.5**) and through fitting the data in **Figure 5.14** with **equation 5.7**. Values of $\tau_{c,0}^{-1}$, E_a and λ are extracted from the fits to the data in **Figure 5.14**.

$\omega_1/2\pi$ /kHz	Method	K /Hz^2	$\tau_{c,0}^{-1}$ /s^{-1}	E_a /eV	λ
25	Maxima	6(1)x10^8	9.0x10^{12}	0.67(5)	0.94
	Simulation	5.4(3) x10^8			
50	Maxima	7(1) x10^8	2.3x10^{12}	0.60(6)	0.99
	Simulation	6.4(3) x10^8			
80	Maxima	8(1) x10^8	4.8x10^{11}	0.53(5)	1
	Simulation	8.0(4) x10^8			
Average	Maxima	7(1) x10^8	3.9x10^{12}	0.60(6)	0.98
	Simulation	6.6(3) x10^8			

At the ^{7}Li $T_{1\rho}^{-1}$ maxima, substituting **equation 5.5** into **equation 5.7** enables experimental determination of K, a value of 7(1) x 10^8 Hz^2, averaged over the three consistent values of K for the three spin-lock frequencies were extracted for $Li_3P_5O_{14}$ which agrees well with the average value of 6.6(3) x 10^8 Hz^2 obtained from the fitting of the experimental data in **Figure 5.14**. This is to be expected as the two methods are models of the same expression (**equation 5.7**) however the method used from the experimental maxima will likely be slightly less accurate, as the value of $T_{1\rho}^{-1}$ obtained experimentally may not be the maximum, it is very unlikely that the exact temperature chosen to record this data was the optimum temperature to achieve the highest value of $T_{1\rho}^{-1}$. This value of K can then be used in order to convert experimental $T_{1\rho}^{-1}$ values

to τ_c estimates at each temperature using **equation 5.7** (**Figure 5.16**) and allows access to NMR-reived τ_c^{-1} values at all temperatures.

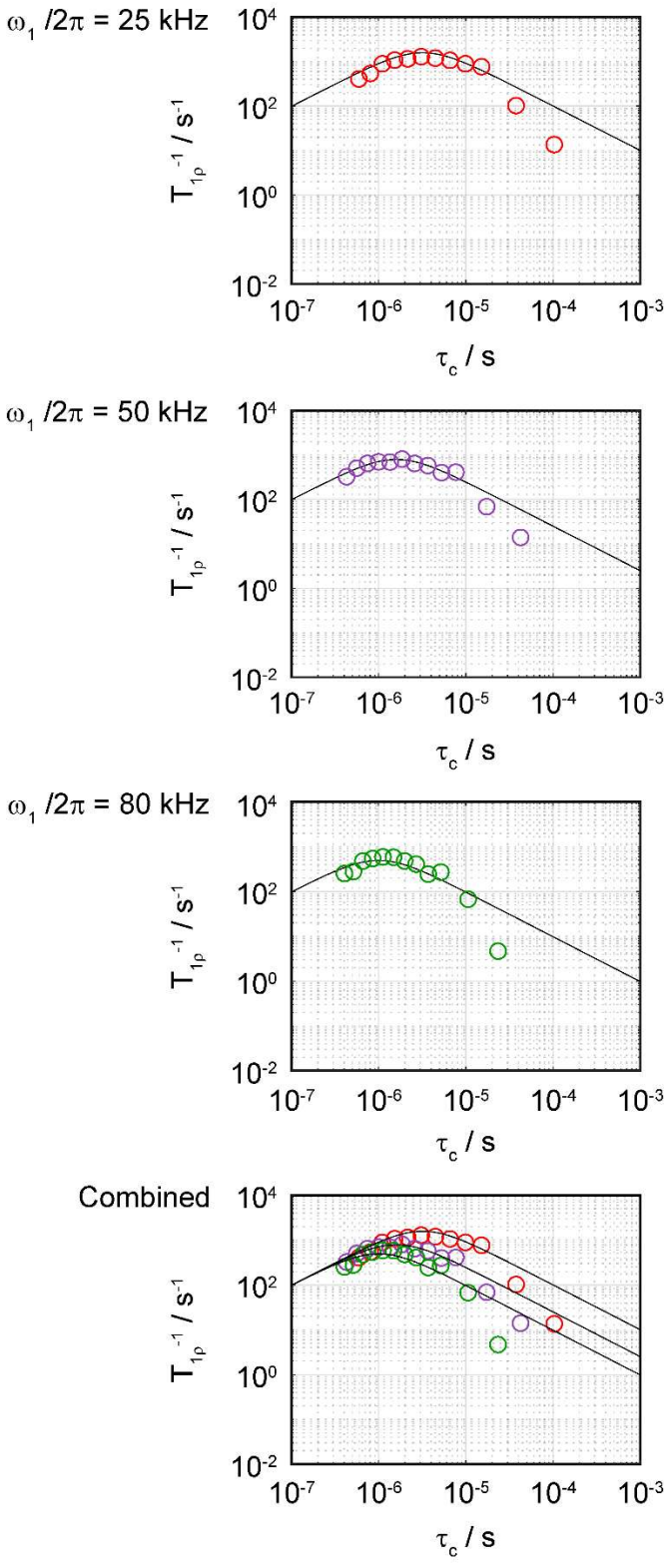

Figure 5.16 ^{7}Li $T_{1\rho}^{-1}$ versus τ_c for $Li_3P_5O_{14}$, collected at spin-lock frequencies of $\omega_1/2\pi$ of 25 (red), 50 (purple) and 80 kHz (green), the solid lines are those obtained from **equation 5.6** using the experimentally determined local field fluctuation term of 7 x 10^8 Hz^2 (average value from **Table 5.3**).

SLR $T_{1\rho}^{-1}$ rate constants at different frequencies provide information on the dimensionality of the Li^+ diffusion process and, for diffusion-induced rates in solids, the high temperature limits of the spectral density function $J(\omega_1)$ have the following frequency dependence to $(\tau_c/\omega_1)^{0.5}$, $\tau_c \ln(1/\omega_1\tau_c)$ and τ_c for one, two and three-dimensional diffusion processes, respectively.[54,55] The $T_{1\rho}^{-1}$ rate constants on the high temperature flank of $Li_3P_5O_{14}$ are independent of the spin-lock frequency $\omega_1/2\pi$ (**Figure 5.14**), strongly demonstrating experimentally the presence of three-dimensional Li ion mobility in this material, which is in good agreement with the bond valence sum (BVS)[56] mapping previously reported and arising from DFT data.[1] This 3D pathway is believed to occur both via an inter-layer (transport between two adjacent Li polyhedral layers with c-direction connectivity) and intra-layer, (transport in the Li polyhedral layer in the *ab* plane. The ordered $Li_6O_{16}^{26-}$ chains shown in **Figure 5.12** along with the vacant tetrahedral sites form a possible intra-layer lithium diffusion pathway in the Li polyhedral layer. The intra-layer migration could occur either by a hopping mechanism of Li ions along the $Li_6O_{16}^{26-}$ chains or by hopping between the two types of $Li_6O_{16}^{26-}$ chains, where the local jumps between the two types of $Li_6O_{16}^{26-}$ chains involved are between the two tetrahedral vacancies and adjacent LiO_4 tetrahedra or the distorted square pyramid site. The potential inter-layer Li migration pathway occurs between the 12-membered $P_{12}O_{36}^{12-}$ rings that provide a window that mobile Li ion can traverse.

5.5.6 ^{7}Li Spin-Alignment Echo NMR

T_1 and $T_{1\rho}$ measurements probe Li ion mobility on the MHz and kHz scale, respectively, and slower motion on the Hz and sub-Hz scale can be obtained from SAE NMR, approach which also has the added benefit of allowing for direct measurement of τ_c^{-1} at any given temperature.[49,57-59] The underlying principle of SAE NMR spectroscopy is similar to that of 2D EXSY NMR,[60] where instead of utilising a change in the chemical shift interactions, SAE NMR takes advantage of a change in the interactions between the quadrupole moment of the nucleus with the EFG tensor when exchange occurs. For this purpose, ^{7}Li SAE NMR spectra of $Li_3P_5O_{14}$ were recorded as a function of τ_m at temperatures of 295, 330 and 373 K and the resulting data capturing the echo amplitude decays are shown in **Figure 5.17**. If sufficiently long τ_m values are used, the resulting echo amplitudes have a two-step decay as can be seen in (**Figure 1.11** in **Chapter 1**), where the first decay step is directly characterised by the Li ion jump processes between electronically inequivalent sites, while the second decay step is characterised by the quadrupolar component of the SLR, $T_{1,Q}$. Thus the part of the curve governed by Li ion motion is captured in the decay curves of $Li_3P_5O_{14}$. Solid lines in **Figure 5.17** show fits to **equation 5.1** through which, Li ion τ_c^{-1} values of 0.6(1), 7(1) and 114(8) s^{-1} were obtained at 295, 330 and 373 K, respectively. A linear slope between these three data points yields an activation barrier of 0.62(5) eV, in good agreement with the values obtained from ^{7}Li line narrowing and SLR measurements.

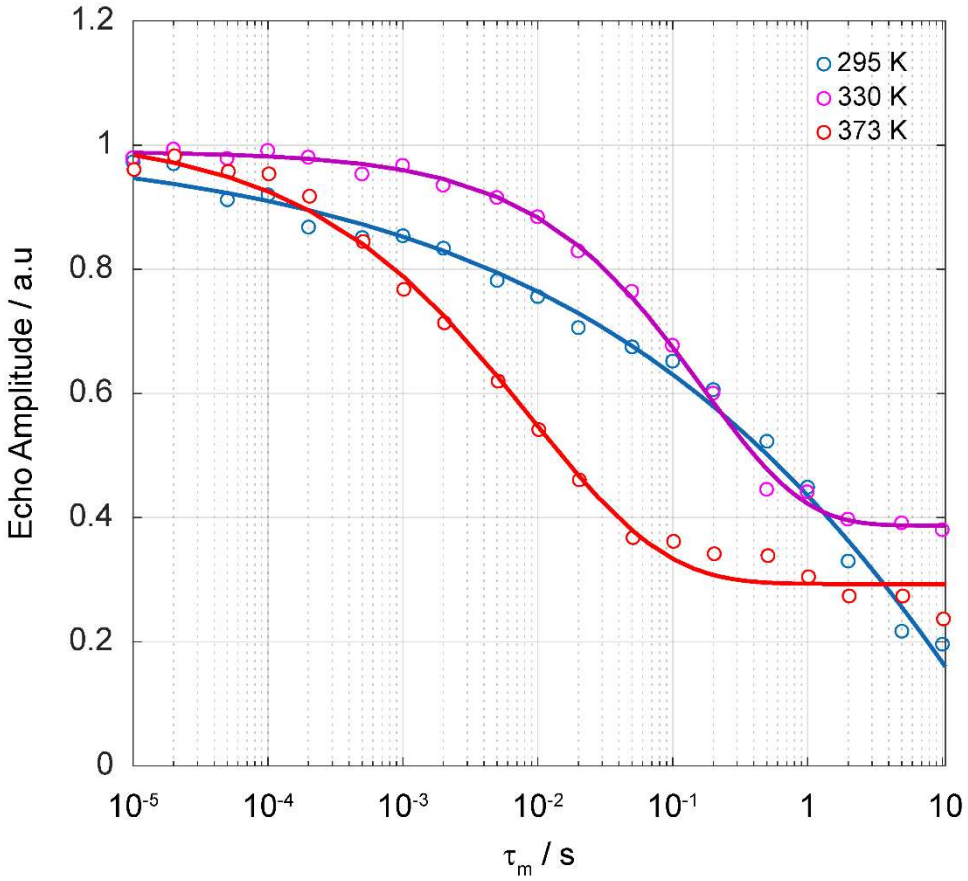

Figure 5.17 ^{7}Li SAE NMR echo amplitude as a function of τ_m at 295, 330 and 373 K. Solid lines show fits to the one-time correlation function (**equation 5.1**) with stretch exponential values γ of 0.62, 0.56 and 0.65 for the three temperatures, respectively.

5.5.7 NMR-derived Li^+ ion τ_c^{-1} values

NMR-derived jump rates τ_c^{-1} obtained from ^{7}Li line narrowing experiments (**Figure 5.13**), SAE (**Figure 5.17**), relaxometry experiments (**Figure 5.14**) and BPP simulation for $\omega_1/2\pi$ = 25 kHz are plotted against reciprocal temperature in **Figure 5.18** (data for $\omega_1/2\pi$ = 50 and 80 kHz are given in **Figures 5.19** and **5.20**, respectively). There is an excellent agreement between the τ_c^{-1} values obtained from ^{7}Li line narrowing spectra, SAE and relaxometry data and this

data agrees reasonably well with the τ_c^{-1} values obtained from the BPP simulations. An activation barrier for Li ion mobility in $Li_3P_5O_{14}$ of 0.9(2) eV is obtained from the slope of the experimentally obtained data points (excluding the BPP simulations, which appear to overestimate τ_c^{-1} at temperatures below ~460 K), noting particularly large degrees of uncertainty are observed here, likely due to the combination of various methods used. Hence, the energy barriers obtained from ^{7}Li line narrowing, SAE and SLR experiments are likely more informative. The activation barriers obtained via the various spectroscopic methods used here is summarised in **Table 5.4** and are consistently of around 0.6 – 0.7 eV. In particular there is a strong agreement between E_a values obtained through ^{7}Li line narrowing, $T_{1\rho}^{-1}$ on the high temperature flank, BPP simulation and SAE experiments. Values obtained for ^{7}Li $T_{1\rho}^{-1}$ on the low temperature flank and through combining all jump rate values obtained through the various methods however are not in full agreement with the range of 0.6 – 0.7 eV. The discrepancy in the $T_{1\rho}^{-1}$ on the low temperature flank is likely as a result of the large errors associated with collecting this data due to the very long $T_{1\rho}$ times that require continuous rf pulsing for a duration that exceeds the probe capabilities and are hence not measurable. While the discrepancy in the jump rate plots (**Figures 5.18-5.20**) are likely due to the combination of various different methods which probe dynamics in largely different ways.

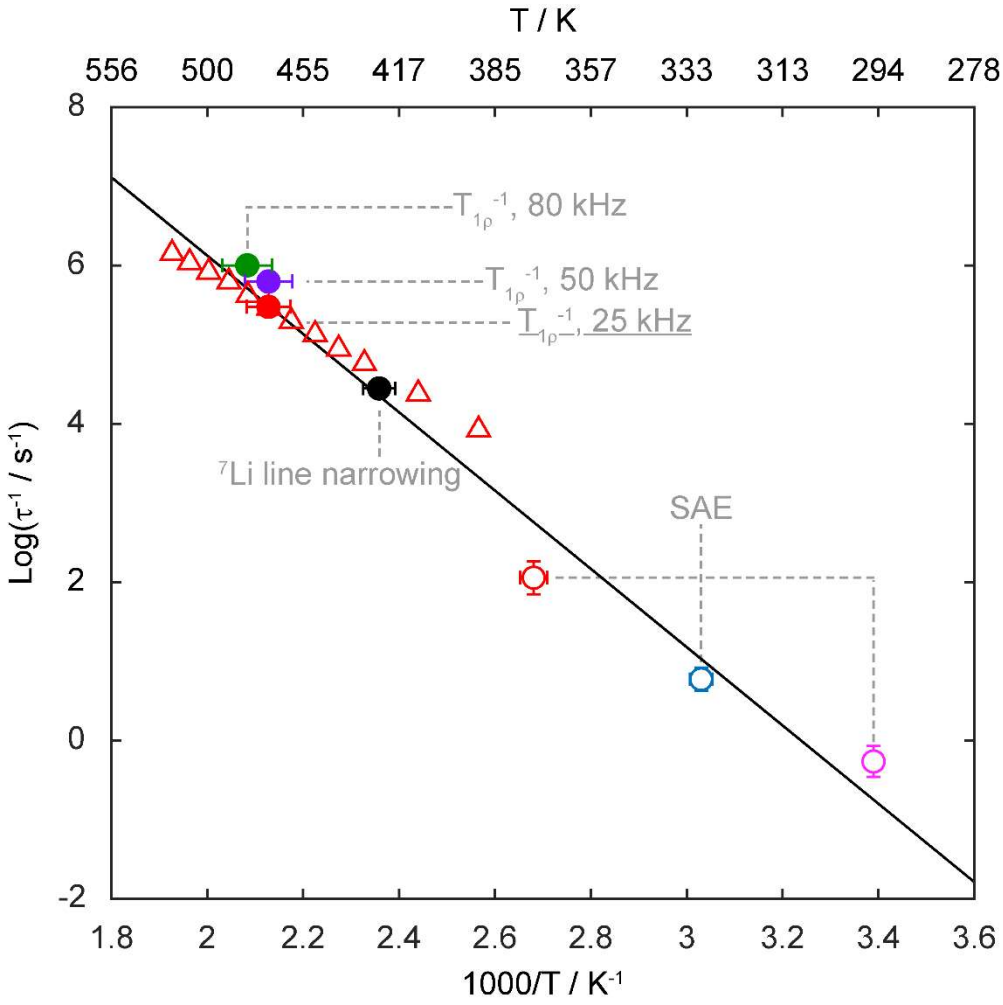

Figure 5.18 Arrhenius plot of Li jump rates τ_c^{-1} showing data points obtained from BPP simulations (red triangles, $\omega_1/2\pi = 25$ kHz), extracted from the onset of ^{7}Li line narrowing of the variable temperature ^{7}Li NMR spectra (black circle, **Figure 5.13**), ^{7}Li SAE experiments (empty coloured circles, **Figure 5.17**), SLR rates in the rotating frame ($T_{1\rho}^{-1}$) experiments (filled coloured circles, **Figure 5.14**) at spin lock frequencies $\omega_1/2\pi$ of 25 (red), 50 (purple) and 80 kHz (green), respectively. The label for the spin locking frequency used in the BPP simulation for this figure is underlined. Errors in the jump rate τ_c^{-1} are within the data points.

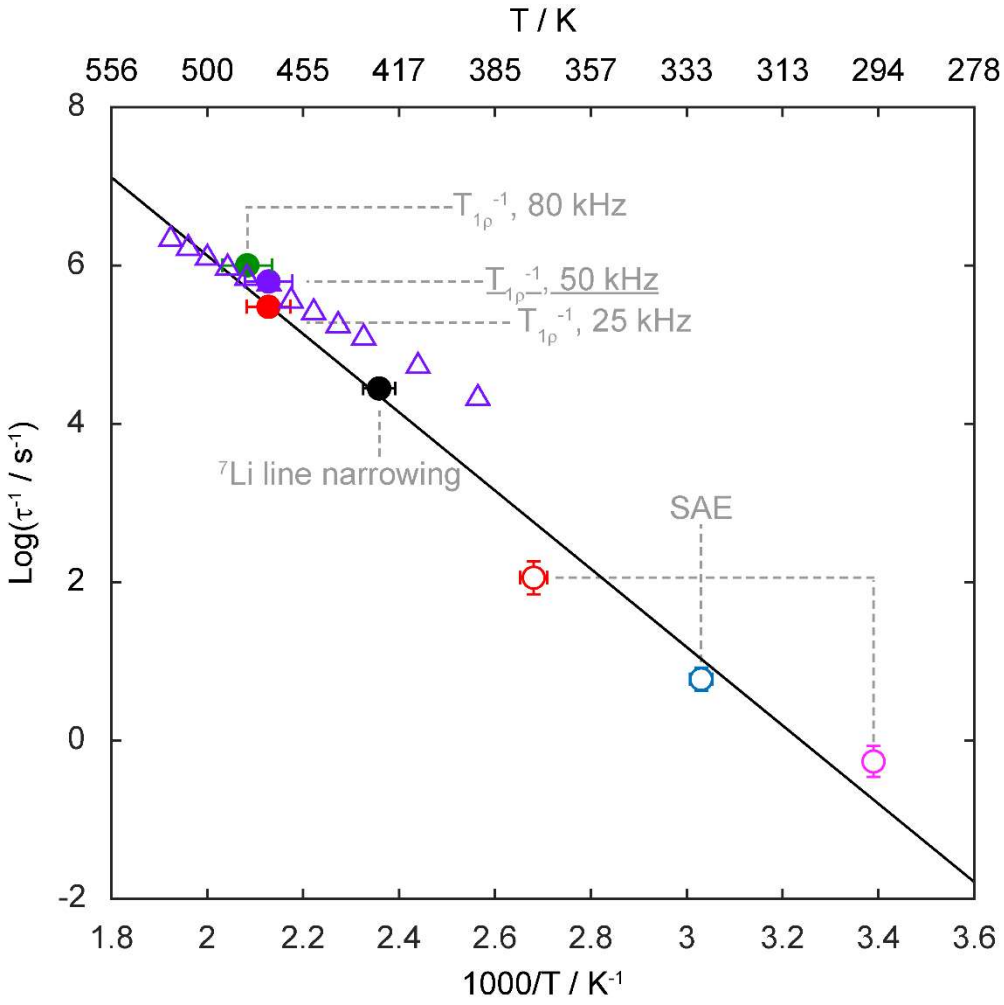

Figure 5.19 Arrhenius plot of Li jump rates τ_c^{-1} showing the points obtained from BPP simulations (purple triangles, $\omega_1/2\pi = 50$ kHz) Data were extracted from the onset of ^{7}Li line narrowing of the variable temperature ^{7}Li NMR spectra (black circle, **Figure 5.13**), ^{7}Li SAE experiments (empty coloured circles, **Figure 5.17**), SLR rates in the rotating frame ($T_{1\rho}^{-1}$) experiments (filled coloured circles, **Figure 5.14**) at spin lock frequencies $\omega_1/2\pi$ of 25 (red), 50 (purple) and 80 kHz (green), respectively. The label for the spin locking frequency used in the BPP simulation for this figure is underlined. Errors in the jump rate τ_c^{-1} are within the data points.

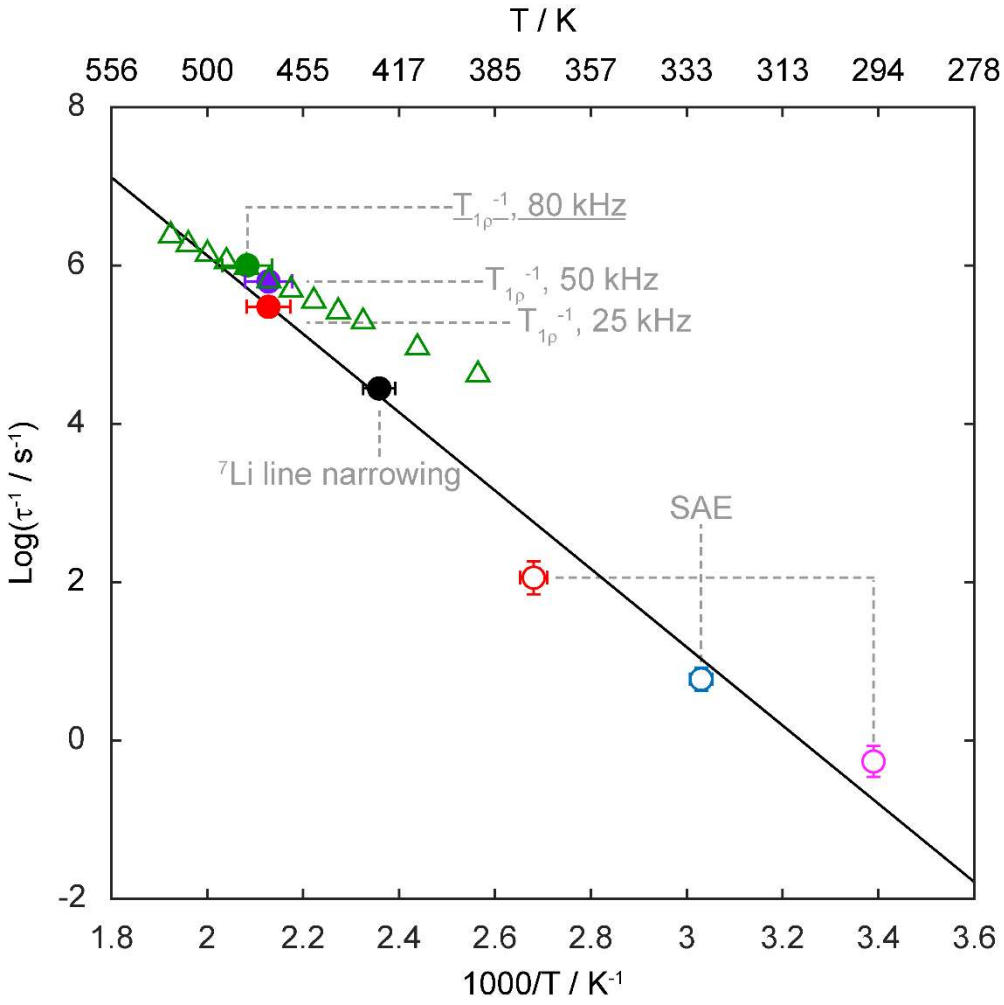

Figure 5.20 Arrhenius plot of Li jump rates τ_c^{-1} showing the points obtained from BPP simulations (green triangles, $\omega_1/2\pi = 80$ kHz) Data were extracted from the onset of ^{7}Li line narrowing of the variable temperature ^{7}Li NMR spectra (black circle, **Figure 5.13**), ^{7}Li SAE experiments (empty coloured circles, **Figure 5.17**), SLR rates in the rotating frame ($T_{1\rho}^{-1}$) experiments (filled coloured circles, **Figure 5.14**) at spin lock frequencies $\omega_1/2\pi$ of 25 (red), 50 (purple) and 80 kHz (green), respectively. The label for the spin locking frequency used in the BPP simulation for this figure is underlined. Errors in the jump rate τ_c^{-1} are within the data points.

Table 5.4 Summary of the activation barrier for $Li_3P_5O_{14}$ extracted from electrical impedance spectroscopy (EIS),[1] ^7Li motional narrowing[39] from **Figure 5.13**, SAE NMR from **Figure 5.17** and SLR data in the laboratory frame (T_1) and rotating frame ($T_{1\rho}$) from **Figure 5.14**. Activation barriers on both the high and low temperature flanks of the BPP curve are quoted, along with the activation barrier obtained from the jump rate plots shown in **Figures 5.18 – 5.20**.

Activation Energy /eV							
EIS[1]	Waugh -Fedin	T_1	$T_{1\rho,LT}$	$T_{1\rho,HT}$	BPP fit	SAE	Jump rate
0.43(7)	~0.6	0.58(7)	0.9(2)	0.7(1)	0.60(6)	0.62(5)	0.9(2)

5.6 Conclusion

In this chapter, the characterisation of the structure and quantification of the Li ion dynamics in the newly synthesised $Li_3P_5O_{14}$ has been reported. The structure of the material was characterised initially through single crystal X-ray diffraction (performed by Craig Robertson) and the local Li and P environments investigated further via ^{6}Li and ^{31}P MAS NMR in conjunction with DFT calculations in order to assign the large number of distinct sites. ^{31}P-^{31}P spin diffusion experiments were employed in order to attempt to reinforce the assignment of the P sites in $Li_3P_5O_{14}$, however further work is required here in order to fully assign the wide range of P sites. We employed a number of complementary ^{7}Li NMR approaches in order to capture the Li ion dynamics in $Li_3P_5O_{14}$. Static ^{7}Li VT NMR, SAE NMR and relaxometry allowed for the quantification of the Li ion dynamics. Moreover the frequency dependence of the ^{7}Li SLR rates in the rotating frame of reference, allowed for the experimental verification of the proposed 3D Li ion pathway in $Li_3P_5O_{14}$. Future progress is also required in order to further characterise the Li ion mobility pathways in $Li_3P_5O_{14}$ in order to quantify the ion exchange rates between the many different sites. (For details of future work see **Chapter 6**)

5.7 References

1. Han, G.; Vasylenko, A.; Neale, A. R.; Duff, B. B.; Chen, R.; Dyer, M. S.; Dang, Y.; Daniels, L. M.; Zanella, M.; Robertson, C. M.; Kershaw Cook, L. J.; Hansen, A. L.; Knapp, M.; Hardwick, L. J.; Blanc, F.; Claridge, J. B.; Rosseinsky, M. J., Extended Condensed Ultraphosphate Frameworks with Monovalent Ions Combine Lithium Mobility with High Computed Electrochemical Stability. *Journal of the American Chemical Society* **2021,** *143* (43), 18216.

2. Kim, A.; Woo, S.; Kang, M.; Park, H.; Kang, B., Research Progresses of Garnet-Type Solid Electrolytes for Developing All-Solid-State Li Batteries. *Frontiers in Chemistry* **2020,** *8*.

3. Xiao, Y.; Jun, K.; Wang, Y.; Miara, L. J.; Tu, Q.; Ceder, G., Lithium Oxide Superionic Conductors Inspired by Garnet and NASICON Structures. *Advanced Energy Materials* **2021,** *11* (37), 2101437.

4. Thilo, E., The Structural Chemistry of Condensed Inorganic Phosphates. *Angewandte Chemie International Edition in English* **1965,** *4* (12), 1061.

5. Corbridge, D. E. C., The structural chemistry of phosphates. *Bulletin de Minéralogie* **1971,** *94*, 271.

6. Kanepe, Z. Y.; Konstant, Z. A.; Krasnikov, V. V., ChemInform Abstract: Aluminium Cyclohexaphosphate. *Chemischer Informationsdienst* **1986,** *17* (2).

7. Guitel, J. C.; Tordjman, I., Structure cristalline de polyphosphate de lithium $LiPO_3$. *Acta Crystallographica Section B Structural Crystallography and Crystal Chemistry* **1976,** *32* (11), 2960.

8. Chudinova, N. N. P., K. K.; Karmanovskaia, N. B.; Maximova, S. I.; Chibiskova, N. T., Double Ultraphosphate of Iron and Sodium $Na_3FeP_8O_{23}$ Having a New Anion Shape. *Proceedings of the USSR Academy of Sciences* **1989,** *306* (33), 635.

9. Tranqui, D.; Shannon, R. D.; Chen, H. Y.; Lijima, S.; Baur, W. H., Crystal structure of ordered Li_4SiO_4. *Acta Crystallographica Section B Structural Crystallography and Crystal Chemistry* **1979,** *35* (11), 2479.

10. Tordjman, L.; Bagieu-Beucher, M.; Zilber, R., Structure cristalline de l'ultraphosphate de calcium: CaP_4O_{11}. **1974,** *140* (3-4), 145.

11. Gorbunova, Y. E. L., S. A.; Lavrov, A. V., New type of high-polymer anion $3/\infty[P_6O_{17}]^{4-}$ in the structure of uranyl ultraphosphate $(UO_2)_2P_6O_{17}$. *Zhurnal Neorganicheskoi Khimii* **1981,** *26* (3), 713.

12. Ivanov-Shitz, A. K.; Kireev, V. V.; Mel'Nikov, O. K.; Demianets, L. N., Growth and ionic conductivity of γ-Li_3PO_4. *Crystallography Reports* **2001,** *46* (5), 864.

13. Oudahmane, A.; Mbarek, A.; El-Ghozzi, M.; Avignant, D., Aluminium cyclohexaphosphate. *Acta Crystallographica Section E Structure Reports Online* **2010,** *66* (3), i17.

14. Gordon, M. I.; Hoch, M. J. R., Quadrupolar spin-lattice relaxation in solids. *Journal of Physics C: Solid State Physics* **1978,** *11* (4), 783.

15. Gabriel, J.; Petrov, O. V.; Kim, Y.; Martin, S. W.; Vogel, M., Lithium ion dynamics in Li_2S+GeS_2+GeO_2 glasses studied using ^{7}Li NMR field-cycling relaxometry and line-shape analysis. *Solid State Nuclear Magnetic Resonance* **2015,** *70*, 53.

16. Huynh, T. V.; Messinger, R. J.; Sarou-Kanian, V.; Fayon, F.; Bouchet, R.; Deschamps, M., Restricted lithium ion dynamics in PEO-based block copolymer electrolytes measured by high-field nuclear magnetic resonance relaxation. *The Journal of Chemical Physics* **2017,** *147* (13), 134902.

17. Jeener, J.; Broekaert, P., Nuclear Magnetic Resonance in Solids: Thermodynamic Effects of a Pair of rf Pulses. *Physical Review* **1967,** *157* (2), 232.

18. Böhmer, R., Multiple-Time Correlation Functions in Spin-3/2 Solid-State NMR Spectroscopy. *Journal of Magnetic Resonance* **2000,** *147* (1), 78.

19. Bielecki, A.; Burum, D. P. D. P., Temperature Dependence of ^{207}Pb MAS Spectra of Solid Lead Nitrate. An Accurate, Sensitive Thermometer for Variable-Temperature MAS. *Journal of Magnetic Resonance, Series A* **1995,** *116* (2), 215.

20. Beckmann, P. A.; Dybowski, C., A Thermometer for Nonspinning Solid-State NMR Spectroscopy. *Journal of Magnetic Resonance* **2000,** *146* (2), 379.

21. Becker, K. D., Temperature dependence of NMR chemical shifts in cuprous halides. *The Journal of Chemical Physics* **1978,** *68* (8), 3785.

22. Wu, J.; Kim, N.; Stebbins, J. F., Temperature calibration for high-temperature MAS NMR to 913 K: ^{63}Cu MAS NMR of CuBr and CuI, and ^{23}Na MAS NMR of $NaNbO_3$. *Solid State Nuclear Magnetic Resonance* **2011,** *40* (2), 45.

23. Clark, S. J.; Segall, M. D.; Pickard, C. J.; Hasnip, P. J.; Probert, M. I. J.; Refson, K.; Payne, M. C., First principles methods using CASTEP. *Zeitschrift für Kristallographie - Crystalline Materials* **2005,** *220* (5/6), 567.

24. Kohn, W.; Sham, L. J., Self-Consistent Equations Including Exchange and Correlation Effects. *Physical Review* **1965,** *140* (4A), A1133.

25. Perdew, J. P.; Burke, K.; Ernzerhof, M., Generalized Gradient Approximation Made Simple. *Physical Review Letters* **1996,** *77* (18), 3865.

26. Vanderbilt, D., Soft self-consistent pseudopotentials in a generalized eigenvalue formalism. *Physical Review B* **1990,** *41* (11), 7892.

27. Monkhorst, H. J.; Pack, J. D., Special points for Brillouin-zone integrations. *Physical Review B* **1976,** *13* (12), 5188.

28. Pickard, C. J.; Mauri, F., All-electron magnetic response with pseudopotentials: NMR chemical shifts. *Physical Review B* **2001,** *63* (24), 245101.

29. Yates, J. R.; Pickard, C. J.; Mauri, F., Calculation of NMR chemical shifts for extended systems using ultrasoft pseudopotentials. *Physical Review B* **2007,** *76* (2), 024401.

30. Santibáñez-Mendieta, A. B.; Didier, C.; Inglis, K. K.; Corkett, A. J.; Pitcher, M. J.; Zanella, M.; Shin, J. F.; Daniels, L. M.; Rakhmatullin, A.; Li, M.; Dyer, M. S.; Claridge, J. B.; Blanc, F.; Rosseinsky, M. J., $La_3Li_3W_2O_{12}$: Ionic Diffusion in a Perovskite with Lithium on both A- and B-Sites. *Chemistry of Materials* **2016,** *28* (21), 7833.

31. Davies, E.; Duer, M. J.; Ashbrook, S. E.; Griffin, J. M., Applications of NMR Crystallography to Problems in Biomineralization: Refinement of the Crystal Structure and ^{31}P Solid-State NMR Spectral Assignment of Octacalcium Phosphate. *Journal of the American Chemical Society* **2012,** *134* (30), 12508.

32. Losso, P.; Schnabel, B.; Jäger, C.; Sternberg, U.; Stachel, D.; Smith, D. O., ^{31}P NMR investigations of binary alkaline earth phosphate glasses of

ultra phosphate composition. *Journal of Non-Crystalline Solids* **1992,** *143*, 265.

33. Harris, R. K.; Wasylishen, R. E.; Duer, M. J., *NMR crystallography*. Wiley: 2009.

34. Apperley, D. C.; Harris, R. K.; Hodgkinson, P., *Solid-State NMR: Basic Principles and Practice*. 1st ed ed.; Momentum Press: New York, 2012.

35. O'Dell, L. A.; Guerry, P.; Wong, A.; Abou Neel, E. A.; Pham, T. N.; Knowles, J. C.; Brown, S. P.; Smith, M. E., Quantification of crystalline phases and measurement of phosphate chain lengths in a mixed phase sample by ^{31}P refocused INADEQUATE MAS NMR. *Chemical Physics Letters* **2008,** *455* (4), 178.

36. Guerry, P.; Smith, M. E.; Brown, S. P., ^{31}P MAS Refocused INADEQUATE Spin−Echo (REINE) NMR Spectroscopy: Revealing J Coupling and Chemical Shift Two-Dimensional Correlations in Disordered Solids. *Journal of the American Chemical Society* **2009,** *131* (33), 11861.

37. Döhler, F.; Mandlule, A.; van Wüllen, L.; Friedrich, M.; Brauer, D. S., ^{31}P NMR characterisation of phosphate fragments during dissolution of calcium sodium phosphate glasses. *Journal of Materials Chemistry B* **2015,** *3* (6), 1125.

38. Xu, Z.; Stebbins, J. F., ^{6}Li nuclear magnetic resonance chemical shifts, coordination number and relaxation in crystalline and glassy silicates. *Solid State Nuclear Magnetic Resonance* **1995,** *5* (1), 103.

39. Waugh, J. S.; Fedin, E. I., Determination of hindered-rotation barriers in solids. *Soviet Phsics-Solid State* **1963,** *4* (8), 1633.

40. Faske, S.; Eckert, H.; Vogel, M., ^{6}Li and ^{7}Li NMR line-shape and stimulated-echo studies of lithium ionic hopping in $LiPO_3$ glass. *Physical Review B* **2008,** *77* (10), 104301.

41. Storek, M.; Böhmer, R.; Martin, S. W.; Larink, D.; Eckert, H., NMR and conductivity studies of the mixed glass former effect in lithium borophosphate glasses. *The Journal of Chemical Physics* **2012,** *137* (12), 124507.

42. Kim, N.; Hsieh, C. H.; Huang, H.; Prinz, F. B.; Stebbins, J. F., High temperature ^{17}O MAS NMR study of calcia, magnesia, scandia and yttria stabilized zirconia. *Solid State Ionics* **2007,** *178* (27-28), 1499.

43. Deng, Y.; Eames, C.; Chotard, J. N.; Laleìre, F.; Seznec, V.; Emge, S.; Pecher, O.; Grey, C. P.; Masquelier, C.; Islam, M. S., Structural and Mechanistic Insights into Fast Lithium-Ion Conduction in Li_4SiO_4-Li_3PO_4 Solid Electrolytes. *Journal of the American Chemical Society* **2015,** *137* (28), 9136.
44. Yu, C.; Ganapathy, S.; De Klerk, N. J. J.; Van Eck, E. R. H.; Wagemaker, M., Na-ion dynamics in tetragonal and cubic Na_3PS_4, a Na-ion conductor for solid state Na-ion batteries. *Journal of Materials Chemistry A* **2016,** *4* (39), 15095.
45. Ohno, S.; Bernges, T.; Buchheim, J.; Duchardt, M.; Hatz, A.-K.; Kraft, M. A.; Kwak, H.; Santhosha, A. L.; Liu, Z.; Minafra, N.; Tsuji, F.; Sakuda, A.; Schlem, R.; Xiong, S.; Zhang, Z.; Adelhelm, P.; Chen, H.; Hayashi, A.; Jung, Y. S.; Lotsch, B. V.; Roling, B.; Vargas-Barbosa, N. M.; Zeier, W. G., How Certain Are the Reported Ionic Conductivities of Thiophosphate-Based Solid Electrolytes? An Interlaboratory Study. *ACS Energy Letters* **2020,** *5* (3), 910.
46. Heitjans, P.; Kärger, J. r., *Diffusion in condensed matter : methods, materials, models*. Springer: 2005.
47. Levitt, M. E., *Spin Dynamics: Basics of Nuclear Magnetic Resonance*. 2nd ed.; Wiley: 2008; p 740.
48. Epp, V.; Gün, Ö.; Deiseroth, H. J.; Wilkening, M., Long-range Li+ dynamics in the lithium argyrodite Li_7PSe_6 as probed by rotating-frame spin–lattice relaxation NMR. *Physical Chemistry Chemical Physics* **2013,** *15* (19), 7123.
49. Hogrefe, K.; Minafra, N.; Zeier, W. G.; Wilkening, H. M. R., Tracking Ions the Direct Way: Long-Range Li+ Dynamics in the Thio-LISICON Family Li_4MCh_4 (M = Sn, Ge; Ch = S, Se) as Probed by ^{7}Li NMR Relaxometry and ^{7}Li Spin-Alignment Echo NMR. *Journal of Physical Chemistry C* **2021,** *125* (4), 2306.
50. Hanghofer, I.; Gadermaier, B.; Wilkening, H. M. R., Fast Rotational Dynamics in Argyrodite-Type Li_6PS_5X (X: Cl, Br, I) as Seen by ^{31}P Nuclear Magnetic Relaxation—On Cation–Anion Coupled Transport in Thiophosphates. *Chemistry of Materials* **2019,** *31* (12), 4591.
51. Abragam, A., *The principles of nuclear magnetism*. Clarendon Press: 1983.

52. Stiegel, A.; Spiess, H. W., *Dynamic NMR spectroscopy*. Springer: Berlin Heidelberg, 1978.

53. Pietrass, T.; Taulelle, F.; Lavela, P.; Olivier-Fourcade, J.; Jumas, J.-C.; Steuernagel, S., Structure and Dynamics of Lithium-Intercalated SnS_2. ^{6,7}Li and ^{119}Sn Solid State NMR. *J. Phys. Chem. B* **1997,** *101* (34), 6715.

54. Sholl, C. A., Nuclear spin relaxation by translational diffusion in liquids and solids: high- and low-frequency limits. *Journal of Physics C: Solid State Physics* **1981,** *14* (4), 447.

55. Kuhn, A.; Sreeraj, P.; Pöttgen, R.; Wiemhöfer, H.-D.; Wilkening, M.; Heitjans, P.; Pöttgen, R.; Wiemhöfer, H. D.; Wilkening, M.; Heitjans, P.; Pöttgen, R.; Wiemhöfer, H.-D.; Wilkening, M.; Heitjans, P., Li Ion Diffusion in the Anode Material $Li_{12}Si_7$: Ultrafast Quasi-1D Diffusion and Two Distinct Fast 3D Jump Processes Separately Revealed by ^{7}Li NMR Relaxometry. *Journal of the American Chemical Society* **2011,** *133* (29), 11018.

56. Brown, I. D., Recent Developments in the Methods and Applications of the Bond Valence Model. *Chemical Reviews* **2009,** *109* (12), 6858.

57. Kuhn, A. E., V.; Schmidt, G.; Narayanan, S.; Thangadurai, V.; Wilkening, M., Spin-alignment echo NMR: probing Li^+ hopping motion in the solid electrolyte $Li_7La_3Zr_2O_{12}$ with garnet-type tetragonal structure *Journal of Physics: Condensed Matter* **2012,** *24*, 035901.

58. Wilkening, M.; Heitjans, P., From Micro to Macro: Access to Long-Range Li^+ Diffusion Parameters in Solids via Microscopic ^{6,7}Li Spin-Alignment Echo NMR Spectroscopy. *ChemPhysChem* **2012,** *13* (1), 53.

59. Langer, J.; Wilkening, M., Ultra-slow Li ion jump diffusion in Li_2SnO_3 studied by two-time ^{7}Li spin-alignment echo NMR and ^{7}Li NMR relaxometry. *Solid State Ionics* **2016,** *293*, 85.

60. Xu, Z.; Stebbins, J. F., Cation Dynamics and Diffusion in Lithium Orthosilicate: Two-Dimensional Lithium-6 NMR. *Science* **1995,** *270* (5240), 1332.

6. Overall Conclusions and Outlook

6.1 Conclusions

Throughout this thesis the research presented has utilised solid-state nuclear magnetic resonance (NMR) spectroscopy in order to probe both the structures and the Li ion dynamics of a variety of potential solid-state electrolyte candidates for use in all solid-state batteries. The identification of factors limiting long-range translational Li diffusion and understanding the effects of structural modification on Li-ion mobility provide a framework for the further development of more highly conductive Li solid electrolytes.

Chapter 3 was comprised of a series of works[1-3] regarding the newly synthesised aluminium sulfides, Li_3AlS_3 and $Li_{4.3}AlS_{3.3}Cl_{0.7}$. ^{6}Li and ^{27}Al MAS techniques in conjunction with density functional theory and x-ray diffraction were used in order to derive the structures of the two phases, while a range of variable temperature ^{6}Li and ^{7}Li nuclear magnetic resonance approaches were used in order to determine Li-ion mobility pathways, quantify Li-ion jump rates, and subsequently identify the limiting factors for Li-ion diffusion. Static ^{7}Li NMR line narrowing spectra of Li_3AlS_3 show the existence of both mobile and immobile Li ions, with the latter limiting long-range translational ion diffusion, while in $Li_{4.3}AlS_{3.3}Cl_{0.7}$, a single type of fast-moving ion is present and responsible for the higher conductivity of this phase. The slowly moving ions hop between non-equivalent Li positions in various structural layers, as shown by the ^{6}Li-^{6}Li exchange spectroscopy (EXSY) spectra of Li_3AlS_3. Li-ion jump rates that are considerably higher for the doped material were extracted

through spin-lattice relaxation (SLR) data, which also identifies three-dimensional Li mobility pathways in both materials.

Chapter 4 contained the NMR contribution to the analytical techniques used in the collaborative work, reporting an unsupervised machine learning technique for the identification of new materials.[4] The newly synthesised $Li_{3.3}SnS_{3.3}Cl_{0.7}$ was identified through this method and the structure characterised through diffraction and NMR techniques. ^{7}Li line narrowing and relaxation measurements allowed for the quantification of Li ion jump rates which were extrapolated and converted to a room temperature conductivity value of 2.6(7) x 10^{-5} S cm^{-1}. When combined with the findings from the nuclear density obtained using the maximum entropy technique, detailed analysis of the frequency dependence of the NMR relaxation rates showed low-dimensional Li-ion diffusion, which revealed the Li ion pathway to be one-dimensional. This pathway was found to pass through a shared face along the c-axis through Li octahedra.

Finally, **Chapter 5** contained the NMR contribution to the original reporting of the structure and quantification of the Li-ion mobility in the ultraphosphate phase $Li_3P_5O_{14}$[5] along with the ongoing work probing the local structure and ion dynamics through solid-state NMR. Li3P5O14 is reported to have the highest Li-ion conductivity (8.5(5) x 10^{-7} S cm^{-1}) and lowest activation energy (0.43(7) eV) of all of the ternary lithium phosphates, with a conductivity comparable to that of LiPON glass thin film electrolytes, with an increased thermodynamic stability against oxidation. ^{6}Li and ^{31}P magic-angle spinning (MAS) NMR were utilised in order to characterise the local Li and P environments in conjunction with density functional theory in order to

tentatively assign the large number of crystallographically distinct sites. The Li-ion dynamics were quantified using static ^{7}Li line narrowing NMR, spin-alignment echo (SAE) NMR, and relaxometry. Further, the experimental confirmation of the suggested 3D Li ion pathway in $Li_3P_5O_{14}$ was made possible by the frequency dependence of the ^{7}Li SLR rates in the rotating frame of reference.

Overall, the solid-state NMR spectroscopy research of four newly reported solid-state electrolyte candidates has been presented in this thesis, three of which are sulfides while the final material is an oxide. In each case, the local structure of the constituent atoms have been determined through MAS NMR. The Li-ion dynamics of all four materials have been probed via ^{6,7}Li NMR over a wide range of timescales from ns to s, with such a broad range of timescales being inaccessible through other experimental techniques.

6.2 Future Work

Both **Chapter 3** and **4** demonstrate a full characterisation of the structures and ion dynamics in the materials being reported, through a combination of diffraction techniques along MAS NMR and a range of complimentary ^{6,7}Li NMR techniques. **Chapter 5** requires further work in order to expand upon the Li-ion dynamics in $Li_3P_5O_{14}$, while the ion dynamics have been quantified through ^{7}Li line narrowing, SAE NMR and relaxometry, the site specific information that leads to the identification of the Li-ion mobility pathway and potential rate-limiting steps (such as in Li_3AlS_3 in **Chapter 3**) has not been accessed.

Assessing the site specific Li-ion jump rates for the large number of Li sites is challenged by the lack of resolution in the ^{6}Li MAS NMR spectrum. Two possible methods for quantifying these Li-ion jump rates are firstly, ^{6}Li MAS spectra as a function of temperature and observing the peak coalescence as a result of motional averaging (see **Chapter 3**) and secondly ^{6}Li-^{6}Li EXSYs as a function of the mixing time, in order to model the resulting cross-peak build ups. The challenge here, along with the lack of resolution, is the extremely long ^{6}Li SLR time massively increasing experiment time. One solution to both of these challenges is to perform these experiments at higher field, the increased field strength increases resolution and signal, allowing for fewer scans and a decreased experiment time.

Another aspect of the solid-state NMR data for $Li_3P_5O_{14}$ that requires further work is the assignment of the ^{31}P resonances. In **Chapter 5**, the assignment of the ^{31}P NMR spectrum (**Figure 6.1(a)**) relies upon the calculation of the

NMR parameters from the geometry optimised structure using the GIPAW approach.[6,7] However, the assignment of these resonances does not fully agree with the experimental correlations observed in the ^{31}P-^{31}P spin diffusion NMR (**Figure 6.1(b)**). This is unsurprising, due to the large number of P sites in extremely similar environments in $Li_3P_5O_{14}$ and the relatively small chemical shift range.

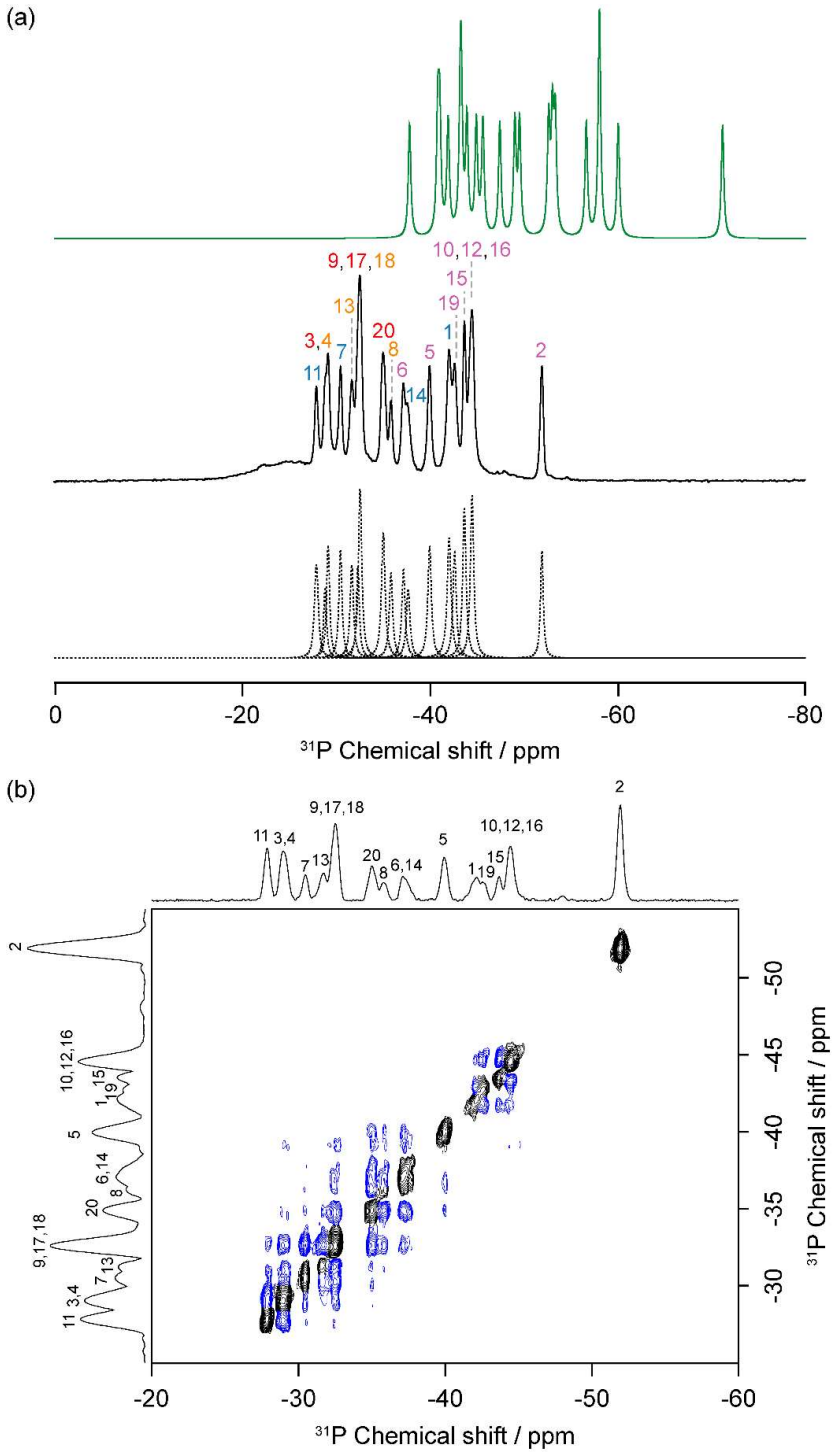

Figure 6.1 (a) ^{31}P MAS spectrum of $Li_3P_5O_{14}$ collected 9.4 T and $\omega_r/2\pi$ = 10 kHz with the spectral assignment based off the DFT simulations. The experimental spectrum (full black line), spectral deconvolution (dotted lines) and GIPAW-simulated spectrum (green line) are shown. (b) 2D ^{31}P-^{31}P spin-diffusion NMR spectra of $Li_3P_5O_{14}$ recorded at a mixing time of 1 s with diagonal and cross peaks shown in black and blue, respectively.

In order to expand upon the ^{31}P NMR and rationalise further the NMR data with the crystal structure, one option to enhance the results here would be to perform further ^{31}P-^{31}P spin diffusion experiments as a function of tm, in order to plot the cross peak build up and extract dipolar coupling constants by modelling the data.[8] A second option would be further correlation experiments such as ^{31}P-^{31}P Incredible Natural Abundance Double Quantum Transfer Experiment (INADEQUATE) allowing for the correlation of the various P atoms that share bridging O atoms through $^{2}J_{PP}$ coupling[9-11] or ^{6,7}Li-^{31}P Rotational-Echo Double Resonance (REDOR) NMR with refocussing on ^{31}P, in order to extract heteronuclear dipolar coupling constants between the Li and P sites.[12]

6.3 References

1. Gamon, J.; Duff, B. B.; Dyer, M. S.; Collins, C.; Daniels, L. M.; Surta, T. W.; Sharp, P. M.; Gaultois, M. W.; Blanc, F.; Claridge, J. B.; Rosseinsky, M. J., Computationally Guided Discovery of the Sulfide Li_3AlS_3 in the Li–Al–S Phase Field: Structure and Lithium Conductivity. *Chemistry of Materials* **2019,** *31* (23), 9699.

2. Gamon, J.; Dyer, M. S.; Duff, B. B.; Vasylenko, A.; Daniels, L. M.; Zanella, M.; Gaultois, M. W.; Blanc, F.; Claridge, J. B.; Rosseinsky, M. J., $Li_{4.3}AlS_{3.3}Cl_{0.7}$: A Sulfide-Chloride Lithium Ion Conductor with Highly Disordered Structure and Increased Conductivity. *Chemistry of Materials* **2021,** *33* (22), 8733.

3. Duff, B. B.; Elliott, S. J.; Gamon, J.; Daniels, L. M.; Rosseinsky, M. J.; Blanc, F., Toward Understanding of the Li-Ion Migration Pathways in the Lithium Aluminum Sulfides Li_3AlS_3 and $Li_{4.3}AlS_{3.3}Cl_{0.7}$ via $^{6,7}Li$ Solid-State Nuclear Magnetic Resonance Spectroscopy. *Chemistry of Materials* **2023,** *35* (1), 27.

4. Vasylenko, A.; Gamon, J.; Duff, B. B.; Gusev, V. V.; Daniels, L. M.; Zanella, M.; Shin, J. F.; Sharp, P. M.; Morscher, A.; Chen, R.; Neale, A. R.; Hardwick, L. J.; Claridge, J. B.; Blanc, F.; Gaultois, M. W.; Dyer, M. S.; Rosseinsky, M. J., Element selection for crystalline inorganic solid discovery guided by unsupervised machine learning of experimentally explored chemistry. *Nature Communications* **2021,** *12*, 5561.

5. Han, G.; Vasylenko, A.; Neale, A. R.; Duff, B. B.; Chen, R.; Dyer, M. S.; Dang, Y.; Daniels, L. M.; Zanella, M.; Robertson, C. M.; Kershaw Cook, L. J.; Hansen, A. L.; Knapp, M.; Hardwick, L. J.; Blanc, F.; Claridge, J. B.; Rosseinsky, M. J., Extended Condensed Ultraphosphate Frameworks with Monovalent Ions Combine Lithium Mobility with High Computed Electrochemical Stability. *Journal of the American Chemical Society* **2021,** *143* (43), 18216.

6. Pickard, C. J.; Mauri, F., All-electron magnetic response with pseudopotentials: NMR chemical shifts. *Physical Review B* **2001,** *63* (24), 245101.

7. Yates, J. R.; Pickard, C. J.; Mauri, F., Calculation of NMR chemical shifts for extended systems using ultrasoft pseudopotentials. *Physical Review B* **2007,** *76* (2), 024401.

8. Dusold, S.; Kümmerlen, J.; Schaller, T.; Sebald, A.; Dollase, W. A., A ^{31}P Spin Diffusion and ^{31}P–^{113}Cd CP/MAS NMR Study of Polycrystalline $Cd_3(PO_4)_2$. *The Journal of Physical Chemistry B* **1997,** *101* (33), 6359.

9. O'Dell, L. A.; Guerry, P.; Wong, A.; Abou Neel, E. A.; Pham, T. N.; Knowles, J. C.; Brown, S. P.; Smith, M. E., Quantification of crystalline phases and measurement of phosphate chain lengths in a mixed phase sample by ^{31}P refocused INADEQUATE MAS NMR. *Chemical Physics Letters* **2008,** *455* (4), 178.

10. Guerry, P.; Smith, M. E.; Brown, S. P., ^{31}P MAS Refocused INADEQUATE Spin−Echo (REINE) NMR Spectroscopy: Revealing J Coupling and Chemical Shift Two-Dimensional Correlations in Disordered Solids. *Journal of the American Chemical Society* **2009,** *131* (33), 11861.

11. Döhler, F.; Mandlule, A.; van Wüllen, L.; Friedrich, M.; Brauer, D. S., ^{31}P NMR characterisation of phosphate fragments during dissolution of calcium sodium phosphate glasses. *Journal of Materials Chemistry B* **2015,** *3* (6), 1125.

12. van Wüllen, L.; Eckert, H.; Schwering, G., Structure−Property Correlations in Lithium Phosphate Glasses: New Insights from ^{31}P ↔ ^{7}Li Double-Resonance NMR. *Chemistry of Materials* **2000,** *12* (7), 1840.